

Towards a Global Classification of Volcanic Tremor

by

Katharina Claudia Unglert

B.Sc., Technical University/Ludwig-Maximilians-Univ., Munich, Germany, 2008

M.Sc., Victoria University of Wellington, New Zealand, 2011

A THESIS SUBMITTED IN PARTIAL FULFILLMENT OF
THE REQUIREMENTS FOR THE DEGREE OF

DOCTOR OF PHILOSOPHY

in

The Faculty of Graduate and Postdoctoral Studies

(Geophysics)

THE UNIVERSITY OF BRITISH COLUMBIA

(Vancouver)

August 2016

© Katharina Claudia Unglert 2016

Abstract

Volcanic tremor, a seismic signal with longer durations and lower frequency content compared to local earthquakes, is often observed before or during eruptions and may consequently be useful for eruption forecasting. However, the processes generating volcanic tremor are still poorly understood. The main goal of this thesis is to assess systematic similarities and differences among tremor from a global sample of volcanoes, which is crucial to successfully constrain plausible source mechanisms. Using time series analysis of seismic signals accompanying three eruptive episodes at Kīlauea Volcano, Hawai‘i, I show that two characteristic phases of seismicity accompany dike intrusions, and that a different type of tremor occurs during a period of explosive activity. The signals differ in their spatial, temporal, and most strongly in their spectral properties. I thus construct a synthetic dataset of spectra that mimic the different spectral shapes observed in Hawai‘i. I use this dataset to evaluate the performance of two pattern recognition algorithms that may facilitate a global comparison of volcanic tremor spectra. A variety of tests with the synthetic spectra including different numbers and character of spectral patterns, as well as increasing levels of noise reveal that Principal Component Analysis and hierarchical clustering, in combination with a newly developed criterion to determine the ideal number of groupings in the data, can successfully identify the correct number and character of the known spectra. I thus develop a detection algorithm for volcanic tremor and apply the pattern recognition approach to detect patterns in tremor spectra from Kīlauea, Okmok, Pavlof, and Redoubt volcanoes. By analyzing the station network for each volcano individually, I show that tremor has distinct spatial and temporal characteristics for each of the volcanic settings. A subsequent comparative analysis suggests that several volcanic settings share common spectral tremor characteristics. I identify at least four types of volcanic tremor with systematic variations among the four settings, which indicates relationships to volcanic controls such as magma storage depth and viscosity. Further analysis of tremor from a larger sample of volcanoes will help to constrain plausible source processes and ultimately improve eruption forecasting.

Preface

This thesis is based on three papers: One has been published, one has been accepted, and one is in preparation for publication. Consequently, there is some cross-over among the different papers, in particular in the introductory sections. Furthermore, some information from Chapter 1 is repeated in the papers.

The idea to investigate volcanic tremor on a global scale was Mark Jellinek's. I did the necessary background research, developed the approach to undertake the multi-volcano comparison, obtained the data, and performed all analyses unless indicated otherwise below.

A version of Chapter 2 has been published in *Journal of Geophysical Research: Solid Earth*. The co-authors are Katharina Unglert (first author) and Mark Jellinek. The data analyzed in this chapter were kindly provided by the Hawaiian Volcano Observatory (HVO). I discovered the two characteristic phases of seismicity and associated frequency gliding, performed all the calculations and analyses up to (and including) Section 2.3, made the figures, and wrote the manuscript except for Section 2.4.3. The scalings in Section 2.4.3 were derived by Mark Jellinek on the basis of discussions between him and me about the results. The writing of Section 2.4.3 was a combined effort. Mark Jellinek also provided scientific guidance throughout and commented on the manuscript.

A version of Chapter 3 has been published in *Journal of Volcanology and Geothermal Research*. The co-authors are Katharina Unglert (first author), Valentina Radić, and Mark Jellinek. The data from the three volcanoes shown in this chapter were kindly provided by HVO and the Alaska Volcano Observatory (AVO). I developed the idea to use spectral shapes for pattern recognition and to apply automated algorithms to identify the characteristic spectral shapes. Furthermore, I decided to evaluate the performance of pattern recognition algorithms in a comparative study with synthetic data before conducting the global comparison on real data. I generated the synthetic dataset, performed all the calculations and analyses, made the figures, and wrote the manuscript. The only exception are the additional tests on non-traditional clustering approaches in Section 5.2, that were suggested and run by Valentina Radić in preparation of a follow-up publication separate from my PhD. Mark Jellinek and Valentina Radić provided scientific guidance throughout the data development and analysis stage, and commented on the manuscript.

A version of Chapter 4 has been submitted for publication. The co-authors are Katharina Unglert (first author) and Mark Jellinek. The data from the four volcanoes shown in this chapter were kindly provided by HVO and AVO. I developed the idea to perform the analysis separately on the individual station networks before conducting the multi-volcano comparison. I prepared all datasets for processing, performed all calculations and analyses, made the figures and wrote the manuscript. Mark Jellinek provided scientific and editorial guidance throughout.

Journal Papers

Chapter 2

Unglert, K., and A.M. Jellinek (2015), Volcanic Tremor and Frequency Gliding during Dike Intrusions at Kilauea – A Tale of Three Eruptions, *Journal of Geophysical Research: Solid Earth*, *120*(2), 1142–1158, doi: 10.1002/2014JB011596.

Chapter 3

Unglert, K., V. Radić, and A.M. Jellinek (2016), Principal Component Analysis vs. Self-Organizing Maps Combined with Hierarchical Clustering for Pattern Recognition in Volcano Seismic Spectra, *Journal of Volcanology and Geothermal Research*, *320*, 58–74, doi: 10.1016/j.jvolgeores.2016.04.014.

Chapter 4

Unglert, K., and A.M. Jellinek (in review), Spectral Pattern Recognition Reveals Distinct Classes of Volcanic Tremor.

Table of Contents

Abstract	ii
Preface	iii
Table of Contents	v
List of Tables	viii
List of Figures	ix
Acknowledgements	xi
1 Introduction & Motivation	1
1.1 Overview	1
1.2 Tremor Observations	2
1.2.1 Time Domain	2
1.2.2 Tremor Locations	2
1.2.3 Frequency Domain	4
1.2.4 Association with Other Observables	7
1.2.5 Tremor Mechanisms	8
1.3 The Need for a Global Classification	12
1.3.1 Guiding Hypotheses	12
1.3.2 Methods	13
1.3.3 Thesis Outline	16
2 Volcanic Tremor & Frequency Gliding at Kīlauea	19
2.1 Introduction	20
2.2 Three Eruptions at Kīlauea, Hawai‘i	20
2.2.1 The 2007 Father’s Day Eruption	21
2.2.2 The 2008 Halema‘uma‘u Explosions	22
2.2.3 The 2011 Kamoamoā Eruption	22
2.3 Data & Results	22
2.3.1 Network & Data Processing	22
2.3.2 Overview of Seismic Signals	23
2.3.3 Phases of Seismicity During Intrusions	26

Table of Contents

2.3.4	Frequency Gliding	28
2.3.5	Summary of Main Results	29
2.4	Discussion	29
2.4.1	Tremor & Eruptive Styles	30
2.4.2	Phase I: The Early Stages of Intrusion	31
2.4.3	Temporal & Spatial Constraints on Tremor	31
2.4.4	Remaining Challenges	38
2.5	Conclusions	39
3	Principal Component Analysis vs. Self-Organizing Maps	41
3.1	Introduction	42
3.2	Data and Preprocessing	43
3.2.1	Synthetic Spectra	45
3.2.2	Preprocessing Steps	47
3.3	Principal Component Analysis	48
3.3.1	PCA and Clustering	48
3.3.2	Performance of PCA and Clustering at Higher Noise Levels	53
3.4	Self-Organizing Maps	54
3.4.1	SOM Topology Size	56
3.4.2	Results and Clustering of SOM Patterns	58
3.5	Discussion	60
3.5.1	Summary of Steps Taken for Each Method: Parameter Choices	60
3.5.2	Limitations of Typical Volcano Seismic SOM Approach	61
3.5.3	Limitations of our Synthetic Data and the PCA Approach	63
3.6	Conclusions	69
4	Spectral Pattern Recognition Reveals Distinct Classes of Volcanic Tremor	71
4.1	Introduction	72
4.2	Volcanic Settings	72
4.3	Data and Preprocessing	73
4.3.1	Distinguishing Tremor from the Background	74
4.3.2	Removing Earthquake Signals	74
4.3.3	Obtaining Tremor Spectra	77
4.4	Spectral Pattern Recognition	77
4.4.1	Overview	77
4.4.2	PCA for Multiple Stations at Individual Settings	81
4.4.3	PCA for Comparison Between Volcanic Settings	91
4.5	Discussion	97
4.5.1	Kīlauea: 2007, 2008, 2011	97
4.5.2	Okmok: 2008	99

Table of Contents

4.5.3	Pavlof: 2007, 2013	100
4.5.4	Redoubt: 2009	101
4.5.5	Implications for Tremor Detection Algorithm	102
4.5.6	Joint Analysis: Lessons Learned	103
4.6	Conclusions	108
5	Concluding Remarks	110
5.1	Summary of Work and Context for Each Publication	110
5.2	Revisiting the Hypotheses	112
5.3	Outlook	114
	Bibliography	116
	Appendix	
A	Use of Color Maps and Human Perception	137
A.1	Challenges with Color Maps	137
A.2	Some Ideas for Improvement	139
A.2.1	Using Line Graphs Instead of Images	139
A.2.2	Greyscale Color Maps	139
A.2.3	Perceptually Uniform Color Maps	141

List of Tables

3.1	Quality measurements and clustering results for different noise levels, PCA vs. SOM	50
3.2	Quality measurements and clustering results for different SOM sizes at noise level 0.1	56
3.3	Quality measurements and clustering results for different noise levels based on difference criterion, PCA vs. SOM	67
3.4	Clustering results for different frequency bands, PCA vs. SOM	68
4.1	Summary of volcanoes, stations, data time period, and number of tremor windows .	76

List of Figures

1.1	Example seismograms for volcanic tremor.	3
1.2	Example spectrograms for harmonic tremor and frequency gliding.	6
1.3	Schematic for selected tremor mechanisms	10
1.4	Schematic for Principal Component Analysis	14
1.5	Schematic for Self-Organizing Maps algorithm	14
1.6	Schematic for hierarchical clustering algorithm	16
2.1	Map of Kīlauea and timeline of important events.	21
2.2	Spectrograms for 2007, 2008, and 2011.	24
2.3	Spectrograms during intrusions in 2007 and 2011.	25
2.4	Spectra and RMS velocity in 2007, 2008, and 2011 at AHU.	27
2.5	Spectrograms showing gliding during 2007 and 2011.	28
2.6	Simplified cartoon of Kīlauea plumbing system.	34
3.1	Examples of different spectral shapes and transitions between them from Kīlauea, Redoubt, and Okmok.	44
3.2	Synthetic data setup	46
3.3	Normalized synthetic data used as input for pattern recognition algorithms	48
3.4	PCA results for noise level 0.1	49
3.5	Cluster evaluation diagnostics, noise level 0.1	52
3.6	PCA results for noise level 1.5	53
3.7	Output from SOM algorithm, noise level 0.1	55
3.8	Examples of feature spectra from SOM	57
3.9	Clustering of SOM topology, noise level 0.1	59
3.10	Clustering of SOM topology, noise level 0.1, manual selection of $k = 3$	60
3.11	PCA plus clustering method applied to synthetic dataset with flipped Phase II pattern	64
3.12	PCA plus clustering method applied to synthetic dataset with modified Phase II pattern	65
4.1	Examples for background signal estimation	75
4.2	Example seismogram showing different cases of our tremor detection	75
4.3	PCA and clustering results for network analysis at Kīlauea, 2007, 2008, and 2011	79
4.4	Clustering time series for network analysis at Kīlauea, 2007	80

List of Figures

4.5	Clustering time series for network analysis at Kīlauea, 2008	82
4.6	Clustering time series for network analysis at Kīlauea, 2011	83
4.7	PCA and clustering results for multistation analysis at Okmok, 2008	85
4.8	Clustering time series for network analysis at Okmok, 2008	86
4.9	PCA and clustering results for network analysis at Pavlof, 2007 and 2013	87
4.10	Clustering time series for network analysis at Pavlof, 2007	88
4.11	Clustering time series for network analysis at Pavlof, 2013	88
4.12	PCA and clustering results for network analysis at Redoubt, 2009	90
4.13	Clustering time series for network analysis at Redoubt, 2009	91
4.14	PCA and clustering results for combined analysis, for proximal stations	93
4.15	Clustering results for combined analysis, for proximal stations	94
4.16	Clustering time series for combined analysis, proximal stations	95
4.17	PCA and clustering results for combined analysis, for distal stations	96
4.18	Clustering time series for combined analysis, distal stations	97
4.19	Zoom into temporal evolution of main clusters during intrusions at Kīlauea	99
4.20	Detection rates at station RSO during several days in May 2009	102
4.21	Summary of tremor types in relation to volcano and eruption characteristics	105
A.1	Color use in geoscience publications.	138
A.2	Ordering issues for rainbow color maps.	139
A.3	Line graph spectrograms	140
A.4	Greyscale spectrogram	140
A.5	Spectrogram from Hawai‘i with different color maps.	142

Acknowledgements

Several people have helped me in one way or another during the course of my PhD, and deserve my gratitude. I would like to thank my supervisor, Mark Jellinek, whose continuous enthusiasm about our work was extremely inspiring, and whose support extended far beyond simple academic questions. Thanks also to my committee, Catherine Johnson, Valentina Radić, Diana Roman, and Michael Bostock, for their guidance and encouragement throughout.

This work would not have been possible without the data so generously shared by the USGS volcano observatories, and the countless fruitful discussions with Milton Garces, Jess Johnson, Kostas Konstantinou, Jonathan Lees, Steve McNutt, Mike Poland, John Power, Glenn Thompson, Wes Thelen, Aaron Wech, and many more. Funding through a UBC 4-Year-Fellowship and a Vanier Scholarship were a tremendous help. Thanks also to Keegan Lensink, whose work during his summer internship was a great help for my data processing.

Over the years, my office was always filled with amazing colleagues and friends who never hesitated to offer a word of advice or a listening ear. My thanks goes to Thomas Aubry, Eric Deal, Kirsten Hodge, Yoshi Gilchrist, Anna Grau, Anna Mittelholz, Geneviève Savard, Reka Winslow, and everyone else.

Furthermore, I would like to thank the Graduate Student Council and of course all the awesome volunteers in the Pacific Museum of Earth and with Let's Talk Science for giving me the chance to explore some non-academic ways of involvement.

I am grateful to the Crichtons, who gave me a home and took me into their family as if I had always been there. Thanks also to Susi Iberle, the best friend anyone could wish for, and to all my other friends and family, near and far, who are always there for me. Last but not least, thanks to James Hickey, for everything.

Chapter 1

Introduction & Motivation

1.1 Overview

Volcanic eruptions are often preceded and accompanied by a low-frequency (approximately 0.5–10 Hz) seismic signal called “volcanic tremor” (*Aki and Koyanagi, 1981; Neuberg, 2000; Konstantinou and Schlindwein, 2002; McNutt and Nishimura, 2008*), hereafter referred to as “tremor”. Tremor persists for minutes to weeks. Its occurrence is often interpreted as a sign of an impending eruption (e.g., *D’Agostino et al., 2013; Chardot et al., 2015*). The reliability of tremor as a forecasting tool is, however, uncertain, because the underlying physical processes remain unclear (e.g., *Chouet, 1986; Julian, 1994; Benoit and McNutt, 1997; Ripepe and Gordeev, 1999; Neuberg et al., 2000; Lesage et al., 2006; Jellinek and Bercovici, 2011; Dmitrieva et al., 2013; Bean et al., 2014*). Tremor is ubiquitous in all tectonic settings, despite the fact that these settings can be fundamentally different e.g. in terms of magma composition. Tremor can be described by properties such as frequency content, amplitudes, or source depth. The spatial and temporal relationships between tremor properties and other observables¹ are often unknown and potentially complicated. A range of tremor observations in different locations (*Konstantinou and Schlindwein, 2002; McNutt and Nishimura, 2008*) suggests that tremor may be the expression of a variety of underlying mechanical processes depending on volcanic and tectonic controls (e.g. volcano type, magma composition, tectonic setting, etc.). A systematic classification of tremor from a variety of volcanoes is thus necessary to improve understanding of the source processes of volcanic tremor. This is the goal of my PhD.

This section provides the necessary background for the following chapters. I give an overview of tremor observations at many different volcanoes in Section 1.2, and discuss the need for a global classification of tremor and outline the most important methods in Section 1.3.

¹“Other observables” here and in the following sections refers to monitoring parameters such as visual observations of eruptive activity, ground deformation, infrasound, gas emissions, or composition of erupted products.

1.2 A Global Survey of Tremor Observations

The term “tremor” has been used to describe various seismic signals since the early 20th century (e.g., on Kīlauea, *Jaggard*, 1920). More recently, tremor has been defined as a low-frequency², long-lasting³ seismic signal associated with active volcanism (*McNutt*, 1992; *Chouet and Matoza*, 2013). Volcanic tremor has been observed in many tectonic and volcanic settings from basaltic ocean islands (e.g. Kīlauea, *Omer*, 1950; *Ferrazzini et al.*, 1991; *Patrick et al.*, 2011a) to more silicic arc volcanoes (e.g., Mount St. Helens, USA *Fehler*, 1983; Augustine, USA *Reeder and Lahr*, 1987; or Cordón Caulle, Chile *Bertin et al.*, 2015). In the following sections, I give an overview of tremor in terms of its temporal, spatial, and spectral characteristics, discuss their relation to other types of observations, and review constraints on source mechanisms. The range of observations summarized in the following sections motivate a systematic global classification of volcanic tremor.

1.2.1 Time Domain

Most volcanic tremor episodes have an emergent onset (e.g. Pavlof, USA *McNutt*, 1987a, Fig. 1.1(a), or Soufrière Hills Volcano, Montserrat *Neuberg et al.*, 1998). However, tremor events with impulsive onsets have also been observed (e.g. Karymsky, Russia, *Johnson and Lees*, 2000, or Kīlauea, USA, *Aki and Koyanagi*, 1981). Individual episodes can persist for minutes to hundreds of hours (e.g. *Brandsdóttir and Einarsson*, 1992; *Lesage et al.*, 2006; *McNutt and Nishimura*, 2008). Tremor amplitudes sometimes vary on timescales of seconds to minutes (e.g. Arenal, Costa Rica *Lesage et al.*, 2006, Kīlauea, *Patrick et al.*, 2011a, or Redoubt, USA, Fig. 1.1(c)). The temporal evolution of these amplitude variations can be systematic such as on Grímsvötn, Iceland, (“tremor bursts”, *Brandsdóttir and Einarsson*, 1992) or on Nevado del Ruiz, Colombia, (“cyclic tremor”, *Chouet*, 1992), or irregular such as on Arenal, or Redoubt, (“spasmodic” *Lesage et al.*, 2006, , Fig. 1.1(c)). Furthermore, such amplitude variations can transition from one into the other (*Brandsdóttir and Einarsson*, 1992). Long-period earthquakes (LPs) have sometimes been observed to become more closely spaced in time and merge into continuous tremor (e.g., at Soufrière Hills Volcano, *Neuberg et al.*, 1998, Fig. 1.1(b), Kīlauea, *Koyanagi et al.*, 1987, and Redoubt, *Hotovec et al.*, 2013).

1.2.2 Tremor Locations

LP Locations

An inability to identify clear phase arrivals within tremor episodes as well as their emergent onset prevent the use of traditional earthquake location methods (e.g. *Konstantinou and Schlindwein*,

²Tremor is often combined into one category with long-period earthquakes (LPs) or very long period earthquakes (VLPs) based on the hypothesis that tremor is a series of closely spaced LPs (*Powell and Neuberg*, 2003). For this thesis, LPs are defined as earthquakes with longer periods/lower frequencies than tectonic or volcano-tectonic earthquakes, loosely based on the definitions of *Minakami* (1960) and *Latter* (1981). My definition of LPs also includes “hybrid” events from *Neuberg et al.* (1998). The terms “tremor” and “LPs” here stand for distinct seismic signals that are in general not assumed to be directly related. Potential links between them will be discussed specifically, e.g. if it is a necessary part of a model or observation.

³The long duration is in comparison to local earthquakes.

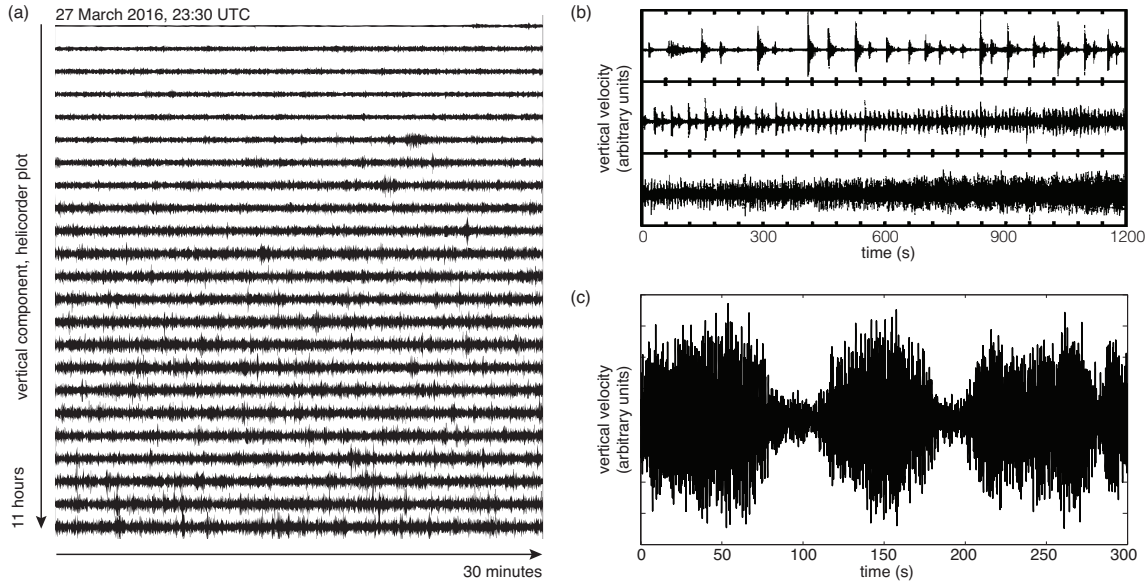


Figure 1.1: Example seismograms for volcanic tremor. (a) Tremor shows emergent onset at Pavlof Volcano, USA, station PVV during an eruptive period in March 2016. (b) Three consecutive 20-minute seismograms on vertical component of broadband station MBGA at Soufrière Hills Volcano, Montserrat, time of recording unknown. LPs become more closely spaced in time and eventually merge into tremor (*Neuberg et al., 1998*). *Reproduced with permission from Wiley*. (c) Tremor amplitude varies over timescales of tens of seconds at Redoubt Volcano, USA, station RSO in January 2009.

2002). However, there are other approaches to locating volcanic tremor. Tremor and LPs sometimes occur during the same period, show similar attenuation of amplitudes with distance, and/or have similar spectral characteristics (e.g. Soufrière Hills Volcano, *Neuberg et al., 1998*, or Kīlauea, *Koyanagi et al., 1987*). These similarities could indicate a common source mechanism for tremor and LPs (e.g. *Koyanagi et al., 1987; Neuberg et al., 1998*). Consequently, the first approach to locating tremor is to identify LP locations, for example on the basis of differential arrival times (*Neuberg et al., 1998*). *Koyanagi et al. (1987)* identify three tremor source depth intervals on Kīlauea. The shallow (<5 km) and intermediate (5–15 km) intervals show tremor confined to the summit and the East Rift Zone (ERZ), whereas the deep (30–60 km) tremor source region appears to be further south and not associated with active vents. Similar to shallow tremor at Kīlauea, *Neuberg et al. (1998)* identify a region approximately 2–3 km beneath the active lava dome as the source for tremor at Soufrière Hills Volcano. *Hotovec et al. (2013)* find repeating earthquakes that are assumed to merge into tremor at a depth of approximately 2 km beneath the vent at Redoubt.

Tremor Amplitude Decay with Distance

The amplitude of tremor and its spatial distribution has been used to pinpoint tremor to the summit region with the central craters at Etna, Italy (*Riuscetti et al., 1977; Patanè et al., 2013*). Furthermore, on the basis of frequency dependent decay of amplitudes with distance, *Riuscetti et al. (1977)* are

able to distinguish between different source depths for two spectral peaks of the tremor spectrum, one directly beneath the crater floor, and the other approximately 0.5–1 km beneath that surface. *Patanè et al.* (2013) find tremor sources up to 3 km below the active craters. *Aki and Koyanagi* (1981) use the spatial distribution of tremor amplitudes to identify deep tremor at Kīlauea (~40 km, *Aki and Koyanagi*, 1981). At Piton de la Fournaise, Réunion, *Battaglia and Aki* (2003) use the site corrected amplitude distribution in different frequency bands to identify tremor sources at shallow depths of a few kilometers in close proximity to active vents. *Kumagai et al.* (2010) develop a more general version of this method, which accounts for anisotropic wave radiation. *Ogiso and Yomogida* (2012) apply this method to identify a migrating tremor source at 1–2 km within a few kilometers of the active crater at Meakandake Volcano. Similarly, tremor locations at Ontake Volcano, Japan, are found to originate from an increasingly deeper source beneath the active craters before the onset of the 2014 eruption (*Ogiso et al.*, 2015). *Jones et al.* (2012) detect the source of isotropically radiated P-waves based on seismic amplitudes in different frequency bands at Erta 'Ale. They find tremor sources below the previously active northern crater, the currently active lava lake and in between, at depths of a few hundred meters below the surface and shallower (*Jones et al.*, 2012).

Array Analysis

If a seismic array⁴ is used, wavefield properties such as time delays of wave arrivals between different stations or wave azimuth can be used to make inferences about tremor source locations. *Chouet et al.* (1997) find tremor to be located generally less than 200 m below the summit crater at Stromboli. Array analysis at Etna is used to identify a tremor source below the central crater during non-eruptive periods (*Del Pezzo et al.*, 1993), in agreement with the results by *Riuscetti et al.* (1977) mentioned above. Similarly, *Métaxian et al.* (1997) determine the tremor source location at Masaya Volcano a few hundred meters below the volcanic surface in the lava lake in Santiago crater. By showing that array analysis techniques can be extended to larger seismic station networks for very long period (<0.5 Hz) signals, *Haney* (2010) identify a tremor source location at 2.4 km below the surface at Okmok Volcano, close to the site of a new cone built during the 2008 eruption.

In summary, tremor source locations appear to be restricted to two depth intervals: Deep tremor at a depth of a few tens of kilometers has only been found at Kīlauea. Shallow tremor is commonly found between the surface and up to a few kilometers depth. It is often located close to current and former eruptive vents.

1.2.3 Frequency Domain

Snapshots of Frequency Content

The most diagnostic tremor properties are often apparent in the frequency domain. I first discuss snapshots of frequency content at isolated moments in time or averaged over a time window, without

⁴i.e. several seismometers with narrow interstation spacing and an overall array size on the order of hundreds of meters to a few kilometers (e.g., *Gordeev et al.*, 1990; *Chouet et al.*, 1997)

taking into account the temporal evolution. I consider the temporal evolution of tremor frequency content in the next section.

Typically, the “low” frequency content observed in tremor signals in comparison to local earthquakes quantitatively ranges between 0.5–10 Hz with most of the energy concentrated between 1–3 Hz (*Konstantinou and Schlindwein, 2002; McNutt and Nishimura, 2008*). Notable exceptions to both the upper and the lower limit include tremor at Redoubt (up to ~ 30 Hz, *Hotovec et al., 2013*), the Volcano Island Arc (up to 40 Hz on submarine records, *Dziak and Fox, 2002*), Okmok and Stromboli (very long period tremor, 0.02–0.5 Hz, *De Lauro et al., 2005; De Martino et al., 2005; Haney, 2010*) and Usu (≤ 0.1 Hz, *Yamamoto et al., 2002*).

A distinction between narrowband (e.g. Hekla, 1.5–3 Hz, *Brandsdóttir and Einarsson, 1992*, or Ruapehu, 1.8–2.3 Hz, *Hurst and Sherburn, 1993*) and broadband (e.g. Deception Island, 1–10 Hz, *Vila et al., 1992*; or Piton de la Fournaise, 1–5 Hz, *Battaglia et al., 2005*) tremor exists⁵. Furthermore, tremor is sometimes harmonic with a fundamental mode (typically between 0–2 Hz) and one or more harmonics (Fig. 1.2) such as on Semeru (*Schlindwein et al., 1995*), Arenal (*Lesage et al., 2006*), Karymsky (*Lees et al., 2004*), Redoubt (*Hotovec et al., 2013*), and Kīlauea (*Koyanagi et al., 1987*).

Temporal Evolution of Frequency Content

Many cases of harmonic tremor show a phenomenon called “frequency gliding”. Gliding refers to the gradual shift in frequency of a spectral peak in time. This behaviour has been observed at Kīlauea for several decades (e.g. *Finch, 1949; Aki and Koyanagi, 1981*). To my knowledge the term “gliding” was first introduced by *Dibble (1972)* for a gradually shifting spectral peak in the tremor spectrum at Pu‘u Huluhulu (Kīlauea) during the Mauna Ulu eruption in February 1971. The term then became more common in the 1990s (e.g. *Hurst and Sherburn, 1993*). Gliding can be divided into groups according to three distinct behaviours (Fig. 1.2):

1. Sinusoidal, where the location of peaks in spectral space changes approximately periodically over time (Semeru, *Schlindwein et al., 1995*).
2. Exponential, where frequency increases or decreases exponentially with time (e.g. Soufrière Hills Volcano, *Neuberg et al., 1998*, or Redoubt, *Hotovec et al., 2013*).
3. Irregular, where frequency peaks shift up and down in a seemingly random way (e.g. Arenal, *Benoit and McNutt, 1997; Lesage et al., 2006*, or Langila, *Mori et al., 1989*).

Gliding episodes typically last from a few minutes (e.g. Redoubt, *Hotovec et al., 2013*) to approximately half an hour (e.g. Soufrière Hills Volcano, *Powell and Neuberg, 2003*). However,

⁵Note that the observation of frequency ranges discussed in this section is often based on visual assessment of colored spectrograms, such as the ones presented in Figure 1.2. Typically, the color maps used for these displays are generic and not specifically suited for the purpose. Appendix A summarizes some of the challenges related to the use of colormaps, and discusses some possible improvements to the status quo. Whereas such improvements have not been applied in Chapter 2, the subsequent chapters include only color maps that are perceptually uniform to avoid bias.

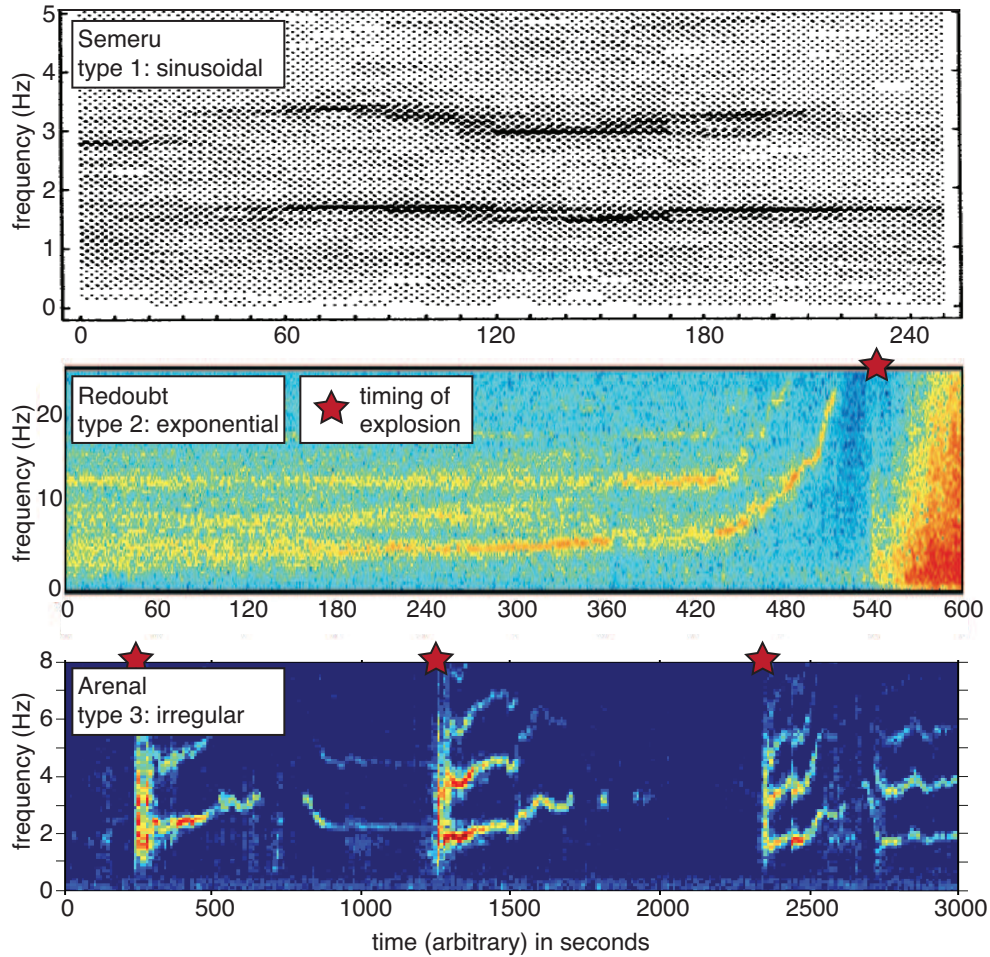


Figure 1.2: Example spectrograms for harmonic tremor and each type of frequency gliding. (1) Sinusoidal gliding at Semeru, timing relative to explosion unknown (*Schindwein et al.*, 1995). *Reproduced with permission from Wiley.* (2) Exponential upglide at Redoubt prior to an explosion (red star, *Hotovec et al.*, 2013). *Reproduced with permission from Elsevier.* (3) Irregular up- and downglides at Arenal before and after 3 explosions (*Benoit and McNutt*, 1997). *Reproduced with permission from Wiley.*

I revisit gliding and introduce a newly discovered, long duration gliding signal (compared to the episode lengths mentioned above) at Kīlauea in Chapter 2. Often, all harmonics in the spectrum glide together, with the lowest harmonic increasing or decreasing in frequency between 0.5–6 Hz (e.g. *Mori et al.*, 1989; *Schlindwein et al.*, 1995; *Powell and Neuberg*, 2003). A notable exception is Redoubt, where spectral peaks glide up to 30 Hz. The occurrence and character of gliding is often used to identify a source mechanism for volcanic tremor. I discuss temporal coincidence of tremor with variations of other observables and briefly give an overview of potential source mechanisms below.

1.2.4 Association with Other Observables

Character and Timing Relative to Eruptions

Many studies have shown a qualitative temporal correlation of tremor with other observations, such as eruptive activity and its temporal evolution. *McNutt* (1992) suggested that 30-60% of tremor episodes⁶ accompany volcanic eruptions. If tremor always occurs before the start of an eruption it could be used for eruption forecasting. However, only approximately 20% of tremor episodes precede eruptions by 10 days or less (*McNutt*, 1992). Frequency gliding sometimes precedes explosions (e.g. *Powell and Neuberg*, 2003; *Hotovec et al.*, 2013). In other cases, however, gliding follows explosions (*Benoit and McNutt*, 1997), or the timing relative to eruptions is unknown (*Schlindwein et al.*, 1995; *Neuberg et al.*, 1998). Some volcanoes show different tremor characteristics during eruptive vs. non-eruptive periods: At Shishaldin, USA, tremor shows higher frequencies during a sub-plinian eruption in 1999 in comparison to tremor during non-eruptive periods and Strombolian eruptions (*Thompson et al.*, 2002). Tremor during intrusions at Krafla typically has frequencies above 3 Hz, whereas tremor during eruptions is dominated by energy below 3 Hz (*Brandsdóttir and Einarsson*, 1992). At Piton de la Fournaise, background tremor appears to have a narrow peak at 1 Hz (*Battaglia and Aki*, 2003), whereas eruption tremor is more broadband between 1–5 Hz (*Battaglia et al.*, 2005). In contrast, tremor at Hekla, Iceland, before and during eruptive phases looks similar (*Brandsdóttir and Einarsson*, 1992). During eruptive episodes, tremor amplitude appears to be correlated with eruption intensity in terms of erupted products in some cases (e.g. lava fountaining and spattering on Kīlauea in the East Rift Zone, at Pu’u Ō’ō, and at Mauna Ulu, *Koyanagi et al.*, 1987; “vigor” of eruptive activity at Krafla, Iceland, and tephra production rate at Hekla, *Brandsdóttir and Einarsson*, 1992; ash venting at Soufrière Hills Volcano, *Neuberg et al.*, 2000).

Relation to Monitoring Parameters

Tremor is often accompanied by surface deformation. LPs merging into tremor occurs, for example, during inflationary tilt of the active lava dome at Soufrière Hills Volcano (*Miller et al.*, 1998). *Voight et al.* (1998) observe that maximum seismic amplitude at Soufrière Hills Volcano coincided with

⁶An episode is defined by tremor amplitude exceeding the local background amplitude for at least 2 minutes (*McNutt*, 1987b).

the change from inflationary to deflationary tilt. At Kīlauea, tremor amplitudes at the summit are elevated after periods of high tilt rates, sometimes with a time lag of a few hours (*Koyanagi et al.*, 1987). In other cases, shallow and intermediate summit tremor at Kīlauea occurs during times of inflation/deflation (*Jaggard*, 1920; *Koyanagi et al.*, 1987). Similarly, tremor amplitudes during intrusions at Krafla are high during deflation (*Brandsdóttir and Einarsson*, 1992).

Tremor is also observed on infrasonic records (i.e., acoustic tremor). At Fuego, Guatemala, both seismic and acoustic harmonic tremor is present during a phase of mostly Vulcanian explosions in 2009, whereas Strombolian activity in 2008 only produced harmonic tremor on seismograms (*Lyons et al.*, 2013). Similarly, lava effusion at Shinmoedake, Japan, in January 2011 produced harmonic tremor visible on seismograms, whereas Vulcanian activity in February 2011 produced seismo-acoustic harmonic tremor (*Ichihara et al.*, 2013). Acoustic emissions are observed together with volcanic tremor at Arenal (*Benoit and McNutt*, 1997): Broadband tremor (0.5–7 Hz) accompanies small eruptions, usually followed by harmonic tremor and audible gas “chugging”. Similarly, at Karymsky, 10–20% of explosions are followed by seismic and infrasonic harmonic tremor and audible chugging (*Johnson et al.*, 1998). Chugging and the corresponding seismic and acoustic tremor are also observed at Sangay, Ecuador (*Lees and Ruiz*, 2008). The infrasonic signal at Karymsky and Sangay usually lags approximately 4 s behind the onset of seismic tremor at comparable distances from the vent. For long lasting tremor episodes at Kīlauea, seismic tremor has been observed in combination with infrasonic tremor (*Matoza et al.*, 2010).

A relation between tremor and infrasound suggests coupling of some part of the tremor mechanism with the atmosphere. For example, gas escape may cause a momentum exchange of the volcanic system with the atmosphere as well as the ground. Indeed, at Fuego, SO₂ emissions coincide with high tremor amplitudes, typically with time lags between a few and 60 s (*Nadeau et al.*, 2011). High tremor amplitudes also correspond to high SO₂ emissions at other volcanoes such as Villarrica, Chile (*Palma et al.*, 2008) or Etna (*Leonardi et al.*, 2000).

To summarize, several different volcano monitoring parameters have been associated with volcanic tremor in space or time in different settings. Many studies utilize the temporal coincidence of tremor and another observable to constrain potential source mechanisms.

1.2.5 Tremor Mechanisms

Similar to the diversity of observed tremor behaviours, an equally large variety of tremor mechanisms has been explored. Several models can be classified in terms of the effective viscosity of the magma (Fig. 1.3).

Moving Bubbles

At low and intermediate magma viscosities (basalts), excitations related to bubbles in magma are often used to explain volcanic tremor signals (Fig. 1.3a). *Jones et al.* (2012) speculate about the role of bubbles in the lava lake at Erta 'Ale, Ethiopia, as source of tremor between approximately

2–10 Hz. The signal is thought to be related to the detachment of a larger slug from its bubbly wake, on the basis of the interpretation of acoustic signals in the same setting (*Bouche et al.*, 2010). Alternatively, they suggest tremor caused by the interaction of bubbles with the lava lake surface (*Jones et al.*, 2012), similar to bubble coalescence at Stromboli, (*Ripepe and Gordeev*, 1999). In the case of Stromboli, Italy, *Ripepe and Gordeev* (1999) propose a cycle of bubble coalescence and subsequent bursting to explain seismic and acoustic signals, respectively. They predict an inverse relation between tremor frequency and magma viscosity (*Ripepe and Gordeev*, 1999). Similarly, *Matoza et al.* (2010) interpret tremor at Kīlauea to be related to the coupled dynamics of magma and bubbles: According to their model, the broadband component of acoustic tremor is caused by oscillation of a bubble cloud in the conduit system at Pu’u Ō’ō crater. Acoustic spectral peaks are related to resonance of this oscillation signal in cavities at the vent, and the seismic signal is caused by coupling of this resonance with the solid parts of the system (*Matoza et al.*, 2010). All of the mechanisms described above apply to lava lakes and the uppermost part of the plumbing system (i.e., they are limited by bubble nucleation starting at a few kilometres depth for basaltic magmas; *Toramaru*, 1989). I am unaware of detailed studies of the effect of CO₂ exsolution on tremor at deeper levels, and address this issue, in part, in Chapter 2.

Overpressure Driven by Gas Accumulation

Studies have suggested that gas exsolution and accumulation can also play a role in tremor generation for slightly higher viscosity magmas (andesites or basaltic andesites, Fig. 1.3(b)). In these models, oscillations are not due to freely moving bubbles as in the low viscosity open vents, but due to accumulation and periodic release of larger volumes of gas in a closed vent system. A “pressure cooker” analogue is invoked to explain cyclic “chugging” at Karymsky: Gas accumulates beneath a plug of explosion rubble in the vent, until the overpressure leads to an explosive eruption accompanied by harmonic tremor on seismic and acoustic records (*Johnson et al.*, 1998; *Johnson and Lees*, 2000). The “clarinet model” at Arenal includes a similar gas overpressure mechanism which causes gases to escape periodically through fractures in the plug, but adds a contribution from resonance of fluid in the conduit excited by a pressure wave due to the sudden release of gases at the top (*Lesage et al.*, 2006).

Resonating Fluid Filled Magma Pathways

A fluid filled resonator has been previously suggested for Arenal by *Benoit and McNutt* (1997) and *Garcés et al.* (1998). Other examples of resonating fluid filled conduits (Fig. 1.3(c)) as the source for long period seismicity (LPs and tremor) include Soufrière Hills Volcano (*Neuberg et al.*, 2000). *Chouet and Julian* (1985), *Chouet* (1986) and *Ferrazzini and Aki* (1987) theoretically predict harmonic long period seismicity related to crack waves excited by a fluid flow induced pressure transient. Whereas these models focus on the resulting oscillations of cracks or conduits, *Julian* (1994) emphasize the importance of the excitation mechanism. His model suggests excitation of elastic channel walls caused by pressure changes related to nonlinear instabilities in fluid flow,

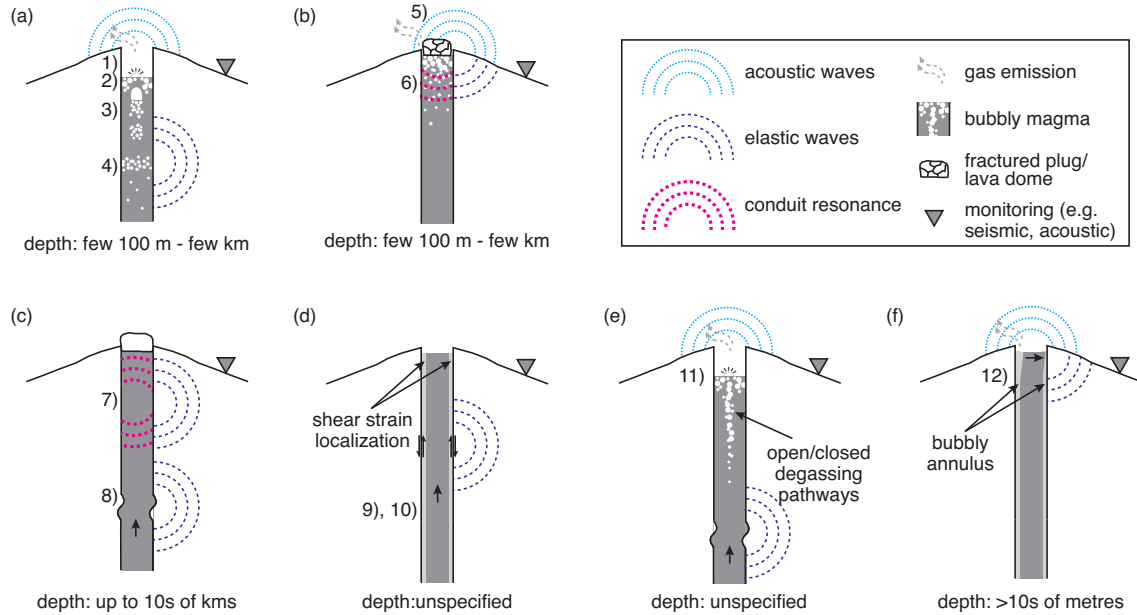


Figure 1.3: Schematic for selected tremor mechanisms including approximate depth constraints. (a)–(d) summarize a variety of mechanisms conceptually, (e)–(f) specifically depict two models that integrate a variety of observations (such as acoustic and seismic data, as well as including observations from more than just one volcanic setting). In (a) and (b), degassing plays a major role for generating tremor. The individual models are: 1) resonance of acoustic waves in vent/cavity (*Matoza et al.*, 2010), 2) bubble bursting (*Ripepe and Gordeev*, 1999), 3) bubble coalescence, ascent, and detachment of wake (*Ripepe and Gordeev*, 1999; *Jones et al.*, 2012), 4) bubble cloud oscillation (*Matoza et al.*, 2010), 5) gas escape through fractures and/or explosion caused by overpressure (*Johnson et al.*, 1998; *Johnson and Lees*, 2000), 6) conduit resonance due to pressure wave (*Lesage et al.*, 2006), 7) fluid filled resonator (*Neuberg et al.*, 2000), 8) crack waves/nonlinear excitation of conduit walls (note that crack/conduit can also be horizontal, e.g. dike, *Chouet*, 1986; *Julian*, 1994), 9) stick slip movement of magma column (*Denlinger and Hoblitt*, 1999), 10) frictional faulting due to high strain rates (*Thomas and Neuberg*, 2012), or due to high stressing rates (*Dmitrieva et al.*, 2013), 11) degassing induced oscillations of valve (analogue to crack waves) and atmosphere (*Lyons et al.*, 2013), 12) oscillation of magma column in bubbly annulus (*Jellinek and Bercovici*, 2011). Note that the mechanisms depicted here are highly schematic. In particular, more complicated plumbing and/or hydrothermal systems allow for similar mechanisms to act in parts of the plumbing other than straight conduits, and may cause interactions between different mechanisms and a variety of observations such as frequency gliding.

enhanced by the Bernoulli effect (*Julian, 1994, 2000*). This type of model is not necessarily limited to the uppermost parts of the volcanic system, and has thus been invoked to explain deep tremor in Hawai'i (*Julian, 1994*).

Earthquake-like Mechanisms

Models for volcanic tremor for high viscosity magmas can be similar to earthquake generation along fault planes (Fig. 1.3(d)). Frictional faulting, magma rupture near the conduit walls at high shear strain rates, or stick slip movement of magma along the conduit walls are thought to cause individual LPs, which can become more closely spaced in time and eventually merge into tremor (at sufficiently high strain or stressing rates, e.g. Soufrière Hills Volcano, *Denlinger and Hoblitt, 1999; Thomas and Neuberg, 2012; Redoubt, Dmitrieva et al., 2013*). In particular, these models are well suited to explain cyclic behaviour of eruptive activity, seismicity and tilt (e.g., *Thomas and Neuberg, 2012*). *Denlinger and Moran (2014)* suggest that a combination of shear failure in high viscosity magma combined with conduit resonance as discussed above causes non-eruptive tremor at Mount St. Helens.

Integrative Models

Often, models have been restricted to explaining one or multiple features of the expression of tremor on seismograms. Recently, attention was turned to incorporate other observables such as infrasound or tilt (e.g., *Thomas and Neuberg, 2012*). *Lyons et al. (2013)* investigate the switch from seismic only to seismo-acoustic tremor through laboratory experiments (schematically applied to a volcano in Fig. 1.3(e)): They find that valve oscillation (similar to crack waves, e.g., *Chouet, 1986*) related to bubble flow can produce seismic harmonic tremor, whereas acoustic tremor is restricted to high stiffness fluids and attributed to the existence of open degassing pathways (*Lyons et al., 2013*). Geared towards higher magma viscosities, *Jellinek and Bercovici (2011)* and *Bercovici et al. (2013)* suggest an oscillation of the magma column within a springy bubble foam or annulus that forms due to plug flow and shearing of bubbles at high strain rates near the conduit walls (Fig. 1.3(f)). They explain not only the observed content and evolution of frequency and amplitude for some cases of tremor, but also observations such as time-dependent gas flux.

No Direct Relation to Magma

A further class of models requires the flow of gas or hydrothermal fluids. These models are linked through the assumption that the source mechanism underlying volcanic tremor may be unrelated to magma flow. *Hellweg (2000)*, for example, suggests vortex shedding, slug flow, or the periodic release of gas through a small outlet as tremor source mechanisms, where each of the three represents a part of a continuous range of flow regimes of hydrothermal fluids or gas. Similarly, *Jones et al. (2012)* find tremor between 0.4-1.4 Hz located near an area of active fumaroles, and attribute tremor to gas flow through cracks. *Balmforth et al. (2005)* conclude that only fluids at higher flow

velocities than magma can cause volcanic tremor as postulated by the fluid flow model by *Julian* (1994).

Additionally, recent studies have shown that the characteristic low-frequency content and long durations observed in discrete LPs can be attributed to slow, brittle failure of faults and wave propagation in poorly consolidated volcanic materials (*Bean et al.*, 2008, 2014; *Eyre et al.*, 2015). Whereas a direct relationship to continuous tremor has not (yet) been shown, the effects may have implications for tremor that future work will have to assess.

1.3 The Need for a Global Classification

Tremor is ubiquitous at volcanoes in virtually all tectonic settings (see Section 1.2; e.g. *Aki and Koyanagi*, 1981; *Neuberg*, 2000; *Konstantinou and Schlindwein*, 2002; *McNutt and Nishimura*, 2008). Most groups of tremor mechanisms outlined in Section 1.2.5 depend on the regime of magma/fluid flow, and are linked to magma/fluid viscosity. Magma composition influences viscosity, and may thus be an important factor contributing to tremor properties. However, despite decades of observational and modelling studies, there are significant challenges to understanding the variety of tremor properties in relation to their underlying mechanics:

- The term “tremor” is an umbrella for a large variety of observations. It is unclear how the characteristics of these observations can be separated into groups that relate to the underlying physics.
- The terminology for tremor is confusing and lacks consistency. For tremor frequency content, for example, the reported values can be the frequency of the highest spectral peak, mean frequency (*Thompson et al.*, 2002), first spectral peak (e.g. *Benoit and McNutt*, 1997), frequency range (*Neuberg et al.*, 2000; *Powell and Neuberg*, 2003), or frequency bands (*Chouet et al.*, 1997).
- Few studies systematically examine links between the temporal evolution of tremor properties (e.g., frequency gliding) and volcanic processes (e.g., *Benoit and McNutt*, 1997; *Jellinek and Bercovici*, 2011; *Hotovec et al.*, 2013; *Bercovici et al.*, 2013).
- No systematic comparisons of tremor properties as a function of tectonic setting exist.

1.3.1 Guiding Hypotheses

A thorough classification of the complexity of tremor observations in their volcanic and tectonic context for a range of settings is crucial to address these challenges. This classification is the main goal of this thesis. My work is based on the following four hypotheses:

- (i) Tremor is an expression of volcanic processes, which are also expressed in other monitoring parameters.

- (ii) Volcanic tremor expresses itself in a variety of temporal, spatial, and spectral properties. These properties are distinct for different types of tremor.
- (iii) The complexity of tremor properties, in combination with other monitoring parameters, can be mapped into a parameter space based on the volcanic and tectonic context to identify characteristic “fingerprints”.
- (iv) If plausible source mechanisms are identified for different tremor fingerprints, volcanic tremor may be reliably used for eruption forecasting.

1.3.2 Methods

Traditional Ways of Analyzing Volcanic Tremor

Traditionally, two types of analysis have been applied to volcanic tremor: (i) classical time series analysis including assessment of temporal and spatial variations of tremor amplitudes and spectral character (e.g., *Riuscetti et al.*, 1977; *Benoit and McNutt*, 1997; *Johnson et al.*, 1998; *Hotovec et al.*, 2013; *Patanè et al.*, 2013), and (ii) studies incorporating non-linear dynamics (e.g., *Julian*, 1994, 2000; *Konstantinou and Lin*, 2004; *Konstantinou et al.*, 2013). For both types, the analysis is commonly confined to one volcanic setting, sometimes limited to only a few tremor episodes from an individual eruption or eruptive cycle, and patterns are typically identified manually. However, compared to studies at just one volcanic setting, the larger amounts of data inherent to a global classification of volcanic tremor require tools for automated pattern recognition. I describe three such tools that are relevant to this thesis in the following sections, where I emphasize the basic methodology and introduce important terminology. Context, details, and reasoning for using each method will be given in Chapter 3.

Automated Pattern Recognition

In Chapter 3, I evaluate two combinations of three methods that can be used for pattern recognition. Principal Component Analysis mainly aims at dimensionality reduction, whereas cluster analysis combines observations into groups based on similarity of observations. Self-Organizing Maps (SOM) can be thought of as both dimensionality reduction and grouping of observations, as I discuss below.

Principal Component Analysis Principal Component Analysis aims to reduce the dimensionality of a dataset by aligning the original coordinate system of N dimensions with mutually orthogonal directions of maximum variance in the data (e.g., *Hotelling*, 1933; *Bishop*, 2006). These directions are called eigenvectors (or modes), following terminology of *Hsieh* (2009). If the data show preferential alignment along one or more directions in the original coordinate system (Fig. 1.4), then this alignment is captured by the eigenvectors, and a lower number of dimensions can be used to describe the most important variations in the dataset.

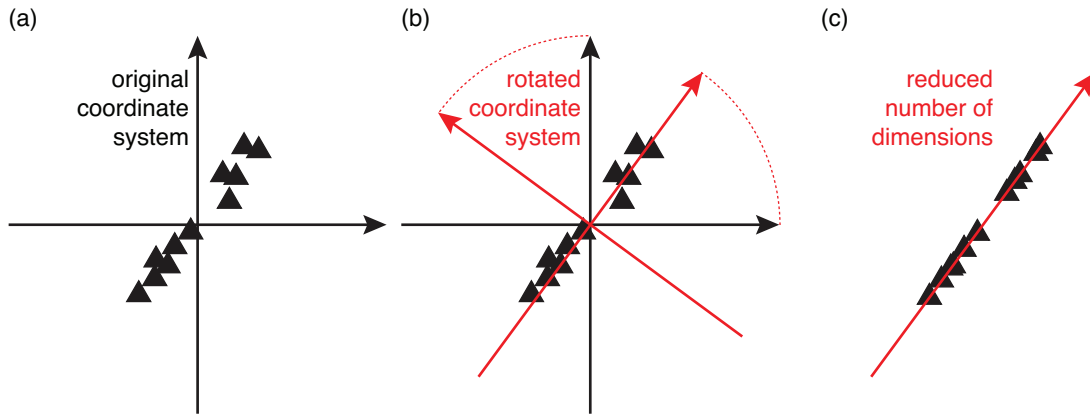


Figure 1.4: Schematic for Principal Component Analysis. (a) Observations (triangles) in original coordinate system (black, number of dimensions $N = 2$) show strong alignment. (b) Rotated coordinate system (red), aligned with directions of maximum variance. (c) Rotated coordinate system with reduced number of dimensions ($N = 1$), capturing most of the variance in the data.

Self-Organizing Maps The Self-Organizing Map was introduced by *Kohonen* (1982, 1990). The goal of the SOM approach is to identify patterns in a multidimensional input data space by “mapping” the original data onto a 2D map of nodes that represents a feature space (Fig. 1.5).

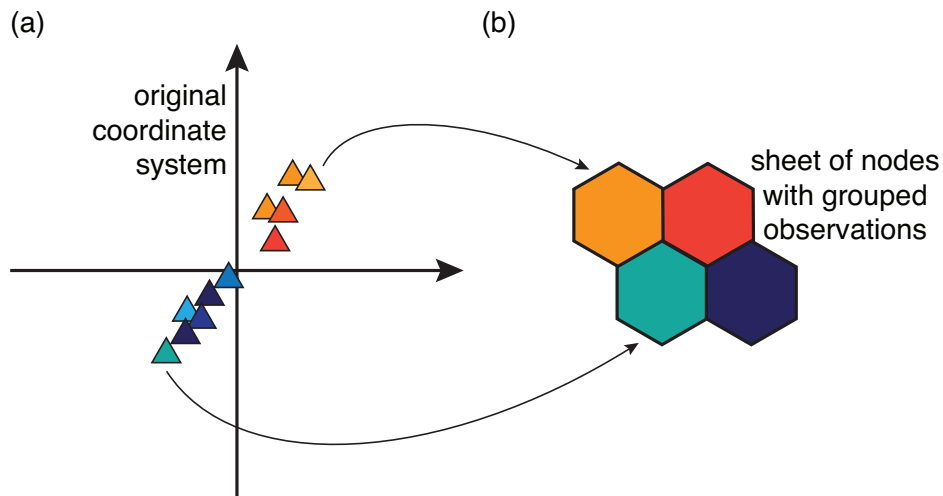


Figure 1.5: Schematic for Self-Organizing Maps algorithm. (a) Observations in original coordinate system, colored according to “similarity” (arbitrary in this case). (b) Two-by-two feature space of hexagonal nodes onto which observations are mapped (and thus grouped) according to similarity in the original coordinate system.

Each node r_i is associated with a model vector m_i with N coordinates according to an N -dimensional input data space. The initial model vectors $m_i^{(0)}$ are assigned based on the input data space. Each data vector X_n (where n is the number of observations) is then assigned to a model vector by finding the minimum Euclidean distance $d_{ni}^{(0)} = \|X_n - m_i^{(0)}\|$. When a data vector X_n is assigned to a model vector, the corresponding node r_b (“best-matching unit”) and the ones surrounding it are updated towards the mean of the input data vectors according to

$m_i^{(1)} = m_i^{(0)} + h_{ni}^{(0)} [X_n - m_i^{(0)}]$, where the neighborhood is determined by, for example, a Gaussian kernel

$$h_{ni}^{(0)} = \alpha^{(0)} \exp\left(-\frac{\|r_b - r_i\|^2}{2(\sigma^{(0)})^2}\right). \quad (1.1)$$

Here, α is the learning rate factor and σ dictates the width of the Gaussian kernel, i.e. the radius of samples that belong to a “neighborhood”. Both α and σ decrease with increasing processing time step. This process is called the “learning process” and is repeated for a fixed number of processing steps. Ideally, after a sufficiently large number of iterations the feature vectors and their locations on the 2D map no longer change, and observations are thus assigned to nodes representing a final feature space and grouped according to similarity (on the basis of Euclidean distances).

The algorithm is available as a MATLAB® toolbox *Vesanto et al.* (1999, 2000) (freely available on <http://www.cis.hut.fi/projects/somtoolbox/>). Many parameters in the toolbox can be adjusted, out of which the most important ones include:

- node lattice size (either as guideline for total number of nodes, or specific x- and y-dimensions), where larger maps can generally capture finer details and variations among observations;
- node shape (hexagonal or rectangular) and consequently number of neighbors for each node;
- lattice shape (sheet, cylindrical, or toroidal), where cylindrical and toroidal maps imply connections of nodes across the ”edges” of the sheet;
- shape (e.g., Gaussian or bubble) and radii of neighborhood relationships;
- random or linear initialization of model vectors.

The number of possible configurations of parameters is large, and the ideal choice depends on the dataset and the questions driving the analysis. My data as shown in Chapter 3 did not show a strong sensitivity to these parameters in several possible configurations. I discuss more details on some of the parameters and my final configuration in Chapter 3.

Cluster Analysis Agglomerative hierarchical clustering is one of many methods to group observations. Observations are grouped into pairs on the basis of their Euclidean distances and two pairs each are then merged into subclusters to minimize

$$d_{ij} = \sqrt{\frac{2n_i n_j}{n_i + n_j}} \|\bar{X}_i - \bar{X}_j\| \quad (1.2)$$

where n_i is the number of observations in cluster i , and \bar{X}_i is the corresponding centroid location (Ward’s method, *Ward Jr*, 1963). Two subclusters each are subsequently combined into larger subclusters, and so forth, until the limit of one large cluster including all observations is reached (Fig. 1.6).

The best clustering can be obtained by examining the cluster hierarchy (“dendrogram”, similar to an inverted tree, Fig. 1.6), where a cut-off can be introduced at any given number of clusters.

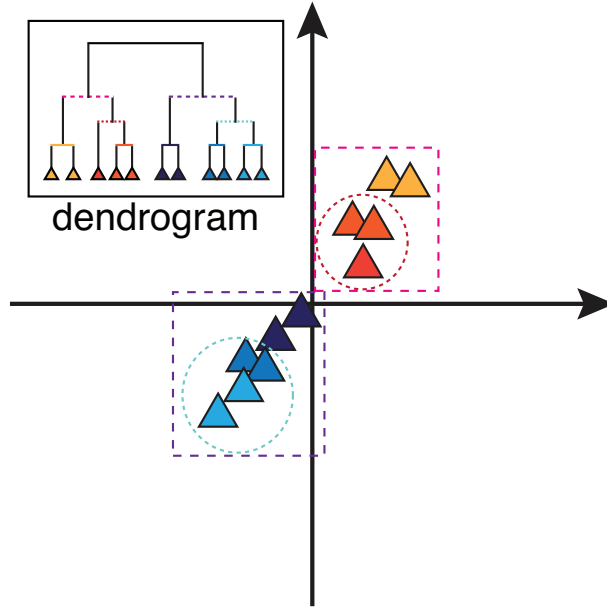


Figure 1.6: Schematic for hierarchical clustering algorithm. Observations are grouped iteratively until the limit of one large cluster is reached. Inset shows dendrogram depiction of cluster structure, indicated by corresponding colors and dashed lined around observations.

One of the biggest challenges in cluster analysis is that it requires identification of this cut-off, or equivalently an a priori number of clusters k (e.g. *Jain, 2010*). The “ideal” k depends on the dataset and the main goal is to find a k that represents the number of clusters that are naturally present in the data. A variety of criteria exist in the pattern recognition community to determine an optimal choice for k (e.g. *Davies and Bouldin, 1979*; *Tibshirani et al., 2001*; *Pakhira et al., 2004*; *Kuncheva and Vetrov, 2006*). Many of these criteria are applied in the same space where clustering is performed, and assess clustering based on a measure of variability of observations within individual clusters in comparison to a measure of variability among different clusters. For example, a common choice is the Davies-Bouldin index (*Davies and Bouldin, 1979*), which seeks the number of clusters k which maximizes

$$DB = \frac{1}{k} \sum_{i=1}^k \max_{i \neq j} \left\{ \frac{s(i) + s(j)}{S_{ij}} \right\} \quad (1.3)$$

with $S_{ij} = \|\bar{X}_i - \bar{X}_j\|$, i.e. the Euclidian centroid-centroid distance of each cluster pair, and the summed within-cluster distance $s(j) = \sum_{i=1}^{n_k} d_{ij}$, where n_k is the number of samples within the k -th cluster. I discuss an alternative choice of criterion in Chapter 3.

1.3.3 Thesis Outline

I use the hypotheses and methods to analyze tremor from four different volcanoes in Alaska and Hawai‘i to address the aforementioned challenges in the following way.

In Chapter 2, I analyze seismicity during a series of eruptive episodes at Kīlauea Volcano, Hawai‘i, to determine the best metric to characterize different types of volcanic tremor. I use clas-

sical time series analysis to identify two phases of seismicity characteristic for dike intrusions, that differ in terms of the location of their strongest expression, their temporal appearance and evolution, as well as their overall spectral shapes. Only the second of the two phases is considered tremor according to our definition. I explore oscillations of bubble clouds in a geometrically complex plumbing system as a possible tremor mechanism by taking into account constraints from (i) the (dis)similarities of tremor properties during two similar dike intrusions, and (ii) the differences to the other seismic signals. In contrast to the varying properties between the two phases, the differences between the tremor signal and the seismicity during more explosive eruptions at Kīlauea lie dominantly in their respective spectra. Because of their similarities in the time domain and the lack of systematic and comparable placement of seismometers at different volcanoes, spectral information thus appears a useful criterion for classification to distinguish between different types of tremor.

The manual analysis of the data from Kīlauea proved to be too cumbersome to examine time periods on the order of several weeks or months for several volcanoes. However, to achieve a global comparison, time series of volcanic tremor should be as long as possible. To be able to analyze such long time series efficiently, in Chapter 3 I rigorously test two automated pattern recognition approaches with a newly constructed and purposely designed synthetic dataset of volcano seismic spectra. The original goal was to assess the performance of an algorithm formed by a combination of Self-Organizing Maps (SOM) and hierarchical clustering. However, my work reveals that an approach that combines Principal Component Analysis (PCA) and hierarchical clustering is more effective at recovering the major elements of the synthetic data.

Following Chapter 3, I apply the newly developed and thoroughly tested combination of PCA and clustering to classify volcanic tremor from four different volcanic settings (Kīlauea, Okmok, Pavlof, and Redoubt volcanoes) in Chapter 4. I design an algorithm to detect tremor in continuous seismic data by measuring absolute amplitude compared to a specifically defined background signal. For each tremor window I then obtain the corresponding spectrum, and analyze the tremor spectra (i) from a given station network to assess spatio-temporal and spectral properties of tremor at each volcano individually, and (ii) from one station from each of the volcanoes to characterize similarities and differences among tremor signals from a range of settings, which may relate to attributes such as edifice type (e.g., stratovolcano vs. shield volcano). The network analysis (i) shows that several spectral signatures of volcanic tremor occur within a given setting. Their variations in time and space sometimes relate to different processes of volcanic activity, and path effects do not appear to strongly affect spectral shapes at the distances of the stations analyzed here. The multi-setting analysis (ii) reveals that at least four types of tremor are observed across the four settings, and that systematic relationships to volcano characteristics such as open vent volcanism may exist.

In summary, my work highlights the importance of analyzing tremor in the light of multiple eruptive cycles through the Kīlauea case study. Furthermore, I provide the necessary pattern recognition tools to undertake such analysis in an efficient and objective way. The promising results from the comparison of tremor from four volcanoes show that a global comparison is achievable

1.3. The Need for a Global Classification

and may hold the key for a more complete understanding of the processes driving volcanic tremor, which ultimately may improve eruption forecasting.

Chapter 2

Volcanic Tremor and Frequency Gliding during Dike Intrusions at Kīlauea – A Tale of Three Eruptions⁷

Summary

To characterize syneruptive/intrusive deviations from background volcanic tremor at Kīlauea, Hawai‘i, we analyze the spatial and temporal properties of broadband tremor during dike intrusions into the East Rift Zone (ERZ) in 2007 and 2011, as well as during explosive eruptive activity at Kīlauea’s summit in 2008. Background tremor was similar for each event, and the 2008 explosions did not affect its properties. In contrast, the intrusions were accompanied by departures from this background in the form of two phases of seismicity that were separated in space and time. In both 2007 and 2011, Phase I was characterized by a quick succession of discrete events, which were most intense at the onset of intrusion near the presumed locations of the dikes intruding into the ERZ. Phase II, marked by continuous broadband tremor around the summit, followed 10–14 h later. In 2007, Phase II tremor was accompanied by a monotonic downward shift (glide) of spectral peaks between ~ 0.6 and 1.5 Hz over at least 15 h. During Phase II in 2011, a gradual upward and subsequent symmetric downward glide between ~ 0.6 and 6.6 Hz occurred over 5–10 h, respectively. The spectra during both phases differed from the background and 2008, as well as from each other, indicating different physical mechanisms. Phase I in 2007 and 2011 is probably related to the mechanics of dike intrusion. Phase II tremor may be characteristic for evolving magma-bubble dynamics related to the geometry of the plumbing system and the style of magma flow.

⁷Reprinted from *Journal of Geophysical Research: Solid Earth*, with permission from Wiley.

2.1 Introduction

Volcanic eruptions are often preceded and accompanied by low-frequency (approximately 0.5–10 Hz) volcanic tremor (*McNutt and Nishimura, 2008*), that persists for minutes to many months (*Konstantinou and Schlindwein, 2002*). The appearance of this seismic signal is often interpreted as a sign of an impending eruption (*McNutt, 1996, 2005; Sparks et al., 2012*). The reliability of tremor as a forecasting tool is, however, uncertain. A central challenge is that existing constraints on the characteristic spatial and temporal properties of tremor can be interpreted in terms of many physical processes that can act to drive ground oscillations on the order of 1 Hz in volcanic systems (see reviews such as *Chouet, 1996b; Konstantinou and Schlindwein, 2002; McNutt, 2005*, and references therein).

A problem common to many studies is that there is insufficient information to recognize whether the emergence of tremor or, say, the rate of change in its frequency or amplitude is critically indicative of an impending eruption. Such a characterization of baseline tremor and deviations from the baseline requires observations over multiple eruptive cycles, which is impractical at many volcanoes because eruptions occur infrequently. Three eruptions at Kīlauea, Hawai‘i, over the last decade provide a novel opportunity to explore deviations from baseline tremor during eruptions with varying styles in one volcanic setting: In 2007 and 2011, intrusions and fissure eruptions in the East Rift Zone (ERZ) involved redistribution of magma in the plumbing system (*Poland et al., 2008; Montgomery-Brown et al., 2011; Lundgren et al., 2013*). In contrast, more explosive eruptions in 2008 were probably related to rockfalls and degassing at the summit (*Wilson et al., 2008; Chouet et al., 2010; Orr et al., 2013*). Few studies have systematically examined tremor during different styles of eruptions (e.g., fissure versus cylindrical vent, Strombolian versus lava fountaining versus sub-Plinian activity) (*McNutt, 1992; Thompson et al., 2002; Alparone et al., 2003*). To provide reliable constraints on the extent to which the temporal and spatial properties of tremor are reliable indicators of characteristic physical mechanisms driving volcanic unrest, we present the first systematic analysis of broadband tremor at Kīlauea over multiple eruptive cycles. We characterize statistically stationary as well as time- and space-dependent tremor properties within the contexts of these three eruptions, which are described in Section 2.2. We then use constraints from our data analysis (Section 2.3) to investigate temporal and spatial relationships between two observed phases of seismicity and to discuss how these relationships restrict plausible models for the excitation and frequency modulation of intrusion tremor signals at Kīlauea (Section 2.4).

2.2 Three Eruptions at Kīlauea, Hawai‘i

Kīlauea Volcano on the Island of Hawai‘i has been erupting almost continuously since 1983 (*Garcia et al., 1992; Heliker and Mattox, 2003; Poland et al., 2012*). Beneath this basaltic shield, magma moves up from mantle depths and is stored in a reservoir a few kilometers below the summit caldera (*Tilling and Dvorak, 1993; Dawson et al., 1999*). At the surface, the caldera with Halema‘uma‘u Crater in the west is separated from Pu‘u ‘Ō‘ō Crater in the east by a linear system of faults and

craters defining the East Rift Zone (ERZ) (Fig. 2.1). Magma entering the ERZ from the summit is transported downrift through a horizontal conduit at 2–3 km depth, from where it feeds the ongoing Pu‘u ‘Ō‘ō-Kūpa‘ianahā eruption (Tilling and Dvorak, 1993; Johnson, 1995; Okubo et al., 1997; Dawson et al., 1999).

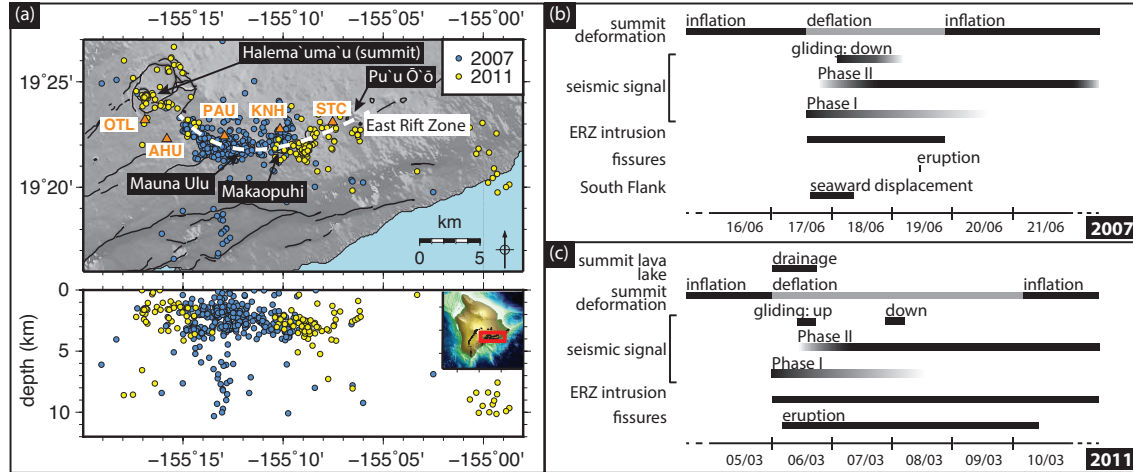


Figure 2.1: (a) Map and cross section show located earthquakes over 7 days from ANSS catalog starting on 16 June 2007 and earthquakes from the HVO catalog starting 5 March 2011, respectively. Inset in cross section shows location of map area on the Island of Hawai‘i. Seismic stations are shown as orange triangles. East Rift Zone and other major features mentioned in the text are labeled. (b and c) Timeline of important events over seven days before, during, and after 2007 Father’s Day and 2011 Kamoamoā eruption. Phase I, Phase II, and gliding will be discussed in detail in the following section. Only events analyzed in 2008 were two out of multiple explosions (19 March and 3 September) and the subsequent first sighting of the lava lake, so no timelines are shown.

We analyze seismic data from three eruptive episodes since 2007: The 2007 Father’s Day intrusion and eruption, a period of explosive eruptions related to the formation of the lava lake at the summit in 2008, and the 2011 Kamoamoā eruption. Whereas the 2007 and 2011 events involved magma transport from the summit into the ERZ (Poland et al., 2008; Lundgren et al., 2013), the 2008 episode was characterized by discrete explosions involving magma only at the summit (Chouet et al., 2010; Orr et al., 2013). Similarly, the excitation time scales varied from seconds during explosions to days during magma flow related to intrusions. The three eruptions thus involved excitation over disparate time scales within distinct parts of the magmatic plumbing system. A careful comparison of the tremor signals provides a unique opportunity to identify reliable spatial, temporal, and spectral fingerprints for distinct types of volcanic unrest. To provide context for our analysis, we describe the main features of each of these events, respectively.

2.2.1 The 2007 Father’s Day Eruption

At 1216 UTC on 17 June 2007, tilt at the summit indicated a change from inflation to rapid deflation (Fig. 2.1; all times here and in the following sections are UTC). A few minutes later, tilt at Pu‘u ‘Ō‘ō also changed to deflation and the crater floor began to collapse (Poland et al., 2008). A simultaneous

increase in seismicity and inflationary tilt in the ERZ close to Mauna Ulu suggested dike intrusion (Poland *et al.*, 2008). This intrusion lasted until 2030 UTC, 19 June, and was accompanied by a small eruption from 1015 to 1045 UTC, 19 June (Poland *et al.*, 2008; Fee *et al.*, 2011a). Note that hereafter, “time periods of eruption” refers to the emission of lava and/or ash at the surface, whereas “intrusion” refers to the period of subsurface dike intrusion inferred from deformation.

2.2.2 The 2008 Halema‘uma‘u Explosions

After a vigorously degassing fumarole appeared in Halema‘uma‘u crater on 12 March 2008, the first explosive eruption on 19 March at 1258 UTC created a vent with a ~ 35 m diameter (Wilson *et al.*, 2008). Over 5 months, this vent widened to > 150 m through > 20 intermittent bursts of degassing and explosions (Chouet *et al.*, 2010; Fee *et al.*, 2010; Orr *et al.*, 2013). In addition to the first explosion in March, we chose the largest of these explosions (in terms of mass) for further analysis. This second event occurred on 3 September at 0613 UTC. It was followed by the first appearance of a lava lake on 5 September (Orr *et al.*, 2008). Lava flows continued to be active between Pu‘u ‘Ō‘ō and the ocean to the south (Smithsonian Institution, 2010).

2.2.3 The 2011 Kamoamoā Eruption

Eruptive activity from the end of 2010 to early 2011 was dominated by spatter and lava flows from Pu‘u ‘Ō‘ō, and lava lake convection and inflation at Halema‘uma‘u (Lundgren *et al.*, 2013; Orr *et al.*, 2015). Seismicity close to the summit and in the Upper ERZ increased in November 2010. Furthermore, seismicity increased close to Makaopuhi (Orr *et al.*, 2015). At 2342 UTC on 5 March 2011, seismicity increased further and tilt at Pu‘u ‘Ō‘ō rapidly changed from inflation to deflation at 2345 UTC (Fig. 2.1). At approximately 0010 UTC the summit also showed signs of rapid deflation (Lundgren *et al.*, 2013). The crater floor at Pu‘u ‘Ō‘ō started to collapse. The lava lake at the summit started to drain, and magma withdrawing from the summit and Pu‘u ‘Ō‘ō fed a dike intrusion close to Makaopuhi uprift from Pu‘u ‘Ō‘ō (Lundgren *et al.*, 2013; Carbone *et al.*, 2013). This intrusion culminated with a fissure eruption from 0309 UTC, 6 March to 0830 UTC, 10 March, just east of Makaopuhi (Orr *et al.*, 2015).

2.3 Data & Results

2.3.1 Network & Data Processing

Continuous, vertical component seismic velocity data were sampled at 100 Hz. For a good spatial coverage of seismic signals on Kīlauea from the summit to Pu‘u ‘Ō‘ō, we chose five short-period sensors (Mark Product L-4 seismometers with a natural frequency of 1 Hz) for further analysis (Fig. 2.1). Prior to analysis, we correct for the effect of the instrument to ensure a flat response between 0.5 and 15 Hz, subsample the time series at 50 Hz, and demean and detrend the data. Unless indicated otherwise, we compute power spectra over 30 min windows with 50% overlap.

We use this approach to optimize a practical tradeoff between temporal resolution and processing speed and chose values similar to other studies (e.g. *Power et al.*, 2013; *Richardson and Waite*, 2013). Our results are, however, independent of the specific choices of window length and overlap.

To capture the background state as well as the eruptive/intrusive processes, we included 1 week of data for each event. Because of our interest in deviations from the steady state of the system, and due to the relative lack of constraints on processes in the plumbing system during quieter periods in comparison to the events in 2007, 2008, and 2011, this only includes approximately 1 day of background tremor before each of the intrusion events.

2.3.2 Overview of Seismic Signals

The emergence and the evolution of the seismic signals accompanying the intrusions in 2007 and 2011 were distinct from those in 2008. Accordingly, we first describe key features of these signals in space and time during the two intrusion and ERZ eruption periods in 2007 and 2011 in chronological order. Second, we summarize seismicity during two explosions at the summit in 2008 when there were no dike intrusions in the ERZ. Figure 2.2 shows spectrograms over 7 days for the five seismic stations between the summit and Pu'u Ō'ō for the four time periods. During all time periods, the seismic signals close to the summit (west) were distinct from the ERZ/Pu'u Ō'ō area (east), with the biggest differences in 2007 and 2011.

In 2007, continuous tremor with power concentrated below 5 Hz preceded the intrusion close to Pu'u Ō'ō (Fig. 2.2(a)). During the intrusion and eruption, there were two phases of seismicity. We define “Phase I” as a strong broadband signal covering our entire frequency range (0.5–15 Hz, Fig. 2.2(a)), which was strongest in the ERZ (in this case at station PAU). It started with the onset of intrusion and gradually disappeared over the following 1–3 days (Figs. 2.1 and 2.2(a)). The end of Phase I overlapped in time on 17 June with the emergent onset of a comparatively continuous “Phase II.” Its broadband character is similar to Phase I, and it was strongest at station OTL close to the summit. Phase II decayed to a background level over the following 3–4 days (Figs. 2.1 and 2.2(a)).

Before the 2011 Kamoamoā eruption, there was no preintrusion tremor phase such as in 2007. The onset of intrusion just before midnight on 5 March was, however, accompanied by a similar Phase I signal (Figs. 2.1 and 2.2(a)). A Phase II signal emerged after approximately 0.5 days. This signal was concentrated near the summit and persisted for more than 5 days. A strong broadband signal at station STC (closest to the eruption site) was not visible on any of the other stations. It faded out earlier than Phase II. The notable short period of high spectral power on 11 March coincides approximately with the expected arrival of surface waves related to the 2011 Tōhoku earthquake.

In terms of the location of the highest intensity and their timing relative to each other, Phases I and II were remarkably similar in 2007 and 2011 (Fig. 2.3). Furthermore, both Phase II signals in 2007 and 2011 were accompanied by frequency gliding (i.e., the gradual shift in frequency of a spectral peak over time, on 18–19 June 2007, and on 6–8 March 2011, respectively; Figs. 2.1 and

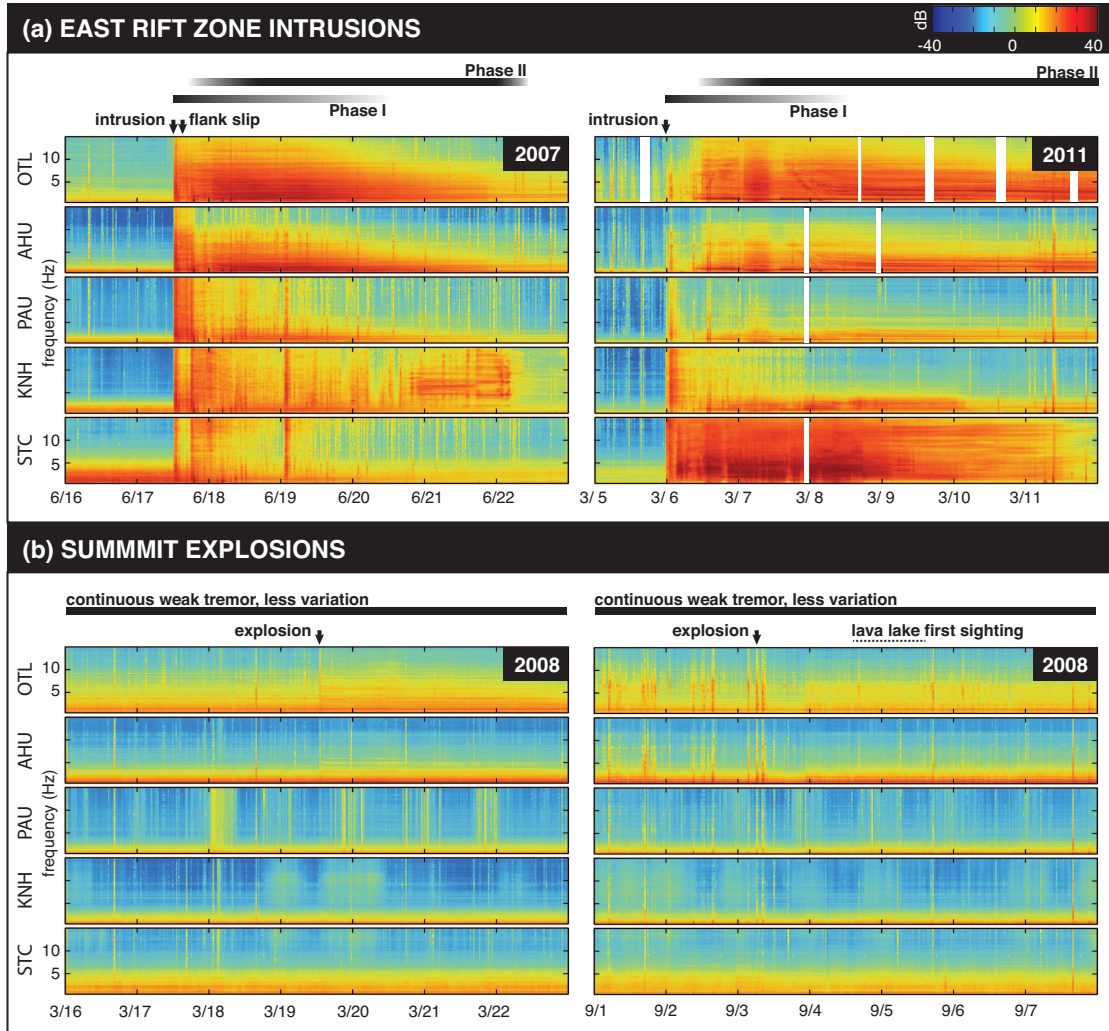


Figure 2.2: (a) Spectrograms over 7 days for the 2007 Father’s Day, and the 2011 Kamoamoa intrusions/eruptions, and (b) for two explosions at the summit in 2008. Each panel shows five stations ordered from west to east. White areas are periods with data gaps.

2.2(a)). To assess the similarity of each phase during the two intrusions in greater detail, we describe the statistically stationary properties of the two phases and the gliding episodes in Sections 2.3.3 and 2.3.4.

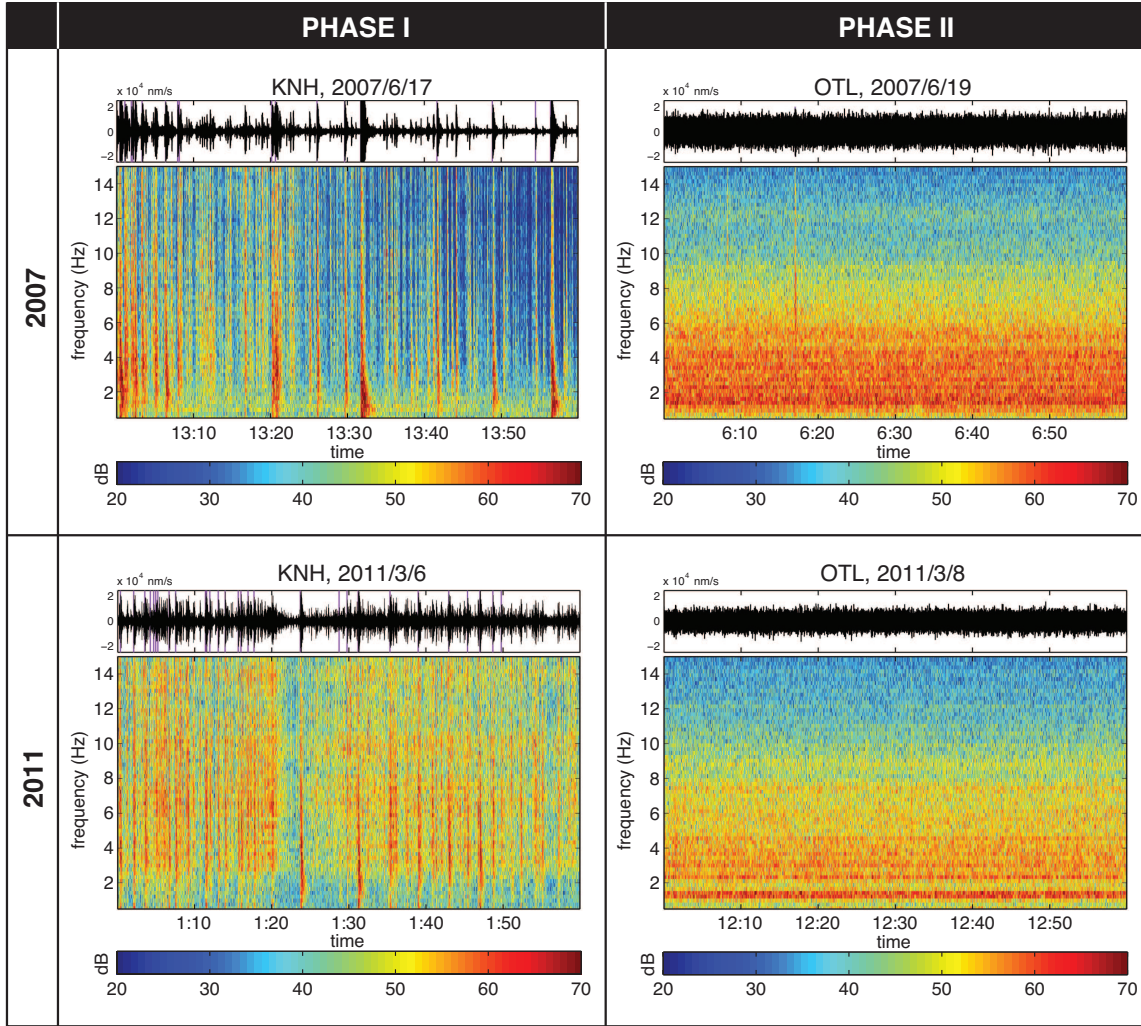


Figure 2.3: Spectrograms over 1 h (with 4.5 s windows) during intrusions in (top) 2007 and (bottom) 2011. One station in the east (KNH) and one in the west (OTL) were chosen for Phase I and Phase II, respectively. Vertical purple lines in seismograms indicate located earthquakes (locations in Fig. 2.1). During both intrusions, (left) Phase I is dominated by individual events, whereas (right) Phase II shows continuous, nonharmonic tremor.

During the weeks that included the explosions on 19 March and on 3 September 2008, there was continuous tremor with a lower intensity than tremor during the intrusions (peak RMS amplitudes not exceeding $\sim 1.6 \times 10^3$ nm/s, versus peak RMS up to $\sim 6.6 \times 10^3$ nm/s, Fig. 2.4). This weaker, continuous signal in 2008 was strongest at station AHU close to the summit, weaker in the ERZ, and slightly stronger again at station STC close to Pu'u 'Ō'ō (Figs. 2.2(b) and 2.4). Both explosions are visible as short increases in spectral power. The first explosion was accompanied by a slight increase in tremor frequency bandwidth. A similar change in tremor frequency bandwidth followed

the second explosion, but more than half a day later (Fig. 2.2(b)). The spectra before and after the explosions were very similar for both March and September 2008, and resembled the background spectra in 2007 and 2011 with a power-law decay of spectral power from low to high frequencies (Fig. 2.4).

2.3.3 Phases of Seismicity During Intrusions

Figure 2.3 shows 1 h velocity seismograms and spectrograms for typical Phase I and II signals in 2007 and 2011 from one station in the east (KNH) and one in the west (OTL), respectively. Figure 2.4 shows 1 h spectra from preintrusion/explosion, synintrusion and postexplosion time periods from station AHU. We chose this station because signals from the 2008 explosions as well as from Phase I and Phase II in 2007 and 2011 were each expressed.

The Phase I signals shown are approximately 1 h after onset of intrusion and are dominated by individual events (Fig. 2.3). Larger spikes in the traces correspond to located earthquakes (Fig. 2.1) that show up as vertical stripes, i.e., short-duration broadband signals in the spectrograms. The slope of a power spectrum is of particular interest because it indicates the similarities and differences in the energetics of the tremor oscillations: Both the power delivered to the motions and the nature of the dissipation influence the spectral slope. The spectra for Phase I were relatively flat between 1 and 10 Hz for both years. In contrast, the preintrusion background in 2007 and 2011, and the spectra from preexplosion and postexplosion periods in 2008 were similar with an approximately power law decay from low to high frequencies. The 2007 Phase I signal was strongest at station PAU with an RMS amplitude of $\sim 3.3 \times 10^3$ nm/s. The 2011 Phase I was shorter in duration and farther east compared to 2007 (strongest RMS amplitude $\sim 3.1 \times 10^3$ nm/s at station KNH; Fig. 2.4). Locations based on envelope cross correlation confirm that Phase I occurred closest to the location of intrusion in both years (A. Wech, personal communication, 2014) as indicated by the amplitude and power distribution (Figs. 2.2–2.4).

Very few individual earthquakes occurred during Phase II in both 2007 and 2011. The signals showed continuous oscillations with spectral power concentrated generally at frequencies below 3 Hz. The two highest spectral peaks at station AHU were at ~ 0.9 and 1.7 Hz in 2007, and at ~ 1.1 and 1.4 Hz in 2011 (Fig. 2.4). There were several other peaks at irregular intervals, i.e., not harmonic overtones, and spectral power decayed in a way similar to the background tremor spectra (Fig. 2.4). The amplitudes during Phase II were strongest near the summit ($\sim 3.9 \times 10^3$ nm/s and $\sim 2.8 \times 10^3$ nm/s for 2007 and 2011, respectively; Fig. 2.4), confirmed by envelope cross correlations of shorter tremor bursts during this period (A. Wech, personal communication, 2014). The high amplitudes toward station STC during Phase II in 2011 (Fig. 2.4) were related to a different, strong broadband signal that rapidly decayed with distance and that appears to be independent from Phase II (Fig. 2.2). Because of its absence in 2007, we do not treat this signal as part of the Phase II signature and only briefly discuss it again in Section 2.4.1.

Overall, the similarities in the succession of the two phases, their approximate durations, and their spectral features in 2007 and 2011 suggest that they may be characteristic signatures of intru-

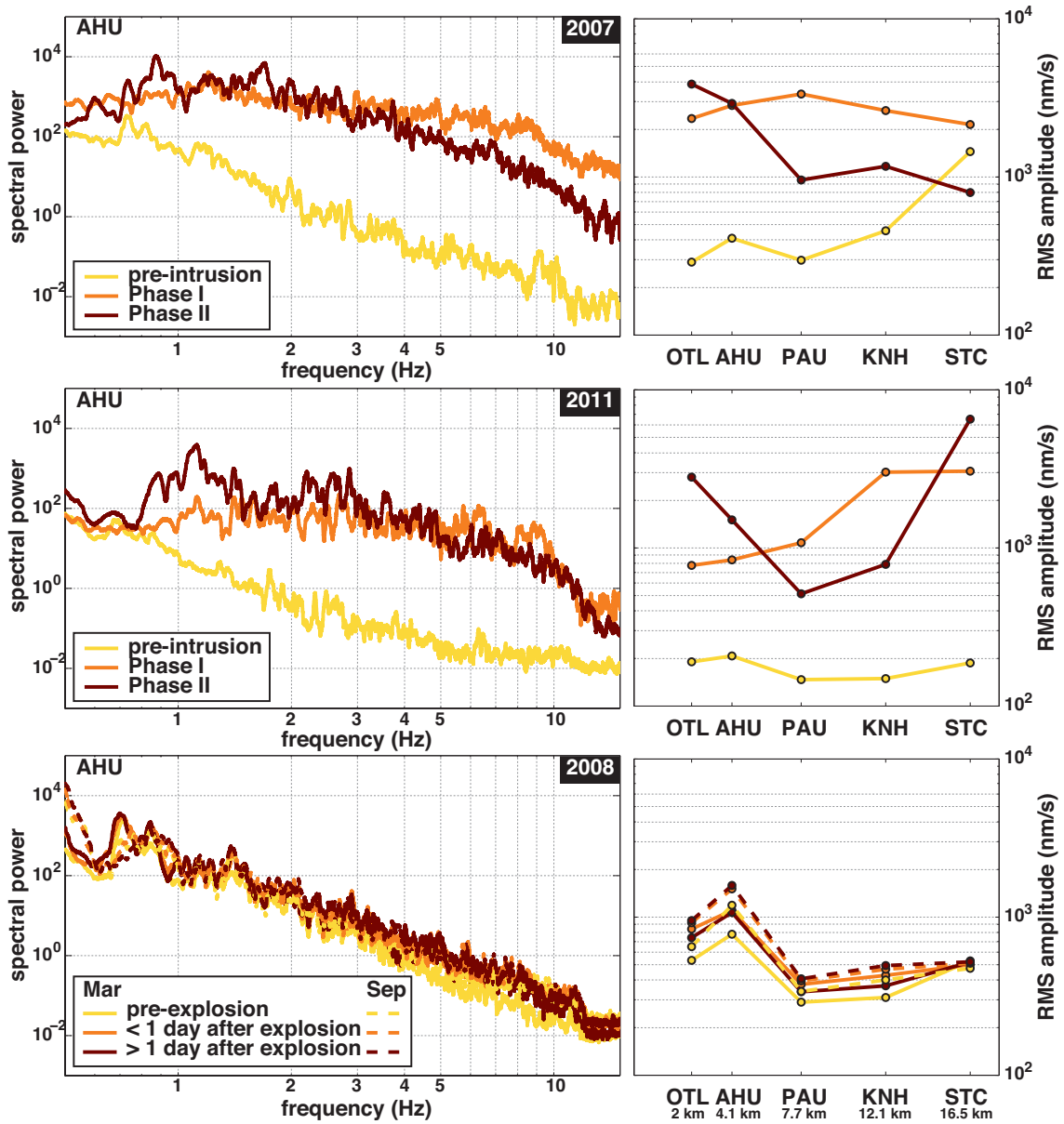


Figure 2.4: Spectra over 1 h during intrusions in (top) 2007 and (middle) 2011, and during explosions in (bottom) 2008 for different phases at station AHU (left column) smoothed with a 100 point moving average ($= 0.056$ Hz), and RMS velocity amplitudes at all stations from west to east during the same time periods. During both intrusions, Phase I has a relatively flat spectrum, whereas Phase II shows continuous, nonharmonic tremor with peaks below 3 Hz. Phase I has the highest amplitudes in the ERZ (stations are ordered from west to east, with distance from the summit in kilometers given below the station name), whereas Phase II is strongest close to the summit (for high Phase II amplitudes toward STC in 2011, see text). Spectra in 2008 show no strong differences at different points in time, and amplitudes are strongest at station AHU, generally higher than the background for 2007 and 2011 but lower than during the intrusions. Note that amplitudes are not corrected for site effects and thus do not provide accurate locations.

sion seismicity.

2.3.4 Frequency Gliding

Figure 2.5 shows frequency gliding at station OTL during the intrusions in 2007 and 2011. We chose station OTL because gliding is strongest close to the summit (Fig. 2.1). In both years, gliding occurred during Phase II over a time scale of several hours to days. The gliding peaks are diffuse and buried in other signals, so there is considerable uncertainty in onset times (≥ 30 mins) and frequency range (≥ 0.1 Hz). There was no gliding in 2008.

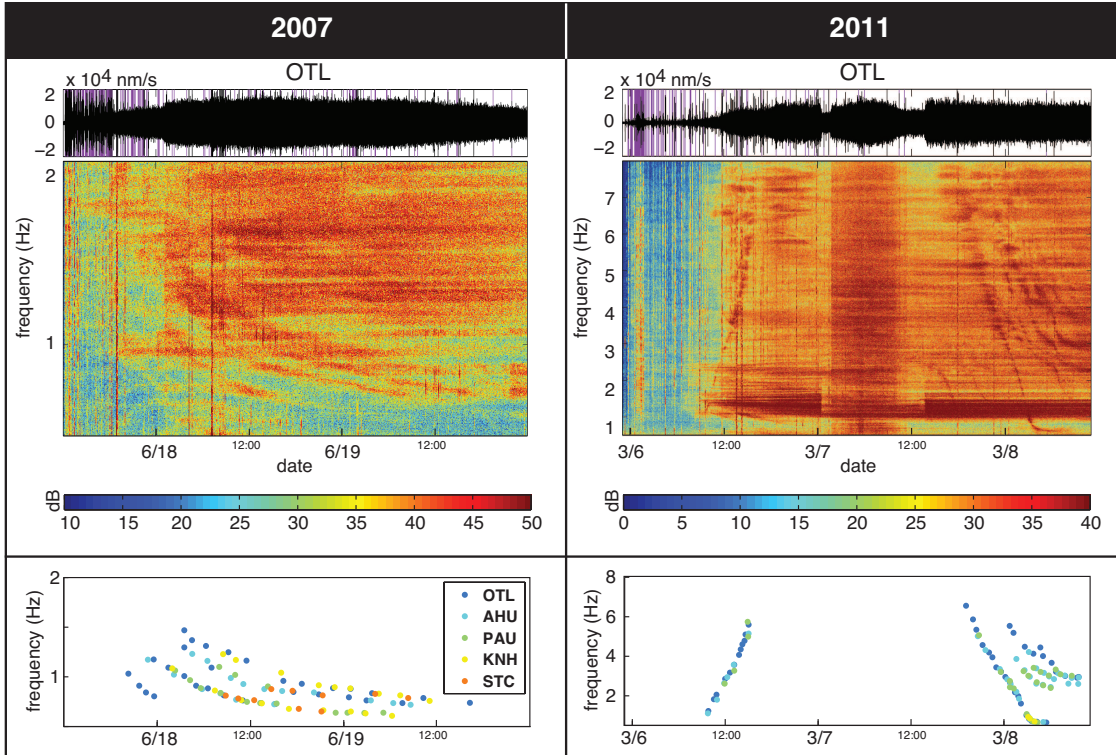


Figure 2.5: Spectrograms over 60 h (with 360 s windows) during intrusions in (left) 2007 and (right) 2011. Panels show (from top to bottom) seismogram, spectrogram below 8 Hz for 2007/below 2 Hz for 2011 at station OTL and gliding traced at all stations for comparison. Time starts approximately 1 h before the onset of intrusion in each case. Vertical purple lines in seismograms indicate located earthquakes (locations in Fig. 2.1). Phase I, Phase II, and gliding are visible in both years. In 2007, gliding is directed downward between 0.6 and 1.5 Hz. In 2011, both upward and downward gliding range between 0.6 and 6.6 Hz. All stations show the same gliding frequencies and temporal evolution during 2007 and 2011, respectively, but the signal is strongest close to the summit.

In 2007, multiple frequency peaks between 0.6 and 1.5 Hz started gliding downward approximately 14 h after onset of intrusion on 18 June. The gliding event lasted for 15 h, with some further slight shifts occurring for another 16 h. During the time of gliding of some peaks, several other frequency peaks with similar spectral power remained at constant frequencies. We discuss this simultaneous occurrence of gliding and stable peaks (i.e., frequency peaks that do not show gliding) in Section 2.4.3.

In 2011, gliding started approximately 10 h after onset of intrusion, on 6 March. The temporal evolution differed from 2007: One frequency peak climbed upward from ≤ 1.2 Hz to at least 5.6 Hz over 5 h. The upglide was accompanied by increasingly stronger tremor between ~ 1 and 6 Hz with a sharp (compared to the duration of Fig. 2.5) amplitude decrease around 0000 UTC on 7 March and a similarly sharp amplitude increase around 1200 UTC. Approximately 28 h after the end of the upglide, there was a symmetric downglide from at least 6.6 Hz to 0.6 Hz over 10 h (and longer for the weaker, nonharmonic overtones).

Despite the differences in gliding frequency range and the direction in time (i.e., upglide versus downglide), the character and remarkable longevity of gliding episodes in 2007 and 2011 are similar and each episode occurs concurrently with the onset of Phase II.

2.3.5 Summary of Main Results

The main results of our systematic analysis are:

1. Seismic signals (above 0.5 Hz) during eruption periods in the ERZ associated with dike intrusion are stronger than during explosions at the summit.
2. The frequency content and the slopes of 1 h time-averaged spectra before and after the explosions in 2008 are similar to the background preintrusion signal recorded in both 2007 and 2011.
3. Intrusions and eruptions in the ERZ are marked by two phases of seismicity that overlap in time but are separate in space and distinct in character:
 - a. Phase I is characterized by discrete events, coincides in space and time with the onset of the intrusions, and lasts for several hours. Its spectral slope is relatively flat over a 1–10 Hz frequency band.
 - b. Phase II has an emergent onset 10–14 h after the start of the intrusion, is continuous, is strongest close to the summit, and persists after the end of the eruptions. It is not harmonic and has peak frequencies mainly between 0.7 and 3 Hz, where its spectral slope is approximately flat. Above 3 Hz Phase II shows decaying spectral power similar in character to the preintrusion background in 2007 and 2011 and to the signals before and after the explosions in 2008.
 - c. Monotonic frequency gliding over several hours is associated with Phase II. Whereas the 2011 eruption is characterized by symmetric upglides and downglides, the 2007 event is marked by downgliding alone.

2.4 Discussion

We discuss how our observations and their temporal and spatial relationships indicate a dependence of tremor properties on eruptive style and location (i.e., tremor in 2008 versus 2007/2011 and tremor

during 2011 at the summit versus in the ERZ; Section 2.4.1). Furthermore, we discuss why Phase I is likely related to dike intrusion (Section 2.4.2). In Section 2.4.3 we show how our observations restrict plausible Phase II tremor mechanisms using the example of two models for coupled bubble-magma interactions that can account for many of the key features in our data. Lastly, we summarize the remaining limitations of our analysis and highlight the steps necessary to better understand Phase II tremor (Section 2.4.4).

2.4.1 Tremor & Eruptive Styles: Summit Explosions Versus ERZ Intrusions and Fissure Eruptions

Additional observations are necessary to interpret key differences between the 2008 and 2007/2011 episodes, as well as between the tremor signals at the summit and in the ERZ in 2011. Broadband tremor accompanying the intrusions is stronger than tremor accompanying explosive activity at the summit (Fig. 2.4), suggesting that either a different process was causing the signal in 2008, or that the same process was weaker in 2008 than in 2007 and 2011. Long-period (LP) and very long period (VLP) seismicity ($f < 0.5$ Hz) was present during the 2008 summit eruptions (*Dawson et al.*, 2010; *Ballmer et al.*, 2013; *Dawson and Chouet*, 2014) and is interpreted in terms of fluid processes related to degassing, resonance of a fluid-filled crack, and/or rockfall events at the top of the magma column that couple into the wall rock at a geometric constriction at approximately 1 km depth (*Chouet et al.*, 2010; *Dawson et al.*, 2010; *Patrick et al.*, 2011b; *Dawson and Chouet*, 2014). Because the weak 2008 broadband tremor coincides with the observation of the LP and VLP signals, it is possible that the observations in these two frequency bands are related. In contrast, there were no VLP signals during our observed Phase II in 2007 and 2011, which then suggests a different underlying physical mechanism for our observations. The background spectra for 2007/2011 and 2008 have similar shapes, and none of the spectra during 2008 deviate strongly from this background (Fig. 2.4). Phases I and II during the intrusions, however, have distinctly shaped spectra with energy delivered to the oscillation at 1–10 Hz for Phase I and 0.7–3 Hz for Phase II (Fig. 2.4). This observation indicates that the underlying physical processes governing the signals during the 2007 and 2011 intrusions were distinct from those at work prior to the intrusions and during the 2008 explosions.

In 2011, there is a strong seismic signal at STC that appears to be independent from Phases I and II (Figs. 2.2 and 2.4). Station STC is closest to the erupting fissures, and the amplitude of the signal correlates with activity at the fissures (*Orr et al.*, 2015) and decays quickly with distance. Because of the localized nature and easily distinguished spectral character compared to the other Phase I and II signals, as well as its absence in 2007, we do not treat this signal as part of the characteristic intrusion seismicity. A shallow source mechanism related to spattering at the lava surface (*Patrick et al.*, 2011a) or to magma flow through a dike intruding toward the fissure (e.g. *Chouet*, 1988) are plausible. We focus the remainder of our discussion on the Phase I and Phase II signals in 2007 and 2011.

2.4.2 Phase I: The Early Stages of Intrusion

During other volcanic eruptions discrete events such as those that constitute Phase I merge into a continuous signal like Phase II (e.g. *Neuberg et al.*, 1998; *Hotovec et al.*, 2013). Furthermore, *Richardson and Waite* (2013) point out that waveforms from individual LPs show extended signal codas at distances of a few kilometers away from the source. This suggests that Phase II could be due to Phase I events becoming more closely spaced in time. However, at Kīlauea Phases I and II are distinct in space, time, and character (Figs. 2.1, 2.2, and 2.4), which suggests distinct mechanisms for each phase. In both 2007 and 2011, the onset of Phase I temporally coincides with the onset of deflation at the summit, lava lake drainage (2011), intrusion in the ERZ, and crater collapse at Pu‘u ‘Ō‘ō (see Fig. 2.1). Generally, magma moves through the previously existing ERZ conduit at Kīlauea, often without deformation or seismicity (*Johnson*, 1995; *Montgomery-Brown et al.*, 2011; *Bell and Kilburn*, 2012). However, *Bell and Kilburn* (2012) show that shallow dike intrusions are often preceded or accompanied by sequences of volcano-tectonic earthquakes related to magma overpressure. Phase I appeared to be dominated by discrete events and was strongest closest to the respective onset area of dike intrusion in 2007 and 2011 (*Poland et al.*, 2008; *Lundgren et al.*, 2013). Located earthquakes during this period were confined to the ERZ at shallow depths of 0–4 km (Fig. 2.1). It is thus likely that Phase I is related to the mechanics of dike intrusion in the ERZ, which is consistent with a fading of Phase I as the rate of intrusion declines.

2.4.3 Temporal & Spatial Constraints on Potential Phase II Tremor Mechanisms

In contrast to Phase I, Phase II is strongest close to the summit and shows long-duration continuous tremor. Many mechanisms can act in a shallow low-viscosity magma-filled plumbing system to drive a persistent order 1 Hz ground oscillation. In this section we briefly summarize which mechanisms have been suggested previously and show how our observations over multiple eruptive cycles can be used to test whether a mechanism (in this case oscillating bubble clouds (e.g., *Matoza et al.*, 2010)) is a plausible source for the signal.

Within the elastic walls of the plumbing system the periodic deformation of fluid-filled fractures can drive oscillations and resonance (*Aki and Koyanagi*, 1981; *Chouet*, 1996a; *Rust et al.*, 2008) or time-dependent fracture propagation (*Aki et al.*, 1977). Within the magma itself, flow through conduit constrictions and/or vigorous or turbulent overturning motions can impart pressure variations at the walls that are ultimately transmitted to seismometers (*Julian*, 1994; *Chouet*, 1996a; *Garcés et al.*, 1998; *Hellweg*, 2000) with a period that depends on the geometry of the conduit and magma flow regime. Depending on the level of volatile oversaturation and configuration of the plumbing system, such flow conditions can also give rise to the nucleation and convection of bubbles leading to bubble gradients (*Cardoso and Woods*, 1999), foams (*Jaupart and Vergnolle*, 1988), and to the formation of “bubble clouds,” which can act as driven oscillators (see below) (*Matoza et al.*, 2010). Interactions of bubbles with the top of the magma column in lava lakes and open vents can also introduce oscillations with similar amplitude and frequency properties (*Fee et al.*, 2010; *Matoza et al.*, 2010; *Jones et al.*, 2012; *Richardson and Waite*, 2013).

In our case, mechanisms that require an open vent cannot explain the observed Phase II signal because the lava lake, i.e., the free surface of the magma column required, e.g., for bubble bursting mechanisms (Chouet *et al.*, 2010; Richardson and Waite, 2013) did not exist in 2007. Furthermore, neither Phase II nor gliding were observed in infrasound data in 2011 (M. Garces, personal communication, 2013). Similarly, based on the continuous character of Phase II from start to end at all stations and its distinct temporal, spatial, and spectral properties compared to Phase I, we favor a mechanism that is not based on individual events such as bursting gas slugs (e.g. Chouet *et al.*, 2010; Richardson and Waite, 2013). The lack of harmonic overtones indicates that mechanisms as discussed in, e.g., Chouet (1988) or Hellweg (2000) are unlikely here.

Frequency gliding accompanying tremor is comparatively less well-studied. It is commonly associated with low intensity eruptions and small explosions at basaltic-andesitic arc volcanoes such as Arenal (Costa Rica (Benoit and McNutt, 1997)), Langila (Papua New Guinea (Mori *et al.*, 1989)), Redoubt (USA (Hotovec *et al.*, 2013)), Sakurajima (Japan (Maryanto *et al.*, 2008)), Sangay (Ecuador (Johnson and Lees, 2000)), Soufrière Hills (Montserrat (Neuberg *et al.*, 1998)), and Veniaminof (USA (De Angelis and McNutt, 2007)). We are aware of only one other basaltic system where approximately syneruptive gliding has been observed, although it is not well-characterized: submarine NW Rota-1 (Mariana Arc (Caplan-Auerbach *et al.*, 2013)).

In general, frequency gliding can be related to time-dependent changes in either the continuous tremor source (e.g. Aki and Koyanagi, 1981; Powell and Neuberg, 2003; Jellinek and Bercovici, 2011; Hotovec *et al.*, 2013) or in the elastic properties of the medium through which pressure waves are transmitted. Gliding has, for example, been analyzed in terms of time-dependent path effects such as vertical and lateral variations in the gas content, bubble size distribution or bubble nucleation rate (Chouet *et al.*, 1997; Neuberg *et al.*, 2000; Garcés *et al.*, 1998).

The time scales over which such path effects act and evolve are probably determined by motions in rising magma, which advect existing bubbles and stir dissolved volatiles to form gradients and cause bubble nucleation. For erupting Hawaiian magmas ascending at $V_m \sim 1$ m/s (“ \sim ” means “scales as” or “is of the same order of magnitude as”), the time scale to produce path effects related to bubble size gradients depends on the ascent distance, in this case the vertical distance from the volatile exsolution depth toward the surface h_e . For CO₂, SO₂, and H₂O this time scale

$$\tau_g \sim h_e/V_m \approx 1 - 20 \text{ min} \quad (2.1)$$

with $h_e \sim 100\text{--}1000$ m (Gerlach, 1986; Dixon *et al.*, 1995; Newman and Lowenstern, 2002). Bubble concentration and size gradients can also be modified as a result of cross-conduit stirring driven in response to constrictions, changes in geometry, or inertial effects. An advective “cross-flow” time scale for this stirring across an average dike or conduit width $D \approx 2$ m (Parfitt and Wilson, 1994; Edmonds *et al.*, 2013) is

$$\tau_f \sim D/V_m \approx 2 \text{ s.} \quad (2.2)$$

On the basis of these time scales, it is not straightforward to understand gliding over hours to days. Additional clues lie in the similarities and differences between the eruptions in 2007, 2008,

and 2011. In contrast to 2008, the 2007 dike intrusion involved gradual deflation and ~ 1 MPa decompression of the summit, paced by slow slip of the south flank of the volcano (*Poland et al., 2009; Montgomery-Brown et al., 2011*). In 2011, similar summit deflation associated with dike intrusion in the ERZ suggest a comparable ~ 1 MPa decompression, which was accompanied by gradual draining of the Halema‘uma‘u lava lake (*Lundgren et al., 2013; Carbone et al., 2013*). However, our observations require a mechanism for Phase II that does not rely on a connection to the atmosphere (see above). Taken together with the spatial and temporal correlations of gliding with summit deflation and ERZ intrusions/eruptions (Figs. 2.1 and 2.5), the observations thus point toward a mechanism that is related to the movement of magma in the summit area. In the following sections we illustrate how our observations over two similar intrusion/eruption periods restrict plausible length scales and time scales with the example of a tremor mechanism based on bubble cloud oscillations.

Magma stirring and bubble cloud oscillations

Qualitative similarities among the spatial, temporal, and spectral properties of Phase II tremor in 2007 and 2011 suggest a common underlying process. That these episodes emerged and evolved with the time-varying magma overpressure regimes inferred to drive violent unrest suggests that Phase II may be a characteristic response of the present-day Kilauean magmatic system to changing magma flow conditions. The systematic shift in 1-h time-averaged spectral slopes from an approximately power law decline during preintrusion phases to relatively flattened spectra, characterized by power delivered to the oscillations over 0.7–3 Hz frequency band, reinforces this picture (Fig. 2.4). In particular, these results suggest that intrusions involve periodic motions in the magma acting on time scales of 0.3–1.4 s. Magma stirring and overturning over these time scales, forced by flow through the geometrically complex volcanic plumbing system (Fig. 2.6), is one way to produce this steady forcing.

One class of physical model that enables us to explore temporal connections to changing magma dynamical regimes and exploit additional constraints on the structure of the present-day volcanic plumbing system (Fig. 2.6) (*Ryan et al., 1981; Johnson, 1995; Lundgren et al., 2013; Edmonds et al., 2013*) is a modified form of the “oscillating bubble cloud” model, which has been applied to understand infrasonic tremor observed at Pu‘u ‘Ō‘ō in 2007 (*Matoza et al., 2010*). Oscillating bubble clouds with distinct spectral properties are well-known sources of acoustic noise in the near-surface ocean and are commonly produced and maintained by breaking waves and turbulent mixing (*Leighton, 1994*). Similarly, *Matoza et al. (2010)* argue that turbulent accelerations in rising magma, acting potentially in concert with inertial effects related to flow interactions with solid boundaries, can drive oscillations in compressible “springy clouds” of exsolved gas bubbles with a characteristic frequency

$$f_c = \frac{1}{2\pi} \sqrt{\frac{3P_e}{\phi \rho_m L_c^2}}, \quad (2.3)$$

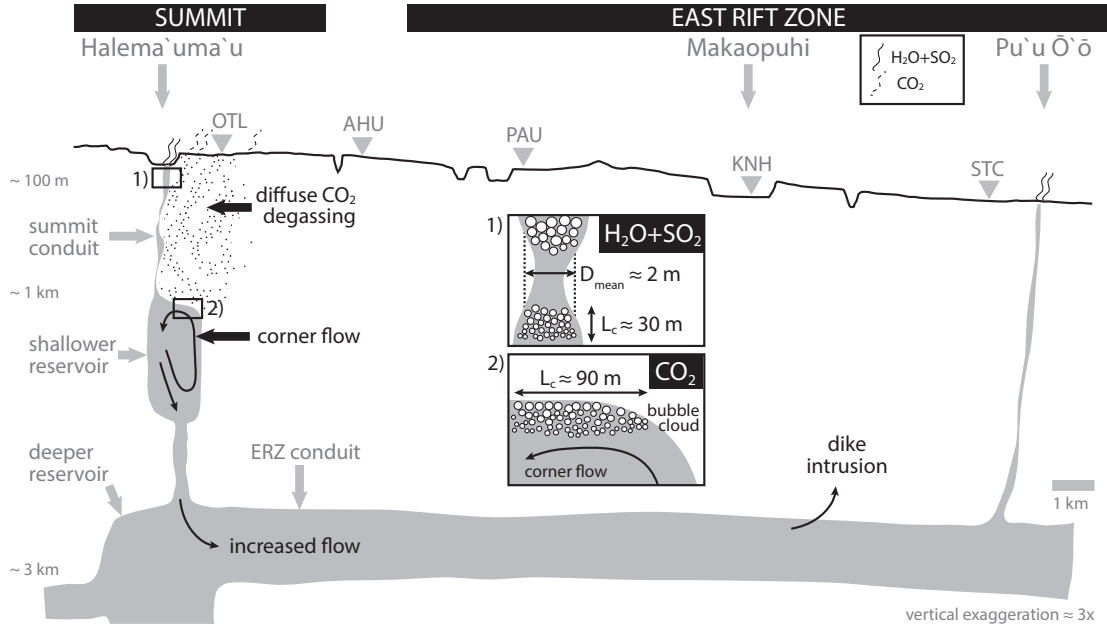


Figure 2.6: Simplified cartoon of Kīlauea plumbing system. Bubble accumulation occurs at two depths in the summit region, depending on volatile species (insets 1 and 2). Resulting bubble clouds can drive oscillations that are modulated by magma flow into the ERZ due to dike intrusions such as Phase II tremor. See text for more details.

which reflects a balance between inertial forces in the magma and a restoring spring forces governed by the gas pressure. Here, $P_e = \rho_m g h_e$ is the hydrostatic pressure in the magma at the volatile exsolution depth h_e , $\bar{\phi}$ is the average porosity of the cloud, ρ_m is the magma density, and L_c is the characteristic scale length for the cloud.

Guided by *Matoza et al.* (2010), for H_2O in the conduit we use $\rho_m = 2700 \text{ kg/m}^3$ and $h_e = 100 \text{ m}$. We take $\bar{\phi} = 0.1$ as a lower bound required to define continuous cloud mixture physical properties such as density, viscosity, and compressibility (*Crowe et al.*, 2011), noting that magma viscosities become very large for $\bar{\phi} \geq 0.4$ (*Gonnermann and Manga*, 2007; *Moitra and Gonnermann*, submitted). We thus require $L_c \approx 30\text{--}10 \text{ m}$ to give $f_c \sim 1\text{--}3 \text{ Hz}$. In more detail, the gas phase or phases contributing to the cloud gas spring force depend on the depth at which these oscillations are driven (*Gerlach*, 1986; *Gerlach et al.*, 2002). Because SO_2 exsolution occurs at depths comparable to H_2O we assume that both volatile phases contribute to the gas spring force at shallow depths (*Gerlach*, 1986; *Gerlach et al.*, 2002). Whereas in 2011 the presence of the lava lake confirms magma at these shallow depths at the summit and thus makes this mechanism plausible, the lack of a vent in 2007 raises the question whether magma was comparably shallow (i.e., $\sim 100 \text{ m}$) and thus whether this mechanism can account for the similarities between 2007 and 2011. In contrast, in the summit reservoir at depths below $\sim 1 \text{ km}$ a cloud in the form of a confined CO_2 bubble-rich layer will plausibly form in contact with the roof of a reservoir undergoing either natural convection (*Woods and Cardoso*, 1997) or forced overturning driven by flow into the ERZ conduit (Fig. 2.6), which we discuss below. In this case equation (2.3) implies $L_c \approx 90\text{--}30 \text{ m}$

horizontally for $f_c \sim 1\text{--}3$ Hz.

One interpretation for similarities between Phase II in 2007 and 2011 is that L_c was similar. In general, the concentration of a given dissolved volatile is approximately $\propto \sqrt{P_g}$ and the exsolved gas volume $\propto 1/P_g$, where P_g is the pressure in the exsolved gas phase at depths less than h_e . Consequently, the mass and volume fractions of an exsolved volatile will increase continuously from h_e to the surface, suggesting that cloud length scales are either on the order of h_e or proportional to the interval from h_e to the depth at which the volatile phase is exhausted (whichever distance is smaller). However, for H_2O in the shallow conduit, $\bar{\phi} = 0.1$ with $L_c \sim h_e = 100$ m gives frequencies below what we observe (and resolve). If $\bar{\phi}$ is also increased to better capture the large vertical variations in porosity that will occur from h_e to the surface (*Gonnermann and Manga, 2007*), f_c will decline significantly further below our observations.

Alternatively, cloud scales are set by the dynamics of magma flow and their relationship to the geometric structure of the Kilauean plumbing system. In the shallow reservoir (Fig. 2.6), prior to eruption bubble gradients will grow at the roof in response to natural convection (*Woods and Cardoso, 1997*), and L_c is probably governed by the horizontal length of roof to which the bubble cloud layer is coupled mechanically. Magma draining into the ERZ during eruption will induce a corner flow that may cause bubbles to collect in a triangular region (Fig. 2.6) where L_c is reduced and plausibly proportional to the square root of the area of this confined region.

By contrast, the complex geometry of the summit conduit including irregular bends and constrictions can give rise to three-dimensional “boundary-driven” flows including lateral motions that stir magma across the conduit (*Julian, 1994; Hellweg, 2000*), disrupting otherwise vertically continuous bubble clouds, in turn. Such a mechanical control on L_c is not unexpected. L_c and $\bar{\phi}$ in the ocean can, for example, be related quantitatively to the character and turbulent mixing properties of breaking waves that act to both form and disaggregate bubble clouds (*Leighton, 1994*). However, for such inertial effects to occur in the summit magma system at Kilauea, the Reynolds number Re of the flow must be much larger than around 10^3 . In the summit conduit $Re = \bar{\rho}_m V_m D / \mu \approx 10\text{--}20$ with magma viscosity $\mu = 250\text{--}400$ Pa s (*Shaw, 1969*) and $\bar{\rho}_m = 2340$ kg/m³, where $\bar{\rho}_m$ is the average density of the magma assuming $\bar{\phi} = 0.1$, and V_m and D are as above. Under these moderate Re conditions lateral turbulent accelerations will be very small compared to the momentum flux carried by the mean flow, unless they are enhanced as a result of geometric effects that drive and guide cross-conduit flows. Assuming the speed of this boundary-driven stirring is comparable to V_m and taking D for a characteristic dike width, the dynamic pressure force corresponding to the momentum flux carried by these cross-conduit flows $\sim \bar{\rho}_m V_m^2 L_c D$. The resistance of a bubble cloud to disruption is challenging to characterize. We assume that bubble cloud break up is akin to the disruption of solid particle-fluid mixtures (*Hodge et al., 2012; Moitra and Gonnermann, submitted*) where the resistance can be described by a mixture “yield force” $\sim \sigma_y D^2$, where the effective yield stress for disaggregation of the mixture σ_y depends on the cloud microstructure (*Wildemuth and Williams, 1984; Hoover et al., 2001; Moitra and Gonnermann, submitted*), and the effective stiffness of the cloud depends on the cloud cross-sectional area D^2 . Balancing this yield force with the pressure force gives a condition for disrupting vertically extensive bubble clouds to produce

smaller clouds with a characteristic length:

$$L_c \sim \frac{\sigma_y D}{\rho V_m^2} \propto \frac{1}{V_m^2}. \quad (2.4)$$

To sustain long-lived Phase II tremor signals probably requires continuous excitation. Oscillations with a frequency $f_c \sim 1/\tau_f = 0.5$ Hz can be driven by the same steady cross-conduit stirring that gives rise to the clouds, provided that oscillations are damped over a time scale that is long in comparison to the time scale of mechanical forcing τ_f . Driving magma motions will be retarded by viscous stresses proportional to the larger of the strain rates ($V_m/D, V_m/L_c$). In the summit conduit, where $L_c \gg D$, viscous communication across the conduit width will damp oscillations over a time scale

$$\tau_v \sim \bar{\rho}_m D^2 / \mu \approx 20\text{--}40 \text{ s}. \quad (2.5)$$

For CO₂ in the reservoir, assuming that magma stirring with speed V_m during intrusions is over reservoir length scales $D \sim 100$ m (Fig. 2.6), $\tau_f \approx 100$ s, whereas $\tau_v \approx 10^4\text{--}10^5$ s. An important difference to flow in the conduit is that overturning motions in the reservoir are at $Re \sim 1000$ and in a comparatively unbounded geometry. Strong vertical and lateral turbulent accelerations in the corner flow are expected can contribute to driving oscillations in the bubble cloud layer, potentially over a range of frequencies.

A question remains whether fresh magma is supplied (input) at a rate faster than the loss of CO₂ through the summit vent and/or the diffuse degassing region (output), i.e., whether CO₂ can remain in the plumbing system long enough to form bubble clouds. Output of CO₂ is mostly confined to the diffuse degassing region (Fig. 2.6) (Poland *et al.*, 2009; Edmonds *et al.*, 2013). Typically, magma supply, i.e., input, is estimated based on gas emission, it is thus difficult to obtain independent estimates. However, the accumulation of CO₂ bubbles close to the top of the summit reservoir has been suggested previously in relation to deformation around the summit and cyclic activity during some eruptions (Vergnolle and Jaupart, 1990; Johnson, 1992; Woods and Cardoso, 1997). Furthermore, Poland *et al.* (2009) suggest that CO₂ bubbles may segregate from their parental melt and ascend at higher velocities. Accumulation of CO₂ bubbles thus does not necessarily imply accompanying input of fresh magma. It is possible that this accumulation of bubbles happens at a geometric constriction around 1 km depth below Halema'uma'u, as discussed in Section 2.4.1, at the roof of a large magma reservoir or at the top of dikes and sills.

A plausible source mechanism for Phase II in 2007 and 2011 must account for the lack of a similarly strong, long-lasting Phase II oscillation in 2008. It must also account for essential differences between the time-averaged Phase II and postexplosion spectral slopes in Figure 2.4. The explosions in 2008 have been attributed to rockfalls from the crater wall (Patrick *et al.*, 2011b; Orr *et al.*, 2013) or ascent of large gas slugs (Chouet *et al.*, 2010; Chouet and Dawson, 2011). The longevity of signals driven by impulsive magma displacements is governed in form by equation (2.5). The characteristic length scale $D \approx 10$ m for either mode of excitation (Chouet *et al.*, 2010; Orr *et al.*, 2013) in the uppermost parts of the conduit gives $\tau_v \approx 600\text{--}1000$ s, which implies that oscillations

driven this way will decay within $\sim 10\text{--}20$ min (or less). Alternatively, bubble cloud oscillations can occur and persist at shallow levels if they are driven by, e.g., convection at modest Re in the lava lake in the top few 100 m (Carey *et al.*, 2013). However, convection velocities $V_m \sim 0.1$ m/s (Carey *et al.*, 2013) imply driven oscillations will have a frequency $f_c \sim 0.001$ Hz (equation (2.2), with $D \approx 100$ m), which is below the frequencies we resolve. Finally, whether bubble clouds can coexist with (or quickly reestablish after) disturbances due to rockfalls or ascending gas slugs is unclear. Taken together, these predictions suggest that conduit H_2O bubble cloud oscillation cannot readily explain weak tremor in 2008. In contrast, slightly deeper oscillations of CO_2 clouds due to reservoir convection may not be strongly affected by the events at the summit vent. The relatively constant weak tremor without gliding in 2008 may thus be due to bubble cloud oscillations in the shallow reservoir (Fig. 2.6). The differences in the shapes of the spectra, however, still point toward a different underlying physical mechanism for 2008 compared to 2007/2011.

How might changes in magma flow cause gliding?

Assuming that bubble cloud oscillations can be excited as we describe, the magnitude of frequency gliding in 2007 and 2011 (Fig. 2.5) can be understood through gradual changes in L_c (equation (2.4)), P_e and $\bar{\phi}$ (equation (2.3)) related to evolving flow and overpressure conditions in the magmatic system. Through equations (2.3) and (2.4), the change in frequency $\Delta f_c \propto \Delta V_m^2 / \sqrt{\Delta \bar{\phi}}$. The switch from inflation to deflation at the summit in both 2007 and 2011 and the onset of dike intrusion implies a rapid increase in the speed V_m of magma flowing from the summit conduit and reservoir into the ERZ, that is followed, in turn, by a slow decrease in V_m related to a relatively slow relief of magmatic overpressure. This speed is reduced further because an increase in $\bar{\phi}$ from 0.1 to 0.2, say, will cause magma viscosity to rise by a factor of ~ 2 (Gonnermann and Manga, 2007; Moitra and Gonnermann, submitted). Consequently, we expect the downglide of f_c in 2007 to be by a factor of > 4 or more through effects on V_m , assuming a factor of 2 decrease in flow speed. The frequency will, however, decrease by an additional factor $1/(\sqrt{2})$ for a factor ~ 2 increase in $\bar{\phi}$. Qualitatively, this trend is similar to our observations (Fig. 2.5). We note that the magnitude of the inferred change in $\bar{\phi}$ is constrained by its effect on magma rheology: As $\bar{\phi} \rightarrow 0.4$, μ_m becomes very large and $\tau_v \rightarrow 0$, making our observed oscillations impossible (i.e., $Re \rightarrow 0$).

For CO_2 in the summit reservoir, the change in V_m is arguably less important than the geometric effect on the structure of the motions in the reservoir related to its draining into the ERZ. Assuming that preruption CO_2 bubble cloud oscillations involve a layer of bubble magma extending across the ~ 100 m or longer roof, the corresponding $f_c \approx 0.02$ Hz is below our detection limit. At the onset of intrusion, gradually increasing flow into the ERZ will introduce a corner flow into the reservoir that will decrease L_c (Fig. 2.6) depending on the geometry of this flow and increase f_c , in turn. A slow deflation of the summit will cause a concomitant decrease of P_e , a corresponding increase in $\bar{\phi}$ and a corresponding downglide (equation (2.3)). A further increase in $\bar{\phi}$ through a decrease in the magma overpressure related to a seaward displacement of Kīlauea’s south flank in 2007 (Montgomery-Brown *et al.*, 2011) may enhance this effect and explain why the downglide in

2007 reaches lower frequencies than in 2011.

Apart from the lack of flank displacement, tilt data suggest that the temporal evolution of magma transport from the summit into the ERZ in 2011 was similar to 2007 (Poland *et al.*, 2008; Lundgren *et al.*, 2013). The observed upglide in 2011 is, thus, initially puzzling. Yet the drop in lava lake level (Carbone *et al.*, 2013) implies that magma that has lost most of its CO₂ (Edmonds *et al.*, 2013) reenters the summit reservoir. On the basis of the occurrence of the upglide at the end of the lava lake drainage we suggest that mixing this CO₂-poor magma with magma at the top of the shallow reservoir (Fig. 2.6) reduces $\bar{\phi}$ and L_c , causing the observed upglide (assuming that this effect is stronger than the simultaneous and opposing effects of deflation). When lake draining stops the upglide disappears as a corner flow is reestablished. Assuming $V_m \leq 1$ m/s and overturning length scales ~ 2 km (Fig. 2.6), if steady state is recovered over, say, ~ 5 –10 overturns (Jellinek *et al.*, 1999) this implies mixing time scales $\geq 10^4$ s, the same order of magnitude as the 28 h break between the upglide and the downglide in 2011. Subsequently, the effects of deflation, i.e., decreasing pressure and correspondingly increasing $\bar{\phi}$ and L_c , can drive the observed downglide.

A key feature of the data in Figure 2.5 is that the gliding frequencies in 2007 and 2011 are not integer multiples of the lowest frequency (fundamental) modes. Through equation (2.3) the appearance of distinct gliding frequencies suggests vertical variations in $\bar{\phi}$ or L_c related to either spatially complicated changes in the geometry of the summit reservoir or to differing pressure-dependent contributions of exsolved H₂O, SO₂, and CO₂ to the composition of the bubble clouds. Variations in geometry that lead to isolated bubble clouds with varying properties are likely particularly in the deeper (~ 1 km) parts of the plumbing system, e.g., if the summit is underlain by a region of interconnected cracks and reservoirs (Chouet *et al.*, 2010; Baker and Amelung, 2012). Furthermore, we speculate that oscillations of isolated bubble clouds in a potentially complicated shallow plumbing system may not strongly be affected by, e.g., changing flow conditions, which could explain the simultaneous presence of stable spectral peaks during gliding episodes.

The ratios of the gliding frequencies to the fundamental are approximately preserved as the intensity of the tremor decays with distance from the summit. Thus, the source for the majority of the signal is reliably in the summit region. If the cloud model holds, the fact that Phase II tremor is strongest around the summit and is not observed in the ERZ implies that the majority of magma degassing is concentrated at the summit. Degassing measurements indicate that this is true for CO₂ which leaves the plumbing system mainly through an area of diffuse degassing east of Halema‘uma‘u, but not for H₂O or SO₂, which are found in plumes along the ERZ (Gerlach and Graeber, 1985; Gerlach, 1986; Greenland, 1987) (Fig. 2.6). This suggests that the CO₂ cloud model is a more likely scenario for the source of summit tremor.

2.4.4 Remaining Challenges

We have illustrated how key temporal and spatial aspects of Phase II tremor in 2007 and 2011 might be explained by magma flow-driven bubble cloud oscillations in the conduit or the shallow reservoir beneath the summit. This mechanism is also consistent with an absence of Phase II in

2008. Distinguishing between the two scenarios (i.e., conduit $\text{H}_2\text{O}/\text{SO}_2$ versus reservoir CO_2 bubble cloud oscillations) is not straightforward. A remaining question is the exact location(s) of the tremor source(s). Phase II and gliding are expressed most strongly close to the summit. However, whether the exact location corresponds to the shallow lava lake and the underlying conduit, or deeper parts of the plumbing system related to a bigger reservoir is unknown. Accurately locating tremor could help to identify the exact location of Phase II tremor within the summit region.

Further limitations remain with both bubble cloud models. It is unclear, for example, why the onset of Phase II is delayed by ~ 10 h compared to the onset of deflation. The bubble cloud oscillation model would predict the motions driving the oscillations to start with the onset of intrusion, and similarly, the onset of gliding to coincide with the onset of pressure changes and/or changes in magma flow velocity. In addition, whereas bubble cloud oscillations may be the driving force behind the similar peaks at low frequencies in the Phase II spectra during 2007 and 2011, these oscillations cannot explain the differences in spectral slope above 10 Hz between 2007 and 2011, which indicates that energy is dissipated in potentially different ways during the two intrusion periods.

We explore a magma-driven bubble cloud oscillation model because of the demanding spatial and temporal characters and similarity of Phase II tremor properties in 2007 and 2011. This is one physical picture and others are certainly possible, if they are permitted by the full set of observations over three eruptive cycles. To make progress, a further study could, for example, focus on comparing tremor during quieter periods such as in *Matoza et al. (2010)* to the intrusion tremor analyzed here. Systematic differences or similarities in terms of its location, intensity, and appearance in infrasound data can help to confirm or reject the presence of the common underlying physics we propose. As monitoring data sets become longer, future studies over similarly long time scales might hold the key to improving our understanding of processes accompanying volcanic eruptions.

2.5 Conclusions

We systematically analyzed broadband volcanic tremor (peaks below 3 Hz) during three eruptions on Kīlauea, Hawai‘i, from 2007 to 2011. Our results show that whereas explosive activity at the summit in 2008 was marked by continuous weak tremor very similar to the preintrusion background in 2007 and 2011, intrusions and eruptions in the ERZ in 2007 and 2011 were accompanied by two phases of seismicity that were separate in space and time. Phase I is characterized by discrete events in ERZ that may be related to dike intrusion, Phase II is a continuous broadband tremor signal close to the summit. Phase II is accompanied by long-duration frequency gliding (hours to days) with different temporal evolutions and frequency content during two different intrusions. We suggest that the weak tremor during explosive activity may have a different mechanism than tremor during the episodes of intrusion and eruption. Tremor and gliding properties during the intrusions in 2007 and 2011 cannot be linked to mechanisms related to an open vent, but, among others, permit an explanation in terms of driven oscillations of H_2O bubble clouds in the shallow parts (~ 100 m) of the summit conduit system or of CO_2 bubble clouds near the top of the shallow summit reservoir

(~1 km).

These observations over three eruptions provide critical restrictions in space and time on plausibility of models for the underlying mechanics. On the basis of qualitative similarities in 2007 and 2011, we argue that Phase II is a characteristic response of Kīlauea to intrusions: It is a consequence of how magma moves through the present-day geometrically complex plumbing system. Our discussion highlights two key knowledge gaps that are useful for future work. Better constraints on the source location including depth of volcanic tremor in the summit region at Kīlauea, and detailed imaging of the summit plumbing system are necessary to determine which of the two bubble cloud scenarios is more likely as the source for summit tremor during intrusions in the ERZ, or whether contributions from both the conduit and the shallow reservoir are required.

Chapter 3

Principal Component Analysis vs. Self-Organizing Maps Combined with Hierarchical Clustering for Pattern Recognition in Volcano Seismic Spectra⁸

Summary

Variations in the spectral content of volcano seismicity related to changes in volcanic activity are commonly identified manually in spectrograms. However, long time series of monitoring data at volcano observatories require tools to facilitate automated and rapid processing. Techniques such as Self-Organizing Maps (SOM) and Principal Component Analysis (PCA) can help to quickly and automatically identify important patterns related to impending eruptions. For the first time, we evaluate the performance of SOM and PCA on synthetic volcano seismic spectra constructed from observations during two well-studied eruptions at Kīlauea Volcano, Hawai‘i, that include features observed in many volcanic settings. In particular, our objective is to test which of the techniques can best retrieve a set of three spectral patterns that we used to compose a synthetic spectrogram. We find that, without a priori knowledge of the given set of patterns, neither SOM nor PCA can directly recover the spectra. We thus test hierarchical clustering, a commonly-used method, to investigate whether clustering in the space of the principal components and on the SOM, respectively, can retrieve the known patterns. Our clustering method applied to the SOM fails to detect the correct number and shape of the known input spectra. In contrast, clustering of the data reconstructed by the first three PCA modes reproduces these patterns and their occurrence in time more consistently. This result suggests that PCA in combination with hierarchical clustering is a powerful practical tool for automated identification of characteristic patterns in volcano seismic spectra. Our results indicate that, in contrast to PCA, common clustering algorithms may not be ideal to group patterns on the SOM and that it is crucial to evaluate the performance of these tools on a control dataset prior to their application to real data.

⁸Reprinted from *Journal of Volcanology and Geothermal Research*, with permission from Elsevier.

3.1 Introduction

In volcano monitoring, scientists are faced with the task of correctly identifying patterns of unrest critically indicative of impending eruptions (e.g. *Sparks et al.*, 2012; *Carniel*, 2014). A key component of volcano monitoring is seismic activity (*Sparks et al.*, 2012). Seismic signals on volcanoes can be classified in terms of their frequency content: Whereas volcano tectonic earthquakes often have a broadband spectrum, low frequency seismicity including long-period events, very long period events, and volcanic tremor predominantly cover lower frequency ranges of 0.01–5 Hz (*Fehler*, 1983; *Neuberg*, 2000; *McNutt and Nishimura*, 2008; *Chouet and Matoza*, 2013). Based on its distinct spectral properties, this low frequency seismicity is commonly explained by processes involving fluid movement: Examples include moving bubbles (*Ripepe and Gordeev*, 1999; *Matoza et al.*, 2010; *Jones et al.*, 2012), gas accumulation (e.g. *Johnson et al.*, 1998; *Lesage et al.*, 2006), resonating fluid pathways (*Chouet*, 1986; *Leet*, 1988; *Julian*, 1994; *Benoit and McNutt*, 1997; *Neuberg et al.*, 2000; *Hellweg*, 2000; *Balmforth et al.*, 2005), or bubble/magma flow (*Denlinger and Hoblitt*, 1999; *Jellinek and Bercovici*, 2011; *Thomas and Neuberg*, 2012; *Dmitrieva et al.*, 2013; *Lyons et al.*, 2013). Each of these mechanisms imply a relationship between properties of low frequency seismicity and volcanic activity. Indeed, approximately 80% of a global sample of volcanic tremor episodes have been shown to precede or accompany volcanic eruptions (*McNutt*, 1992). For a given volcanic setting, knowledge of typical seismicity and the corresponding spectral patterns before, during, and after eruptions (e.g. *Carniel et al.*, 1996; *Unglert and Jellinek*, 2015) is thus crucial for eruption forecasting.

A common approach to analyzing the temporal evolution of volcano seismicity is the visual inspection of spectrograms. For example, *Unglert and Jellinek* (2015) identify two characteristic phases of seismicity that accompanied two intrusions at Kīlauea Volcano, Hawai‘i. This kind of analysis requires manual identification of characteristic spatio-temporal patterns, which is practically cumbersome, inherently subjective, and informed by the experience of the analyst. For instance, which spectral properties distinguish non-eruptive from eruptive unrest is unclear. Consequently, to be able to objectively identify patterns and extract key information related to imminent or active volcanism, analysts are increasingly reliant on automated algorithms (e.g., *Carniel*, 2014; *Cortes et al.*, 2015).

Pattern recognition and machine learning methods provide a possible solution and are used in a wide range of disciplines (e.g., *Kaski et al.*, 1998; *Oja et al.*, 2002; *Bishop*, 2006). In particular, “unsupervised” methods imply that no a priori knowledge of patterns is necessary, i.e. the algorithm self-learns from the data (e.g. *Bishop*, 2006; *Langer et al.*, 2009). In volcano monitoring, this feature is essential because the temporal evolution of patterns in monitoring time series is often unknown (e.g. *Sparks et al.*, 2012). A good review of different, unsupervised feature extraction methods and their application to volcano seismicity can be found in *Orozco-Alzate et al.* (2012) and *Carniel* (2014). Such studies have used Self-Organizing Maps (SOM) and other techniques to detect different types of seismicity (e.g., *Carniel*, 1996; *Langer et al.*, 2009; *Carniel et al.*, 2013a; *Curilem et al.*, 2014), or link changes in time series from volcano monitoring with different eruptive

vents or type of eruptions (e.g., *Esposito et al.*, 2008; *Di Salvo et al.*, 2013). Several studies first use SOM to reduce the amount of data to be analyzed, and subsequently apply clustering algorithms to obtain final groupings (e.g., *De Matos et al.*, 2006; *Köhler et al.*, 2009; *Messina and Langer*, 2011; *Carniel et al.*, 2013a).

SOM can generate a visual representation of the similarities and differences between patterns in a dataset (e.g., *Esposito et al.*, 2008), require no a priori knowledge of patterns (e.g., *Murtagh and Hernández-Pajares*, 1995), and can thus be useful for detecting distinctive spectral characteristics of volcanic tremor. In fields such as oceanography or meteorology, it is common to evaluate pattern recognition techniques against each other, against other methods, and with synthetic data (e.g., *Reusch et al.*, 2005; *Liu et al.*, 2006). In seismology, different methods including SOM have been tested against each other at individual volcanic settings (e.g., *Langer et al.*, 2009; *Cortes et al.*, 2015), and SOM performance has been tested with artificial data consisting of parameters from the time and frequency domains (e.g., *Köhler et al.*, 2009). However, to our knowledge no studies applying SOM combined with cluster analysis to volcanic tremor evaluate the functionality of SOM in spectral space with a synthetic dataset. Thus, the following key knowledge gaps persist:

1. The performance of SOM against more standard techniques such as Principal Component Analysis (PCA) has not been systematically evaluated with synthetic datasets of spectra.
2. Appropriate benchmarking datasets closely aligned with real observations, and with known patterns and their occurrence in time do not exist (*Orozco-Alzate et al.*, 2012).
3. It is not clear that the features of interest (e.g., relative spectral power at different frequencies, occurrence and evolution of various spectral shapes in time) are captured by SOM, or how noise affects the results. The limitations of the method in terms of its application to volcano seismic spectra are thus unclear.

Accordingly, in Section 3.2, we produce synthetic spectra on the basis of detailed manual extraction of two characteristic spectral signatures during eruptive periods at Kīlauea Volcano, Hawai‘i (*Unglert and Jellinek*, 2015). Specifically, we address two questions:

1. Can hierarchical clustering, a common approach to identify groupings in data used in previous studies of volcano seismicity, applied to the results from PCA (Section 3.3) and SOM (Section 3.4) correctly identify the known spectra and their occurrence/evolution in time in a typical volcanic spectrogram?
2. How do the clustering results differ between the two techniques, and what are the limitations of each of the methods and of our synthetic dataset (Section 3.5)?

3.2 Data and Preprocessing

Many methods exist for classifying volcano seismicity in both the time and the frequency domains (e.g., *Langer and Falsaperla*, 2003; *Ibs-von Seht*, 2008; *Curilem et al.*, 2009). However, *Castro-*

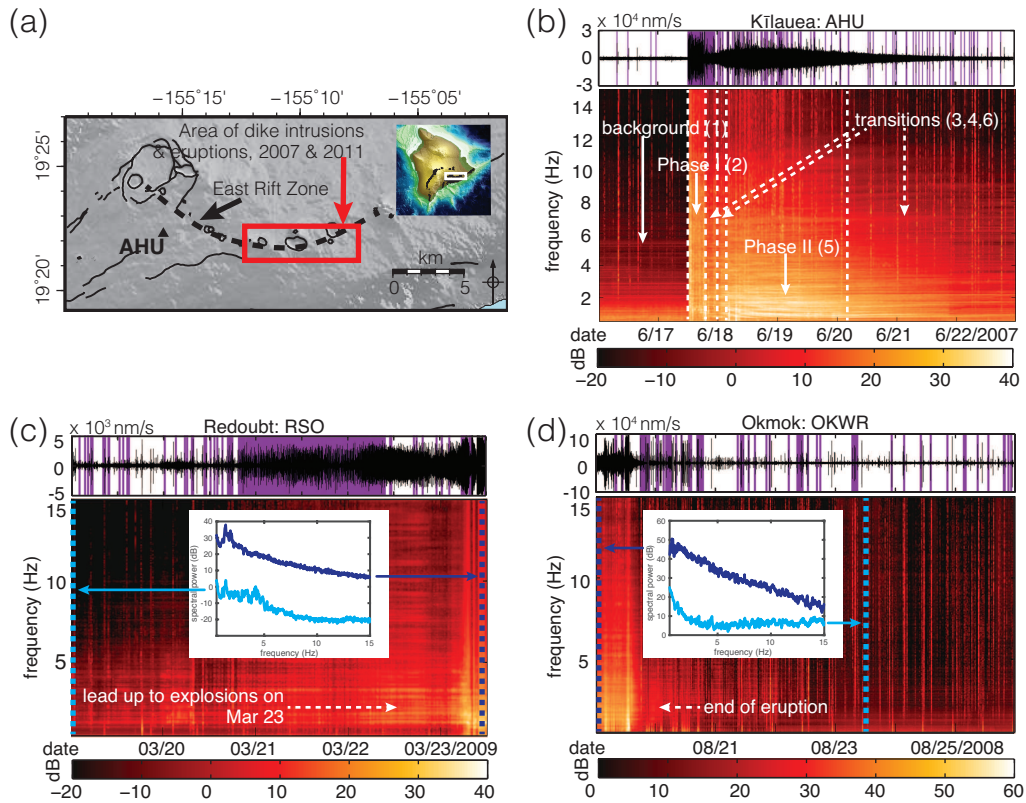


Figure 3.1: (a) Location of station AHU and eruptions on Kīlauea Volcano, Hawai‘i. (b) Spectrogram shows characteristic evolution of seismic data from background through an event phase (Phase I; see purple bars in seismogram indicating located earthquakes) to a tremor phase (Phase II), as discussed by *Unglert and Jellinek (2015)*. White solid and dashed arrows point to periods used as the model for our simplified synthetic dataset (Section 3.2.1). (c) Spectrogram from station RSO during Redoubt 2009 eruption. Inset shows one spectrum from the beginning and the end of shown time period (dashed lines in spectrogram). (d) Spectrogram from station OKWR during Okmok 2008 eruption. Inset shows one spectrum from the beginning and halfway through the shown time period (dashed lines in spectrogram). Both (c) and (d) show different spectral shapes, as well as impulsive and emergent variations of those shapes over time, similar to Kīlauea. Our synthetic dataset is based on Hawai‘i, but captures the same spectral features observed at other volcanoes, regardless of the exact temporal evolution or the underlying processes.

Cabrera et al. (2014) found that classification utilizing entire spectra performs better than classification utilizing sets of other temporal and spectral parameters such as the mean amplitude or mean frequency in a given time window. Furthermore, previous work shows that distinct spectral shapes and transitions between them may relate to the underlying physical processes (e.g., *Aki et al.*, 1977; *Benoit and McNutt*, 1997; *Maryanto et al.*, 2008; *Unglert and Jellinek*, 2015).

To evaluate whether SOM or PCA are suitable for automated analysis of time varying spectral signatures, and more accurate and efficient than visual inspection of spectrograms, we create a synthetic dataset of volcano seismic spectra on the basis of the major spectral characteristics of seismic signals from Kīlauea Volcano, Hawai‘i between 2007–2011 (Fig. 3.1(a); *Unglert and Jellinek* (2015)). During this period, two dike intrusions and accompanying fissure eruptions in the East Rift Zone showed a phase of discrete, seismic events near the intruding dikes (Phase I, Figs. 3.1(b) and 3.2), followed by a phase of continuous tremor near the summit (Phase II, Figs. 3.1(b) and 3.2) with a stronger decrease of spectral power from low to high frequencies compared to Phase I (*Unglert and Jellinek*, 2015). A prominent feature of Phase II is gliding of spectral lines (*Unglert and Jellinek*, 2015). However, because the gliding was expressed at different frequencies during the two intrusions, and because it did not affect the overall character of Phase II, we do not include gliding spectral peaks in Phase II of our synthetic dataset. Such gradual variations in the frequencies of individual spectral peaks are, in principle, similar to transitions over time from one phase to another, which are included in our synthetic dataset. We touch upon this subject again in Section 3.5.3.

The eruptive phases at Kīlauea and their temporal variations are not representative of volcano seismicity in general, but they capture some of the main features of pre- and syn-eruptive seismicity observed in other settings such as Redoubt Volcano, (Fig. 3.1(c)) or Okmok Volcano, (Fig. 3.1(d)), such as different spectral shapes and impulsive and emergent variations of those shapes over time (e.g., *Carniel et al.*, 1996; *Neuberg*, 2000; *Ruiz et al.*, 2006; *Curilem et al.*, 2009; *Langer et al.*, 2009; *Buurman et al.*, 2012)). The particular value of our dataset is that it enables reliable performance evaluation of SOM and PCA on well understood data that are drawn from well-established observations.

3.2.1 Synthetic Spectra

To create the three spectra, we choose three 5-minute windows of continuous seismic data corresponding to the background state, Phase I, and Phase II at station AHU from Kīlauea as described above (Figs. 3.1-3.2). Station AHU is situated between the inferred locations of Phase I and II (close to the area of dike intrusion and below the summit, respectively) and showed both phases clearly and with relatively similar strength. The data are demeaned, detrended, tapered, and Fourier transformed. The resulting spectra are then smoothed and subsampled with a 50 point moving average to obtain the trends of spectral power (Fig. 3.2(a)). For the tests in this study, we limit the frequencies to 0.5–10 Hz unless otherwise indicated. The lower frequency limit is dictated by contamination of volcanic signals with low frequency (≤ 0.3 Hz) seismic noise from the ocean (*McNamara and Buland*, 2004; *Bromirski et al.*, 2005), and by decreasing sensitivity of short period instruments below

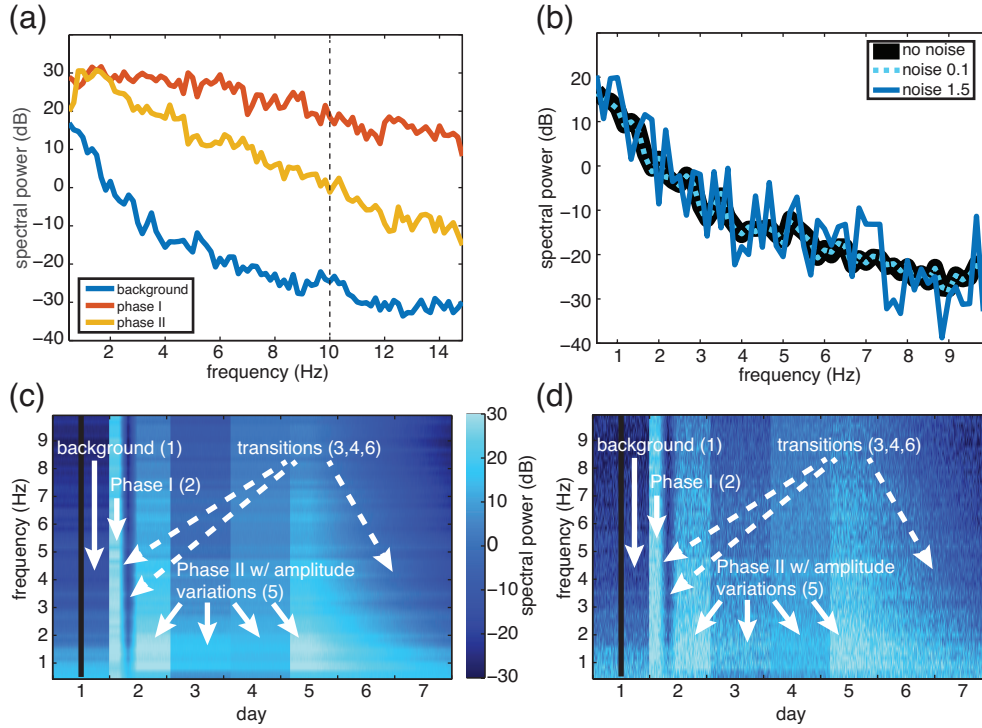


Figure 3.2: Synthetic data setup. (a) Original spectra representing background, Phase I, and Phase II, respectively. Dashed vertical line indicates upper frequency limit for first part of this study. Different frequency ranges will be discussed in Section 3.5.3. (b) Example for different noise levels: Background spectrum at noise levels 0, 0.1, and 1.5. (c) Spectrogram based on the three representative spectra with phases and transitions between them, noise level 0.1. White solid and dashed arrows point to periods described in Section 3.2.1. Black vertical line indicates time for spectrum in (b). (d) Same spectrogram as in (c), but at noise level 1.5.

1 Hz (Mark Product L-4 seismometers with a natural frequency of 1 Hz). The upper limit is chosen to include the frequency range where the (non-normalized) spectra differ the most (Figs. 3.1(b) and 3.2(a)). Different frequency bounds will be discussed in Section 3.5.3.

The three spectra in Figure 3.2(a) capture the main differences between the three time periods: The background state has a relatively monotonic, steep decay of spectral power between 0.5–4 Hz, and flattens slightly at higher frequencies; Phase I and Phase II have increasing spectral power between 0.5–1 Hz (stronger for Phase II), and lower, approximately linear slopes from 1 Hz towards higher frequencies (compared to the background; *Unglert and Jellinek, 2015*). These features suggest differences in the underlying physical processes (*Unglert and Jellinek, 2015*). The stronger spectral power at low frequencies during Phase II compared to the background is, for example, explained by bubble cloud oscillations in a magma reservoir below Kīlauea’s summit, whereas the relatively even, strong contributions at all frequencies during Phase I result from discrete fracture events related to dike intrusion (*Unglert and Jellinek, 2015*).

On the basis of these natural spectra, we construct a synthetic spectrogram with a spectrum every 15 minutes that consists of the following components:

1. Background (24 hours)
2. Phase I (4 hours)
3. Linear transition in time at each frequency from Phase I to background (4 hours)
4. Linear transition in time at each frequency from background to Phase II (4 hours)
5. Phase II (3 days)
6. Linear transition in time at each frequency from Phase II to background (2.5 days)

Phase II includes 100 spectra shifted to lower values, and 100 spectra scaled by 0.5. Because the spectral shape of Phase II is preserved during these periods, our aim is to classify them as one group. The transitions between the phases and the background represent the possible emergent onset or disappearance of signals such as volcanic tremor (*Konstantinou and Schlindwein, 2002; McNutt and Nishimura, 2008*).

To investigate the effect of small variations in spectral power at each frequency, we add different levels of noise to the synthetic spectrogram (Fig. 3.2 (b), (c), and (d)). Noise level 0.1 indicates that the range of the noise (from minimum to maximum) is 10% of the mean spectral power value S_{mean} , which is achieved by adding or subtracting a random value drawn from a uniform distribution between $\pm 0.5 \cdot 0.1 \cdot S_{\text{mean}}$. This noise is not to be confused with “seismic noise”, which may have a specific shape in the frequency domain. Our white noise represents the temporal variability of spectral power, affects the location of individual peaks, and may or may not mask the overall shape of the spectrum.

The resulting spectrograms have 672 spectra, i.e., observations in time, with 57 frequency samples each (Fig. 3.2(c) and (d)).

3.2.2 Preprocessing Steps

The characteristic feature in our dataset is the shape of the spectra, which relates to known differences in source processes (*Unglert and Jellinek, 2015*). In contrast, differences in spectral amplitude can be readily distinguished in spectrograms and are not related to changing source processes. To only focus on source processes, the input spectra must consequently be normalized to remove any differences in amplitude. Typically, normalization is performed by demeaning spectral power at each frequency and dividing it by its standard deviation (e.g., *Langer et al., 2009*). However, with such preprocessing, important information about the relative amplitude from one frequency to another (e.g., *Carniel, 2014; Unglert and Jellinek, 2015*) gets lost. We therefore normalize our input data in the following way:

1. For each spectrum, each spectral power value is divided by the sum of all absolute spectral power values to account for spectra with similar shapes but scaled with respect to each other.
2. Each spectrum is shifted to have a 0 dB median to remove differences between spectra with the same shape that are shifted with respect to each other (Fig. 3.3(a)).

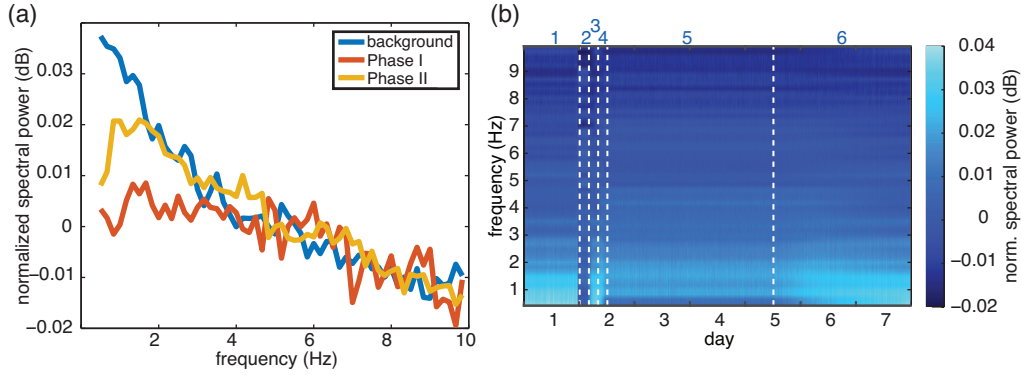


Figure 3.3: Normalized synthetic data used as input for pattern recognition algorithms. (a) Normalized model spectra representing background, Phase I, and Phase II, respectively. Note the lower spectral power values compared to the originals (Fig. 3.2(a)). (b) Spectrogram based on the normalized spectra, noise level 0.1. Vertical, dashed white lines and small blue numbers indicate periods of change described in Section 3.2.1.

The amplitude variations introduced during Phase II disappear with these preprocessing steps (time period 5, cf. Fig. 3.2(c) vs. Fig. 3.3), so all of the spectra can now be classified solely on the basis of their spectral shapes.

3.3 Principal Component Analysis

The basic idea of dimensionality reduction with PCA is to rotate the original, multidimensional coordinate system into a new coordinate system of mutually orthogonal vectors along the directions of maximum variance. In our case the dimensions are the 57 frequency samples. Volcano seismic applications of PCA and similar methods include *Langer and Falsaperla* (1996, 2003); *De Lauro et al.* (2005) and *De Martino et al.* (2005). For our purpose, PCA provides a simple, well established method to go from many frequencies to a lower dimensional space where data can be classified on the basis of a smaller number of dimensions. We apply a subsequent clustering algorithm to the results and use this as a benchmark to compare against the performance of SOM. Because the nomenclature for PCA concepts varies widely in the literature, we align our use of terminology with *Hsieh* (2009): The directions of maximum variance are called *modes* or *eigenvectors*, their coordinates in relation to the original coordinate system are called *loadings*, the new, rotated coordinate system is called *Principal Component (PC) Space*, and the projections of the spectra in PC space are called *principal components*.

3.3.1 PCA and Clustering

Similar to previous work by *Langer and Falsaperla* (2003) or *Carniel et al.* (2013b), the input data for our MATLAB® based PCA algorithm are the normalized synthetic spectrograms at different noise levels, starting at noise level 0.1. The fraction of the total variance explained by each mode (Fig. 3.4(a), with the total number of modes necessary to explain 90% of the variance summarized

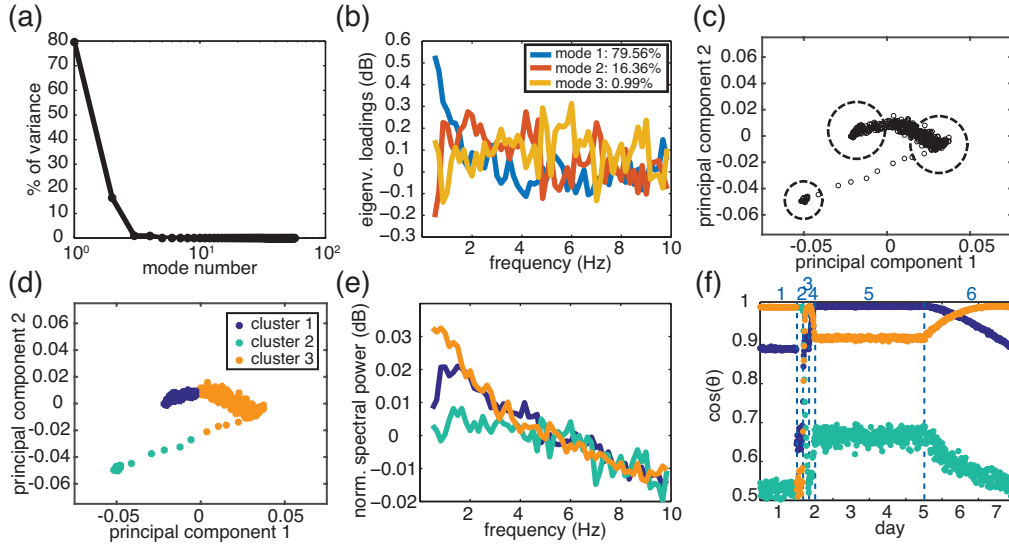


Figure 3.4: PCA results for noise level 0.1. (a) Percentage of variance explained by each mode. (b) Loadings for first three eigenvectors. Small numbers in legend indicate amount of variance accounted for by each mode. (c) Projection of observations in space spanned by principal components 1–2. Dashed circles indicate approximate cluster centers for three clusters, determined by visual inspection. (d) Clustering of observations in PC space for three clusters from hierarchical clustering, with clusters 1, 2, and 3 in blue, green, and yellow, respectively. (e) Reconstructed spectrum from center (median) of each cluster, from superposition of first three modes. (f) Time series of angles between observed (synthetic) spectra and reconstructed spectrum (e) for each cluster when spectra are treated as vectors. Values close to 1 indicate strong alignment. More detail can be found in main body of text. Vertical, blue dashed lines and small numbers same as in Fig 3.3(b).

in Table 3.1 for different noise levels) shows that the first two modes together explain 95.9% of variance: The first mode explains 79.6%, and the second 16.4%. Much of the remaining variance, expanded by the remaining modes, is probably due to contributions from noise. The first two to three modes explain most of the variance for all noise levels (Section 3.3.2). We thus choose a consistent but generic cut-off and only include the first three modes in any further analysis.

Consistent with results from other applications of PCA (Liu *et al.*, 2006; Hsieh, 2009), the eigenvectors for the first three modes (Fig. 3.4(b)) fail to reproduce the known patterns (Fig. 3.3(a)), except for few aspects (such as the decay of amplitude from 0.5 to 4 Hz for eigenvector 1). To retrieve the actual frequency patterns, the data can be reconstructed as a superposition of the first three modes, i.e. the sum over the product between each eigenvector and its principal component. The principal components are shown in Figure 3.4(c) (note that only the first two components are shown). We apply clustering in the space spanned by the first three principal components to test whether the resulting clusters will replicate the three known patterns in the data. This approach is similar to clustering the reconstructed spectra based on the first three modes.

To do this, we use an agglomerative hierarchical clustering algorithm (cf. Wu and Chow, 2004; Hastie *et al.*, 2009; Jain, 2010). This clustering technique iteratively merges pairs of individual observations on the basis of the squared Euclidean distances $d_{ij} = \|X_i - X_j\|^2$ between observations

Table 3.1: Quality measurements and clustering results for different noise levels determined by RMS value of cross correlation coefficient between reconstructed spectra, comparison between PCA and SOM. Columns from left to right are: Noise level, number of modes necessary to explain 90% of the total variance, best cluster number k , misfit E (dB) for cluster number k , dimensions of the SOM topology, quantization error QE (dB), topographic error TE, best cluster number k and misfit E (dB) as for PCA, and misfit E^* (dB) for manual selection of three nodes from SOM (without clustering, see Fig. 3.8).

Noise	PCA			SOM			k	E	E^*
	90% var.	k	E	Map size	QE	TE			
0.1	2	3	16e-4	19×7	42e-4	387e-4	4	23e-4	10e-4
0.5	35	3	41e-4	19×7	17e-4	283e-4	13	36e-4	
1	44	3	91e-4	19×7	284e-4	238e-4	6	77e-4	
1.5	46	3	122e-4	19×7	366e-4	223e-4	14	107e-4	
2	47	5	135e-4	17×8	426e-4	193e-4	6	136e-4	
4	48	24	190-4	13×10	553e-4	238e-4	25	200e-4	

i and j . The algorithm then successively combines these subclusters containing two observations each into larger clusters using the same distance metric to assess similarity. We use Ward’s method to form the clusters, which assures that at each formation of a larger cluster there is the minimum increase in total within-cluster variance after merging. Ward’s method is known as the best hierarchical clustering method (*Gong and Richman, 1995*) and is commonly used. The optimal cluster number k must be determined from the resulting cluster structure. In this case, by visually inspecting Figure 3.4(c), we obtain a rough estimate for $k = 3$ clusters (a less subjective choice of cluster number will be discussed later). Figure 3.4(d) shows the cluster memberships for this case in PC space.

To enable evaluation and interpretation of the three clusters, we extract the median value for the first three components in each of the three clusters, and reconstruct a representative spectrum for each cluster by using the eigenvectors and the median principal components (Fig. 3.4(e)). Visually, the resulting spectra match the three known input spectra (Fig. 3.3(a)) well. We will discuss a more quantitative evaluation later.

To examine the temporal evolution of our synthetic signal (Figs. 3.2-3.3) in terms of the three clusters, we project the observed spectra S_n at each time step onto each of the reconstructed, representative spectra R_j . If each projection is normalized by $\|S_n\| \cdot \|R_j\|$, the resulting value is equal to the cosine of the angle θ between the two vectors. In this time series (Fig. 3.4(f)), if $\cos(\theta) \rightarrow 0$, the vectors are approximately orthogonal and our reconstructed spectra do not capture any part of the data. Alternatively, $\cos(\theta) \rightarrow 1$ indicates strong alignment of the two vectors, and thus we successfully represent the data by the reconstructed spectrum (e.g., cluster 3 shows good representation of the data during day 1, confirming the visual assessment that it is similar to the background, Fig. 3.4(e)-(f)). The changes in time from one dominating cluster to the next generally agree with the known changes from the synthetic input spectrogram during background, Phase I, and Phase II. Furthermore, during transitional time periods, when the spectra are known to gradually change from

one phase to another, one cluster slowly “decreases in importance” (i.e. the resemblance between the observed spectra and the representative spectrum for this cluster decreases), whereas another one increases (e.g., during time period 6, the alignment between the observations and cluster 1 decreases, while the alignment with cluster 3 increases, in accordance with the known change from Phase II to background). This way of projecting the data overcomes the main drawback of showing the results only as cluster indexes in time, where each observation is uniquely assigned one cluster index (often referred to as “hard” or “crisp” clustering, Köhler *et al.*, 2009; Messina and Langer, 2011) and which therefore cannot capture the gradual transitions from one pattern to another.

To evaluate how closely the reconstructed cluster spectra match the known input for a given cluster number k , we introduce the following misfit metric. For each known input spectrum S_i (Fig. 3.3(a)), we find the best-fitting reconstructed spectrum S_j (Fig. 3.4(e)) by identifying the minimum value of the RMS difference D_{ij} between S_i with all S_j . The misfit is determined as $E = \sum_{i=1}^3 (\min_{j=1}^3 (D_{ij}))$. For noise level 0.1, $E = 0.0016$ dB. The difference between maximum and minimum value of Phase I spectrum (i.e., the spectrum with the smallest range, Fig. 3.3(a)) is approximately 0.03 dB, and E thus corresponds to less than $\sim 2\%$ difference per spectrum relative to this smallest range. An advantage of measuring the misfit between the reconstructed spectra and the known input is that we can explicitly compare the results from our PCA analysis with the SOM method (Table 3.1), which we describe in detail in Section 3.4.

One of the biggest challenges in clustering data is to find the optimal cluster number k (e.g., Davies and Bouldin, 1979; Carniel *et al.*, 2013a), which we set manually on the basis of the known input for illustrative purposes above. Previous studies have applied cluster evaluation measures in the space where the clustering was done (i.e., the principal component space; e.g. Farzadi and Hesthammer, 2007), for example by using a dendrogram (Fig. 3.5(a)), i.e., the tree-like visualization of the cluster structure from the hierarchical clustering (e.g., Carniel *et al.*, 2013a). The dendrogram in Figure 3.5(a) shows 30 (arbitrarily numbered) subclusters on the x-axis (as opposed to reaching down to the level of joining individual observations, which would be complicated to visualize), and the y-axis indicates the distance between the subclusters joined at any given level. The level at which these distances become relatively small further down the dendrogram is a common choice for a cut-off level to determine the optimum number of clusters (e.g., Marroquín *et al.*, 2008; Hsieh, 2009). In our case, the dendrogram shows that distances become much smaller for $k = 2, 3$ or 4 (Fig. 3.5(a), dashed lines), thus not yielding a unique optimum number of clusters. This somewhat subjective metric is one of the main shortcomings of the dendrogram applications (e.g., Carniel *et al.*, 2013a).

Whereas identifying the cluster number through the dendrogram only utilizes the distances among the clusters after each merging, our goal here is to find the minimum number of clusters whose corresponding reconstructed spectra are the least similar each other. (Fig. 3.4(e)). We thus introduce an independent metric that takes the reconstructed spectra into account. As shown for the case of $k = 3$ from Figure 3.4, similar to McGreger and Lees (2004); Ruiz *et al.* (2006); Carniel *et al.* (2013a) we obtain pairwise Pearson’s cross-correlation coefficients ρ for all $n_c = k!/(2!(k - 2)!)$ unique combinations of reconstructed spectra to estimate (dis)similarity (Fig. 3.5(a)). We then

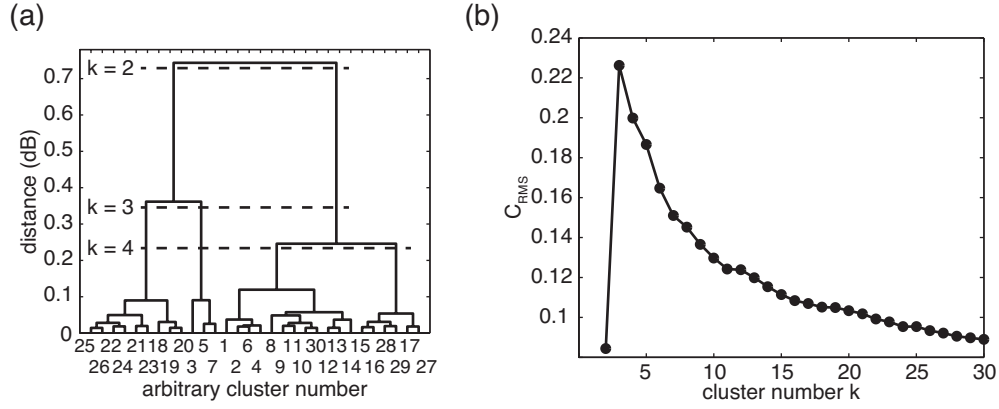


Figure 3.5: Cluster evaluation diagnostics, noise level 0.1. (a) Dendrogram showing cluster structure and distances between clusters. Only up to 30 subclusters (instead of all observations) are shown. The vertical positions of the solid horizontal bars linking different clusters indicate the distance between those clusters. Dashed lines show possible cut off levels related to decreasing distances between cluster below. (b) C_{RMS} value for cross-correlation coefficient between unique combinations of reconstructed spectra from (a), for cluster numbers between 2–30. A large value means that there is a lower correlation between the representative spectra, and thus that the similarity between the spectra for this cluster configuration is low.

use the root-mean square (RMS) error of those correlation coefficients relative to a reference value of 1 (perfect correlation)

$$C_{\text{RMS}} = \sqrt{\frac{\sum_{n=1}^{n_c} (\rho_n - 1)^2}{n_c}} \quad (3.1)$$

as a measure for the similarity between the patterns when clustering the data with this k . We calculate this C_{RMS} value for a number of cluster configurations with $k = 2 \dots 30$ (Fig. 3.5(b)). A smaller value indicates a higher overall correlation between the reconstructed spectra, and thus potentially redundant information from this cluster structure compared to others. The resulting distribution for C_{RMS} has a maximum at $k = 3$, indicating a minimum in similarity, which agrees with the known number of input patterns.

Our approach is similar to that of *Langer and Falsaperla (1996)*; *Falsaperla et al. (1998)* and *Langer and Falsaperla (2003)* in that we use spectral power as input to PCA. However, our normalization (pre-processing) is designed specifically to detect spectral patterns on the basis of their shape, not their absolute amplitude. In addition, we apply cluster analysis in the lower-dimensional PC space. Instead of determining the best number of clusters in principal component space, we develop a criterion based on the reconstructed spectral space. Furthermore, our approach uses the results to reconstruct representative spectra in the original, spectral domain. Lastly, the methodology in *Langer and Falsaperla (1996)*; *Falsaperla et al. (1998)*, and *Langer and Falsaperla (2003)* was directly applied to real data, without the rigorous testing (i.e., benchmarking) with a control dataset we perform here.

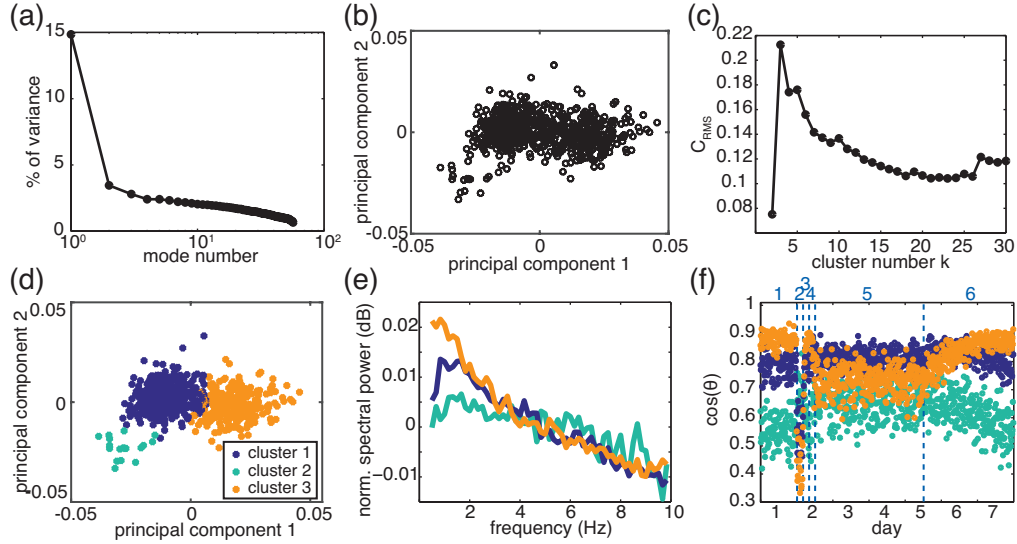


Figure 3.6: PCA results for noise level 1.5. (a) Percentage of variance explained by each mode. (b) Projection of the observations in space spanned by principal components 1 and 2. (c) Evaluation measure for different cluster configurations, with the peak at $k = 3$ indicating the best cluster number. (d)-(f) Same as in Figure 3.4.

3.3.2 Performance of PCA and Clustering at Higher Noise Levels

We next evaluate the sensitivity of our combined PCA and clustering algorithm to different levels of white noise. Table 3.1 summarizes some parameters as well as the misfits, and Figure 3.6 shows the analysis steps for the example case of noise level 1.5. Figure 3.2 shows that this noise level is higher than what is expected from a real dataset (cf. Fig 3.1(b)). Much more of the variance is now carried by the “noisy” higher modes (the first three modes carry only 21.1% of the variance, Fig. 3.6(a)), and the principal components do no longer follow the simple trajectories apparent for noise level 0.1 (Fig. 3.6(b)). C_{RMS} reaches its peak at $k = 3$, correctly indicating the number of known patterns despite the increased noise level. This emphasizes the importance of performing the clustering in the space of first few (in our case three) modes, regardless of how much of the total variance they explain. In PC space, clusters are determined on the basis of the relevant dissimilarity in terms of the spectra instead of the differences in the noise, which is mainly captured in the higher PCA modes that we neglect. This procedure assures that, even for the noise level of 1.5, the clustering can successfully distinguish the relevant differences in the patterns from the “irrelevant” differences introduced by noise.

The bottom row in Figure 3.6 summarizes the outcome of the clustering, the reconstructed spectra, and the temporal evolution for $k = 3$. The background, Phase I, and Phase II still form distinct clusters consistent with the original input spectra, albeit with reduced amplitudes (Figs. 3.3 and 3.6(e)). However, because of the way we normalize the input, absolute amplitude information for comparison between the different spectra cannot be obtained for any noise level, and the difference is, thus, meaningless. For this noise level (1.5), the misfit $E = 0.0122$ dB, i.e., approximately 14% per spectrum. The main differences between the input spectra, e.g., the higher variability at various

frequencies during Phase I and the average slopes of the spectra during the three time periods are still captured, despite the higher level of noise. However, whereas the general trends of the temporal evolution are similar to the low noise case (Fig. 3.4(f) vs. Fig. 3.6(f)), the distinctions between the clusters become unclear.

Table 3.1 shows that the misfit between the known and the reconstructed spectra increases with increasing noise. The clustering algorithm shows a trend towards requiring more clusters ($k > 3$) to identify the three known input patterns (according to C_{RMS}). Our cluster evaluation criterion thus overestimates the total number of clusters and consequently includes redundant patterns in addition to the known three input spectra.

3.4 Self-Organizing Maps

We use the results of our PCA algorithm as benchmarks to evaluate the performance of SOM on the same synthetic seismic dataset. For the SOM algorithm, we use a MATLAB® based SOM toolbox by *Vesanto et al.* (1999, 2000) (freely available on <http://www.cis.hut.fi/projects/somtoolbox/>). The SOM algorithm was introduced by *Kohonen* (1982, 1990). The basic idea is to cluster observations (in our case the spectra) onto a 2D topology of nodes (whose number has to be set) by finding the minimum Euclidean distance between each observed spectrum and the pre-assigned spectrum of a given node. When this so-called best-matching unit (BMU) is identified, its spectrum, as well as the spectra associated with surrounding nodes in a given radius around the BMU are updated to be more similar to the data spectrum. When this process is done iteratively, the map “learns” the main patterns of the input data. On the final topology, neighboring nodes represent similar patterns/spectra, whereas dissimilar patterns are placed farther apart. Even though the SOM approach has been commonly used as a clustering tool (i.e., clustering the data onto a 2-D map), its value lies in its role as a discrete nonlinear PCA (*Cherkassky and Mulier*, 1998). Equivalent to representing the multidimensional PC space by mutually orthogonal eigenvectors, the SOM approximates a dataset in multidimensional space by a flexible grid (typically of two dimensions) of cluster centers.

To examine the SOM results, we visualize the shape of the feature spectra in relation to their location on the SOM topology (Fig. 3.7(a)), the relative distances between feature patterns of the nodes (smaller node size means a larger distance to the neighboring nodes, Fig. 3.7(b)), and the BMU for each observation in time (Fig. 3.7(c)). Both visualizations of the topology can be used to determine which spectra are similar. For the temporal evolution, the y-axis refers to the number of the map nodes, which are numbered first along the rows of the topology, and second along the columns (i.e., in this example node 20 is the node in the first row of the second column for the 19×7 map, Fig. 3.7). The color contains the same information, and helps to visually determine which nodes are close to each other. Excellent resources exist with more details about the SOM algorithm (e.g., *Kohonen*, 1990; *Vesanto et al.*, 2000; *Klose*, 2006; *Langer et al.*, 2009; *Carniel*, 2014). Here, we apply the method combined with clustering in a way similar to previous volcano seismic studies (e.g., *Langer et al.*, 2009; *Messina and Langer*, 2011; *Carniel et al.*, 2013a,b)) to evaluate its capability to capture the main features of our synthetic dataset.

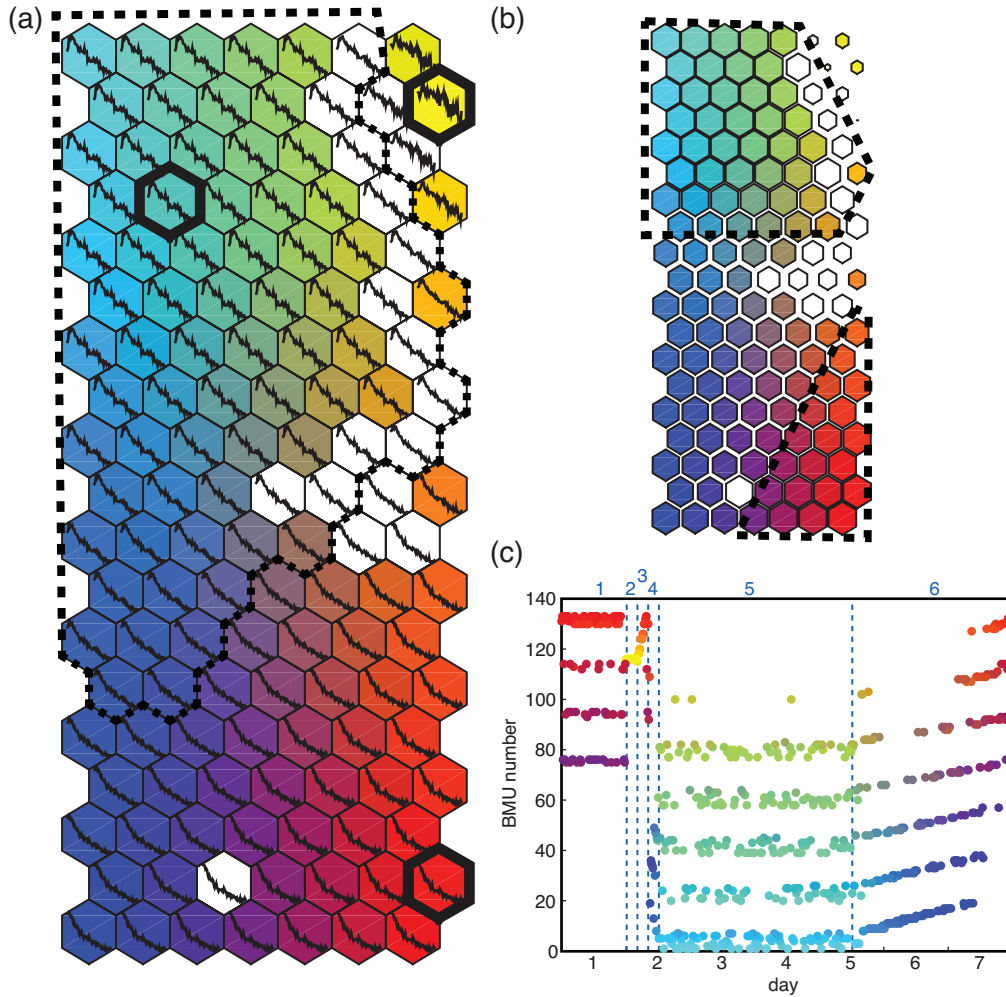


Figure 3.7: Output from SOM algorithm, noise level 0.1. (a) Feature space with representative spectra shown on each node, with color coding for easy referencing. White nodes are “empty”, i.e., not associated with any data in the final map configuration. Three nodes outlined in bold indicate spectra manually chosen for Figure 3.8. Dashed black lines outline approximate grouping according to feature spectra, discussed in Section 3.4.2. (b) Same feature space, but with node size scaled by mean distance to neighbouring nodes (small nodes correspond to large distances, and vice versa). Dashed black lines outline approximate grouping according to distances, discussed in Section 3.4.2. (c) Temporal evolution of BMUs for each observation in time. Certain areas of the SOM topology are only active at certain times. Vertical, blue dashed lines and small numbers same as in Fig 3.3(b).

Table 3.2: Quality measurements and clustering results according to RMS value of cross correlation coefficient between reconstructed spectra, for different SOM sizes at noise level 0.1. Columns from left to right are: Dimensions of the SOM topology, quantization error QE (dB), topographic error TE, best cluster number k and misfit E (dB), and misfit E^* (dB) for manual selection of three nodes from SOM (without clustering, see Fig. 3.8).

Map size	QE	TE	k	E	E^*
2×3	96e-4	0e-4	4	99e-4	99e-4
5×2	83e-4	253e-4	2	105e-4	
8×3	63e-4	1012e-4	2	102e-4	
11×4	53e-4	610e-4	6	42e-4	
14×5	48e-4	565e-4	4	43e-4	
16×6	44e-4	343e-4	4	33e-4	

3.4.1 SOM Topology Size

For a given dataset, many parameters can be modified within the SOM toolbox. To test the method as it is often implemented, we chose values consistent with previous work (e.g., *Langer et al.*, 2009, 2011; *Di Salvo et al.*, 2013). In particular, we use hexagonal units on a sheet topology. The automatic training length calculation results in 3 iterations and a learning rate of 0.5 for the rough training phase, and 9 iterations and a learning rate of 0.05 for the fine tuning phase. Depending on map size, the Gaussian neighbourhood radii are 2–3 and 1 for the two training phases, respectively. The only parameter where we do not choose the default is the initialization of the feature patterns on the topology, because we found linear initialization (i.e., the initial SOM nodes lay on the plane spanned by the two leading PCA eigenvectors) to yield slightly more reproducible results.

In terms of our ability to recover the known phases (Fig. 3.3), one important parameter is the size of the resulting 2D topology (e.g., *Radic and Clarke*, 2011). In particular, a smaller number of nodes will result in broader generalizations of the patterns in the input data space. In contrast, larger SOM are able to capture finer variations in the input data space, which in our case represent differences in the patterns due to the noise. Similarly, if there is noise in the data then patterns that occur only a few times compared to the total length of the dataset may be easier to detect on a large SOM. The toolbox can determine the ideal size and shape (i.e., aspect ratio of the map) on the basis of the dataset length (i.e., the total number of observed spectra) and the ratio of the two largest eigenvalues for the dataset (*Vesanto et al.*, 1999, 2000). For noise level 0.1 the best size as determined by the algorithm is 19×7 . There are two measures for goodness of fit of a topology: The quantization error QE (i.e., the mean RMS difference between each data spectrum and its BMU), and the topographic error TE (i.e., the fraction of the observations for which the first BMU and the second BMU are not neighboring nodes), both of which should be small. The more nodes the map has the better it can fit the data (i.e., generally decreasing QE), but the trade off is that the likelihood of overfitting increases (i.e., generally larger TE, Table 3.2).

Figure 3.8 illustrates the difference in results for varying map sizes. We manually pick three representative spectra from a small 2×3 topology (Fig. 3.8(a)), and from the feature space of the

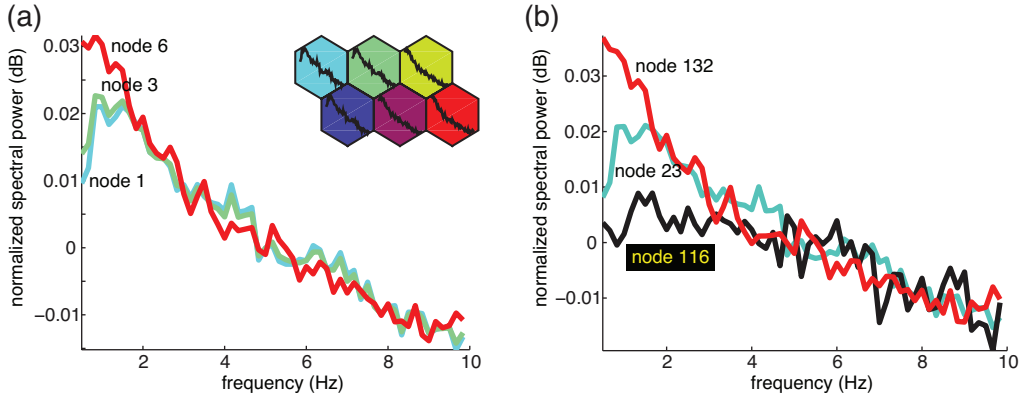


Figure 3.8: Three feature spectra from (a) a small 2×3 topology (inset), and (b) the SOM topology in Fig. 3.7. The nodes were chosen as the approximate centers of groups on the topology representing the three input spectra (Fig. 3.3), determined by eye. Whereas the smaller map cannot distinguish between Phase I and II, the larger map captures the differences related to the input spectra well.

original 19×7 topology (Figs. 3.7 and 3.8(b)) for comparison. The small 2×3 map shows fewer variations in spectral characteristics across the map topology, i.e., the variations of the input spectra are mostly averaged out (which leads to higher QE, Table 3.1), whereas the general shape with a decrease in spectral power from low to high frequencies is preserved. However, despite the fact that six nodes should theoretically be enough “groups” to account for the background and both phases, in practice Phase I and Phase II are grouped by this small topology. Most likely, this result is related to Phase I appearing only for a relatively short amount of time and the pattern is consequently averaged out. In contrast, the “ideal” 19×7 map as determined by the algorithm shows more subtle variations among the feature spectra. The presence of subtle variations for larger maps highlights the importance of map size: A large number of nodes is essential to capture spectral characteristics that may not be represented in many observations and are thus not carrying enough weight to significantly influence the feature patterns (such as Phase I). We tested several topology sizes with the same aspect ratio but a smaller number of nodes (Table 3.2), which may be easier for grouping. QE and TE indicate that the 19×7 topology is the ideal choice.

The automatic size determination provided by the toolbox has been used for previous studies (e.g., *Langer et al.*, 2011) and is our preferred method, mainly because it is automated and reproducible, in particular without a priori knowledge of the patterns. Because the resulting number of nodes on the 19×7 SOM overestimates the known number of three patterns, we follow previous SOM studies (e.g. *De Matos et al.*, 2006; *Köhler et al.*, 2009; *Messina and Langer*, 2011; *Carniel et al.*, 2013a; *Di Salvo et al.*, 2013) and apply clustering to the SOM topology, which we discuss in Section 3.4.2. This is different from reducing the number of nodes as discussed above, since clustering of the topology does not usually depend on the frequency of occurrence of each spectrum, but simply on the distance between the respective patterns of each node.

3.4.2 Results and Clustering of SOM Patterns

In terms of the spectra, the biggest differences among patterns on the SOM appear between the top and the bottom half of the map (cyan, green, yellow vs. dark blue, red, purple; Fig. 3.7(a)), and between the 4–5 spectra at the top right corner and the rest (cyan and green vs. yellow; Fig. 3.7(a)). This division into three groups is partly confirmed by the visualization of the distances between nodes on the topology (Fig. 3.7(b)). However, the larger distances between nodes for a large portion of the bottom half of the map (dark blue, purple, and orange area; Fig. 3.7(b)) suggests that four groups may also be a valid choice. This ambiguity is similar to the difficulties with dendrograms discussed in Section 3.3.1 and indicates that it may be difficult to evaluate how nodes on the map should be grouped without a priori knowledge of the patterns or additional processing.

On the timeline (Fig. 3.7(c)), the “harmonic” character stems from the mapping of the 2D topology onto the (1D) y-axis (i.e., on the 19×7 map node number 1 is adjacent to node number 20, and so on). For example, during time period 5 all the variation in terms of BMUs is confined to the top left corner of the topology (cyan and green), which consists of similar patterns that differ mainly in their white noise level. In contrast, the transitional time periods (e.g., period 6) are shown as gradual changes in BMU from one area of the topology to another over time. This result indicates that dark blue, purple, and red nodes may be representative of this transitional time, and highlights again that grouping of patterns is particularly difficult if gradual transitions exist in the data.

On the basis of these challenges, the large number of nodes necessary to capture short-duration phases (Section 3.4.1), and the similarity of spectral shapes in different areas of the map, we apply the same hierarchical clustering algorithm used for PCA (Section 3.3.1). In this case the clustering is applied to SOM patterns that occur in the data, i.e. we exclude the nodes that never act as a BMU to any of the observed spectra. These “empty” nodes correspond to artificial patterns created solely to “fill in” the gaps in the topology, and should not be considered as real patterns present in the data (e.g., *Liu et al.*, 2006). Following the same approach as for clustering the observations in PC space, we cluster the SOM patterns for $k = 2..30$ and use the C_{RMS} metric to identify the ideal cluster number k (Equation 3.3.1). For noise level 0.1, the ideal $k = 4$ (Fig. 3.9(a)). For each of the resulting clusters we find the corresponding pattern by taking the median of all spectra associated with the nodes within that cluster (Fig. 3.9(b)–(c)), and plot the temporal evolution as done for the PCA results (Fig. 3.9(d)).

Even at low noise, the best clustering structure according to C_{RMS} is obtained for $k = 4$, not $k = 3$ as with PCA. Three out of identified four patterns correspond well to our three known patterns ($E = 0.0023$ dB) which means that the clustering on SOM is able to identify the known set of patterns but only by additionally identifying a redundant pattern. Similar to the results from clustering in PC space on data with noise level 2, the correct three patterns are identified for an overestimated optimal number of clusters ($k > 3$). However, for clustering on SOM this overestimation occurs already at noise level 0.1. Similarly, the clustering algorithm in combination with C_{RMS} consistently overestimates the ideal k on the SOM for higher noise levels. For noise level 0.5, for example, where the ideal $k = 13$, 10 additional, redundant patterns are identified. Because of these

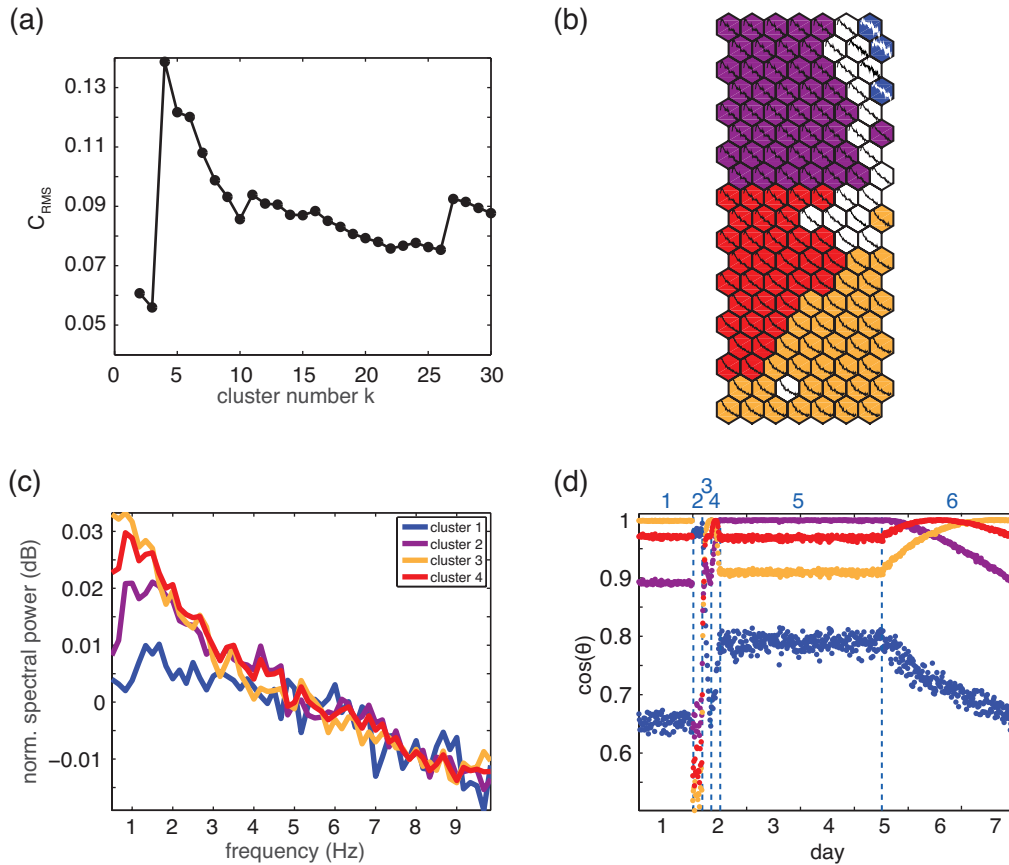


Figure 3.9: Clustering of SOM topology, noise level 0.1. (a) Cluster evaluation measure, with peak indicating $k = 4$. (b) SOM topology with feature spectra, colored according to clustering. Empty nodes in white. (c) Final spectra, reconstructed from the median of all feature spectra included in respective cluster. (d) Time series of angles between observed spectra and central spectrum for each cluster. Values close to 1 indicate strong alignment. Vertical, blue dashed lines and small numbers same as in Fig 3.3(b).

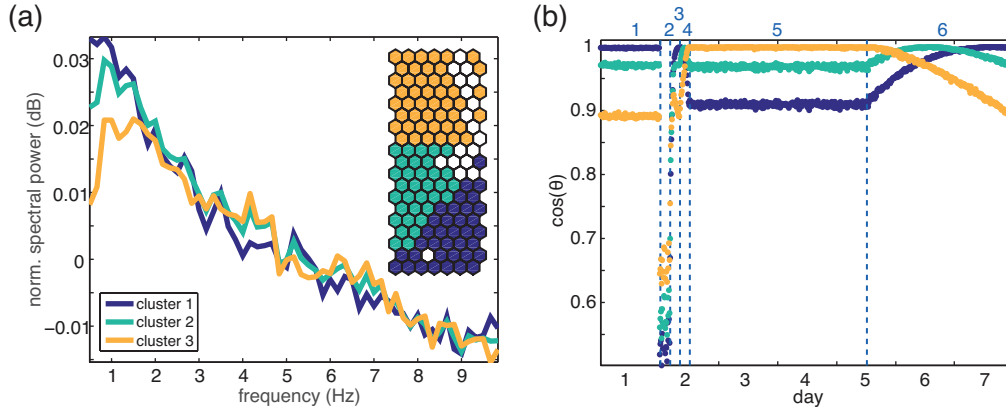


Figure 3.10: Clustering of SOM topology, noise level 0.1, manual selection of $k = 3$. (a) Final spectra, reconstructed from the median of all feature spectra included in respective cluster, with SOM topology colored according to clustering as inset. (b) Time series of angles between observed spectra and central spectrum for each cluster. Values close to 1 indicate strong alignment. Vertical, blue dashed lines and small numbers same as in Fig 3.3(b).

redundant patterns that capture transitions and noise, the misfit for clustering on the SOM is lower than for PCA for the same noise levels (Table 3.1). Manually setting $k = 3$ for the hierarchical clustering for noise level 0.1 only partly reproduces the known phases and corresponding input spectra (Fig. 3.10). The misfit $E = 0.0090$ dB is still over 5 times larger than for clustering applied to the PCA results. We further discuss manual selection of parameters in Section 3.5.2, and potential implications for our cluster evaluation criterion in Section 3.5.3.

3.5 Discussion

In the following, we discuss the main results of our work and the implications for applying the PCA and SOM methods to a synthetic dataset with spectral features (different spectral shapes with both impulsive and emergent variations over time) that can be observed at Kīlauea and other volcanoes. Because our work is aimed at recognizing distinctive spectral patterns we do not include a detailed discussion about the underlying mechanics which may not be unique and which are addressed in numerous other studies (e.g., *Ripepe and Gordeev, 1999; Johnson et al., 1998; Chouet, 1986; Leet, 1988; Julian, 1994; Neuberg et al., 2000; McNutt, 2005; Jellinek and Bercovici, 2011; Unglert and Jellinek, 2015*). Here, we first give a summary of the steps necessary for each method (Section 3.5.1). We then discuss the limitations of the SOM method (Section 3.5.2), and the limitations of the PCA method and our synthetic data (Section 3.5.3).

3.5.1 Summary of Steps Taken for Each Method: Parameter Choices

For PCA, there are two important steps to reliably capture different spectral patterns:

1. Examine variance graph to determine the number of modes to be used for further analysis

(Figs. 3.4(a) and 3.6(a); three modes were kept here to enable comparison between the different cases).

2. Use C_{RMS} (Figs. 3.5(b) and 3.6(c), Equation 3.3.1) to identify the optimal cluster number.

By contrast, for SOM the following choices need to be made:

1. Set parameters (including map size) for SOM algorithm.
2. *Either* use C_{RMS} (Fig. 3.9, Equation 3.3.1),
3. *or* use visual inspection of patterns on SOM topology (Fig. 3.7(a)) to identify the best cluster number.

The comparison between the PCA and SOM cluster analyses of our synthetic spectral dataset indicates that each method has distinct advantages and pitfalls that we will discuss in the following sections. Processing times for both methods were on the order of 100 seconds⁹. In general, our PCA approach was more successful than SOM at reproducing the known number of input patterns at the same noise level in our synthetic dataset.

3.5.2 Limitations of Typical Volcano Seismic SOM Approach

Our cluster evaluation criterion applied to the SOM topology gave $k > 3$ as the best cluster number for all noise levels (Table 3.1), which is inconsistent with the three known input patterns (Fig. 3.3(a)). The three known patterns are identified on the SOM, but clustering cannot successfully distinguish between those and other, redundant patterns. This lack of success demonstrates that the clustering without any a priori information cannot correctly identify the number and appearance of the patterns from the data on the SOM. To overcome this impediment, an additional metric could be introduced to direct the initial groupings around the cluster centers of interest. A type of supervised classification, rather than unsupervised clustering, might thus perform better for this application on SOM. The underperformance of clustering on SOM relative to clustering on PCA may be related to the clustering on the SOM not accounting for some nodes being representative of only very few spectra from the original dataset. Patterns carrying almost no variance may, thus, dominate the clustering, turning the original advantage of clustering not accounting for variance into a disadvantage. Furthermore, clustering on the SOM topology may be complicated by the fact that it is based on the full spectrum (i.e., all 57 frequency samples), as opposed to the low-dimensional PC space (i.e., 3 dimensions out of 57). Similarly, the clustering algorithm does not account for the position of each node on the map topology, which is a crucial part of the information provided by SOM.

Alternatively, nodes characteristic for the main patterns in the data can be manually selected on the SOM topology (Fig. 3.8(b)). However, on the basis of ambiguities with respect to the optimal

⁹On a 2 of 6 core/12 thread Intel® Xeon® CPU E5645 with 2.40 GHz (in effect 12 core/24 thread); 48 GB DDR3 RAM; storage 6x4 TB raid 6 sequential benchmark \approx 500 MB/s.

number of clusters, and the associated subjective choices, we do not investigate this option further. Similarly, manual determination of cluster membership of each node is difficult and subjective, because of the nature of gradual variations of spectral patterns across the SOM topology with changes at many frequencies (Fig. 3.7(a)).

For different map sizes, k varies between 2–6 (Table 3.2), and is more consistent with the three known input spectra than for the automatically determined map size on average because of the low noise level. This suggests that the size of the map topology influences the performance of the clustering algorithm. Running the SOM algorithm with a range of map sizes, and subsequently applying the clustering to each topology may, thus, help to get a better estimate of the best k for a natural dataset with a generally unknown number of patterns. However, in some cases Phase I and Phase II are combined into one cluster (2×3 , 5×2 and 8×3), whereas in others the phases are correctly identified but with additional patterns related to the transitions between the phases (e.g., 11×4). Even with an exhaustive set of topologies, it is not clear how to determine the final best answer without any a priori knowledge.

Our analysis suggests that the clustering methodology appears to be the main inhibiting factor for SOM performance, even when applying the quantitative approach with our cluster evaluation metric. Tests of the method with earlier versions of the synthetic dataset gave good clustering results in some cases, but not in others (for example, with the noise added to spectral amplitude instead of power, resulting in a stronger variability at high frequencies where spectral amplitude/power are low; results not shown). This highlights the strong dependence of the SOM topology and subsequent clustering on the input dataset. Several modifications of the algorithm, including usage of cross-correlation based clustering as suggested by *Carniel et al.* (2013a), and applying PCA to the SOM topology to cluster the nodes in the resulting lower dimensional space did not yield significant improvement. Replacing hierarchical clustering with a different cluster algorithm may help to alleviate the issues. For example, *De Matos et al.* (2006) apply k-means clustering to the SOM topology for the analysis of waveforms to identify seismic facies in the subsurface. Their synthetic test shows good results (*De Matos et al.*, 2006), but more detailed investigation is necessary to evaluate its performance when analyzing features in volcano seismic spectra. Alternatively, replacing traditional clustering algorithms with different ways of grouping the nodes may have a higher chance of success. In particular, any grouping algorithm should account for the information inherent in the SOM topology, which clustering methods typically neglect. *Bauer et al.* (2012) apply grouping of nodes by using the gradient of the distance matrix of the SOM topology to derive a lithological model from inversion results of seismic and magnetotelluric data. Initial tests with a similar method to group nodes on our SOM topology show that accounting for the topological relationships between the nodes may improve the results. Detailed investigation of this new method is beyond the scope of this comparative study, and will be addressed in a future paper.

However, SOM without clustering can be useful in providing an overview of patterns in the data space and their similarities and differences (Fig. 3.7). The temporal evolution of BMUs (Fig. 3.7(c)) can be used to capture continuous transitions from one pattern to another. However, using the SOM output in this way may be subjective. Interpretation of similarity in color on the timeline, for exam-

ple, depends on the subjective perception of color differences (e.g., Rogowitz and Treinish, 1998; Borland and Taylor, 2007), and suffers from mapping the non-linear SOM topology onto a prescribed, typically linear, color scale. To navigate this challenge, Langer *et al.* (2009) apply PCA to the SOM output, and assign red, green, and blue to the first three principal components respectively. Each feature pattern is then projected onto the three principal components, and the corresponding node is given the corresponding mixture of red, green, and blue on the basis of the projections. Similarly, Langer *et al.* (2011) project the nodes onto the first two principal components for visualization of distances, and show the temporal evolution in combination with a separately obtained cluster analysis. Whereas the additional PCA might help to better depict the distances between nodes by using color, the subjectivity in color perception remains unaddressed. Furthermore, their visualization of the temporal evolution of BMUs relies on results from an independently obtained cluster analysis in both studies, and may not be usable on its own.

On the basis of these shortcomings, on the fact that previous studies (Langer *et al.*, 2009, 2011) had to combine SOM, PCA, and cluster analysis, and on the potentially subjective choices that have to be made, the question arises whether skipping the SOM step and using PCA and cluster analysis only might yield characteristic volcano seismic spectra in a more efficient way. We thus focus the remainder of Section 3.5 on discussing the PCA approach and its application to our synthetic data.

3.5.3 Limitations of our Synthetic Data and the PCA Approach

Because of the way we construct the relatively short synthetic dataset, one could argue that the same features could be identified by visual inspection of the spectrograms (e.g., Fig. 3.3). However, the true power of the PCA plus clustering approach is that the algorithm can extract the patterns in the same way for much longer datasets with patterns that are not necessarily temporally grouped. Even if a volcano is exhibiting anomalous signals for only a small period of time (such as Phase I, which represents approximately 2% of the entire dataset), PCA will identify those signals if the variance of the usual patterns is smaller than the difference between the anomalous and the more common signals.

Our synthetic dataset, drawn from volcanic unrest at Kīlauea with features similar to other volcanic settings (Fig. 3.1), is only one of many possible examples for a benchmarking case. To evaluate whether the successful application of the PCA plus clustering method is only due to the nature of our synthetic data, we test a modified version of the dataset, where an additional pattern is added to analyze four instead of three patterns in total. We test two cases, where (i) the additional pattern corresponds to the Phase II spectrum flipped along a vertical axis in frequency space (noise level 0.1, Fig. 3.11), and (ii) the additional pattern is a modified version of Phase II that is not as different from the other spectra compared to the previous case (Fig. 3.12). For the flipped Phase II case, the principal components now show an additional cluster of points (cluster 1, Fig. 3.11(c)) relatively far removed from the observations from the original dataset. The shape of the original principal components is still preserved (clusters 1–3, Figs. 3.4(d), 3.11(c) and 3.11(e)). Because our cluster evaluation criterion favors strong dissimilarity including anti-correlation between clus-

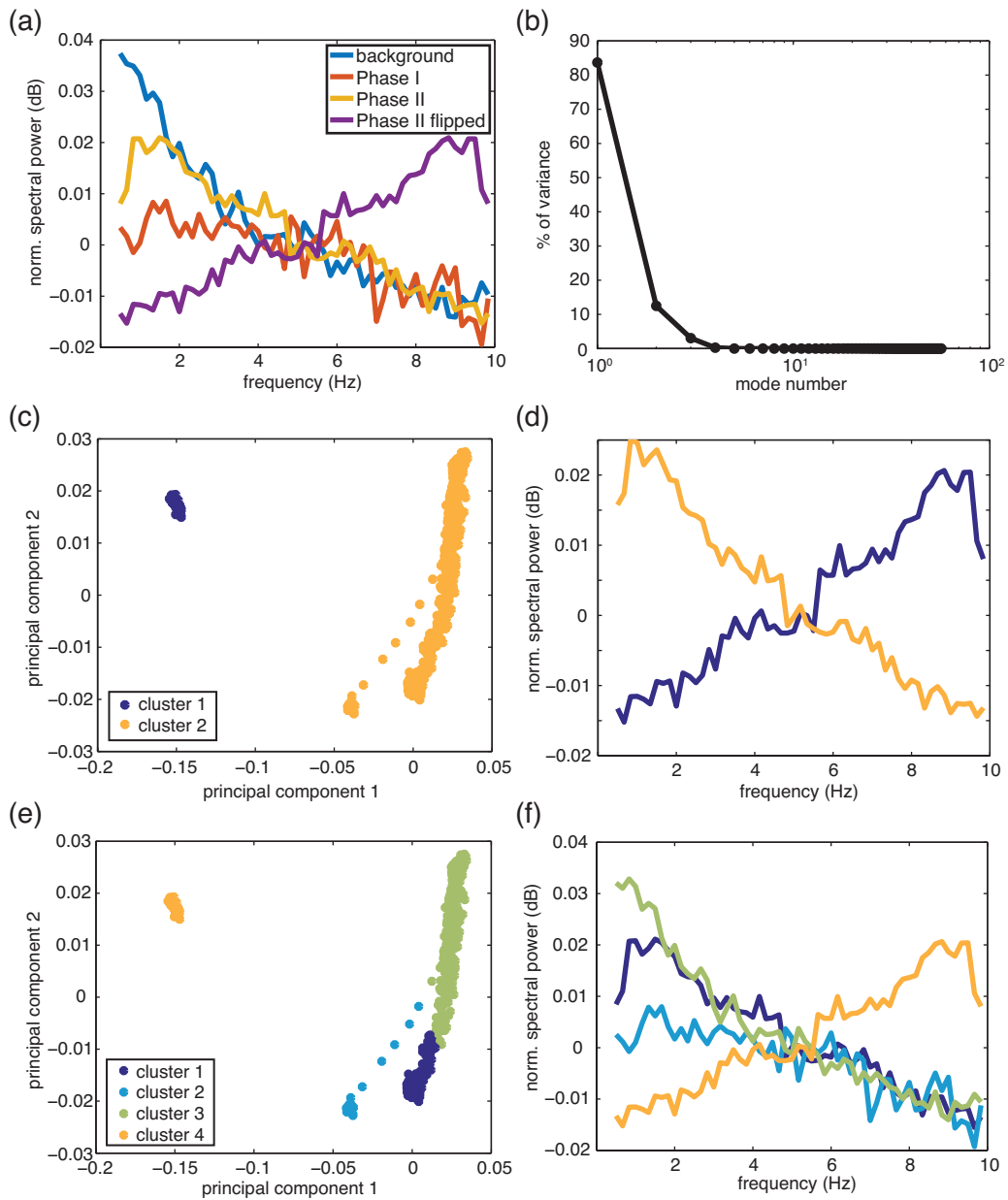


Figure 3.11: PCA plus clustering method applied to same synthetic dataset with flipped Phase II pattern. (a) Known input spectra. Background, Phase I, and Phase II as before, with a flipped Phase II pattern added. (b) Percentage of variance explained by each mode. (c) Clustering of observations in PC space with $k = 2$ determined through C_{RMS} . Note the similarity of the shape of clusters 1–3 compared to the original dataset (Fig. 3.4(c)-(d)). (d) Reconstructed cluster spectra for $k = 2$. (e)-(f) Same as (c)-(d) but for $k = 4$ (k chosen manually by visual inspection of (c)/(e)).

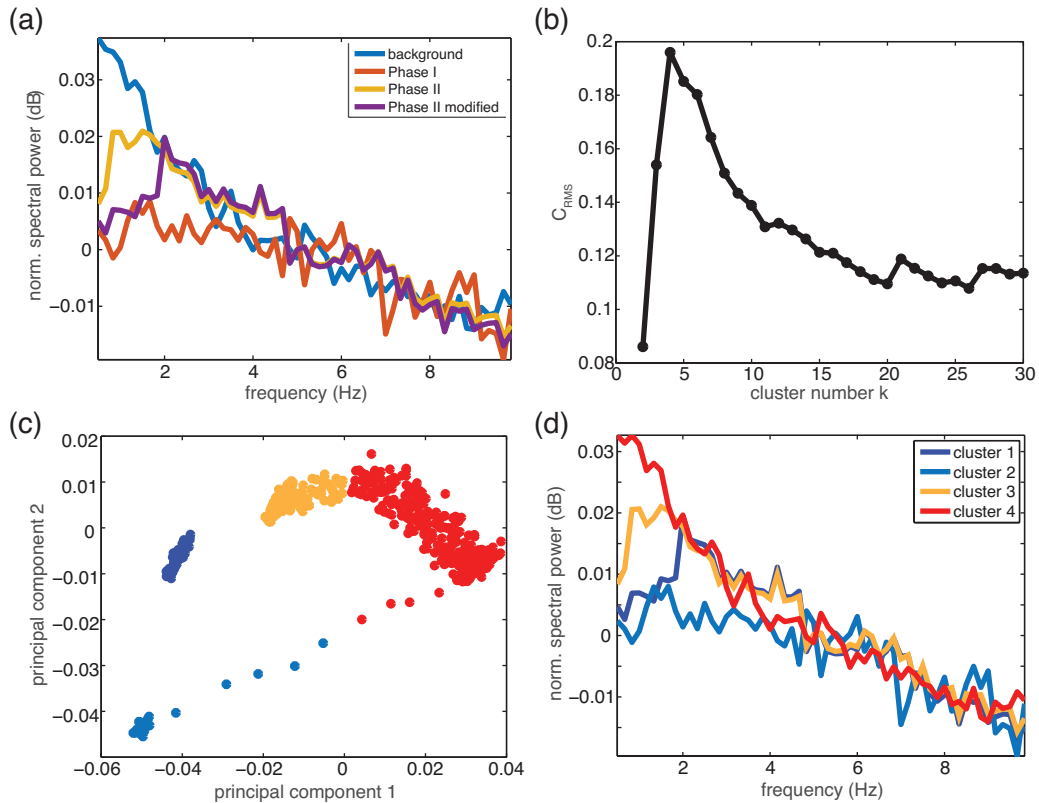


Figure 3.12: PCA plus clustering method applied to same synthetic dataset with modified Phase II pattern. (a) Known input spectra. Background, Phase I, and Phase II as before, with a slightly modified Phase II pattern added. (b) C_{RMS} indicates best $k = 4$. (c) Clustering of observations in PC space with $k = 4$. (d) Reconstructed cluster spectra for $k = 4$.

ters (highest information gain), for this four-pattern case the peak is at $k = 2$, and the three original spectra are combined into one large cluster (Fig. 3.11(c)-(d)). This shows that our clustering approach only works in an automated fashion if the input patterns all are at comparable distances relative to each other in PC space (e.g., as is the case for our three original input spectra). In contrast, for the four patterns that had comparable distances in PC space ((ii), Fig. 3.12) the clustering approach correctly identified $k = 4$ and reproduced the patterns.

For case (i) that includes the flipped Phase II spectrum, the transitions between the three original spectra add observations in the space between their respective cluster centers, further contributing to the spectra being combined into one cluster. However, in such a case visual inspection of the PCA space (e.g., Fig. 3.11(c) and (e)) can help to identify “subclusters” at different scales, and subsequent manual adjustment of the cluster number to $k = 4$ can be used to reconstruct the patterns corresponding to those lower level clusters (Fig. 3.11(f)). In contrast to manually selecting the cluster number on the SOM topology, this approach works in PC space, because the decision is made in the low dimensional PC space that can easily be visualized.

The PCA plus clustering approach works well with our dataset because the data are normalized to account only for their shapes. If some spectra in the dataset were to cover a much larger range of spectral power values than others (similar to the background vs. Phase I, only more extreme than shown in Fig. 3.2(a)), the normalization would remove these differences in range. However, as a trade off, this way the small variations of spectral power between different frequencies may be enhanced for spectra with a small total range of spectral power. For example, the small variations of Phase I before the normalization (Fig. 3.2(a)) are amplified by the way we normalize each spectrum (Fig. 3.3(a)). Because this will be similar for spectra with similar shapes, we do not expect this effect to strongly influence the performance of our algorithm in a negative way. If a different normalization is chosen, amplitude differences may become important. Future studies should be conducted to investigate how different normalizations impact the performance of the algorithm.

Table 3.1 indicates that our cluster evaluation criterion shows a slight dependence on the noise for our PCA method (best $k = 3$ for all but the highest two noise cases for our three pattern dataset). To test the sensitivity of the clustering results to the choice of cluster evaluation criterion C_{RMS} , we test a different criterion (Table 3.3) that obtains the RMS value of the RMS differences between the reconstructed cluster spectra (consistent with Euclidean distances used for clustering in PCA space). The resulting ideal cluster numbers are almost identical for the PCA approach for all cases compared to the cross-correlation criterion, indicating that the results are robust with respect to our cluster evaluation criterion. For the SOM approach the results are less similar, confirming that common clustering algorithms may not be the ideal method to group patterns on the SOM.

We do not suggest that our cluster evaluation criterion can replace other, more generally applicable criteria such as the Davies-Bouldin Index (*Davies and Bouldin, 1979*), but it appears to work well in cases where the data can easily be reconstructed in a physically meaningful space such as spectra in the frequency domain.

The small number of modes (three) used in our PCA approach is justified by the drop off in variance after modes 1–3 for most noise levels. However, this approach does not work if the

Table 3.3: Quality measurements and clustering results for different noise levels based on RMS value of RMS differences between reconstructed spectra, comparison between PCA and SOM. Columns from left to right are: Noise level, number of modes necessary to explain 90% of the total variance, best cluster number k , misfit E (dB) for cluster number k , dimensions of the SOM topology, quantization error QE (dB), topographic error TE, best cluster number k and misfit E (dB) as for PCA.

Noise	PCA			SOM				
	90% var.	k	E	Map size	QE	TE	k	E
0.1	2	3	16e-4	19×7	42e-4	387e-4	4	23e-4
0.5	35	3	41e-4	19×7	17e-4	283e-4	4	68e-4
1	44	3	91e-4	19×7	284e-4	238e-4	6	77e-4
1.5	46	3	122e-4	19×7	366e-4	223e-4	14	107e-4
2	47	6	128e-4	17×8	426e-4	193e-4	8	132e-4
4	48	24	190-4	13×10	553e-4	238e-4	25	200e-4

explained variance has the same order of magnitude for all modes (*Hsieh*, 2009) (e.g., noise level 4, Table 3.1, where all modes explain a percentage of the variance on the order of 1%). We note that the method still performs well in cases where a relatively small amount of variance is explained by the first three modes (e.g. noise level 1.5 with 21.1% of the variance, Section 3.3.2 and Fig. 3.6). However, the choice of the number of modes may not always work in the way shown here, which may result in SOM being the more successful method.

As discussed in Section 3.2, we do not include gliding spectral lines in our synthetic dataset. However, these features are gradual, systematic variations in the change of spectral shapes over time, and are thus similar to the transitions between the different phases. With the PCA approach these transitions are captured by the time series of angles between the reconstructed and the observed synthetic spectra (Figs. 3.4(f) and 3.6(f)). However, the transitions implemented in our synthetic dataset affect large parts of the spectrum. Given that frequency gliding at Kīlauea only involved a few individual peaks, it is questionable if their slow variations have enough weight to strongly change the angles. In contrast, the SOM approach can show such transitions before the application of the clustering (Fig. 3.7(c)), which indicates that it may be better suited to capture gradual variations in time. However, from the time series from either method it is not clear what the nature of such continuous changes in time is (e.g., transition between phases vs. gliding), indicating that spectrograms and/or seismograms have to be consulted after periods of interest have been identified with our automated algorithms.

Our synthetic data were limited between 0.5–10 Hz as discussed in Section 3.2.1. To assess whether the results depend on this frequency band we apply both the PCA and the SOM approach to the same dataset limited to an arbitrary range of different frequency bands (Table 3.4). Intuitively, an increase in information in spectral space (i.e., a larger frequency range resulting in more “dimensions”) should improve the performance of a pattern recognition algorithm. This is partly confirmed by the decreasing misfits for an increasing upper frequency limit (Table 3.4). The ideal cluster number k for PCA hovers around $k = 3$ for all frequency ranges. Both cases of $k = 4$ from

Table 3.4: Clustering results for different frequency bands based on RMS value of cross correlation coefficients between reconstructed spectra for noise level 0.1, comparison between PCA and SOM. Columns from left to right are: Frequency range, best cluster number k and misfit E (dB) for cluster number k from PCA, best cluster number k and misfit E (dB) from SOM.

Frequ. (Hz)	PCA		SOM	
	k	E	k	E
0.5–3	2	543e-4	4	156e-4
0.5–8	4	9e-4	4	47e-4
0.5–10	3	16e-4	4	23e-4
0.5–12	3	7e-4	9	9e-4
0.5–15	4	5e-4	12	9e-4

the PCA approach recover parts of the transition between the two phases and the background as a separate cluster, in addition to correctly identifying the three known input spectra. This separation of the transitions explains the lower misfit for 0.5–8 Hz compared to 0.5–10 Hz.

In contrast, three out of five cases give $k = 4$ on the SOM, and the remaining two cases yield $k = 9$ and $k = 12$. Even forcing $k = 3$ does not recover the known phases correctly. Most likely, the way the synthetic data are set up and normalized, Phase II and the background are seen as two endmembers of the same continuous space on the SOM topology, whereas Phase I is separate, or Phase I and Phase II are combined. Grouping of Phase II and the background may be partly related to the long, gradual transition (time period 6). This result highlights the potential sensitivity of SOM to the normalization, which removes the amplitude differences between the phases and increases the similarity. Other methods of normalizing the data that give more weight to the amplitudes than we do here could be investigated further in future work.

Lastly, previous studies have suggested that non-linear processes may underlie some of the observed volcano seismic signals (e.g., *Shaw and Chouet*, 1988; *Julian*, 1994; *Konstantinou and Lin*, 2004; *Konstantinou et al.*, 2013). The question arises whether PCA as an inherently linear method (e.g., *Hsieh*, 2009) would be suitable to analyze data from such non-linear processes. Because our synthetic spectrograms were explicitly constructed from spectra (instead of first using synthetic waveforms to obtain the spectra), non-linearity can enter the analysis only during the transitions from one phase to another (time periods 3, 4, and 6). Basic tests with exponential instead of linear transitions showed an equally good performance of the method. If, on the other hand, a synthetic dataset were obtained by estimating spectral content from a seismic time series constructed from nonlinear combinations of signal components, it is unclear how well our PCA plus clustering approach would work. However, in such a case, analyzing spectra from Fourier Transforms (which is indirectly linked to our approach, since the characteristic spectra in *Unglert and Jellinek* (2015) were obtained by using FFTs) may not yield useful insight into the source mechanics (*Julian*, 1994; *Konstantinou and Lin*, 2004). To look explicitly for non-linear dynamics, an entirely different, bespoke synthetic data setup and analysis approach (e.g., Singular Spectrum Analysis, *Ghil et al.* (2002)) needs to be designed and tested. Such a detailed analysis of non-linear effects is beyond the scope of this work.

3.6 Conclusions

For the first time, we (i) construct a synthetic dataset as a benchmark to (ii) evaluate the performance of SOM in combination with hierarchical cluster analysis similar to previous studies on volcano seismic spectra, (iii) compare this method to PCA plus clustering, and (iv) introduce a new cluster evaluation criterion specific to the spectral space. The synthetic data are based on Kīlauea Volcano, but the results are generally applicable to seismicity with similar spectral shapes elsewhere. Consequently, our main conclusions are:

- For SOM, large topologies are necessary to capture spectral phases that last for a relatively short amount of time compared to the length of the dataset.
- SOM can detect changes in spectral content, and can give a visually appealing overview of the data space on the SOM topology.
- Further interpretation of the SOM results based on the map topology and temporal evolution of BMUs is difficult and subjective.
- Hierarchical clustering on SOM consistently overestimates the number of optimal clusters, and therefore fails to correctly identify the set of known patterns in the data without adding redundant patterns to the final set.
- PCA in combination with our hierarchical cluster analysis shows consistently better performance and reproduces the known input spectra both at low and high noise levels well.

In summary, where the goal is to detect a small number of distinct patterns, clustering in PC space is our preferred method. By contrast, SOM (without clustering) is useful to give a direct overview of most characteristic patterns in the data. Our results show that it is crucial to evaluate the performance of different machine learning methods before implementing applications. For example, other clustering algorithms should be tested to investigate if they are more successful on clustering SOM topologies. Without control data as we have produced, it may be difficult to evaluate the reliability of the algorithm, and to interpret the results. We suggest that, bearing in mind their individual strengths and weaknesses in relation to volcano seismic spectra, both PCA in combination with clustering and SOM on their own can be used to detect characteristic spectral patterns in volcano seismicity depending on the specific application. Future studies could test different benchmarking datasets. In particular, alternative approaches might involve constructing synthetic seismograms and converting them into the frequency domain. For SOM, more work beyond our direct comparison is necessary with respect to evaluating other clustering algorithms (e.g., k-means) than the ones presented here, and assessing non-traditional ways of grouping nodes on the SOM topology.

The ability to rapidly classify spectra of volcano seismic data without prior knowledge of the character of the seismicity at a given volcanic system holds great potential for real time or near-real time applications, and thus ultimately for eruption forecasting. Several PCA/SOM (and other

3.6. Conclusions

machine learning) toolboxes already provide the necessary computational tools, and even graphical user interfaces exist (e.g., KKAnalysis, *Messina and Langer, 2011*). If monitoring records are sufficiently long (i.e. cover multiple eruptive cycles), the spectral signatures of the (potentially unknown) “background” state of a volcanic system, different stages preceding and during the eruptive cycle, or specific types of volcanic activity can be identified with PCA and SOM, and data could be added in real time to detect changes critically indicative of an impending eruption very quickly.

Chapter 4

Spectral Pattern Recognition Reveals Distinct Classes of Volcanic Tremor¹⁰

Summary

Systematic investigations of the similarities and differences among volcanic tremor at a range of volcano types may hold crucial information about the plausibility of inferred source mechanisms, which, in turn, is important for eruption forecasting. However, such studies are rare. We develop a tremor detection algorithm and identify over 12,000 hours of volcanic tremor on 24 stations at Kīlauea, Okmok, Pavlof, and Redoubt volcanoes. We estimate spectral content over 5-minute tremor windows, and apply a combination of Principal Component Analysis (PCA) and hierarchical clustering to identify patterns in the tremor spectra. Analyzing several stations from a given volcano together reveals different styles of tremor within individual volcanic settings. These types include localized tremor signals related to processes such as lahars or dike intrusions that are only observed on some of the stations within a network. Subsequent application of our analysis to a combination of stations from the different volcanoes reveals that at least four main tremor classes can be detected across all settings. Whereas a regime with a low frequency (1–2 Hz) ridge and a subsequent decay of spectral power towards higher frequencies is observed dominantly at volcanoes (Kīlauea, Okmok, Redoubt) with magma reservoirs centered at less than 5 km below sea level (b.s.l.), a steeper spectrum with a slightly more pronounced peak at 1–2 Hz is observed only in association with open vents (Kīlauea and Pavlof). A third regime with a peak at approximately 3 Hz is confined to the two stratovolcanoes (Pavlof and Redoubt), and a fourth tremor type with a peak close to 10 Hz occurs at Pavlof only and appears to be characteristic for lahars. These observations suggest that there may be generic relationships between the spectral character of the observed signals and volcano characteristics such as magma viscosity, storage depths, and the physical properties of volcanic edifices. Similarities among the spectral patterns detected at stations 4 km and 8–10 km distance from the centers of volcanic activity, respectively, indicate that path effects do not strongly influence spectral shapes at distances of a few kilometers from the inferred source of the signals. On the basis of these promising results, we suggest that further work on data from a larger sample and diverse range of volcano types will be critical. In addition to revealing additional classes of tremor signals in volcanic environments, such work will plausibly more completely identify fingerprints of source processes specific to volcano type, but independent of volcano location.

¹⁰In preparation for submission.

4.1 Introduction

Volcanic eruptions are often preceded and accompanied by a low-frequency (approximately 0.5–10 Hz) seismic signal called “volcanic tremor” (McNutt, 1992; Konstantinou and Schlindwein, 2002; McNutt and Nishimura, 2008), hereafter referred to as “tremor”. Tremor can persist for minutes to weeks and its occurrence is often interpreted as a sign of an impending eruption (e.g., D’Agostino *et al.*, 2013; Chardot *et al.*, 2015). The reliability of tremor as a forecasting tool is, however, uncertain, because the underlying physical processes remain unclear (Konstantinou and Schlindwein, 2002). A range of tremor observations in different locations suggests that such low frequency seismicity may be the expression of a variety of mechanisms (e.g., Chouet, 1986; Julian, 1994; Benoit and McNutt, 1997; Ripepe and Gordeev, 1999; Neuberg *et al.*, 2000; Lesage *et al.*, 2006; Jellinek and Bercovici, 2011; Dmitrieva *et al.*, 2013; Bean *et al.*, 2014). However, systematic investigations of similarities and differences among tremor properties in different volcanic settings that could shed light on the general applicability of potential source processes are rare (e.g., McNutt, 1994, 2004). Accordingly, we specifically address the following questions:

- (1) Within a given volcanic setting:
 - (a) Are there tremor signals with distinct spectral signatures?
 - (b) What are the spatio-temporal properties of such signals?
- (2) Among several volcanic settings:
 - (a) Are there spectral properties of tremor that are common to several volcanoes?
 - (b) Do observations of similarities of tremor properties among different settings relate to the distinctive characteristics of the volcanoes (e.g., magma viscosity, edifice type, geometry of the plumbing system)?

To identify such systematics we use pattern recognition to determine characteristic spectral shapes for tremor from four volcanoes with well-studied and strongly contrasting eruptions. In Section 4.2 we introduce each volcanic setting analyzed here. In Section 4.3, we develop an algorithm to detect volcanic tremor in continuous seismic data on individual stations (“single station detection”) and outline the preprocessing steps to obtain corresponding tremor spectra. These spectra are then analyzed with a recently developed pattern recognition approach that combines Principal Component Analysis (PCA) and hierarchical clustering (Section 4.4; Unglert *et al.*, 2016)). Finally, we discuss our observations, inferences, and potential implications for identifying and understanding underlying physical processes in Section 4.5.

4.2 Volcanic Settings

We analyze data related to volcanic unrest from Kīlauea (2007–2011, USA), Okmok (2008, USA), Pavlof (2007 & 2013, USA), and Redoubt (2009, USA). All datasets are from permanent networks, and all times are in UTC.

Kīlauea Volcano on the Big Island of Hawai‘i is an intraplate shield volcano erupting mostly basaltic magmas ($\sim 49\text{-}50$ wt.% SiO_2 , *Garcia et al.*, 1989, 1992; *Global Volcanism Program*, 2013a). Our data include two time periods of dike intrusions and accompanying small fissure eruptions (19 Jun 2007 and 6-10 March 2011, *Poland et al.*, 2008; *Fee et al.*, 2011a; *Orr et al.*, 2015), and a period of small explosive bursts during the formation of the summit lava lake in 2008 (*Wilson et al.*, 2008; *Houghton et al.*, 2013). All three episodes of volcanic activity are part of the ongoing eruptive sequence with a Volcanic Explosivity Index (VEI) of 1 (*Global Volcanism Program*, 2013a). A shorter version of the same dataset was analyzed extensively by *Unglert and Jellinek* (2015). We thus use it as a benchmark for the pattern recognition algorithm by *Unglert et al.* (2016) that has only been tested on synthetic data.

Okmok, Pavlof, and Redoubt are part of the Aleutian chain, a volcanic arc related to subduction of the Pacific Plate below the North American and Bering Sea plates (e.g., *Buurman et al.*, 2014). Okmok is a shield volcano with volcanic activity focused in a complex of two overlapping calderas (*Global Volcanism Program*, 2013b). Our data from permanent stations operated by the Alaska Volcano Observatory span a large (VEI 4) phreatomagmatic explosive eruption between 12 Jul - 19 Aug 2008 that produced dominantly andesite to basaltic andesite ($\sim 51\text{-}57$ wt.% SiO_2) and a series of lahars (*Larsen et al.*, 2009, 2013, 2015).

Pavlof Volcano is a stratovolcano close to the western end of the Alaska Peninsula with mostly Strombolian to Vulcanian activity and andesite to basaltic andesite magmas ($\sim 53\text{-}58$ wt.% SiO_2 , *Waythomas et al.*, 2008; *Mangan et al.*, 2009; *McGimsey et al.*, 2011; *Waythomas et al.*, 2014). Two eruptions are included in our analysis: A VEI 2 eruption on the southeastern flank between 14 Aug - 13 Sep 2007 (*Waythomas et al.*, 2008), and a VEI 3 eruption on the northwestern flank between 13 May - 1 Jul 2013 (*Waythomas et al.*, 2014). In addition to explosive activity and ash emission, both eruptions included lava fountaining, spatter flows, and lahars on the slopes of the cone (*Waythomas et al.*, 2014).

At Redoubt Volcano, an andesitic stratovolcano at the northeastern end of the arc, a VEI 3 eruptive period between 15 Mar to approximately 1 Jul 2009 included phreatic and magmatic explosions, as well as the effusion and destruction of several lava domes and associated lahars (*Schaefer*, 2011). Our data include a period of precursory seismicity (*Schaefer*, 2011; *Power et al.*, 2013) in addition to the main eruptive phases. The eruption produced mainly andesite with 57-63 wt.% SiO_2 (*Schaefer*, 2011).

4.3 Data and Preprocessing

We combine continuous, vertical component seismic data from short-period sensors from the permanent networks at the volcanoes introduced in Section 4.2. All of the time periods include at least one discrete eruptive event, or are part of an ongoing eruptive phase. We select these volcanoes on the basis of data availability, the detection of volcanic tremor and to cover a large range of volcano types, magma compositions, and eruptive activity. We restrict our analysis to stations that recorded seismicity associated with the eruptive episodes approximately continuously without any technical

issues. We perform an instrument response correction to achieve a flat response between 0.5–15 Hz.

4.3.1 Distinguishing Tremor from the Background

To reduce the amount of data to be analyzed, we develop an algorithm to detect periods of volcanic tremor. In our examples, we define tremor as elevated seismic amplitude compared to the background at each station, sustained over durations much longer than typical local earthquake durations (usually up to 10s of seconds, e.g., *Gómez M and Torres C, 1997; Ketner and Power, 2013*). We choose a value of 5 minutes for the length of the time window, similar to studies of tectonic tremor (e.g., *Wech and Creager, 2008*). However, tests with shorter (3 minutes) and longer (10 minutes) durations give qualitatively similar results. To identify high amplitudes, we take the following approach:

1. Estimate median absolute background amplitude.
2. Divide continuous seismic data into non-overlapping 5-minute windows.
3. Compare median absolute amplitude over each window to median absolute background amplitude.

We introduce the no-overlap criterion to avoid counting tremor episodes twice. We use the median in all cases to reduce the influence of a few large spikes within any given window. To determine the median absolute background amplitude, we obtain the background spectrum (Fig. 4.1(a) and (c)) by identifying the minimum spectral power value at each frequency over time (*Vila et al., 2006*). We then estimate the signal associated with this background spectrum by converting it back into the time domain (Fig. 4.1(b) and (d)), where we take the absolute value of the signal and determine its median.

We compare the median absolute velocity amplitude of each 5-minute window of continuous seismic data to the median obtained from the background signal. If the median in the window exceeds the background by a factor f it is recorded as initial detection. Tests with data from Kīlauea Volcano that were studied in detail by *Unglert and Jellinek (2015)* show that $f = 150$ is a reasonable choice to detect tremor during known periods of activity.

4.3.2 Removing Earthquake Signals

Each successful detection is then tested for the presence of earthquakes. We use two criteria:

1. If the detection window includes the origin time of a local earthquake in the ANSS catalog it is excluded from the analysis.
2. Criterion 1 is insufficient, because some earthquakes may not be recorded in the catalog. We thus test each window for spikes that are larger than 6 standard deviations of the data within the corresponding window to exclude those events.

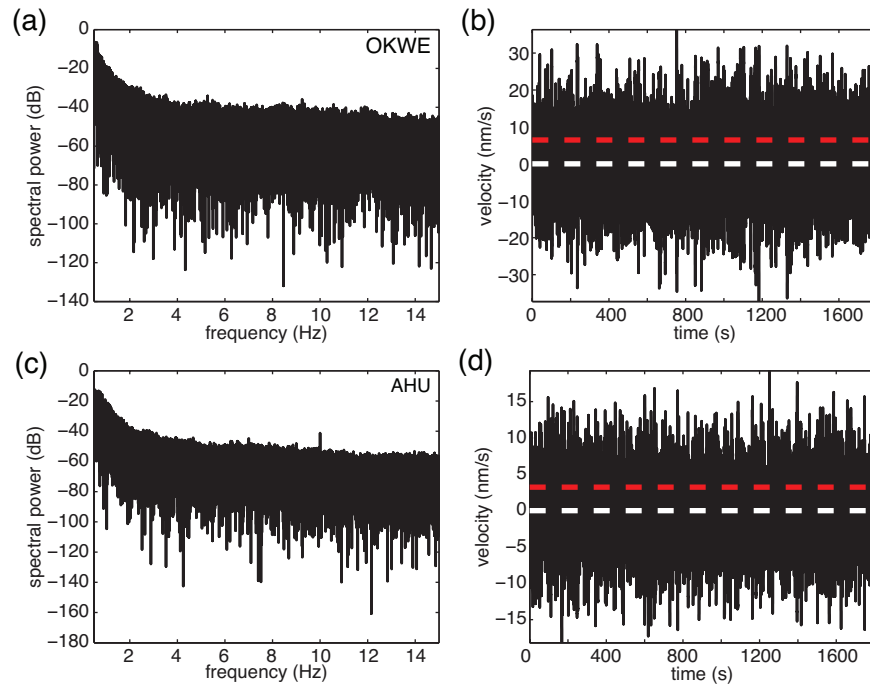


Figure 4.1: Examples for background signal estimation. (a) Estimate for background spectrum, and (b) associated time domain signal at station OKWE (Okmok Volcano, USA). White dashed line indicates zero velocity, and red dashed line shows the median value of the absolute velocity amplitudes. (c) and (d) are same graphs for station AHU (Kilauea Volcano, USA).

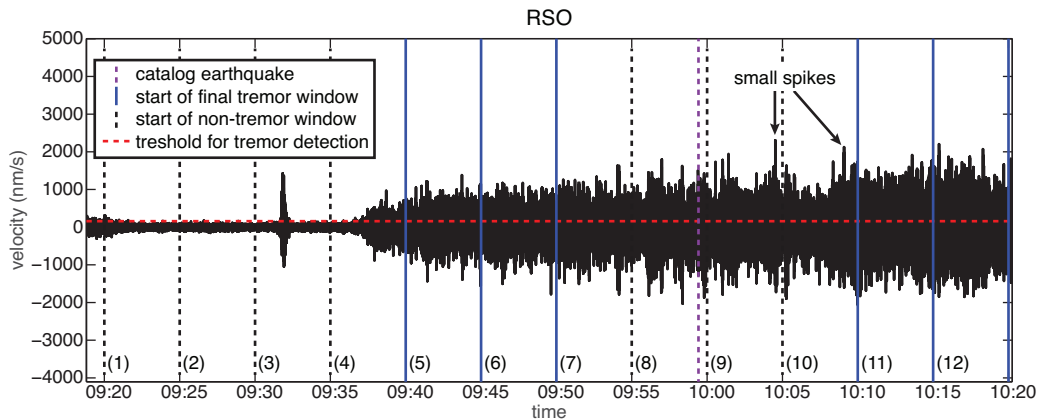


Figure 4.2: Example seismogram showing different cases of our tremor detection, from Redoubt station RSO on 25 Jan 2009. Windows (1)–(4) fall below our detection threshold, window (8) includes a catalog earthquake, and windows (9)–(10) include spikes. Only windows (5)–(7) and (11)–(12) are kept as final detections.

Figure 4.2 shows some of the different cases. Over the course of one hour, seismic amplitudes increase above our tremor threshold (starting in time window (4), Fig. 4.2). Some windows are, however, excluded from detection because of the presence of known earthquakes (window (8), Fig. 4.2) or other spikes (windows (9)–(10), Fig. 4.2). Additionally, some windows have a non-zero mean (not shown), which may be related to transient problems with the instrument. We thus exclude windows with an absolute mean larger than an arbitrary threshold of 100. All steps above are done separately for each station, similar to the envelope based single station detection of tectonic tremor by *Brudzinski and Allen (2007)* or single station event detection by *Ketner and Power (2013)*. The disadvantage of this single station approach is that local non-volcanic processes that only affect one station (e.g., a particularly noisy site) may be included in the analysis. The advantage is that the algorithm works even for locations with only one station. Furthermore, even if multiple stations are available, localized and weaker signals that may only be recorded on one station can be detected, which for our purposes outweighs the drawbacks of a detection algorithm that relies on individual stations.

By using our tremor detection algorithm we identify 148,853 5-minute tremor windows on 24 stations in total. Table 4.1 summarizes the results for the four different volcanoes.

Table 4.1: Summary of volcanoes, stations, data time period, and number of tremor windows. Only overall start and end dates for data periods are given, data gaps may exist in between. Asterisk (*) denotes that more data were available, but not analyzed because of unresolved technical issues.

Volcano	Station	Start	End	Tremor Win- dows
Kīlauea	AHU	2007/04/01	2011/03/11	38,473
	KNH	2007/04/01	2011/03/11	5,917
	OTL	2007/04/01	2011/03/11	38,059
	PAU	2007/04/01	2011/03/11	1,016
	STC	2007/04/01	2011/03/11	28,353
Okmok	OKAK	2008/07/05*	2008/09/08	3,807
	OKRE	2008/07/05*	2008/09/08	5,429
	OKSP	2008/07/05*	2008/09/08	1,059
	OKWE	2008/07/05*	2008/09/08	6,419
	OKWR	2008/07/05*	2008/09/08	4,239
Pavlof	HAG	2007/07/01	2013/08/07	164
	PN7A	2007/07/01	2007/10/31*	22
	PS1A	2007/08/21*	2013/08/07	1,689
	PS4A	2007/07/01	2010/08/07	1,788
	PV6	2007/07/01	2007/10/31*	447
	PVV	2007/07/01	2013/08/07	922
Redoubt	DFR	2009/02/01*	2009/06/03	256
	NCT	2009/02/01*	2009/06/03	204
	RDN	2009/01/01	2009/04/10*	472
	REF	2009/01/01	2009/04/10*	774

4.3.3 Obtaining Tremor Spectra

For each tremor window we obtain a power spectrum, which is smoothed with a 50 point moving average and subsampled at the same interval to reduce the effect of individual peaks and to emphasize the overall trends in the spectra (Unglert *et al.*, 2016). Each spectrum is then scaled by its cumulative spectral power and aligned to achieve a 0 dB median to avoid bias in the results related to amplitude differences between spectra of the same shape (Unglert *et al.*, 2016). To account for variations in the number of points per spectrum at different stations related to differences in their respective sampling rates, we linearly interpolate each spectrum and subsample between 0.75–12 Hz in steps of 0.25 Hz to include the most common tremor frequencies (McNutt and Nishimura, 2008) as far as the data allow. The final spectra are then used as input for our pattern recognition algorithm aimed at identifying characteristic patterns.

4.4 Spectral Pattern Recognition

4.4.1 Overview

We analyze the spectra from the tremor windows obtained above to identify patterns in space and time that may be common to several volcanic settings, specific to one volcano, or be observed at only one location within a station network. We use an approach developed by Unglert *et al.* (2016) that combines Principal Component Analysis (PCA) and hierarchical clustering to obtain characteristic spectra and their temporal and spatial manifestation. In this section, we outline the main steps of the method, followed by a summary of the results. To visualize the theoretical concepts behind the methodology we refer to Figures 4.3 and 4.4 here, and explore the respective results in Section 4.4.2.

PCA is a statistical technique for dimensionality reduction that enables us to identify groupings of points in a space with fewer dimensions than the full spectral bandwidth of our observations. Following Unglert *et al.* (2016), the frequency samples of the input spectra are treated as the original coordinate system, which is rotated to find the mutually orthogonal directions of maximum variance (*modes*; in order of decreasing variance, Fig. 4.3(a)). We then apply hierarchical clustering to identify groupings of points on the basis of their Euclidean distances in the lower dimensional Principal Component (PC) space defined by the first two modes alone. We choose the cut-off after mode 2 as a consistent criterion for all cases because of the relatively small variance carried by higher modes. The resulting clusters can be used to reconstruct spectra corresponding to the main groupings in the data by superposing the first two principal components of each cluster center.

To determine the ideal number of clusters k we use a criterion designed to identify the maximum of all

$$C_{\text{RMS},k} = \sqrt{\frac{\sum_{n=1}^{n_c} (\rho_n - 1)^2}{n_c}}, \quad (4.1)$$

where ρ_n is Pearson's correlation coefficient between the spectra of two clusters for all possible n_c unique combinations of clusters for a given k (Fig. 4.3(b)). $C_{\text{RMS},k}$ ranges between [0..2] for

$\rho = [-1..1]$. The maximum $C_{\text{RMS},k} = 2$ corresponding to $\rho = -1$ indicates the largest deviation from perfect correlation ($\rho = 1$), or lowest similarity between the spectral shapes of each cluster. This minimum correlation thus indicates maximally distinct clusters. The corresponding median cluster spectra capture the main groupings within the full variety of observed spectra. In all our calculations $k = 2..10$ unless otherwise noted. Detailed descriptions and synthetic tests of the method can be found in *Unglert et al. (2016)*.

This analysis can be done (i) on data from one station only to identify the recurrence of similar processes over time; (ii) on data from a station network to identify spatio-temporal systematics of certain spectral patterns related to, for example the station location relative to volcanic activity; or (iii) on data from a combination of stations from different volcanoes to identify systematic differences or similarities among distinct volcanic settings. Because the temporal evolution at each individual station can also be obtained when analyzing the entire network, we focus on cases (ii) and (iii).

For both analysis scenarios, there are several ways of visualizing the results. For each case, we show variance explained by each mode (Fig. 4.3(a)) and the $C_{\text{RMS},k}$ distribution to determine the ideal number of clusters k (Fig. 4.3(b)). The clustering of observations (i.e., each spectrum in time) in PC space and the median of each cluster (Fig. 4.3(c)) is used to obtain the associated reconstructed spectrum for each cluster (Fig. 4.3(d)). Clusters are colored according to their position in PC space and their similarities in terms of spectral character. We then examine the occurrence of the different clusters in space: In Figure 4.3(e), we show histograms with the number of observations from a given cluster at each station, including a station map for reference. For each volcano, we order the stations by approximate distance from their respective center of activity (small numbers next to station names in histogram, Fig. 4.3(e)).

For Kīlauea, because of the long spatial extent of the East Rift Zone with various active parts at different times during the eruptions in 2007, 2008, and 2011, our reference point is the summit vent. At Okmok, the center of activity is defined as the region in the caldera from which the 2008 eruption originated. At Pavlof, we use the summit as our reference location, and at Redoubt we measure the distance from the approximate center of the summit crater¹¹.

At an individual station, the histogram can be used to compare the different clusters to each other in terms of their numbers, and to determine the most common cluster(s). Similarly, the number of detections in each cluster can be compared between the different stations to investigate differences depending on the station location.

To assess the temporal evolution of tremor properties and their timing relative to eruptive events it is useful evaluate time series of detection rates and the cluster that each detection is associated with (Fig. 4.4). For each station, we show the temporal evolution of the tremor detection rate as the number of detections per hour, which can reach a maximum of twelve 5-minute tremor windows (black solid curves at the bottom of each panel). Conceptually, this metric is similar to measurements of average seismic amplitude in time (e.g., real time seismic amplitude measurement

¹¹We do not use the location of dome growth from the 2009 eruption because the exact source location of the precursory hydrothermal phase may not be the same.

4.4. Spectral Pattern Recognition

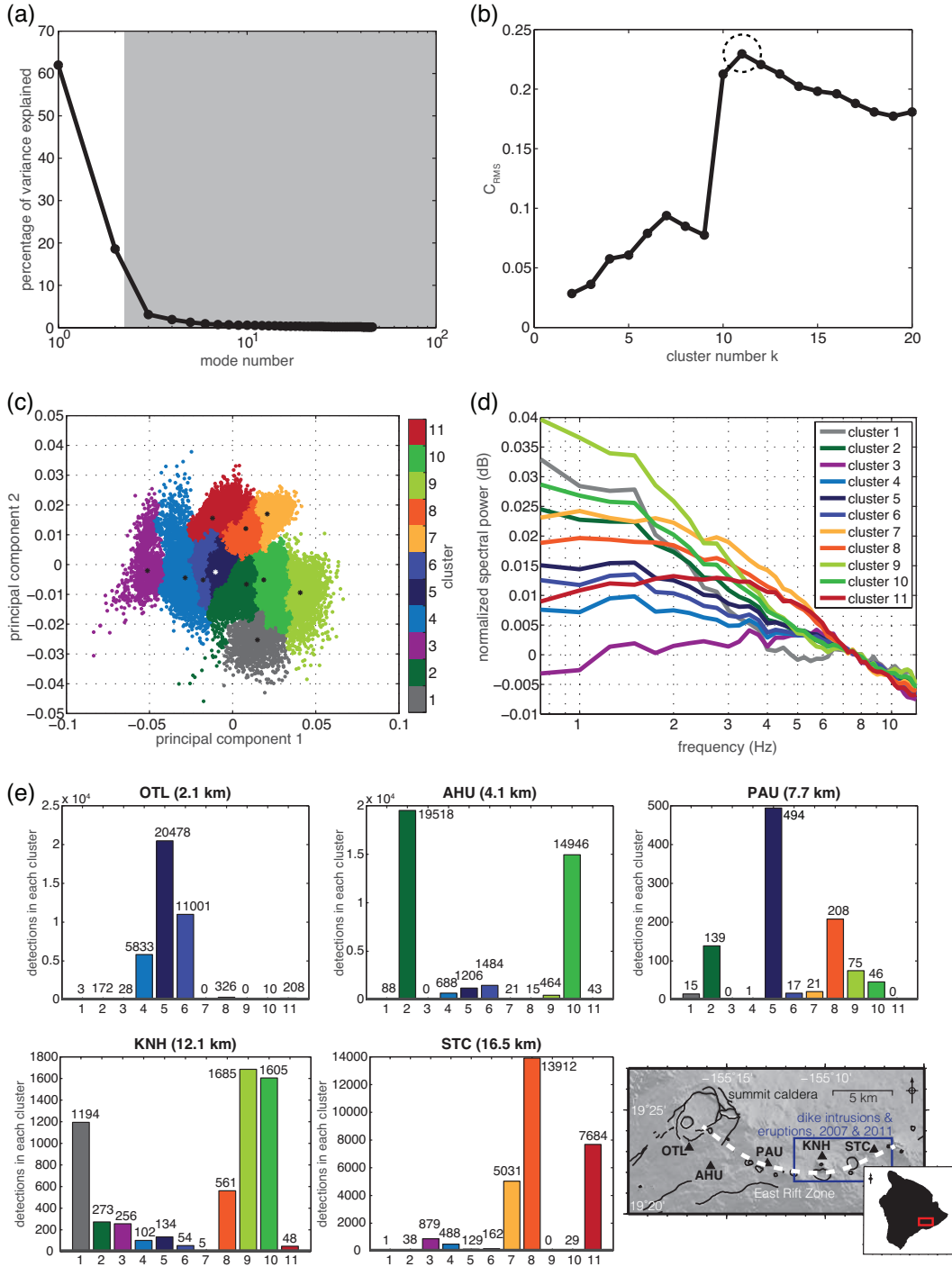


Figure 4.3: PCA and clustering results for network analysis at Kīlauea, 2007, 2008, and 2011. (a) Variance explained by each mode. Grey shaded area indicates modes excluded from further analysis. (b) Cluster evaluation by examining cross-correlation coefficients indicates best clustering for $k = 11$. (c) Clustering of observations in space spanned by first two modes. Asterisk within cluster indicates location of median used to reconstruct spectra. (d) Reconstructed spectra for each cluster. (e) Number of tremor detections associated with each cluster at each station, including station map. Stations ordered from West to East, with increasing distance from Kīlauea's summit (small number next to station name).

4.4. Spectral Pattern Recognition

or RSAM, *Murray and Endo*, 1989). As we show in the following sections, the detection rates are a simple and useful proxy for tremor activity.

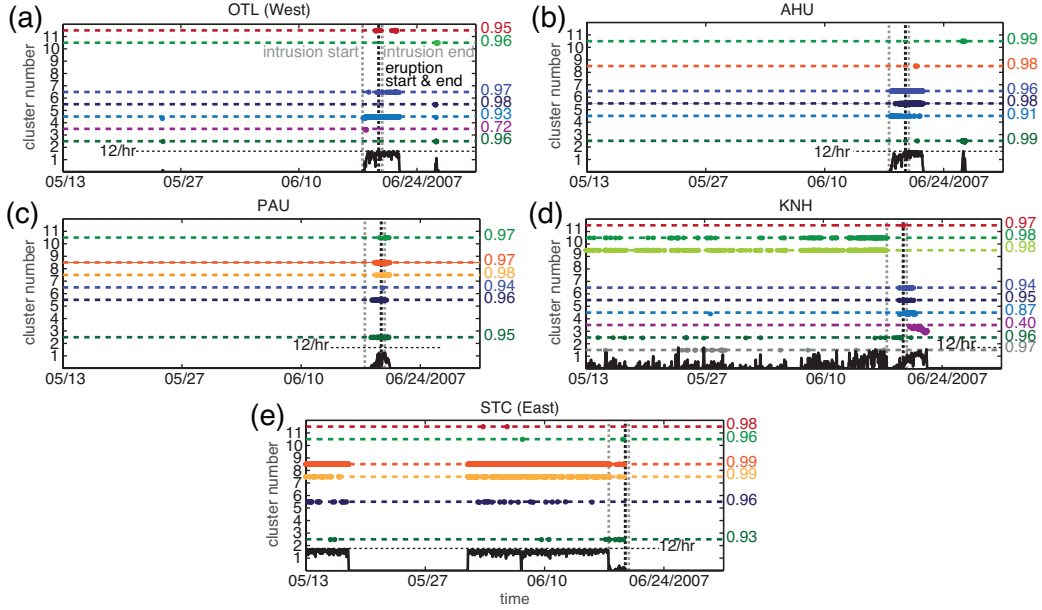


Figure 4.4: Clustering time series for network analysis at Kīlauea, 2007. Stations (a) OTL, (b) AHU, (c) PAU, (d) KNH, and (e) STC, ordered from West to East. For each station, colored time series shows best cluster (values between 1–11). Small offset from cluster number shows alignment between cluster spectrum and actual spectrum observed at the time, where the colored dashed line indicates perfect alignment. Mean alignment $\cos(\phi)$ for each cluster shown as colored number on the right of each time series. Black line at the bottom of the cluster time series shows tremor detection rate at each station, with horizontal dotted line indicating the maximum of twelve tremor windows detected during the preceding hour. Vertical dotted lines indicate important dates. For more details see main body of text.

Furthermore, we introduce the angle between two spectral vectors (i.e., a measure of their orthogonality) as a quantitative measure for the similarity of each observed spectrum \mathbf{S} with the corresponding cluster spectrum \mathbf{R} by measuring

$$\cos(\phi) = \frac{\mathbf{S} \cdot \mathbf{R}}{\|\mathbf{S}\| \|\mathbf{R}\|}. \quad (4.2)$$

Each detection is then slightly offset from the level of its associated cluster by a value of $0.5 \cdot \cos(\phi)$. The dashed colored line slightly above each cluster level indicates a perfect alignment of $0.5 \cdot \cos(0^\circ) = 0.5$. The offset from this line can thus be used to assess how representative a given cluster is for the actual observation at the time. The mean value of $\cos(\phi)$ over all times indicates how well a given cluster represents its associated spectra at each station, and is shown as colored number on the right of the time series. In addition, to evaluate the temporal evolution of each spectral pattern relative to eruptive activity, for example, we indicate the timing of important events as vertical dotted lines (Fig. 4.4).

In summary, with these metrics it is possible to assess the number and character of spectral

patterns as well as their manifestation in space and time. We summarize the results from the analysis of each station network individually in Section 4.4.2, and from the combined analysis of one station from each of the different volcanic settings in Section 4.4.3.

4.4.2 PCA for Multiple Stations at Individual Settings

To explore processes occurring at different locations on individual volcanoes, we apply our technique to station networks at Kīlauea, Okmok, Pavlof, and Redoubt, respectively. By analyzing our data in the space of the first two modes, we account for 80.6% of the variance at Kīlauea, 76.0% at Okmok, 79.0% at Pavlof, and 70.6% at Redoubt. The differences in variance may indicate different levels of white noise, where more noise results in a decrease in variance explained by the first few modes because of even contributions of the noise to all modes/dimensions (cf. *Unglert et al.*, 2016)).

Kīlauea

To evaluate the success of our pattern recognition approach, we first analyze data from five stations at Kīlauea between 2007–2008 and from March 2011 that each record distinct tremor signals related to volcanic unrest (*Unglert and Jellinek*, 2015). On the basis of the first two modes in PC space, $C_{\text{RMS},k}$ indicates $k = 10$. Because this value corresponds to the maximum of the range tested ($k = [2..10]$) and can thus not reliably be identified as a local maximum, we extend the range of k up to 20 and obtain the ideal $k = 11$ (Fig. 4.3).

This ideal $k = 11$, the proximity of the clusters in PC space, and the similarity of the overall shapes and alignment of individual peaks of the different cluster spectra (Fig. 4.3(b)–(d)) indicate that the clusters are mainly representing end members and stages of different regimes, rather than completely independent patterns. Because of the similarities of their individual frequency peaks and spectral slopes, we qualitatively divide the clusters into three categories:

1. The green regime includes clusters 1, 2, 9, 10 with relatively steep slopes of spectral power decaying from low to high frequencies.
2. The blue regime includes clusters 4, 5, 6 with slightly flatter slopes compared to the green group.
3. The red regime includes clusters 7, 8, 11 with a ridge (or broad peak) of spectral power between 1–4 Hz and a decay towards higher frequencies.

In addition to the three regimes, cluster 3 is treated independently because it has features from both the red and the blue regimes. In Figure 4.3(e), the number of detections per cluster and stations shows that the blue and green regimes are dominant in the West, whereas the red regime appears mostly in the East.

Figures 4.4, 4.5, and 4.6 show the presence/absence of the 11 different characteristic spectra at each station in time. We summarize the results for each time period separately.

4.4. Spectral Pattern Recognition

During May and June 2007, the westernmost station OTL shows no large amount of detections up to the beginning of the Father’s Day intrusion on 17 June 2007 (Fig. 4.4(a)). Tremor detection rates gradually increase over approximately 1 day, and then stay close to the maximum until 4 days after the onset of the intrusion, when they rapidly drop to zero over the course of 2 hours. The spectra accompanying these high detection rates are dominantly from the blue regime, but also include detections from the red regime. The only other significant tremor activity at OTL occurs during a short spike of detection rates around 26 June.

At STC, the easternmost station, the results differ strongly (Fig. 4.4(e)). Tremor detection rates are consistently high before the intrusive episode, and drop rapidly with the onset of the intrusion. Whereas at STC the red regime is dominant, the same time period at KNH (Fig. 4.4(d)) is marked mostly by clusters from the green regime. The detection rates at KNH are slightly lower than at STC, and fluctuate on a timescale of hours to days.

None of the other stations further West towards OTL show consistent pre-intrusion detections (Fig. 4.4(b)–(c)). However, after the onset of the Father’s Day intrusion on 17 June 2007, all of the western stations exhibit several days of tremor detections that generally persist after the end of the eruption and the cessation of intrusion (Fig. 4.4(a)–(c)). Tremor rates appear to decrease with increasing distance from OTL during the intrusion. Most associated spectra belong to the blue regime, but also include contributions from the green and red regimes. Cluster 3 (purple) is observed for two days (not directly) following the small eruption on 19 June 2007 (Poland *et al.*, 2008; Fee *et al.*, 2011b) at KNH (Fig. 4.4(d)).

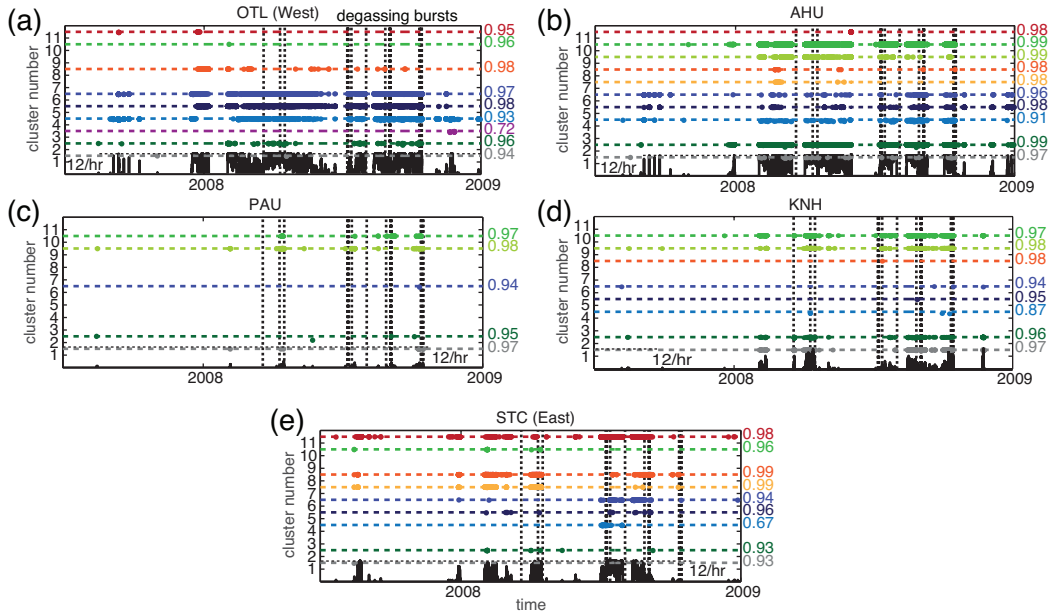


Figure 4.5: Clustering time series for network analysis at Kilauea, 2008. For caption see Figure 4.4.

Throughout the rest of 2007 and 2008 (Fig. 4.5), tremor with characteristic spectra similar to the pre-intrusion tremor in 2007 appear at stations STC (red regime, Fig. 4.5(e)) and KNH (green

regime, Fig. 4.5(d)), the two easternmost stations. Whereas PAU is marked by low detection rates (Fig. 4.5(c)), high detection rates occur at OTL and AHU in the West (Fig. 4.5(a)–(b)), closest to the summit. The predominant clusters there belong to the green and blue regimes, with no systematic changes over time. Detections at AHU generally correspond to detections at OTL, with slightly higher detection rates at OTL compared to AHU. Similarly, STC and KNH show detections at the same time, with higher rates at STC compared to KNH (Fig. 4.5(d)–(e)). There appears to be no relationship between any of the characteristic spectra and the degassings bursts (*Fee et al., 2010*) during this time period.

In 2011, no significant episodes of pre-intrusion tremor detections are observed at any station (Fig. 4.6). However, after the onset of the intrusion, just before 6 March 2011 (*Lundgren et al., 2013; Orr et al., 2015*), tremor mostly belonging to the blue and red regimes is observed at stations OTL through KNH (Fig. 4.6(a)–(d)). These stations show a trend of spectra increasingly evolving from blue to red over time, where stations further East show earlier occurrences of spectra belonging to the red regime than stations in the West. Tremor at OTL and AHU persists after the end of the eruption (Fig. 4.6(a)–(b)). Station STC is dominated by the blue regime and cluster 3, with the first detection directly at the time of the onset of intrusion, and the beginning of nearly continuous detections (Fig. 4.6(e)) just after the start of the fissure eruption early on 6 March 2011 (*Orr et al., 2015*). Both at STC in 2011 and KNH in 2007, cluster 3 appears to be less well aligned on average with the observed spectra than the other clusters ($\cos(\phi) \sim 0.4$, Figs. 4.4(d) and 4.6(e)). Otherwise cluster 3 only occurs a few times at station OTL during all three time periods.

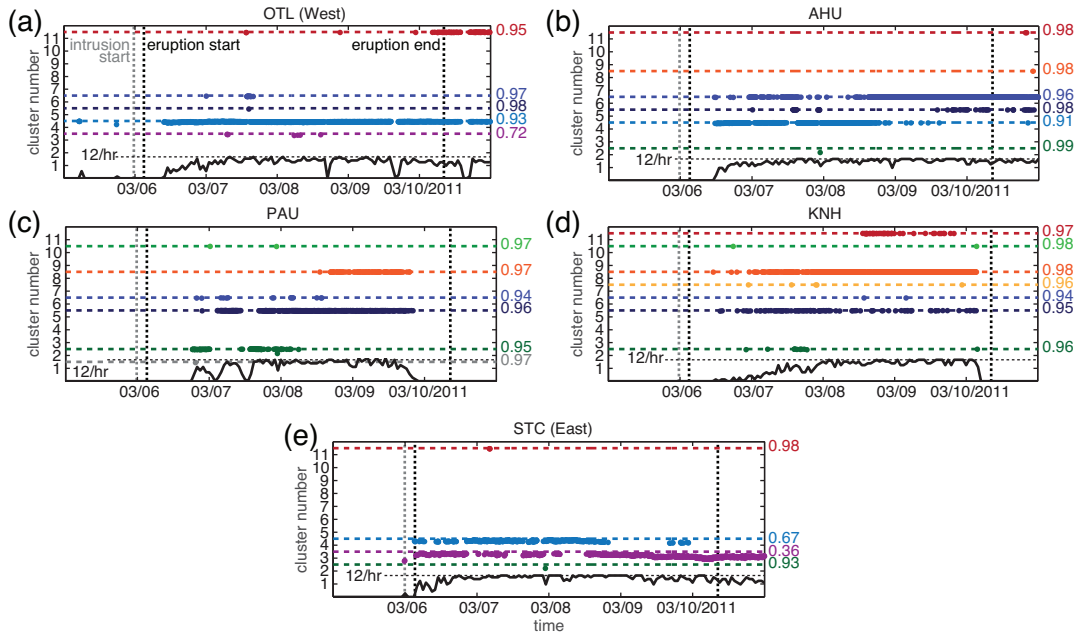


Figure 4.6: Clustering time series for network analysis at Kīlauea, 2011. For caption see Figure 4.4.

Okmok

Figure 4.7 shows the PCA results for the five stations analyzed at Okmok Volcano during the 2008 eruption. Our cluster evaluation criterion (*Unglert et al.*, 2016) suggests $k = 6$ as the ideal number of clusters (Fig. 4.7(b)). However, $C_{\text{RMS},k}$ only varies slightly among the different numbers of clusters, and is generally low ($C_{\text{RMS},k} = [0.02..0.05]$ from full possible range $[0..2]$), indicating strong correlations among the corresponding spectra. Similar to Kīlauea, the observations in the space of the first two principal components form a relatively dense cloud without clear separations between the different clusters (Fig. 4.7(c)). The reconstructed spectra are consequently relatively similar to each other (Fig. 4.7(d)), representing a continuum rather than independent, clearly separated clusters. We divide them into a blue regime (clusters 3–6) with increasingly steeper slopes going from dark to light blue, and a green regime (clusters 1–2) with a ridge of high spectral power between 1–4 Hz on the basis of common spectral peaks.

Histograms of the total number of detections show that clusters 3 and 6 (dark blue) are more common close to the eruption site (< 10 km) than further away (Fig. 4.7(e)). In addition, the green regime seems to occur at close and intermediate range (up to ~ 10 km). In contrast, clusters 4 and 5 (lighter blue) are observed mostly at stations further away (> 15 km).

The temporal evolution of tremor detections and cluster memberships (Fig. 4.8) show that tremor is almost exclusively confined to the time of the eruption. Detection rates start to decrease at the beginning of August, in particular at the stations furthest away from the eruption site (OKAK, OKSP, Fig. 4.8(d)–(e)), and go to zero at the end of the eruption on 19 Aug 2008 (*Larsen et al.*, 2015). There are no systematic variations in terms of the temporal (dis-)appearance of the different clusters. For example, no particular spectrum is associated with the period of higher detection rates in July compared to the lower rates in August, or vice versa.

Pavlof

At Pavlof, our data include two different eruptions (Section 4.2). Figure 4.9 shows the results for the combined PCA and cluster analysis. $C_{\text{RMS},k}$ (Fig. 4.9(b)) has a maximum at $k = 3$. The larger absolute values (up to 1.33) indicate that the reconstructed spectra are more distinct than they are at Kīlauea and Okmok. The observations in PC space (Fig. 4.9(c)) form at least three dispersed groups, and the spectra corresponding to each of the three clusters show distinct characteristics: Cluster 1 (blue) has a ridge at relatively high frequencies (8–9 Hz), cluster 2 (purple) has a low frequency ridge (1–2 Hz) with a gentle decay towards higher frequencies, and cluster 3 (pink) exhibits a low frequency peak (1–2 Hz) with a steeper decay compared to cluster 2. This steeply decaying cluster 3 spectrum appears to occur mostly on the stations towards the Southeast of the volcano, whereas the gently decaying cluster 2 spectrum is observed at all stations to some extent. The high frequency cluster 1 regime is observed most often at station PVV.

PN7A and HAG have very few detections during the 2007 eruption (Fig. 4.10), so the following summary will focus on the remaining three stations. There are no high tremor detection rates preceding the 2007 eruption. Instead, tremor is detected almost exclusively during the eruption at

4.4. Spectral Pattern Recognition

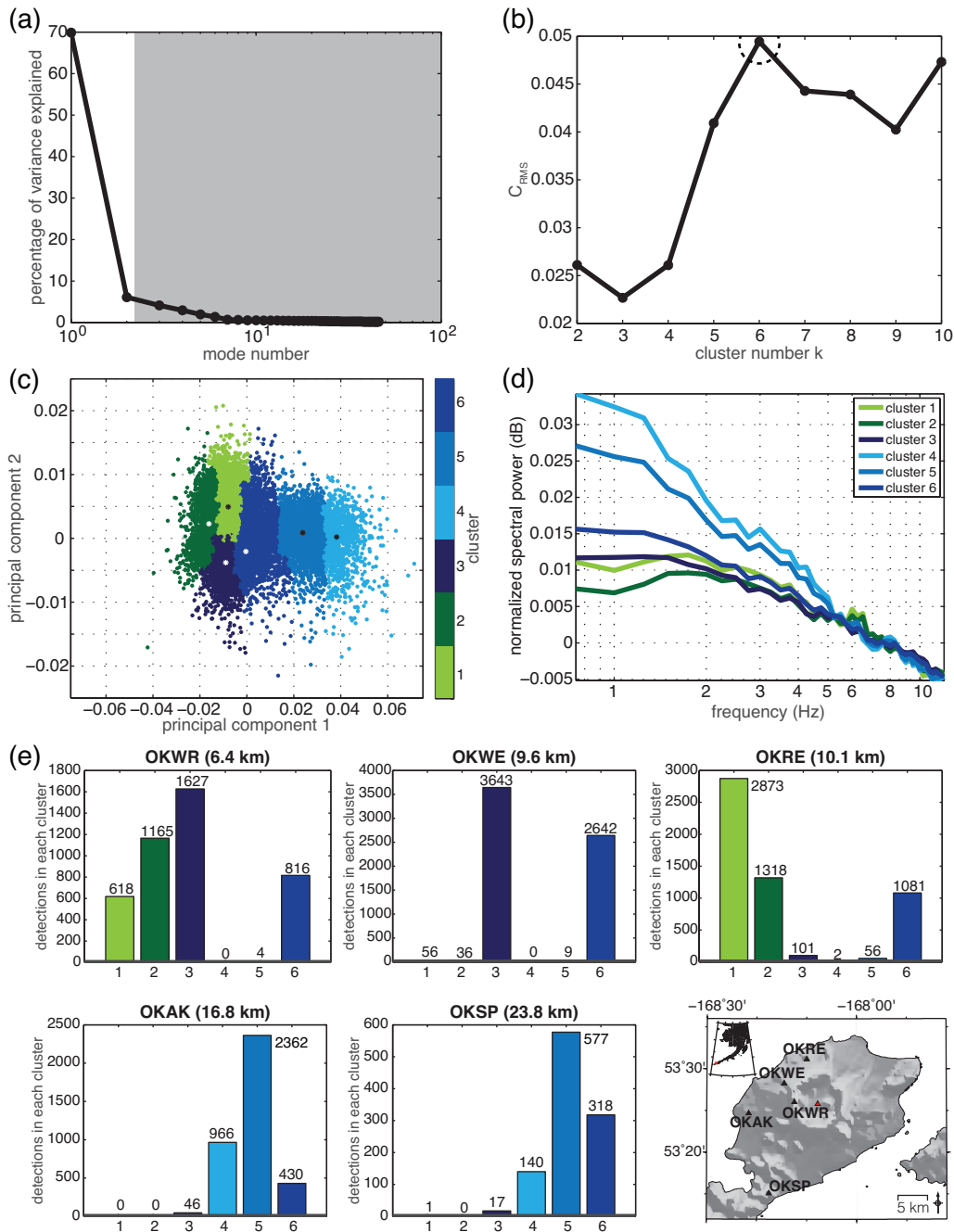


Figure 4.7: PCA and clustering results for multistation analysis at Okmok, 2008. (a) Variance explained by each mode. Grey shaded area indicates modes excluded from further analysis. (b) Cluster evaluation by examining cross-correlation coefficients indicates best clustering for $k = 6$. (c) Clustering of observations in space spanned by first two modes. Asterisk within cluster indicates location of median used to reconstruct spectra. (d) Reconstructed spectra for each cluster. (e) Number of tremor detections associated with each cluster at each station, including station map. Stations ordered by increasing distance from eruption.

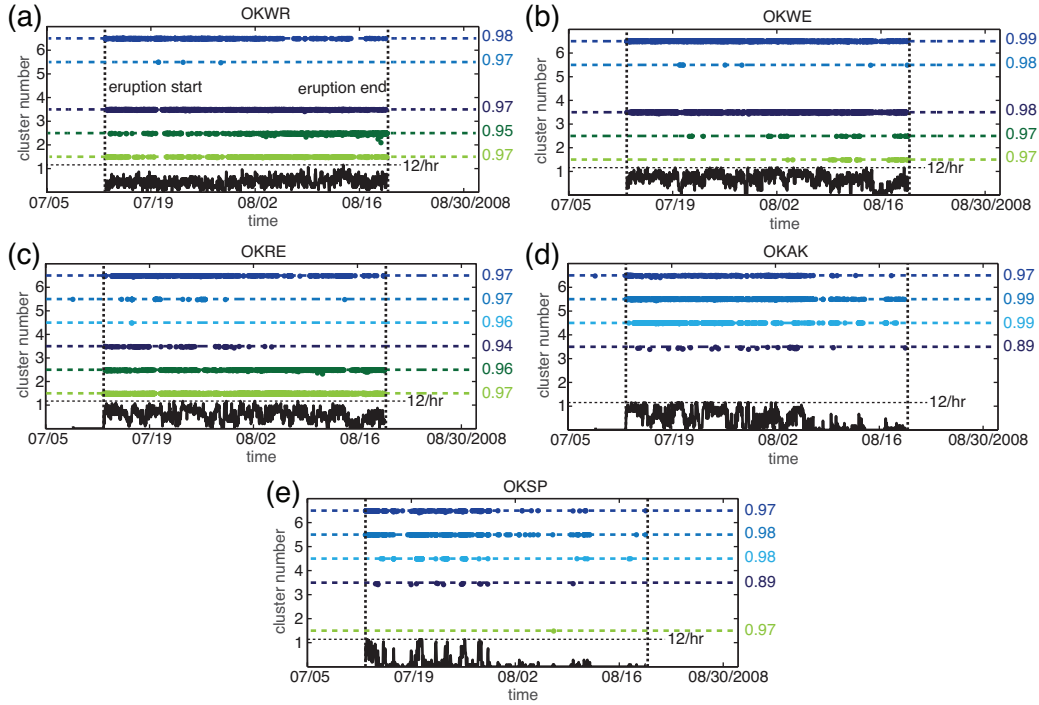


Figure 4.8: Clustering time series for network analysis at Okmok, 2008. For caption see Figure 4.4.

all stations (Fig. 4.10). At PV6 and PS1A, the most common spectrum is the gently decaying regime (cluster 2, Fig. 4.10(a) and (d)). In contrast, at PVV, the high frequency ridge regime (cluster 1) is most commonly observed (Fig. 4.10(c)). Consistent with these differences in the predominant clusters, the angle between the observations at PVV and cluster 1 is lower than the angle for the same cluster at the other stations where a few instances of this cluster are observed, indicating that cluster 1 is a better representation of the observations at station PVV ($\cos(\phi) \sim 0.5$ or $\phi \sim 60^\circ$, vs. $\cos(\phi) < 0$ or $\phi > 90^\circ$ at all other stations). Similar to the observation of a distinct cluster at PVV, the detection rates at PV6 and PS1A show a slow increase in the amount of tremor detections from the onset of the eruption until early September (Fig. 4.10(a) and (d)), whereas the detection rates at PVV (Fig. 4.10(c)) show five pulses surrounded by a few hours to days of slightly lower detection rates that do not follow the same temporal evolution as at the other stations.

The detections during the 2013 eruption show two main pulses of high tremor rates maintained for a few hours to days (Fig. 4.11), one shortly after the onset of the eruption, and one during the final culminating eruptive phase (Waythomas *et al.*, 2014). Similar to 2007, the gently decaying spectrum (cluster 2) is the most common tremor type during the eruption and observed at all stations. Larger amounts of detections associated with the steeply decaying spectrum (cluster 3) are only observed at stations PVV and PS1A (Fig. 4.11(a) and (c)). The high-frequency ridge regime is not observed to a significant extent at any station during 2013, and the few occasions show large angles between the cluster spectrum and the actual observed ones.

4.4. Spectral Pattern Recognition

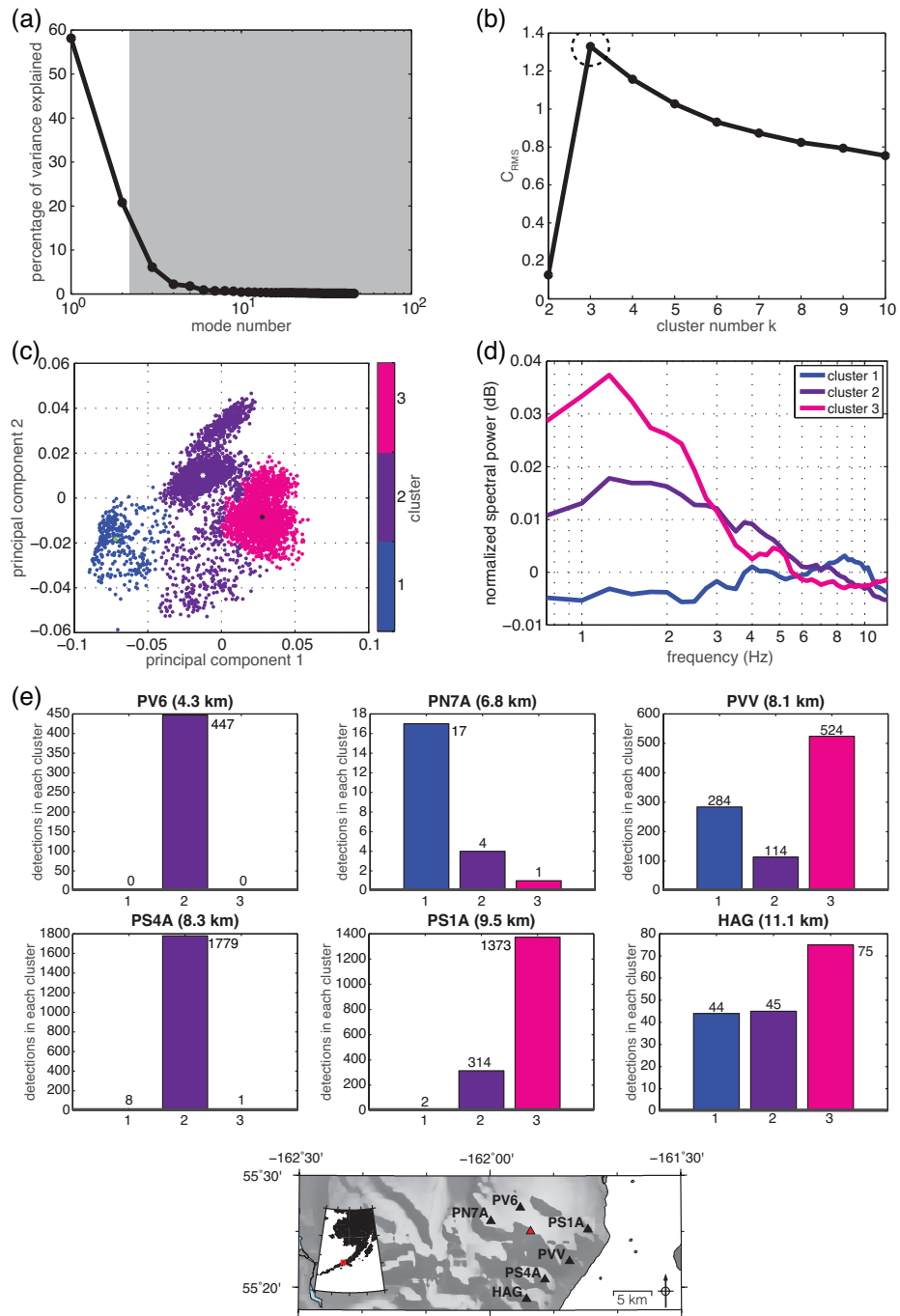


Figure 4.9: PCA and clustering results for network analysis at Pavlof, 2007 and 2013. For caption see Figure 4.7

4.4. Spectral Pattern Recognition

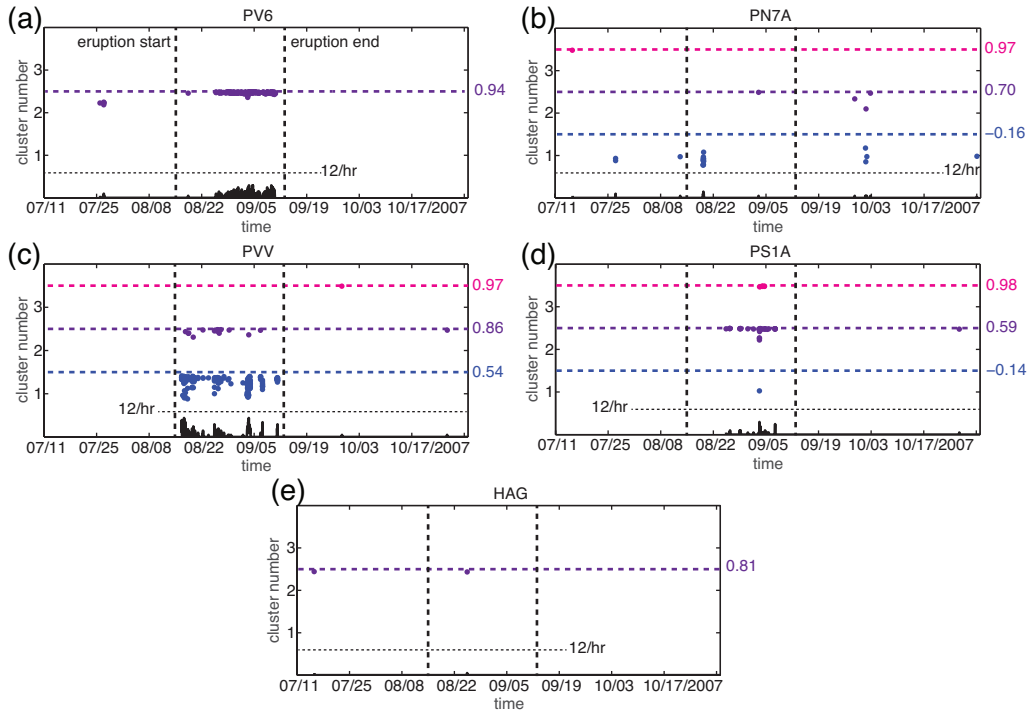


Figure 4.10: Clustering time series for network analysis at Pavlof, 2007. For caption see Figure 4.4.

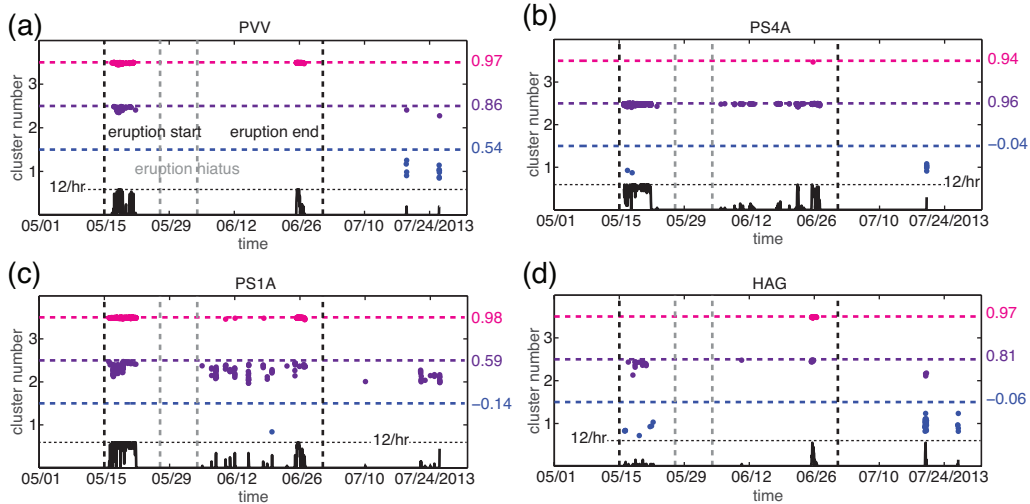


Figure 4.11: Clustering time series for network analysis at Pavlof, 2013. For caption see Figure 4.4.

Redoubt

The variance explained by the first two modes at Redoubt in 2009 is slightly smaller (Fig. 4.12(a)) than at Kīlauea, Okmok, and Pavlof. The observations can be clustered with an ideal $k = 7$ (Fig. 4.12(b)). In PC space, the observations form one big cloud that is less dense and shows clearer separation of the clusters than at Okmok, for example (Fig. 4.12(c) vs. Fig. 4.7(c)). Within this cloud, the clusters capture several regimes, whose differences with respect to each other appear to be stronger than at Kīlauea and Okmok (Fig. 4.12(c)). This pattern is confirmed by the different reconstructed spectra (Fig. 4.12(d)). We divide the clusters into three main categories:

1. The red regime includes clusters 1, 2 and 7 and has a low-frequency (1–5 Hz) plateau of relatively high spectral power with peaks around 3–5 Hz.
2. The dark blue regime includes cluster 5 and has a narrow ridge between 1–2 Hz, from where spectral power decays gently towards higher frequencies.
3. The light blue regime includes cluster 6 and has the same ridge as in the dark blue regime, but less well defined. In addition, the light blue regime shows a kink in the slope around 5 Hz.
4. The green regime includes clusters 3 and 4 and shows an even narrower ridge around 2 Hz compared to the blue regimes, with a steeper decay of spectral power from just above 2 Hz towards higher frequencies.

In terms of absolute numbers of detections, the red and the light blue regimes become less common with increasing distance from the volcanic edifice (Fig. 4.12(e)). In contrast, the dark blue and the green regimes are more common further away from the summit of the volcano.

The temporal evolution reveals two main phases of tremor detections (Fig. 4.13). During the first phase, between late January and late February 2009 approximately one month before the onset of the eruption, a large number of detections coincides with a known period of elevated seismic amplitudes (Buurman *et al.*, 2012; Power *et al.*, 2013). This precursory phase shows the highest detection rates at station REF (Fig. 4.13(a)), and decreases in terms of detection rates with increasing distance from volcano. Only few detections (Fig. 4.13) accompany the time period between the onset of the phreatic and the magmatic explosive phases of the eruptions in mid-March 2009 (for details about the eruptive phases see e.g., Bull and Buurman, 2012). The subsequent magmatic explosive phase shows consistent detections at most stations. After the cessation of explosive activity, no notable tremor detections occur during dome growth.

Spectra from the blue and the red regimes are observed during the precursory phase with decreasing frequency of occurrence for each spectrum with increasing distance from the summit (Figs. 4.12(e) and 4.13(a)–(c)). During the magmatic explosive phase, all tremor types are observed at one or more stations. Whereas the red regime tends to be confined to stations close to the volcano (Fig. 4.13(a)–(b)), the green regime is observed mostly at larger distances (Fig. 4.13(c)–(d)), in line with the trend observed in Figure 4.12(e).

4.4. Spectral Pattern Recognition

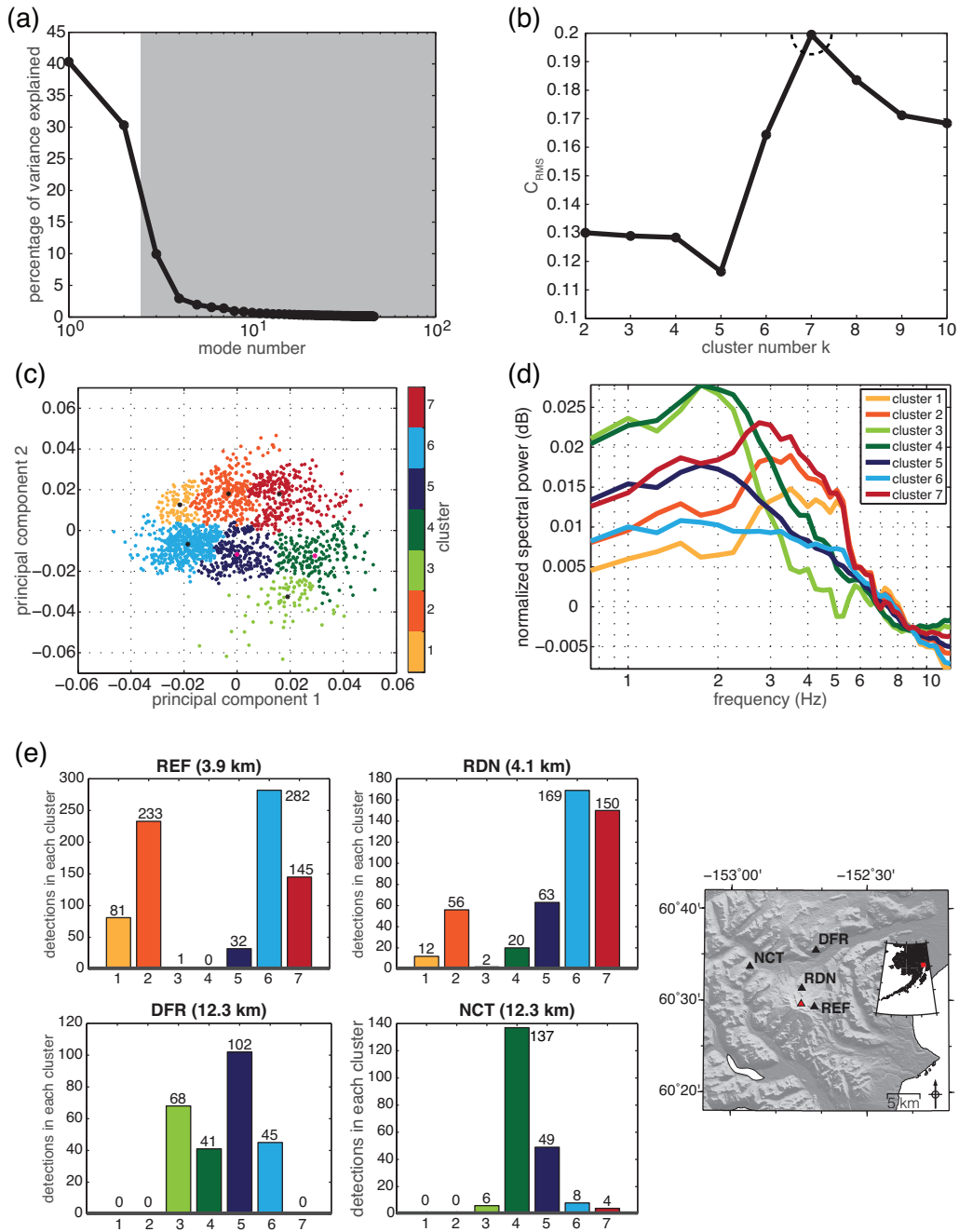


Figure 4.12: PCA and clustering results for network analysis at Redoubt, 2009. For caption see Figure 4.7

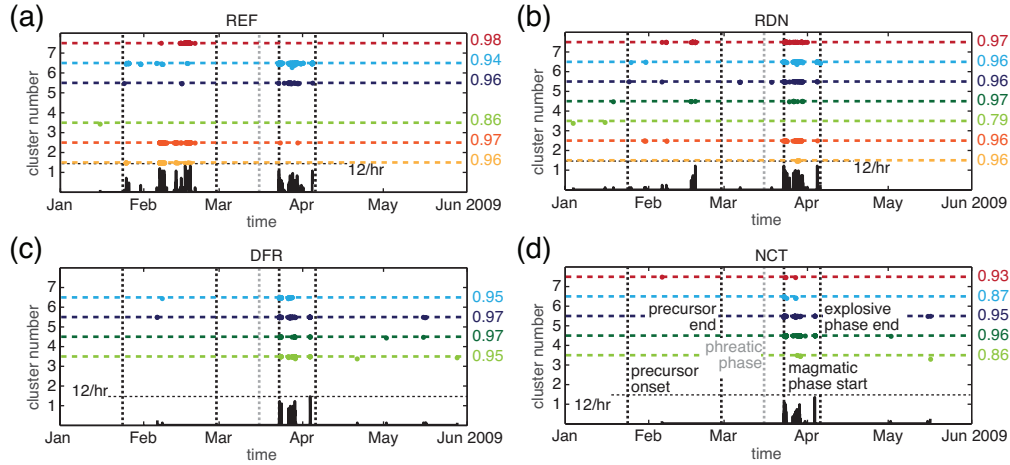


Figure 4.13: Clustering time series for network analysis at Redoubt, 2009. For caption see Figure 4.4. Note event labels in (d) instead of (a) to avoid cluttering.

4.4.3 PCA for Comparison Between Volcanic Settings

To investigate similarities and differences among the volcanic settings, we apply the pattern recognition algorithm to a combined dataset with one station from each of the four volcanoes. To minimize complications related to differences in travel path length of the signals from their source to the seismometer, we base our station choice on the distance from the center of volcanic activity. Applying the reference center points for each volcano defined in Section 4.4.1, we generate two groups of stations at approximately equal distances from their respective volcanic centers:

- The first subset of stations (proximal: 4 km distance) includes AHU (Kīlauea, ~ 4.1 km), PV6 (Pavlof, ~ 4.3 km) and REF (Redoubt, ~ 3.9 km). The closest station at Okmok from the network approach in Section 4.4.2 is located at over 6 km distance, and is thus excluded from the analysis.
- The second subset of stations (distal: 8–10 km distance) includes PAU (Kīlauea, ~ 7.7 km), OKWE (Okmok, ~ 9.6 km), and PVV (Pavlof, ~ 8.1 km). Unfortunately, none of the Redoubt stations analyzed in Section 4.4.2 is at a comparable distance even when considering the larger spread of distances compared to the first group.

The results from these two subsets of stations are summarized in the following sections. Because the number of detections at Kīlauea station AHU is at least one order of magnitude higher than for the stations from the other volcanoes, and because there are no significant, systematic variations in the data from AHU and PAU between July 2007–December 2008 (Fig. 4.5), we restrict the data from the Kīlauea stations to May–June 2007, March–April 2008, and the week around the intrusion in 2011. This shorter dataset includes 12,676 detections for AHU and 929 detections for PAU.

Proximal Tremor Properties: 4 km Distance

Figure 4.14 summarizes the PCA and clustering results for the proximal stations. The first two modes explain 78.5% of the variance (Fig. 4.14(a)), similar to the individual networks. As in Section 4.4.2, we extend the range of k up to 20. The resulting distribution shows $k = 16$, which is larger than the values obtained in any of the individual network analyses. Clustering the observations with $k = 16$ in PC space (Fig. 4.14(c)) and reconstructing the corresponding spectra (Fig. 4.14(d)) reveals similarities among the majority of patterns, suggesting that $k = 16$ may be too large. In such a case where the ideal k is ill-defined, the automated algorithm requires intervention (Unglert *et al.*, 2016). The first local maximum of $C_{\text{RMS},k}$ occurs for $k = 3$ (Fig. 4.14(b)) and we thus hypothesize that $k = 3$ is more appropriate and can capture the main patterns. In support of this value, the points in Figure 4.14(c) appear to form three main clouds, which agrees with the occurrence of three main distinct spectral shapes in Figure 4.14. These observations indicate that our estimated $k = 3$ may be a good choice that qualitatively reproduces the essential features buried in the results for $k = 16$.

Manually setting $k = 3$ and subsequent application of the clustering algorithm (Fig. 4.15) confirms the patterns visually determined for $k = 16$ (cf. Fig. 4.14). The observations in PC space (Fig. 4.15(a)) are clustered in a way very similar to the three main groups visible in Figure 4.14(c), and the corresponding spectra capture the same main features detected with $k = 16$. We thus focus on the manually adjusted $k = 3$ for the following summary and interpretation.

The three spectra in Figure 4.15(b) are a spectrum with a relatively steep decay from low to high frequencies (cluster 3), a spectrum with a low frequency ridge at approximately 1 Hz (cluster 1), and a spectrum with a narrower peak close to 3 Hz (cluster 2). The peaked cluster 2 spectrum appears to occur mostly at Pavlof and Redoubt, whereas the other two are both relatively common at Kīlauea (Fig. 4.15(c)).

The temporal evolution of the clusters at each station for this configuration is shown in Figure 4.16. With this smaller number of clusters compared to the individual network analyses (Section 4.4.2), the variations of the observations at AHU are captured by two clusters only (clusters 1 and 3). Whereas cluster 1 dominates during both intrusions (2007 and 2011, Fig. 4.16(a) and (c)), cluster 3 is the dominant spectrum during 2008 (Fig. 4.16(b)). This spectrum is observed almost exclusively at Kīlauea with over 10,000 detections, compared to 4 and 10 detections at Pavlof and Redoubt, respectively (Fig. 4.15(c)). In contrast, cluster 2 is only observed at Pavlof and Redoubt, which both also show occurrences of cluster 1 (Fig. 4.16(d)–(e)). Whereas cluster 2 is dominant at Pavlof and during the precursory tremor phase at Redoubt, cluster 1 appears predominantly during the eruptive phase at Redoubt. To investigate whether those differences are related to the distance or location of the stations relative to the volcanic centers, we analyze the distal stations in the following section.

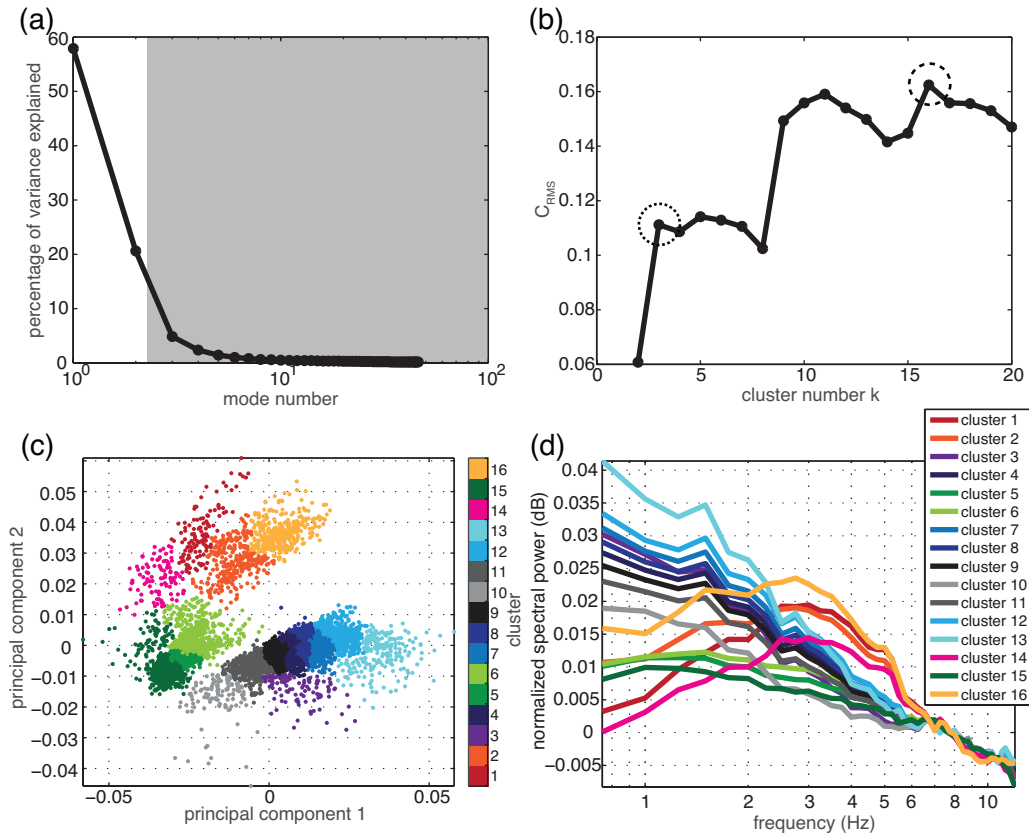


Figure 4.14: PCA and clustering results for combined analysis, for proximal stations (4 km). (a) Variance explained by each mode. Grey shaded area indicates modes excluded from further analysis. (b) Cluster evaluation by examining cross-correlation coefficients indicates best clustering for $k = 16$. (c) Clustering of observations in space spanned by first two modes. (d) Reconstructed spectra for each cluster. Similarities among the 16 spectra in (d), point clouds in (c), and first local maximum of $C_{RMS,k}$ for $k = 3$ (additional dotted circle in (b)) suggest alternative option for choosing k , with corresponding results shown in Figure 4.15. For details see main body of text.

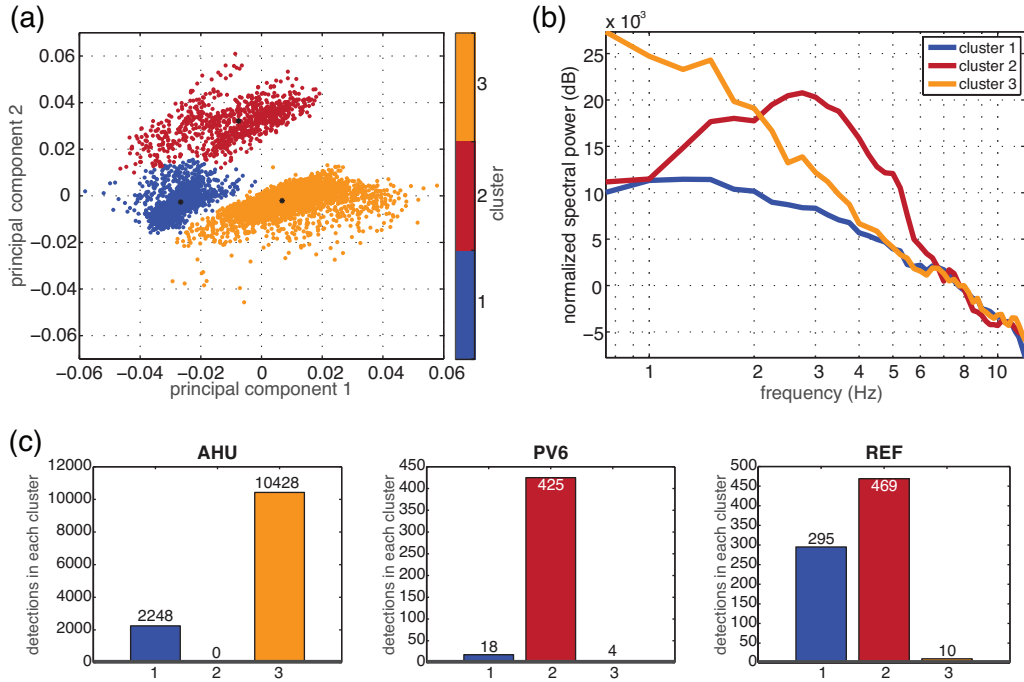


Figure 4.15: Clustering results for combined analysis, for proximal stations (4 km), for 3 clusters. (a) Clustering of observations in space spanned by first two modes. Asterisk within cluster indicates location of median used to reconstruct spectra. (b) Reconstructed spectra for each cluster. (c) Number of tremor detections associated with each cluster at each station.

Distal Tremor Properties: 8–10 km Distance

For the distal stations, the first two PCA modes explain 80.2% of the variance (Fig. 4.17(a)). $C_{\text{RMS},k}$ reveals the ideal $k = 3$ (Fig. 4.17(b)), which corresponds to the manually adjusted value for the close range stations. The three clusters are well separated in PC space (Fig. 4.17(c)), and the corresponding reconstructed spectra capture distinct spectral shapes (Fig. 4.17(d)). Cluster 2 (blue) is similar to cluster 1 from the proximal stations (blue, Fig. 4.15(b)), with a plateau of high spectral power that falls off above 2 Hz. Cluster 3 (orange) has the same steep decay of spectral power from approximately 2 Hz to higher frequencies that can be observed in cluster 3 from the proximal stations (orange, Fig. 4.15(b)), but with a pronounced peak in the 1–2 Hz band, and a distinct flattening of the curve above 6 Hz. Cluster 1 (purple) is similar to cluster 2 from the proximal subset (red, Fig. 4.15(b)), with increased spectral power at higher frequencies than the other two cluster spectra, but its peak is shifted even further to the right to approximately 9–10 Hz compared to station subset 1.

Cluster 1 is observed almost exclusively at Pavlof station PVV (Fig. 4.17(e)). A similar, albeit slightly weaker trend is observed for the steeply decaying cluster 3 spectrum, which occurs over 600 times at Pavlof, compared to 52 and 0 detections at Kīlauea and Okmok, respectively (Fig. 4.17(e)). Those settings are dominated by cluster 2.

The temporal evolution (Fig. 4.18) also shows similarities to the more proximal stations (Fig. 4.16). Kīlauea station PAU is dominated by cluster 2 during the intrusions (Fig. 4.18(a) and (c)), the same

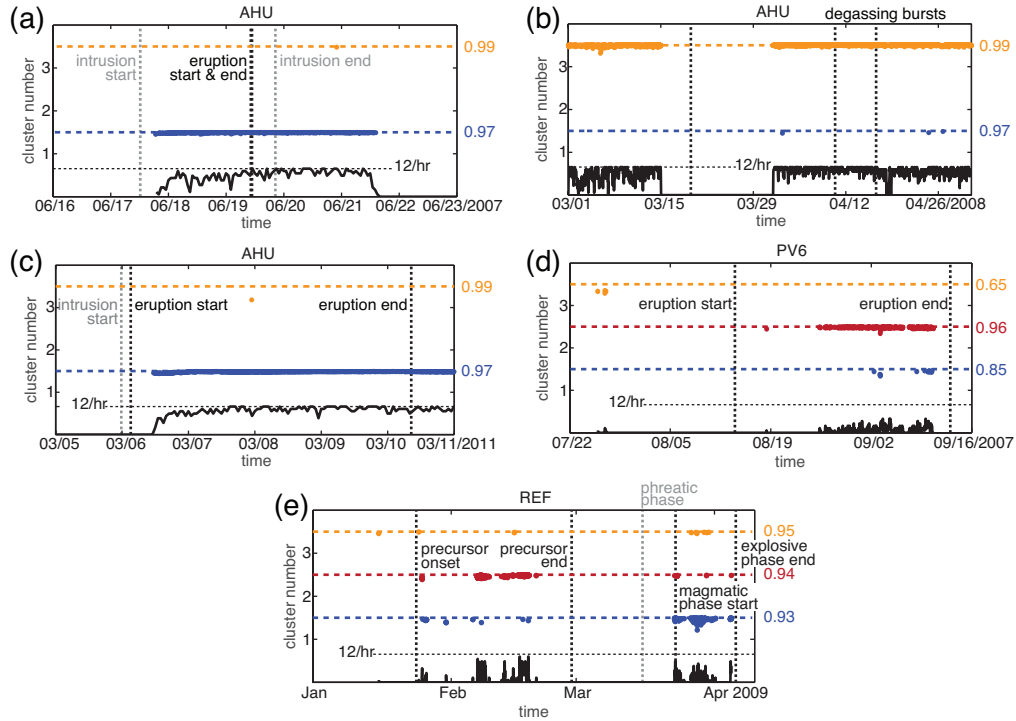


Figure 4.16: Clustering time series for combined analysis, proximal stations (4 km). For each station, colored time series shows best cluster (values between 1–3). Small offset from cluster number shows alignment between cluster spectrum and actual spectrum observed at the time, where the colored dashed line indicates perfect alignment. Mean alignment $\cos(\phi)$ for each cluster shown as colored number on the right of each time series. Black line at the bottom of the cluster time series shows tremor detection rate at each station, with horizontal dotted line indicating the maximum of twelve tremor windows detected during the preceding hour. Vertical dotted lines indicate important dates. For more details see main body of text.

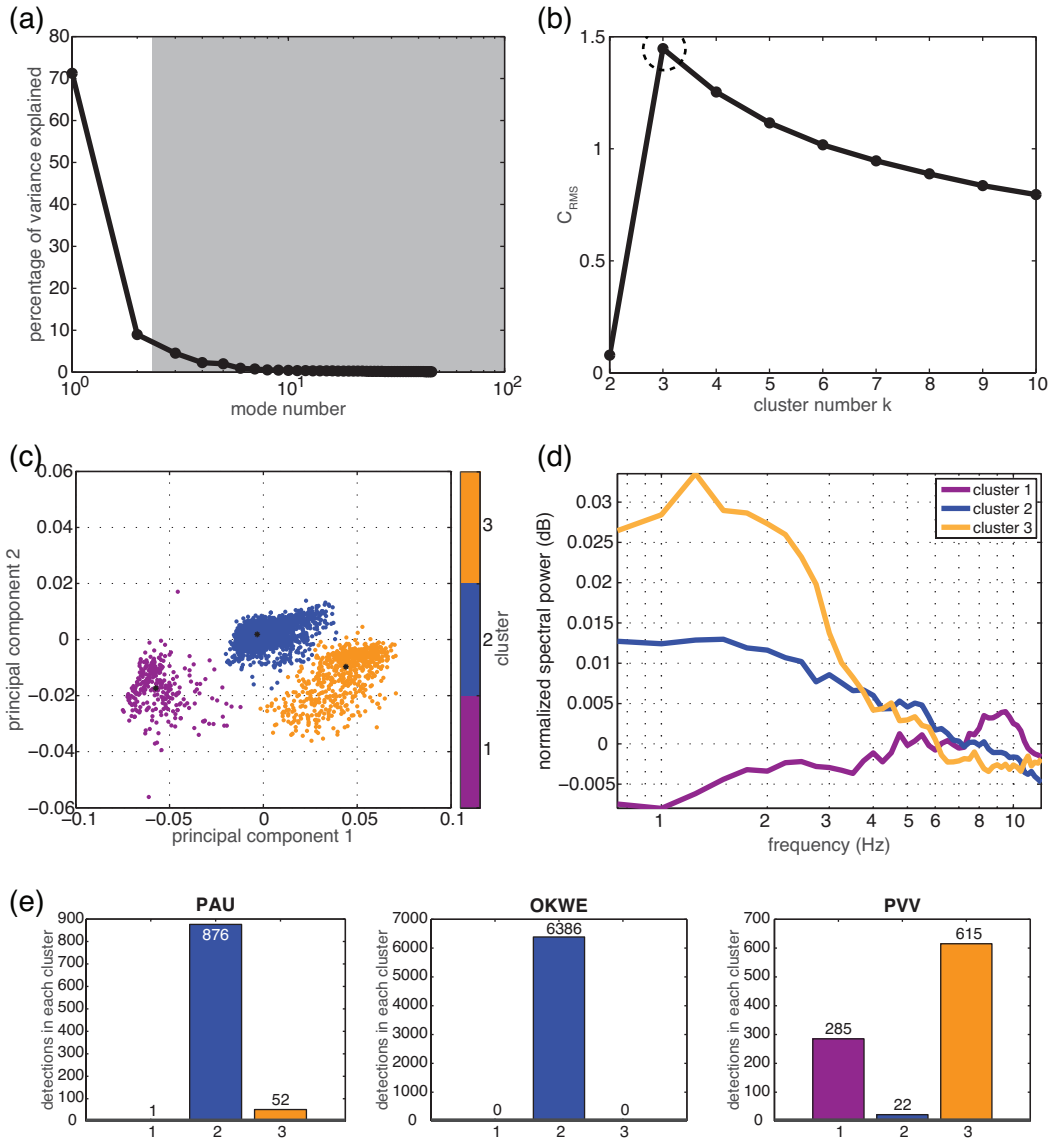


Figure 4.17: PCA and clustering results for combined analysis, for distal stations (8–10 km). (a) Variance explained by each mode. Grey shaded area indicates modes excluded from further analysis. (b) Cluster evaluation by examining cross-correlation coefficients indicates best clustering for $k = 3$. (c) Clustering of observations in space spanned by first two modes. Asterisk within cluster indicates location of median used to reconstruct spectra. (d) Reconstructed spectra for each cluster. (e) Number of tremor detections associated with each cluster at each station.

as the equivalent spectrum at AHU from the proximal stations (Fig. 4.16(a) and (c)). Similarly, cluster 3 is the only spectrum observed in 2008 (Fig. 4.18(b)). In agreement with the relatively small differences between the spectra from the network analysis at Okmok (Figs. 4.7 and 4.8), station OKWE is marked by cluster 2 only (Fig. 4.18(d)). Whereas the 2007 eruption at Pavlof shows mostly cluster 1 spectra at PVV, the detections during the 2013 eruption at the same station belong dominantly to cluster 3 (Fig. 4.18(e)–(f)).

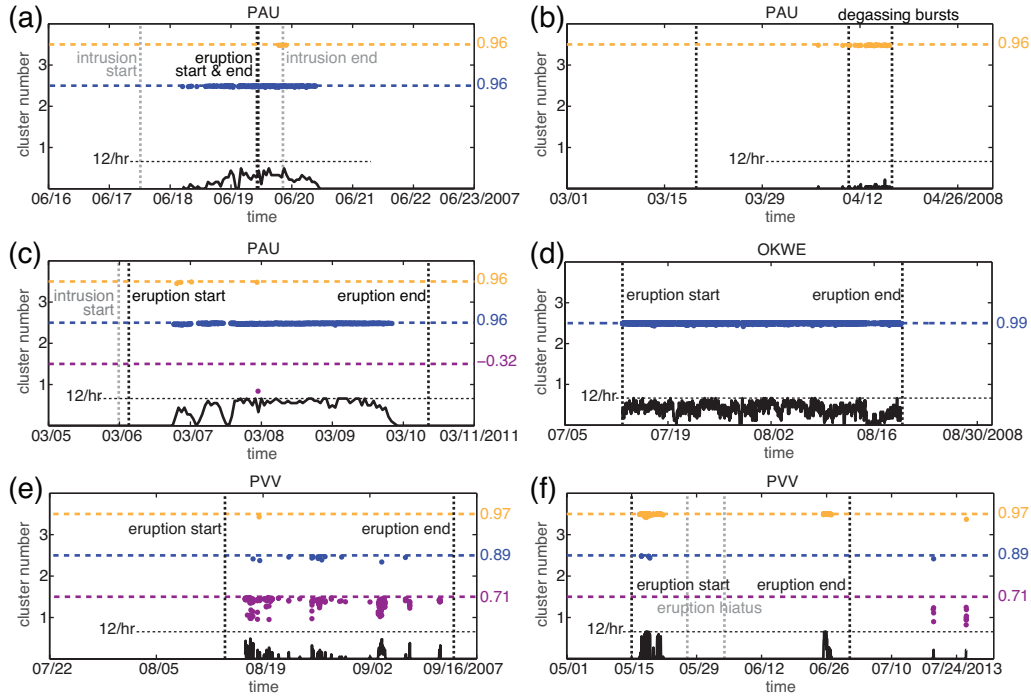


Figure 4.18: Clustering time series for combined analysis, distal stations (8–10 km). For caption see Figure 4.16.

4.5 Discussion

Our pattern recognition approach shows interesting results both for the individual network analyses and the investigation of common patterns between the different volcanic settings. In the following sections, we first discuss the observations related to distinct spectral patterns at each of the locations individually (Sections 4.5.1–4.5.4). Next, we explore the implications of the results for our tremor detection algorithm (Section 4.5.5). Last, we discuss similarities and differences between tremor at different volcanic settings the basis of the multi-setting analysis and the lessons learned in terms of our approach (Section 4.5.6).

4.5.1 Kīlauea: 2007, 2008, 2011

Several of our observations at Kīlauea confirm the results obtained through manual analysis by *Unglert and Jellinek (2015)*. In particular, we confirm the presence of pre-intrusion tremor in

2007 at the eastern stations (Fig. 4.4(d)–(e)). Furthermore, syn-intrusion tremor in 2007 and 2011 dominant at the western stations near the summit (Figs. 4.4(a)–(c) and 4.6(a)–(c)) is consistent with the second phase of continuous tremor observed by *Unglert and Jellinek (2015)*. A lack of changes in spectral character associated with the more explosive degassing bursts at the summit lava lake in 2008 (Fig. 4.5), and the lack of any pre-intrusion signals in 2011 (Fig. 4.6) were also observed by *Unglert and Jellinek (2015)*. The absence of high tremor detection rates in the early phases of the intrusions is expected because of the findings that the first phase of seismicity consists of discrete events (*Unglert and Jellinek, 2015*), which our detection algorithm excludes from analysis (Section 4.3.2).

The similarity of detection rates during all years at the two western and the two eastern stations, respectively, where the westernmost (OTL) and easternmost stations (STC) show the highest rates, confirms that potentially shallow processes at the summit and in the East Rift Zone (Fig. 4.3(e)) can generate different, localized seismicity patterns (*Unglert and Jellinek, 2015*).

At any given time, several clusters are observed at individual stations, almost simultaneously (e.g., several clusters within blue regime at station OTL in 2008, Fig. 4.5(a)). Similarly, different stations show different clusters that appear to coincide in time (e.g., red regime at STC before 2007 intrusion vs. green regime at KNH during the same time period, Fig. 4.4(d)–(e)). These results suggest that the same processes can be expressed in different ways at one station, or at two stations located relatively close to each other. In addition, because the clusters are not well separated in PC space (Fig. 4.3(c)), and because the changes from one cluster spectrum to the next in some cases appear to capture small variations in the slope without altering the main spectral shapes, we suggest that $k = 11$ does not correspond to the actual number of independent processes. Instead, the large number of clusters may represent different stages or end members of only a few processes active concurrently. The spectra associated with the clusters within each of the three main regimes mostly differ in terms of their spectral slopes, but share common frequency peaks. This suggests that the systematic differences between stations may relate to path and location effects, where a given process generates slightly different spectra depending on the distance between the station to the source, for example. Similarly, the near simultaneous occurrence of different clusters at individual stations may stem from small fluctuations of the underlying source process. We discuss these observations in more detail in Section 4.5.6.

Among the 11 clusters obtained for Kīlauea, we do not include cluster 3 (purple) in the three main regimes (Section 4.4.2). This omission is related to its spectral character that appears to be in-between the blue and the red regimes (Fig. 4.3(d)), to its generally poorer alignment with the observed spectra compared to the other clusters (Figs. 4.4, 4.5, and 4.6), and to its occurrence mostly confined to stations KNH (2007) and STC (2011) (Figs. 4.4(d) and 4.6(e)). *Unglert and Jellinek (2015)* attribute a localized signal at STC in 2011 to a shallow source potentially directly related to magma flow dynamics of the ongoing fissure eruption. Because cluster 3 is observed at STC in 2011 (Fig. 4.6(e)) and KNH in 2007 (Fig. 4.4(d)), where STC is closest to the eruption site in 2011 and KNH in 2007, respectively, it is possible that this eruption related source process is active at those stations close to the eruptive fissures. However, a more detailed view of the temporal

evolution (Fig. 4.19) relative to the start and end times of the intrusions and eruptions reveals that the cluster 3 signal is detected after the end of the main intrusion period and after the short eruption at KNH (Fig. 4.19(a)). Similarly, the corresponding signal at STC starts earlier but persists after the end of the eruption (Fig. 4.19(b)). There is a systematic initial decrease of alignment between the observed spectra and the typical cluster 3 pattern, followed by a shorter increase in alignment at both stations, which, together with the previous similarities, indicates a common source process. The manual analysis by *Unglert and Jellinek (2015)* did not allow such detailed investigation of these signals. The new observations provide improved constraints on plausible source mechanism, and imply that processes directly related to the surface expression of the eruption as suggested by *Unglert and Jellinek (2015)* (e.g., lava spattering *Patrick et al., 2011b*) cannot fully explain our observations.

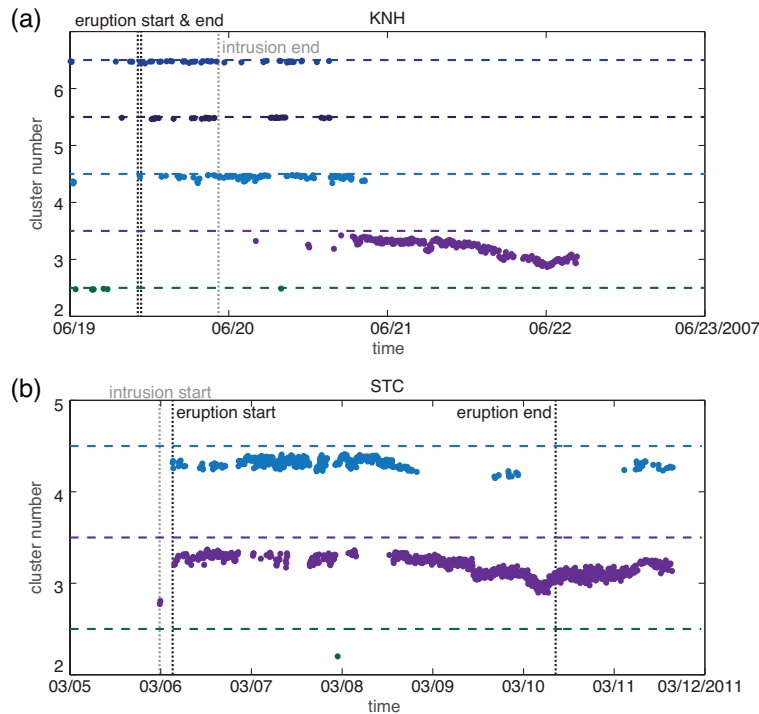


Figure 4.19: Zoom into temporal evolution of main clusters during intrusions at Kīlauea in (a) 2007 at KNH, and (b) 2011 at STC. Vertical level of observations indicates cluster number. Small offset shows alignment between cluster and observed spectra, where +0.5 is perfect alignment (horizontal dashed lines above cluster level), and -0.5 indicates 180° difference between vectors.

4.5.2 Okmok: 2008

The generally consistent and high detection rates throughout the eruption are in agreement with other work on this dataset (*Haney, 2010*). Despite an increase in ash production at the beginning of August (*Larsen et al., 2015*) tremor detection rates showed no significant increase at the same time, a result previously noted by *Larsen et al. (2009)*. In fact, detection rates decreased at the stations further away from the eruptive vent around that time.

Similar to Kīlauea, the cluster spectra at Okmok resemble each other (Fig. 4.7(d)). However, in contrast to Kīlauea, there are no significant systematic changes between the different regimes in terms of their timing relative to the eruption (Fig. 4.8). There are several possible explanations for this behaviour. The observed spectral shapes can look similar if (i) the observed tremor is the expression of only one main source process, that is slightly time-dependent, or if (ii) the volcanic edifice acts as a filter, which restricts all tremor spectra to have similar characteristic shapes, regardless of the underlying process(es). The differences in terms of relative contributions of the clusters at different locations (Fig. 4.7(e)) that do not appear to be reflected in temporal differences do not allow to distinguish between these two scenarios.

Another possibility (iii) is that the main differences between the spectra lie outside of the frequency band analyzed here. A change of the source location of very-long period (VLP) tremor (<0.5 Hz) during the eruption occurred on 2 Aug 2008 (Haney, 2010). We do not observe a change in spectral character at the same time (Fig. 4.8). However, if the movement of the VLP tremor source is accompanied by a change in spectral characteristics, these would naturally be strongest in the VLP band, i.e., below our lower frequency limit, and we would not expect to observe a temporal change in our analysis.

Our higher frequency band (0.75–12 Hz) is generally more prone to path effects than the lower frequencies (e.g., Haney, 2010), and a combination of all three processes may thus have some influence on our results.

As a final remark, several lahars occurred during the Okmok eruption and may be detected by our algorithm and have a specific spectral signature. However, the exact timing of these flows is unknown because they were observed only indirectly in their deposits during intermittent visits to the island (Larsen *et al.*, 2015). Ash isopachs from the eruption at Okmok reveal the thickest ash deposits in the southeast quadrant of the island (Larsen *et al.*, 2015), which may indicate that lahars are most likely to develop in that area. None of the stations used for our analysis are situated close to those deposits (Fig. 4.7(e)), so it is possible that localized signals cause by lahars exist but cannot be detected by our stations. We thus cannot determine whether lahars may be related to specific spectra at Okmok. Similarly, a lack of variations in the temporal evolution of clusters combined with poor knowledge of the exact timing of other syn-eruptive processes makes it difficult to associate any of the observed spectra with processes occurring during the eruption.

4.5.3 Pavlof: 2007, 2013

Detection rates at Pavlof (Figs. 4.10 and 4.11) agree well with previous studies which report the temporal evolution of RSAM over the course of the 2007 and 2013 eruptions (McGimsey *et al.*, 2011; Waythomas *et al.*, 2014). The only exception is station PVV in 2007 (Fig. 4.10(c)), where despite the large number of detections the temporal evolution of the detection rates differs significantly from the other stations. In addition, the dominant cluster is cluster 1 (Fig. 4.10(c)), which appears only very infrequently at other stations or times. The 2007 eruption occurred on the Southeast flank and lava flows as well as over 40 lahars were directed downwards towards PVV (Waythomas *et al.*,

2008; *Global Volcanism Program*, 2013c). Taken together, these observations suggest a relationship between the directionality of the eruption and the differences between PVV and the other stations. Indeed, the first detection of cluster 1 at PVV occurs on 16 Aug 2007 at 15:30. This tremor signal coincides with the detection of the first lahar of the 2007 eruption at the same station (*Waythomas et al.*, 2008). The peaks in detection rates around 17 Aug and 25 Aug at PVV (Fig. 4.10(c)) coincide with the observation of multiple lahars during those times. It is, thus, possible that the cluster 1 signature is directly related to the shaking induced by the flow of material down the slopes of the volcano.

Alternatively, a subsurface process prior to lahar generation could be responsible for the observed signal. However, because lahars were occurring on the southeastern flank, and because cluster 1 is not observed at any other station, we suggest that the former scenario is more likely. *Waythomas et al.* (2008) report that tremor typically preceded the lahars by 11–25 minutes. If the tremor is related to the onset of the lahar higher on the volcano, this time period implies a signal traveling at 20–46 km/h towards PVV (8.5 km distance from the summit, neglecting the relatively small contribution to travel time from seismic wave velocities), which is similar to lahar speeds observed at Popocatépetl Volcano, Mexico (*Muñoz-Salinas et al.*, 2007) and thus makes a surface signal scenario likely. Additional data from other eruptions could help to distinguish between the two mechanisms. The 2013 eruption was directed towards the Northwest, but stations PN7A and PV6 situated in that area were unfortunately not operating during the time (*Waythomas et al.*, 2014). Regardless of the exact mechanisms (surface vs. subsurface), on the basis of our observations we thus suggest that the differences between clusters 2–3 vs. cluster 1 stem from the fact that cluster 1 is related to the lahars on the flanks of the volcano. Our algorithm not only detects the differences in temporal evolution between the different stations, but also provides a specific spectrum associated with the “anomalous” tremor process.

4.5.4 Redoubt: 2009

Our detection rates at Redoubt agree with previously identified periods of increased seismic amplitudes (*Buurman et al.*, 2012). Most detections are observed on the station closest to the summit (REF), in particular during the precursory phase (Fig. 4.13(a)). The precursory tremor has been attributed to activation of the shallow hydrothermal system (*Power et al.*, 2013). This shallow source explains the localization of the signals. *Power et al.* (2013) and *Buurman et al.* (2012) observed large variations in the spectral character of volcanic tremor during this period preceding the eruptive phases. Similarly, a mostly coherent period of detections belonging to the red regime in mid February 2009 is sometimes interspersed with spectra from the blue regime, which are also associated with a small amount of detections before, between, and after the different precursory/eruptive phases (Fig. 4.13(a)).

Whereas the hydrothermal phase is mostly visible on REF (Fig. 4.13(a)), we observe syn-eruptive detections also on stations further away (Fig. 4.13(b)–(d)). The similarities in terms of timing of detections at the different stations suggest that the same process(es) cause detections

everywhere, despite the differences in best matching clusters (Fig. 4.13).

The summit crater at Redoubt, from where the 2009 eruption originated, opens up to the North flank of the volcano into the Drift River valley (Schaefer, 2011). All our stations except REF are located in the same direction. Between 23 March and 4 April 2009 several pyroclastic flows and lahars accompanied dome growth and collapse as well as repeated explosions (Schaefer, 2011; Bull and Buurman, 2012). There is some indication that lahars tend to be accompanied by seismic signals with spectra from the blue regime at stations RDN and DFR, but a clear relationship cannot be identified and not all lahars coincide in time with our detections. Because of the multitude of processes occurring during the explosive phase, our detections switch on and off, and change from one cluster to another over short time intervals, which makes identifying explicit relationships to the eruptive events during the highly energetic explosive phase difficult. If the detections during the explosive phase are not directly associated with energetic lahars that come close to most stations, then the question remains why those detections are visible at all stations, in contrast to the precursory phase that appeared to come from localized processes at the summit. If the precursors stem from shallow processes related to the hydrothermal system, the mechanics underlying the detections during the explosive phase must either be stronger or deeper for them to be detected many kilometers away from their source.

4.5.5 Implications for Tremor Detection Algorithm

The detections from our algorithm mirror the temporal evolution of RSAM at Pavlof (McGimsey et al., 2011; Waythomas et al., 2014) and at Redoubt (Buurman et al., 2012; Power et al., 2013), as well as the known evolution of seismicity at Kīlauea (Unglert and Jellinek, 2015). These matches suggest that our amplitude-based algorithm accurately identifies tremor signals. Furthermore, the detection parameters informed by known characteristics of the data at the Kīlauea (Section 4.3) capture time periods of elevated tremor amplitudes also for other settings.

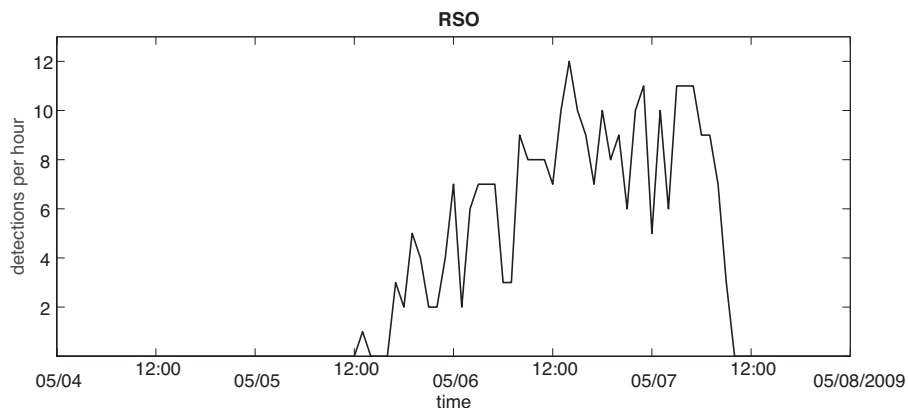


Figure 4.20: Detection rates at station RSO during several days in May 2009. High rates are most likely related to earthquake swarm activity.

However, because of the nature of our algorithm we detect signals that may not be related to

volcanic tremor in its definition as a continuous seismic signal, which we illustrate below. Because of a station outage around the time of the main eruptive phase at Redoubt, station RSO is excluded from our pattern recognition analysis. However, the data from RSO produce valid detections at other times that can be analyzed in terms of detections in order to assess our algorithm. One of those periods is a pulse of detections in early May 2009 (Fig. 4.20), which we attribute to a swarm of small, closely spaced earthquakes. This swarm included peak rates of over 660 earthquakes per hour (Ketner and Power, 2013), resulting in up to 55 earthquakes per 5-minute window. It is thus not surprising that this swarm resembles tremor from the perspective of our detection algorithm. These detections highlight a potential drawback of our method, which detects not only tremor but also discrete earthquakes if they become closely spaced or overlap in time. However, in some volcanic settings including Soufrière Hills Volcano and Redoubt, individual low-frequency earthquakes closely spaced in time merge into tremor (Neuberg *et al.*, 2000; Hotovec *et al.*, 2013). Consequently, it may be desirable to detect such closely spaced individual events as tremor. If, in contrast, such events should be excluded from any tremor analysis a detailed investigation identifying them is required so that event origin times can be included in the tremor detection algorithm (Section 4.3.2). We refer the reader to previous work on this topic for more details about how to detect similar events within swarms or earthquakes buried in other signals (e.g., Green and Neuberg, 2006; Ketner and Power, 2013).

Another “anomalous” signal that was detected by the algorithm are the potential lahar signatures at Pavlof station PVV in 2007 (Fig. 4.10). If these signals are suspected to come from such surface processes, they should ideally be excluded from the analysis where the goal is to detect volcanic tremor only, which is a limitation of our detection methodology. However, our pattern recognition approach is able to clearly recognize the differences between the lahars and most of the other signals at Pavlof, so it would be easy to remove those events before proceeding with any further analysis related to tremor. This result shows that in addition to our detection methodology informing the pattern recognition approach, the process can also work in reverse. The PCA and clustering method can inform any processing following the detections by isolating specific signals in a case where the analysis of the overall similarities and differences between patterns is not the main goal. In contrast, several lahars are observed at Redoubt (e.g., on camera) but are not necessarily detected by our tremor detection algorithm. This lack of detections may be related partly to the threshold set by our algorithm. A possible way to test this hypothesis could be to introduce a variable detection threshold depending on station distance from the suspected center of activity. Further tests are required to determine if this variation of our algorithm helps to detect the lahars at Redoubt.

4.5.6 Joint Analysis: Lessons Learned

The combined analysis of stations from each of the volcanic settings for the two different station subsets reveals interesting results. The lower cluster numbers ($k = 3$) give simplified, but consistent results compared to the individual network analysis (pattern recognition among several stations within one setting, Section 4.4.2). For example, the Kīlauea stations both show similar spectra that

persist consistently throughout the intrusions in 2007 and 2011, and a different spectral signature during the times of degassing bursts in 2008 (Figs. 4.16(a)–(c) and 4.18(a)–(c)), in agreement with the results from the network analysis and the results by *Unglert and Jellinek (2015)*. Similarly, at Okmok the combined analysis reveals no changes in spectral shape during the 2008 eruption (Fig. 4.18(d)), consistent with the results from the network analysis at Okmok. During the 2007 eruption at Pavlof, a narrowly peaked spectrum relative to the other clusters is observed at PV6 (Fig. 4.16(d)), whereas PVV is marked by the high frequency peak spectrum of cluster 1, which is not observed in significant amounts at other times or stations (Fig. 4.18(e)). Last, the temporal evolution of clusters from the combined analysis at Redoubt suggests peaked spectra (~ 3 Hz) during the precursor phase at REF, followed by spectra with a low frequency plateau during the eruptive phase (Fig. 4.16(e)). This confirms the results obtained by analyzing the Redoubt network individually.

Proximal vs. Distal Tremor Properties

Spectra from all four individual network analyses have steeper decays of spectral power from low to high frequencies with increasing distance from the inferred source location (indicated as shades of the same color within the regimes of spectra obtained for each setting). Because our normalization scales each original spectrum by its cumulative spectral power (Section 4.3.3, *Unglert et al., 2016*), such differences in slope still relate to differences in the amplitude of the spectral power curves in the original data. A steeply decaying spectrum is a property of lower overall spectral power, and spectra with flatter slopes are indicative of higher overall spectral power. This relationship indicates that, as expected, the same spectral shape can be observed at the same time at different stations, with spectral power decreasing (i.e., steepening of slopes) with increasing distance from the inferred source location.

Whereas for the distal (8–10 km) stations our algorithm gives a clear peak at $k = 3$ (Fig. 4.17(b)), the proximal results (4 km) show that $C_{\text{RMS},k}$ has several local maxima. This behaviour indicates that the sensitivity to the range of k tested, and that more clusters than the three discussed here may be required to fully explain the data.

The agreement between the network analysis and the combined approach for the manually adjusted $k = 3$ in this case, however, suggest that the obtained spectra are meaningful representations of the data. Comparing Figures 4.14(d) and 4.15(b) shows that the larger number of clusters in Figure 4.14 is related to the differences in slopes, with the main three patterns clearly visible in both Figures 4.14(d) and 4.15(b). The trend towards higher cluster numbers in $C_{\text{RMS},k}$ for the proximal stations compared to distal stations and the implied larger variability in terms of overall spectral power thus raises a question of whether this result is related to the shorter distance to the source of volcanic activity for subset 1. Together with the differences in detection rates discussed in the previous sections, the larger variability in spectral power (manifested in different spectral slopes after our normalization) confirms an intuitive result: Whereas various stages of the same spectral fingerprint (i.e., similar spectral shape) can be detected closer to the center of activity, only

the strongest phases are detected at stations further away. Because the overall patterns for the two station subsets are relatively similar in their character and timing, we suggest that they stem from the same underlying processes, implying that the length (and possibly nature) of the travel paths of these signals do not influence their spectral character. Similar to observations by previous studies (e.g., *Sherburn et al., 1999*), *Bean et al. (2008)* and *Bean et al. (2014)* have recently shown the influence of the seismic wave path on the characteristics of volcanic low frequency seismicity, which may be misinterpreted as effects of the source mechanics if the recording seismometers are more than 500 m away from the source. Because our stations are all at least a few kilometers away from their source, our work does not dispute this result. However, we can conclude from our results that similar qualitative changes to tremor spectra do not occur at larger distances in our data.

Volcano Intercomparison and Some Implications for Source Mechanisms

The identification of systematic similarities and differences in the properties of volcanic tremor among volcanoes globally is the main motivation behind this work. With only four volcanoes analyzed, we cannot conclusively address this goal. However, our results reveal some trends that can be tested in future work, and illustrate the value of such a global comparison, which we discuss below.

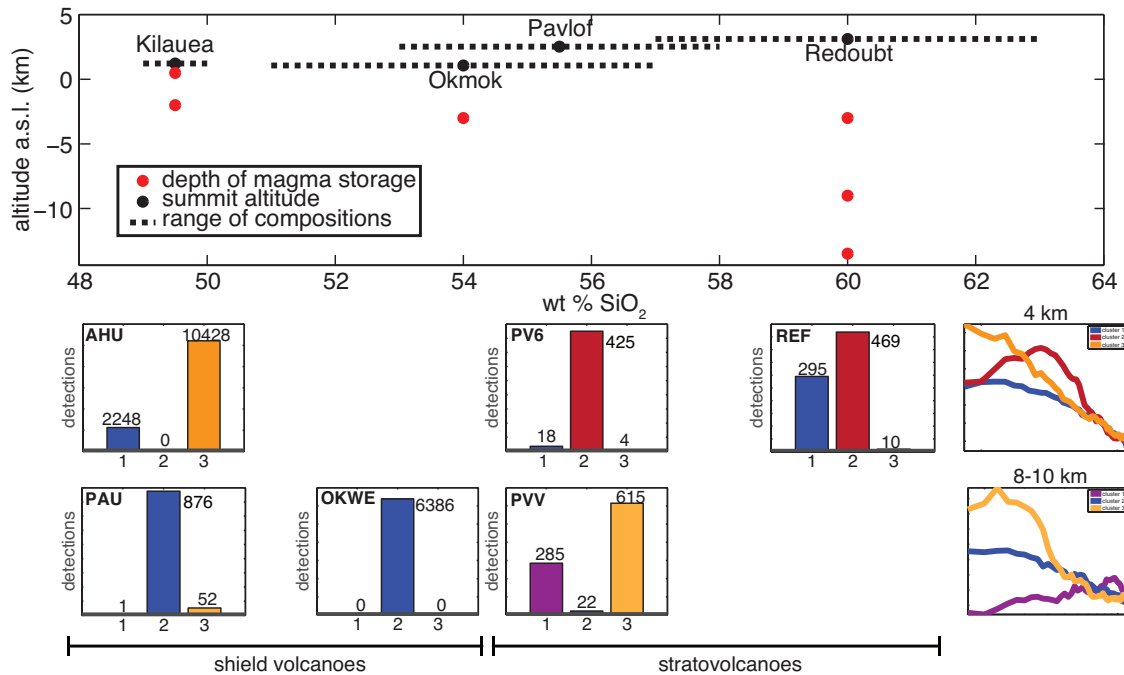


Figure 4.21: Summary of tremor types in relation to volcano and eruption characteristics. Top panel shows dominant composition during data period, summit altitude above sea level (a.s.l.) as proxy for volcano type, and inferred depths of magma storage region(s) for each volcano. Bottom panel shows histograms

Figure 4.21 summarizes some of the characteristics of each the volcanoes that may influence the similarities and differences revealed by our pattern recognition algorithm. Many tremor mech-

anisms that have been suggested in the literature depend on magma viscosity or rheology (e.g., Ripepe and Gordeev, 1999; Johnson and Lees, 2000; Jellinek and Bercovici, 2011; Thomas and Neuberg, 2012). Ripepe and Gordeev (1999), for example, predict a relationship between magma viscosity and tremor peak frequency. In lieu of direct estimates of viscosity or rheology, we use magma SiO₂ as a proxy (e.g., Gonnermann and Manga, 2007; Takeuchi, 2015) and categorize the four volcanoes according to their edifice type including summit altitude (Fig. 4.21). In addition, we show estimates for magma storage depths. Below these essential volcano characteristics, each panel shows the histograms at a particular volcano for the clusters identified through analysis of the stations at 4 km (Fig. 4.21, top row) and 8–10 km distance (Fig. 4.21, bottom row), respectively, with the corresponding spectra on the right for comparison. The blue spectrum is observed at all volcanoes and stations to some extent. By contrast, the other types occur at certain volcanoes only. For example, we only observe the purple spectrum at Pavlof, whereas the red spectrum appears at Pavlof and Redoubt (both stratovolcanoes) and is absent at Kīlauea.

At Pavlof, both the network analysis and the combined approach reveal the presence of a spectrum that is almost exclusively confined to station PVV during a period of lahar activity during the 2007 eruption. We suggest that these flows down the slopes of the volcanic edifice cause the observed signals (Section 4.5.3).

The combined analysis shows that the red spectrum from the proximal stations (4 km) is common to the precursory phase in 2009 at Redoubt and the 2007 eruption at Pavlof (Figs. 4.16(d)–(e) and 4.21). The seismicity at Redoubt during that time when no eruptions occurred has been previously explained as activation of the shallow hydrothermal system (e.g., Power *et al.*, 2013). At Pavlof, however, a similar signal is observed at several stations, albeit with the peak at slightly lower frequencies around 1–2 Hz (Fig. 4.10). Whereas no details about the presence of a hydrothermal system at Pavlof are included in recent conceptual models of the region (Emmons Lake Volcanic Center, Mangan *et al.*, 2009), phreatomagmatic eruptions have been recorded at Pavlof (e.g., McNutt, 1987a). This observation in combination with its persistent ice and snow cover (Waythomas *et al.*, 2014) may suggest the presence of shallow groundwater or the interaction of erupted material with surface water. Both Pavlof and Redoubt are at the higher end of the range of magma SiO₂ content of the volcanoes sampled in our work (Fig. 4.21 and Section 4.2), and form tall stratovolcanoes with summits over 2,500 m above sea level. In particular, similarities in the structure of their edifices and the presence of water may inform explanations of why this spectrum (cluster 2) is common to both volcanoes. Alternatively, processes related to the higher silica content, and thus potentially increased effective viscosity relative to the other two settings (e.g., Jellinek and Bercovici, 2011; Dmitrieva *et al.*, 2013) may drive the observed signal.

Interestingly, the blue spectrum observed at Redoubt during the eruptive phase is also observed at Kīlauea during the dike intrusions, and at Okmok during the 2008 eruption, both at 4 km (cluster 1) and 8–10 km (cluster 2) distance (Figs. 4.16(a) and (c), 4.16(a), (c), and (d) and 4.21). All three volcanoes are inferred to have part of their magma storage centered between 0–5 km below sea level (b.s.l.) (Fig. 4.21; Poland *et al.*, 2009; Masterlark *et al.*, 2010; Grapenthin *et al.*, 2013). In contrast to Kīlauea, Okmok, and Redoubt, the corresponding spectrum is observed for less than 3%

of all detections at Pavlof (Fig. 4.21), which is not known to have a magma reservoir at comparable depths (Lu and Dzurisin, 2014). It is thus possible that the manifestation of this spectrum relates to processes related to magma storage at a few kilometers depth. Unglert and Jellinek (2015) argued, for example, that tremor spectra during the intrusions at Kīlauea in 2007 and 2011 reflected, in part, the dynamics of bubble clouds in magma flowing through a vertically and laterally complex magma plumbing system. However, assuming the observed spectrum is related to the same source process at all three volcanoes, mechanisms that are insensitive to the geometry of the magmatic plumbing system but relate specifically to magma rheology (e.g., magma wagging, Jellinek and Bercovici, 2011, or frictional faulting of high viscosity magma, Dmitrieva *et al.*, 2013), are unlikely explanations for these detections. Instead, the geometry of the magma storage system may play a key role in explaining the observation of this blue spectrum at three volcanoes with strong differences in their magma rheology and eruptive processes.

The last characteristic spectrum from our combined analysis is cluster 3 (orange) for the proximal stations. This cluster is similar to cluster 1, which may indicate an effect of the overall spectral power of the original spectra. In this case, tremor during the degassing bursts in 2008 at Kīlauea may be explained by the same process as tremor during the intrusions (Figs. 4.16(a)–(c) and 4.18(a)–(c)).

Alternatively, if the cluster 3 at the proximal stations reflects distinct mechanisms compared to cluster 1, it is interesting to note that cluster 3 from the distal stations has a similar character (Fig. 4.21), which may indicate that the same processes are observed on the proximal and the distal stations. For both station subsets, this cluster is associated with tremor at Kīlauea during 2008 (Figs. 4.16(c) and 4.18(c)). The processes accompanying the degassing bursts at Kīlauea are related to the formation of the open vent at Kīlauea’s summit (Fee *et al.*, 2010; Patrick *et al.*, 2011b). In addition, the spectrum associated with cluster 3 is observed at Pavlof, where eruptions are typically accompanied by lava fountaining (Waythomas *et al.*, 2014) and which is considered an open vent system (e.g., Mangan *et al.*, 2009). During the 2013 eruption at Pavlof, the phases of increased tremor detections coincide with phases of lava fountaining and explosive activity (Fig. 4.18(f), Waythomas *et al.*, 2014), whereas a phase in early June 2013 dominated only by explosions does not show accompanying tremor. We thus suggest that the observed cluster 3 spectra may be caused by processes related to the presence and/or formation of an open vent, or the presence of shallow (less than a few 100 meters) magma.

In summary, our results show that different types of tremor with distinct spectral features exist. Systematic occurrence of these tremor classes in relation to a variety of volcano characteristics such as magma storage depth or properties of the volcanic edifice indicate that certain volcanoes may have common tremor mechanisms. The notion that each volcano requires its own, unique processes driving volcanic tremor (e.g., Konstantinou and Schlindwein, 2002) may thus need reassessment.

Implications for Pattern Recognition Approach

The results for the pattern recognition analyses that include data from Kīlauea, which we use as a benchmark, confirm that our approach can successfully detect different spectral shapes and identify

their spatial and temporal characteristics. As discussed in *Unglert et al. (2016)*, the algorithm is not suited to detect signals such as gliding spectral lines, which are observed during the intrusion tremor in 2007 and 2011 at Kīlauea (*Unglert and Jellinek, 2015*). In detecting such gliding signals, automated pattern recognition cannot replace more traditional methods such as visual inspection of spectrograms. However, that we were able to identify additional systematics that had not been recognized through exhaustive manual analysis (Section 4.5.1) shows the value of our approach, which is well suited to determine systematic similarities and differences among many thousands of spectra at any desired level of detail (for example, detailed analysis of one cluster over only few days on Kīlauea, Fig. 4.19, vs. large scale multi-setting analysis of the main three patterns over multiple eruptive periods for the stations at close range, Fig. 4.21).

For the multi-setting approach and for all cases of the station network analyses except Pavlof, we combined a relatively large number of clusters k as determined by $C_{\text{RMS},k}$ into a smaller number of regimes, within which spectra share common spectral peaks. This decision has two implications for our algorithm:

1. As discussed in Section 4.5.6, the normalization suggested by *Unglert et al. (2016)* allows amplitude differences to enter the algorithm, albeit at a reduced magnitude. Such amplitude differences lead to different slopes of spectra with otherwise similar frequency peaks. Whereas it is relatively easy to visually group the corresponding spectra, further work may be desirable to reduce the effects and yield a more automated solution.
2. The ideal number of clusters is determined by $C_{\text{RMS},k}$ (*Unglert et al., 2016*). This criterion mostly tends to favor larger cluster numbers than visual inspection would suggest. These larger numbers may be impractical to analyze further from an interpretational point of view. It is unclear to what extent this overestimation of k is related to the $C_{\text{RMS},k}$ criterion, or the normalization discussed above.

The joint analysis of the close range stations (Section 4.4.3), however, shows that even between values of k close to extreme ends of the full range evaluated here ($k = 3$ vs. $k = 16$ for a range of [2..20]), the resulting spectral patterns are qualitatively similar, and only differ in terms of small details that may or may not be desired for any interpretation. This result suggests that, even though it is useful to have a quantitative criterion to guide the decision on the ideal number of clusters, the final choice of a local maximum in $C_{\text{RMS},k}$ might only affect the level of detail, but not the overall interpretation.

4.6 Conclusions

We develop a single station detection algorithm for volcanic tremor on the basis of amplitudes compared to a defined background signal. We use this algorithm to detect tremor with seismic networks on four different volcanoes over the course of seven eruptive episodes in total. For each of the resulting tremor detections we estimate spectral content and apply a pattern recognition

approach that combines PCA and hierarchical clustering to, for the first time, investigate systematic similarities and differences (i) between tremor recorded on multiple stations at one volcano, and (ii) between tremor recorded at one station each from the different volcanic settings. Our results yield the following conclusions:

1. Our tremor detection algorithm successfully detects tremor as confirmed by published analyses of the seismicity at the different volcanoes.
2. Periods of tremor-like signals (such as shaking induced by lahars, or intense earthquake activity that resembles tremor) are also detected by our algorithm, and may be reliably identified and excluded from further analysis if desired.
3. Our pattern recognition approach applied to the individual station networks reveals that different localized tremor signals can be detected and distinguished within a network, and that signals observed at all stations mostly differ in their strength, which depends predominantly on the distance of the station with respect to the inferred source location.
4. Our pattern recognition approach applied to the combination of stations from the different volcanoes reveals that at the proximal and distal locations we investigate (4 km vs. 8–10 km), spectra show similar shapes, suggesting that path effects do not significantly affect frequency content.
5. We show that at least four different tremor types can be observed across the four volcanic settings, and that there may be relationships to common physical characteristics among some of the volcanoes, such as magma viscosity, the presence of magma reservoirs at certain depths, or the existence of an open vent and related shallow activity.

Further work with datasets from a larger sample of volcanoes of differing types is necessary to reliably and more fully identify systematic similarities and differences among the tremor properties characteristic of volcanic unrest. However, our results indicate that a global comparison of volcanic tremor carried out on the basis of its spectral content is a promising avenue to constrain underlying mechanics that are both generically distinctive of the class of volcanic system or specific to a given volcano.

Chapter 5

Concluding Remarks

The main goal of this thesis was to systematically investigate and rigorously characterize similarities and differences in volcanic tremor properties from a variety of volcanoes. In particular, establishing the extent to which spectral properties of tremor are independent of the specific features of a given volcano, or vary among volcanoes of differing class, is a major step forward to constraining plausible source mechanisms. In carrying out this research, I identified several critical knowledge gaps, which led to the publications in Chapters 2, 3, and 4. I rephrase these challenges from the introduction (Chapter 1):

- Few studies systematically investigate the temporal evolution of tremor properties over multiple eruptions.
- No simple metric exists to characterize tremor properties across multiple volcanic settings.
- No algorithms exist to make pattern recognition in tremor datasets inherently objective and time-efficient.

With the aim of producing a careful global comparison, my work systematically addresses these gaps. I summarize the main outcomes of the three parts of my research (Chapters 2, 3, and 4) and the decisions that lead to each subsequent research avenue in Section 5.1. In Section 5.2, I revisit the hypotheses formed in Chapter 1. Finally, I provide an outlook towards future work in Section 5.3

5.1 Summary of Work and Context for Each Publication

In Chapter 2, I undertook a comparison of volcano seismicity at Kīlauea Volcano over three different eruptive periods. The main goal was to identify an optimal way to characterize tremor in relation to other types of seismicity, and to explore the variety and evolution of seismic signals over more than just one eruption. A further goal was to provide explicit and restrictive constraints on tremor source mechanisms related to similarities and differences among the eruptive periods. For the first time, I identified two phases of seismicity that are characteristic for dike intrusions at Kīlauea. Whereas the first phase is marked by discrete events and appears to be directly associated with the intrusion of magma in the shallow crust, the second phase is comprised of continuous tremor that lasts for several days. In contrast, tremor during a period of degassing bursts from Kīlauea's summit is more similar to the background seismic signal. Previously, low-frequency seismicity at Kīlauea, including tremor as observed during the intrusions, has been attributed to processes related to, for example, the presence of the lava lake at Kīlauea's summit (*Fee et al.*, 2010; *Patrick et al.*, 2011b),

or lava spattering during fissure eruptions (*Patrick et al.*, 2011a). Because the lava lake did not exist at the time of the first of the two intrusions, and because the observed Phase II tremor did not directly coincide in time with the eruptions, my research showed that such mechanisms cannot account for the characteristic intrusion tremor. That I was able to exclude a number of processes as potential candidates for volcanic tremor at Kīlauea confirms that a comparison of tremor properties over multiple eruptive cycles is a promising approach and potentially a critical step to systematically comparing tremor from a range of volcanic settings. In addition, the tremor observed during the period of degassing bursts from the summit compared to the intrusion tremor differs mostly in the shape of their respective spectra, which resulted in the decision to use spectral shape as metric for the nature of volcanic tremor.

Following the results from Chapter 2, the next step was to determine the best algorithm to identify different spectral shapes to be able to repeat the analysis from Kīlauea at other volcanoes. Because the manual approach from Chapter 2 is both subjective and time consuming for analyzing the long time series of seismic data typical for volcanic unrest, my goal in Chapter 3 was to develop an automated and largely unsupervised pattern recognition algorithm. In addition, I decided to generate a synthetic dataset based on the different spectral properties of seismicity observed in Hawai‘i to be able to assess the performance of the final algorithm. Self-Organizing Maps (SOM) (*Kohonen*, 1982, 1990) had been applied in a volcano seismic context before (e.g., *Esposito et al.*, 2008; *Messina and Langer*, 2011; *Carniel et al.*, 2013b), and initial tests on the Kīlauea data yielded promising results. However, it became clear that to properly interpret the different patterns on the SOM topology, either a priori knowledge about the expected patterns, or additional supervised processing is required. As shown in Chapter 3, in the subsequent comparison of SOM against Principal Component Analysis (PCA), a more established and widely used technique, both methods were followed by hierarchical clustering to test whether the known spectral patterns can be retrieved reliably. Surprisingly, PCA combined with our cluster evaluation criterion and the hierarchical clustering method gave consistently better results than the SOM approach on the same dataset. Further testing revealed that clustering of the map topology may not always work in the intended straightforward way. Whereas the question of a solution to this problem will be the topic of future work, I identified that PCA, in combination with clustering, is a successful approach to identify patterns in long time series of spectra. This methodology thus enabled me to rapidly classify tremor spectra from several volcanic settings.

Building on the success of the PCA and clustering approach in Chapter 3, in Chapter 4 I developed an algorithm to detect tremor signals in continuous time series of seismic data from well-studied eruptive periods at Kīlauea, Okmok, Pavlof, and Redoubt, i.e., volcanoes that express a range of edifice type, magma compositions, and eruptive styles. I applied the methodology developed in Chapter 3 to the time series of spectra from tremor detections from all stations at each volcano individually, and to the combined detections from one station from each of the settings. The results revealed that path effects do not significantly alter spectral shapes at distances of a few kilometers between our stations and the inferred signal sources. Furthermore, I identified four distinct classes of tremor signals, that may be related to volcano characteristics such as specifics of the

plumbing system or eruptive style.

In summary, the main contributions of my work to the study and understanding of volcanic tremor are:

- (1) A thorough characterization of seismicity associated with dike intrusions at Kīlauea, including volcanic tremor.
- (2) A detailed discussion of the constraints on the mechanics underlying volcanic tremor provided by assessing observations over several eruptions, shown on the example of Kīlauea.
- (3) A rigorous investigation of the performance of two approaches for pattern recognition with a carefully constructed synthetic dataset of spectra with features that are applicable to many volcanoes.
- (4) A systematic analysis of similarities and differences among tremor from four distinct volcanic settings as an avenue towards a global comparison, including the identification of several tremor types that may be related to volcanic controls.

5.2 Revisiting the Hypotheses

In Chapter 1, I listed four hypotheses as the basis of my work. Below, I reassess each of the hypotheses in light of the findings of Chapters 2, 3, and 4:

- (i) Tremor is an expression of volcanic processes, which are also expressed in other monitoring parameters.

My results in Chapters 2 and 4 indicate explicit relationships between volcanic processes, and seismic and other types of monitoring. At Kīlauea, volcanic tremor coincides in time with strong deformation during dike intrusions (*Poland et al.*, 2008; *Lundgren et al.*, 2013), and may be linked to magma flow through a magma reservoir. At Okmok and Pavlof, tremor is observed almost exclusively during eruptions. Whereas at Okmok there appears to be no direct relationship between the strength of the eruption (measured through ash production from explosive activity, *Larsen et al.*, 2015), periods of lava fountaining at Pavlof (*Waythomas et al.*, 2014) coincide in time with the observation of high tremor detection rates. Furthermore, visual observations of lahars at Pavlof (*Waythomas et al.*, 2008) are accompanied by volcanic tremor. At Redoubt, tremor preceding the 2009 eruption is accompanied by high levels of gas emissions (particularly CO₂, *Werner et al.*, 2012) and increased glacial melting rates, indicating an activation of the shallow volcanic system (*Bleick et al.*, 2013). All of these cases show a relation between the occurrence of tremor and volcanic processes. The types of monitoring parameters that correlate with tremor vary between different settings, which may suggest different types of volcanic tremor, or may be related to certain types of monitoring only available for some settings.

- (ii) Volcanic tremor expresses itself in a variety of temporal, spatial, and spectral properties. These properties are distinct for different types of tremor.

Related to (i), there are instances of tremor recorded only on a few stations within a network at any given time. For example, the temporal evolution of tremor properties at Kīlauea differs between the western and the eastern end of the East Rift Zone (Chapters 2 and 4), where pre-intrusion tremor is only observed in the East. Similarly, tremor signals in one location that are not accompanied by tremor detections at other stations, are sometimes associated with distinct spectra (Chapter 4). The variety of these properties can thus be attributed to different types of volcanic tremor.

- (iii) The complexity of tremor properties, in combination with other monitoring parameters, can be mapped into a parameter space based on the volcanic and tectonic context to identify characteristic “fingerprints”.

In Chapter 4, I show that the spectra associated with different types of tremor observed in the four volcanic settings may be related to volcano characteristics such as magma storage depth or edifice structure. This relationship suggests that it is possible to develop a parameter space that maps tremor spectra in relation to the volcanic context where they are observed, and that the plausible source mechanisms for the tremor fingerprints may be identified. For example, the detection of a common spectrum at two snow-covered strato volcanoes (Pavlof and Redoubt) at different times relative to eruptions may indicate that the process driving this signal is related to the presence of shallow groundwater and/or properties of the edifice. Similarly, a common spectrum observed at Kīlauea, Okmok, and Redoubt (with varying eruptive styles and magma properties) suggests that mechanisms related to the depth of magma storage may explain the common signal, whereas magma rheology is not likely to be a major controlling factor. Taken together, these observations indicate that tremor does not necessarily have to show different properties from one volcano to the next, and that the analysis of common behaviour is promising. I do not have enough datasets to assess the contribution of tectonic controls yet, but my thorough comparison of pattern recognition algorithms in Chapter 3 has provided the necessary tool for this question to be addressed in future studies.

- (iv) If plausible source mechanisms are identified for different tremor fingerprints, volcanic tremor may be reliably used for eruption forecasting.

This last hypothesis remains unaddressed. However, I identified spectral fingerprints for at least four different types of volcanic tremor in Chapter 4, and have provided a preliminary parameter space for the four volcanic settings studied here. To reliably assess whether the relationships I observe in this initial case study are valid globally, a larger sample of different volcanoes is necessary.

5.3 Outlook

The identification of at least four types of volcanic tremor and the relationships to volcanic controls detected in four volcanic settings hold promising implications.

Previous investigations of tremor across multiple volcanic settings have typically summarized the observation of different tremor properties without identifying potential links to the characteristics of the volcanoes from which the observations originate (e.g., *Konstantinou and Schlindwein, 2002*). Few studies have identified relationships between tremor properties and other observables, such as amplitude versus explosivity or cross sectional area of the vent (e.g., *McNutt, 1994; McNutt and Nishimura, 2008*). However, such studies may fail to identify distinct correlations if different types of tremor are not recognized and are instead analyzed together. For example, tremor properties from signals that likely originate from magma reservoirs at a few kilometers depth, such as the tremor observed during dike intrusions at Kīlauea (Chapters 2 and 4), would not be expected to show a relationship to vent size. In contrast, such a relationship may exist for tremor associated with open vents such as the signals observed during lava fountaining at Pavlof and the degassing bursts during formation of the lava lake at Kīlauea (Chapter 4). If these two signals are not identified as different types and subsequently analyzed separately, the reservoir tremor may mask a correlation between open vent tremor properties and vent size, and the underlying mechanisms will not be recognized. Identifying different tremor types, as shown here, is thus crucial to reliably determine the processes driving volcanic tremor.

Konstantinou and Schlindwein (2002) summarize tremor observations from many locations, and, similar to many authors, support the notion that tremor sources vary from one volcano to the next. My results show that this concept is certainly true to some extent: The temporal evolution and spatial characteristics of tremor differ between Kīlauea, Okmok, Pavlof, and Redoubt (Chapter 4). However, whereas some spectral fingerprints are unique to certain settings, others are observed at several volcanoes. My results indicate that there are systematic similarities among tremor signals from different volcanoes. This important outcome, in turn, suggests that several volcanic settings share one or multiple common tremor source mechanisms.

There are two key steps towards confirming the relationships suggested by my results, and towards uniquely determining tremor source processes:

1. Apply my approach to data from a larger sample of volcanic settings to confirm the different types of volcanic tremor and their relationship to volcanic controls.
2. Analyze each tremor type independently with respect to potential control parameters depending on the relationships to the volcanic settings where each type is observed, such as vent size (*McNutt and Nishimura, 2008*) for suspected open vent tremor.

Furthermore, additional work could investigate optimal network design on the basis of the observation of certain types of tremor. Additionally, future studies could identify an appropriate metric to characterize tremor in the time domain (e.g., spasmodic vs. continuous, Chapter 1), which could then be applied to recognize time domain patterns within one spectral tremor class, or to identify

the corresponding time domain expression of each spectral type of tremor. For example, if one spectral class of volcanic tremor shows several behaviours in the time domain, such variations may be the expression of the temporal evolution of the underlying process. Understanding this time dependence of the mechanism, in turn, may be critical to identify impending volcanic eruptions.

Together with the promising results from my work, such studies may thus hold the key to successfully using volcanic tremor for eruption forecasting.

Bibliography

- Aki, K., and R. Koyanagi (1981), Deep volcanic tremor and magma ascent mechanism under Kilauea, Hawaii, *Journal of Geophysical Research*, 86(B8), 7095–7109, doi:10.1029/JB086iB08p07095.
- Aki, K., M. Fehler, and S. Das (1977), Source mechanism of volcanic tremor: fluid-driven crack models and their application to the 1963 Kilauea eruption, *Journal of Volcanology and Geothermal Research*, 2(3), 259–287, doi:10.1016/0377-0273(77)90003-8.
- Almendros, J., R. Abella, M. Mora, and P. Lesage (2012), Time-Dependent Spatial Amplitude Patterns of Harmonic Tremor at Arenal Volcano, Costa Rica: Seismic-Wave Interferences?, *Bulletin of the Seismological Society of America*, 102(6), 2378–2391.
- Alparone, S., D. Andronico, L. Lodato, and T. SgROI (2003), Relationship between tremor and volcanic activity during the Southeast Crater eruption on Mount Etna in early 2000, *Journal of Geophysical Research: Solid Earth (1978–2012)*, 108(B5), doi:10.1029/2002JB001866.
- Baker, S., and F. Amelung (2012), Top-down inflation and deflation at the summit of Kilauea Volcano, Hawai'i observed with InSAR, *Journal of Geophysical Research*, 117(B12406), doi:10.1029/2011JB009123.
- Ballmer, S., C. J. Wolfe, P. G. Okubo, M. M. Haney, and C. H. Thurber (2013), Ambient seismic noise interferometry in Hawai'i reveals long-range observability of volcanic tremor, *Geophysical Journal International*, 194(1), 512–523, doi:10.1093/gji/ggt112.
- Balmforth, N., R. Craster, and A. Rust (2005), Instability in flow through elastic conduits and volcanic tremor, *Journal of Fluid Mechanics*, 527, 353–377, doi:10.1017/S0022112004002800.
- Battaglia, J., and K. Aki (2003), Location of seismic events and eruptive fissures on the Piton de la Fournaise volcano using seismic amplitudes, *Journal of Geophysical Research: Solid Earth (1978–2012)*, 108(B8), doi:10.1029/2002JB002193.
- Battaglia, J., K. Aki, and V. Ferrazzini (2005), Location of tremor sources and estimation of lava output using tremor source amplitude on the Piton de la Fournaise volcano: 1. Location of tremor sources, *Journal of Volcanology and Geothermal Research*, 147(3), 268–290.
- Bauer, K., G. Muñoz, and I. Moeck (2012), Pattern recognition and lithological interpretation of collocated seismic and magnetotelluric models using self-organizing maps, *Geophysical Journal International*, 189(2), 984–998, doi:10.1111/j.1365-246X.2012.05402.x.

- Bean, C., I. Lokmer, and G. O'Brien (2008), Influence of near-surface volcanic structure on long-period seismic signals and on moment tensor inversions: Simulated examples from Mount Etna, *Journal of Geophysical Research: Solid Earth*, 113(B8), doi:10.1029/2007JB005468.
- Bean, C. J., L. De Barros, I. Lokmer, J.-P. Métaixian, G. O'Brien, and S. Murphy (2014), Long-period seismicity in the shallow volcanic edifice formed from slow-rupture earthquakes, *Nature geoscience*, 7(1), 71–75.
- Bell, A., and C. Kilburn (2012), Precursors to dyke-fed eruptions at basaltic volcanoes: insights from patterns of volcano-tectonic seismicity at Kilauea volcano, Hawaii, *Bulletin of Volcanology*, 74, 325–339, doi:10.1007/s00445-011-0519-3.
- Benoit, J., and S. McNutt (1997), New constraints on source processes of volcanic tremor at Arenal Volcano, Costa Rica, using broadband seismic data, *Geophysical Research Letters*, 24(4), 449–452, doi:10.1029/97GL00179.
- Bercovici, D., A. M. Jellinek, C. Michaut, D. C. Roman, and R. Morse (2013), Volcanic tremors and magma wagging: gas flux interactions and forcing mechanism, *Geophysical Journal International*, 195(2), 1001–1022.
- Bertin, D., L. Lara, D. Basualto, Á. Amigo, C. Cardona, L. Franco, F. Gil, and J. Lazo (2015), High effusion rates of the Cordón Caulle 2011–2012 eruption (Southern Andes) and their relation with the quasi-harmonic tremor, *Geophysical Research Letters*, 42(17), 7054–7063, doi:10.1002/2015GL064624.
- Bishop, C. M. (2006), *Pattern Recognition and Machine Learning*, 1, 9901 pp., Springer.
- Bleick, H. A., M. L. Coombs, P. F. Cervelli, K. F. Bull, and R. L. Wessels (2013), Volcano–ice interactions precursory to the 2009 eruption of Redoubt Volcano, Alaska, *Journal of Volcanology and Geothermal Research*, 259, 373–388, doi:10.1016/j.jvolgeores.2012.10.008.
- Borland, D., and R. M. Taylor (2007), Rainbow color map (still) considered harmful, *IEEE computer graphics and applications*, (2), 14–17, doi:10.1109/MCG.2007.46.
- Bouche, E., S. Vergnolle, T. Staudacher, A. Nercessian, J.-C. Delmont, M. Frogneux, F. Cartault, and A. Le Pichon (2010), The role of large bubbles detected from acoustic measurements on the dynamics of Erta' Ale lava lake (Ethiopia), *Earth and Planetary Science Letters*, 295(1), 37–48.
- Brandsdóttir, B., and P. Einarsson (1992), Volcanic tremor and low-frequency earthquakes in Iceland, in *Volcanic seismology*, pp. 212–222, Springer.
- Bromirski, P. D., F. K. Duennebier, and R. A. Stephen (2005), Mid-ocean microseisms, *Geochemistry, Geophysics, Geosystems*, 6(4), doi:10.1029/2004GC000768.
- Brudzinski, M., and R. Allen (2007), Segmentation in episodic tremor and slip all along cascadia, *Geology*, 35(10), 907–910.

- Bull, K. F., and H. Buurman (2012), An overview of the 2009 eruption of redoubt volcano, alaska, *Journal of Volcanology and Geothermal Research*.
- Buurman, H., M. E. West, and G. Thompson (2012), The seismicity of the 2009 redoubt eruption, *Journal of Volcanology and Geothermal Research*.
- Buurman, H., C. J. Nye, M. E. West, and C. Cameron (2014), Regional controls on volcano seismicity along the Aleutian arc, *Geochemistry, Geophysics, Geosystems*, 15(4), 1147–1163, doi:10.1002/2013GC005101.
- Caplan-Auerbach, J., R. Dziak, and T. Lau (2013), Hydroacoustic Recordings of Explosion-Induced Tremor at NW Rota-1 Volcano, Marianas, in *AGU Fall Meeting Abstracts*, vol. 1, p. 2800.
- Carbone, D., M. Poland, M. Patrick, and T. Orr (2013), Continuous gravity measurements reveal a low-density lava lake at Kīlauea Volcano, Hawai‘i, *Earth and Planetary Science Letters*, 376, 178–185, doi:10.1016/j.epsl.2013.06.024.
- Cardoso, S. S., and A. W. Woods (1999), On convection in a volatile-saturated magma, *Earth and Planetary Science Letters*, 168(3), 301–310, doi:10.1016/S0012-821X(99)00057-6.
- Carey, R. J., M. Manga, W. Degruyter, H. Gonnermann, D. Swanson, B. Houghton, T. Orr, and M. Patrick (2013), Convection in a volcanic conduit recorded by bubbles, *Geology*, 41(4), 395–398, doi:10.1130/G33685.1.
- Carniel, R. (1996), Neural networks and dynamical system techniques for volcanic tremor analysis, *Annals of Geophysics*, 39(2), doi:10.4401/ag-3967.
- Carniel, R. (2014), Characterization of volcanic regimes and identification of significant transitions using geophysical data: a review, *Bulletin of Volcanology*, 76(8), 1–22, doi:10.1007/s00445-014-0848-0.
- Carniel, R., S. Casolo, and F. Iacop (1996), Spectral analysis of volcanic tremor associated with the 1993 paroxysmal events at Stromboli, *Geological Society, London, Special Publications*, 110(1), 373–381, doi:10.1144/GSL.SP.1996.110.01.26.
- Carniel, R., A. D. Jolly, and L. Barbui (2013a), Analysis of phreatic events at Ruapehu volcano, New Zealand using a new SOM approach, *Journal of Volcanology and Geothermal Research*, 254, 69–79, doi:10.1016/j.jvolgeores.2012.12.026.
- Carniel, R., L. Barbui, and A. Jolly (2013b), Detecting dynamical regimes by Self-Organizing Map (SOM) analysis: an example from the March 2006 phreatic eruption at Raoul Island, New Zealand Kermadec Arc, *Bollettino di Geofisica Teorica ed Applicata*, 54(1), 39–52, doi:10.4430/bgta0077.

- Castro-Cabrera, P. A., M. Orozco-Alzate, A. Adami, M. Bicego, J. M. Londoño-Bonilla, and G. Castellanos-Domínguez (2014), A Comparison between Time-Frequency and Cepstral Feature Representations for the Classification of Seismic-Volcanic Signals, in *Progress in Pattern Recognition, Image Analysis, Computer Vision, and Applications*, pp. 440–447, Springer, doi: 10.1007/978-3-319-12568-8_54.
- Chardot, L., A. D. Jolly, B. M. Kennedy, N. Fournier, and S. Sherburn (2015), Using volcanic tremor for eruption forecasting at White Island volcano (Whakaari), New Zealand, *Journal of Volcanology and Geothermal Research*, 302, 11–23, doi:10.1016/j.jvolgeores.2015.06.001.
- Cherkassky, V., and F. Mulier (1998), *Learning from data : concepts, theory, and methods*, John Wiley & Sons.
- Chouet, B. (1986), Dynamics of a fluid-driven crack in three dimensions by the finite difference method, *Journal of Geophysical Research*, 91(B14), 13,967–13,992, doi:10.1029/JB091iB14p13967.
- Chouet, B. (1988), Resonance of a fluid-driven crack: radiation properties and implications for the source of long-period events and harmonic tremor, *Journal of Geophysical Research*, 93(B5), 4375–4400, doi:10.1029/JB093iB05p04375.
- Chouet, B. (1992), A seismic model for the source of long-period events and harmonic tremor, in *Volcanic seismology*, pp. 133–156, Springer.
- Chouet, B. (1996a), Long-period volcano seismicity: its source and use in eruption forecasting, *Nature*, 380(6572), 309–316, doi:10.1038/380309a0.
- Chouet, B., and P. Dawson (2011), Shallow conduit system at Kilauea Volcano, Hawaii, revealed by seismic signals associated with degassing bursts, *Journal of Geophysical Research*, 116(B12), doi:10.1029/2011JB008677.
- Chouet, B., and B. Julian (1985), Dynamics of an expanding fluid-filled crack, *Journal of Geophysical Research*, 90(B13), 11,187–11.
- Chouet, B., G. Saccorotti, M. Martini, P. Dawson, G. De Luca, G. Milana, and R. Scarpa (1997), Source and path effects in the wave fields of tremor and explosions at Stromboli Volcano, Italy, *Journal of Geophysical Research*, 102(B7), 15,129–15,150, doi:10.1029/97JB00953.
- Chouet, B. A. (1996b), New methods and future trends in seismological volcano monitoring, in *Monitoring and mitigation of volcano hazards*, pp. 23–97, Springer.
- Chouet, B. A., and R. S. Matoza (2013), A multi-decadal view of seismic methods for detecting precursors of magma movement and eruption, *Journal of Volcanology and Geothermal Research*, 252, 108–175, doi:10.1016/j.jvolgeores.2012.11.013.

- Chouet, B. A., P. B. Dawson, M. R. James, and S. J. Lane (2010), Seismic source mechanism of degassing bursts at Kilauea Volcano, Hawaii: Results from waveform inversion in the 10–50 s band, *Journal of Geophysical Research*, *115*(B09311), doi:10.1029/2009JB006661.
- Cortes, G., M. C. Benitez, L. Garcia, I. Alvarez, and J. M. Ibanez (2015), A Comparative Study of Dimensionality Reduction Algorithms Applied to Volcano-Seismic Signals, *IEEE Journal of Selected Topics in Applied Earth Observations and Remote Sensing*, *PP*(99), doi:10.1109/JSTARS.2015.2479300.
- Crowe, C. T., J. D. Schwarzkopf, M. Sommerfeld, and Y. Tsuji (2011), *Multiphase flows with droplets and particles*, CRC press.
- Curilem, G., J. Vergara, G. Fuentealba, G. Acuña, and M. Chacón (2009), Classification of seismic signals at Villarrica volcano (Chile) using neural networks and genetic algorithms, *Journal of volcanology and geothermal research*, *180*(1), 1–8, doi:10.1016/j.jvolgeores.2008.12.002.
- Curilem, M., J. Vergara, C. San Martin, G. Fuentealba, C. Cardona, F. Huenupan, M. Chacón, M. S. Khan, W. Hussein, and N. B. Yoma (2014), Pattern recognition applied to seismic signals of the Llama volcano (Chile): An analysis of the events' features, *Journal of Volcanology and Geothermal Research*, *282*, 134–147, doi:10.1016/j.jvolgeores.2014.06.004.
- Cusano, P., M. Palo, and M. West (2015), Long-period seismicity at shishaldin volcano (alaska) in 2003–2004: Indications of an upward migration of the source before a minor eruption, *Journal of Volcanology and Geothermal Research*, *291*, 14–24, doi:10.1016/j.jvolgeores.2014.12.008.
- Custodio, S., J. Fonseca, N. d'Oreye, B. Faria, and Z. Bandomo (2003), Tidal modulation of seismic noise and volcanic tremor, *Geophysical Research Letters*, *30*(15), 1816, doi:10.1029/2003GL016991.
- D'Agostino, M., G. Di Grazia, F. Ferrari, H. Langer, A. Messina, D. Reitano, and S. Spampinato (2013), Volcano monitoring and early warning on Mt. Etna, Sicily, based on volcanic tremor: Methods and technical aspects, in *Complex Monitoring of Volcanic Activity*, edited by V. M. Zobin, pp. 53–92, Nova Science Publishers, Inc.
- Davies, D. L., and D. W. Bouldin (1979), A cluster separation measure, *Pattern Analysis and Machine Intelligence, IEEE Transactions on*, (2), 224–227, doi:10.1109/TPAMI.1979.4766909.
- Dawson, P., and B. Chouet (2014), Characterization of very-long-period seismicity accompanying summit activity at Kilauea Volcano, Hawai'i: 2007–2013, *Journal of Volcanology and Geothermal Research*, *278-279*, 59–85, doi:10.1016/j.jvolgeores.2014.04.010.
- Dawson, P., B. Chouet, P. Okubo, A. Villaseñor, and H. Benz (1999), Three-dimensional velocity structure of the Kilauea Caldera, Hawaii, *Geophysical Research Letters*, *26*(18), 2805–2808, doi:10.1029/1999GL005379.

- Dawson, P. B., M. Benítez, B. A. Chouet, D. Wilson, and P. G. Okubo (2010), Monitoring very-long-period seismicity at Kilauea Volcano, Hawaii, *Geophysical Research Letters*, 37(L18306), doi:10.1029/2010GL044418.
- De Angelis, S., and S. R. McNutt (2007), Observations of volcanic tremor during the January–February 2005 eruption of Mt. Veniaminof, Alaska, *Bulletin of Volcanology*, 69(8), 927–940, doi:10.1007/s00445-007-0119-4.
- De Lauro, E., S. De Martino, M. Falanga, M. Palo, and R. Scarpa (2005), Evidence of VLP volcanic tremor in the band [0.2–0.5] Hz at Stromboli volcano, Italy, *Geophysical research letters*, 32(17), L17,303, doi:10.1029/2005GL023466.
- De Martino, S., M. Falanga, R. Scarpa, and C. Godano (2005), Very-Long-Period Volcanic Tremor at Stromboli, Italy, *Bulletin of the Seismological Society of America*, 95(3), 1186–1192, doi:10.1785/0120040063.
- De Matos, M. C., P. L. Osorio, and P. R. Johann (2006), Unsupervised seismic facies analysis using wavelet transform and self-organizing maps, *Geophysics*, 72(1), 9–21, doi:10.1190/1.2392789.
- Del Pezzo, E., S. De Martino, S. Gresta, M. Martini, G. Milana, D. Patane, and C. Sabbarese (1993), Velocity and spectral characteristics of the volcanic tremor at Etna deduced by a small seismometer array, *Journal of volcanology and geothermal research*, 56(4), 369–378.
- Denlinger, R. P., and R. P. Hoblitt (1999), Cyclic eruptive behavior of silicic volcanoes, *Geology*, 27(5), 459–462, doi:10.1130/0091-7613(1999).
- Denlinger, R. P., and S. C. Moran (2014), Volcanic tremor masks its seismogenic source: Results from a study of noneruptive tremor recorded at mount st. helens, washington, *Journal of Geophysical Research: Solid Earth*, 119(3), 2230–2251.
- Di Salvo, R., P. Montalto, G. Nunnari, M. Neri, and G. Puglisi (2013), Multivariate time series clustering on geophysical data recorded at Mt. Etna from 1996 to 2003, *Journal of Volcanology and Geothermal Research*, 251, 65–74, doi:10.1016/j.jvolgeores.2012.02.007.
- Dibble, R. (1972), Seismic and related phenomena at active volcanoes in New Zealand, Hawaii, and Italy, Ph.D. thesis, Victoria University of Wellington.
- Dixon, J. E., E. M. Stolper, and J. R. Holloway (1995), An Experimental Study of Water and Carbon Dioxide Solubilities in Mid-Ocean Ridge Basaltic Liquids. Part I: Calibration and Solubility Models, *Journal of Petrology*, 36(6), 1607–1631.
- Dmitrieva, K., A. Hotovec-Ellis, S. Prejean, and E. Dunham (2013), Frictional-faulting model for harmonic tremor before Redoubt Volcano eruptions, *Nature Geoscience*, 6, 652–656, doi:10.1038/ngeo1879.

- Dziak, R., and C. Fox (2002), Evidence of harmonic tremor from a submarine volcano detected across the Pacific Ocean basin, *Journal of Geophysical Research*, 107(B5), doi:10.1029/2001JB000177.
- Edmonds, M., I. Sides, D. Swanson, C. Werner, R. Martin, T. Mather, R. Herd, R. Jones, M. Mead, G. Sawyer, et al. (2013), Magma storage, transport and degassing during the 2008–10 summit eruption at Kīlauea Volcano, Hawai‘i, *Geochimica et Cosmochimica Acta*, 123, 284–301, doi:10.1016/j.gca.2013.05.038.
- Esposito, A., F. Giudicepietro, L. D’Auria, S. Scarpetta, M. Martini, M. Coltelli, and M. Marinaro (2008), Unsupervised neural analysis of very-long-period events at Stromboli volcano using the self-organizing maps, *Bulletin of the Seismological Society of America*, 98(5), 2449–2459, doi:10.1785/0120070110.
- Eyre, T. S., C. J. Bean, L. De Barros, F. Martini, I. Lokmer, M. M. Mora, J. F. Pacheco, and G. J. Soto (2015), A brittle failure model for long-period seismic events recorded at Turrialba Volcano, Costa Rica, *Journal of Geophysical Research: Solid Earth*, 120(3), 1452–1472, doi:10.1002/2014JB011108.
- Falsaperla, S., H. Langer, and S. Spampinato (1998), Statistical analyses and characteristics of volcanic tremor on Stromboli Volcano (Italy), *Bulletin of volcanology*, 60(2), 75–88, doi:10.1007/s004450050217.
- Farzadi, P., and J. Hesthammer (2007), Diagnosis of the Upper Cretaceous palaeokarst and turbidite systems from the Iranian Persian Gulf using volume-based multiple seismic attribute analysis and pattern recognition, *Petroleum Geoscience*, 13(3), 227–240, doi:10.1144/1354-079306-710.
- Fee, D., M. Garcés, M. Patrick, B. Chouet, P. Dawson, and D. Swanson (2010), Infrasonic harmonic tremor and degassing bursts from Halema’uma’u Crater, Kīlauea Volcano, Hawaii, *Journal of Geophysical Research*, 115(B11316), doi:10.1029/2010JB007642.
- Fee, D., M. Garces, T. Orr, and M. Poland (2011a), Infrasonic sound from the 2007 fissure eruptions of Kīlauea Volcano, Hawai‘i, *Geophysical Research Letters*, 38(L06309), doi:10.1029/2010GL046422.
- Fee, D., S. R. McNutt, T. M. Lopez, K. M. Arnoult, C. A. Szuberla, and J. V. Olson (2011b), Combining local and remote infrasonic recordings from the 2009 redoubt volcano eruption, *Journal of Volcanology and Geothermal Research*.
- Fehler, M. (1983), Observations of volcanic tremor at Mount St. Helens volcano, *Journal of Geophysical Research*, 88(B4), 3476–3484, doi:10.1029/JB088iB04p03476.
- Ferrazzini, V., and K. Aki (1987), Slow waves trapped in a fluid-filled infinite crack: implication for volcanic tremor, *Journal of Geophysical Research*, 92(B9), 9215–9223.

- Ferrazzini, V., K. Aki, and B. Chouet (1991), Characteristics of seismic waves composing hawaiian volcanic tremor and gas-piston events observed by a near-source array, *Journal of Geophysical Research*, 96(B4), 6199–6209.
- Finch, R. (1949), Volcanic tremor (Part I), *Bulletin of the Seismological Society of America*, 39(2), 73–78.
- Garcés, M., M. Hagerty, and S. Schwartz (1998), Magma acoustics and time-varying melt properties at Arenal Volcano, Costa Rica, *Geophysical Research Letters*, 25, 2293–2296, doi:10.1029/98GL01511.
- Garcia, M., R. Ho, J. Rhodes, and E. Wolfe (1989), Petrologic constraints on rift-zone processes, *Bulletin of Volcanology*, 52(2), 81–96.
- Garcia, M., J. Rhodes, E. Wolfe, G. Ulrich, and R. Ho (1992), Petrology of lavas from episodes 2–47 of the Puu Oo eruption of Kilauea Volcano, Hawaii: evaluation of magmatic processes, *Bulletin of Volcanology*, 55(1), 1–16, doi:10.1007/BF00301115.
- Gerlach, T., and E. Graeber (1985), Volatile budget of Kilauea volcano, *Nature*, 313, 273–277, doi:10.1038/313273a0.
- Gerlach, T., K. McGee, T. Elias, A. Sutton, and M. Doukas (2002), Carbon dioxide emission rate of Kīlauea Volcano: Implications for primary magma and the summit reservoir, *Journal of Geophysical Research*, 107(B9), 2189, doi:10.1029/2001JB000407.
- Gerlach, T. M. (1986), Exsolution of H₂O, CO₂, and S during eruptive episodes at Kilauea Volcano, Hawaii, *Journal of Geophysical Research*, 91(B12), 12,177–12,185, doi:10.1029/JB091iB12p12177.
- Ghil, M., M. Allen, M. Dettinger, K. Ide, D. Kondrashov, M. Mann, A. W. Robertson, A. Saunders, Y. Tian, F. Varadi, et al. (2002), Advanced spectral methods for climatic time series, *Reviews of Geophysics*, 40(1), 3–1, doi:10.1029/2000RG000092.
- Global Volcanism Program (2013a), Kilauea (332010), in *Volcanoes of the World*, v. 4.4.3, edited by E. Venzke, Smithsonian Institution, doi:10.5479/si.GVP.VOTW4-2013.
- Global Volcanism Program (2013b), Okmok (311290), in *Volcanoes of the World*, v. 4.4.3, edited by E. Venzke, Smithsonian Institution, doi:10.5479/si.GVP.VOTW4-2013.
- Global Volcanism Program (2013c), Pavlof (312030), in *Volcanoes of the World*, v. 4.4.3, edited by E. Venzke, Smithsonian Institution, doi:10.5479/si.GVP.VOTW4-2013.
- Gómez M, D., and R. Torres C (1997), Unusual low-frequency volcanic seismic events with slowly decaying coda waves observed at Galeras and other volcanoes, *Journal of Volcanology and Geothermal Research*, 77(1-4), 173–193.

- Gong, X., and M. B. Richman (1995), On the application of cluster analysis to growing season precipitation data in North America east of the Rockies, *Journal of Climate*, 8(4), 897–931, doi:10.1175/1520-0442(1995)008\$(\$0897:OTAOCA\$)\$2.0.CO;2.
- Gonnermann, H., and M. Manga (2007), The Fluid Mechanics Inside a Volcano, *Annual Review of Fluid Mechanics*, 39, 321–356, doi:10.1146/annurev.fluid.39.050905.110207.
- Gordeev, E. I., V. A. Saltykov, V. I. Sinitsyn, and V. N. Chebrov (1990), Temporal and spatial characteristics of volcanic tremor wave fields, *Journal of volcanology and geothermal research*, 40(1), 89–101.
- Grapenthin, R., J. T. Freymueller, and A. M. Kaufman (2013), Geodetic observations during the 2009 eruption of Redoubt Volcano, Alaska, *Journal of Volcanology and Geothermal Research*, 259, 115–132, doi:10.1016/j.jvolgeores.2012.04.021.
- Green, D., and J. Neuberg (2006), Waveform classification of volcanic low-frequency earthquake swarms and its implication at soufrière hills volcano, montserrat, *Journal of Volcanology and Geothermal Research*, 153(1-2), 51–63.
- Greenland, L. P. (1987), Hawaiian Eruptive Gases, *US Geological Survey Professional Paper*, 1350(1), 759–770.
- Haney, M. (2010), Location and mechanism of very long period tremor during the 2008 eruption of okmok volcano from interstation arrival times, *Journal of Geophysical Research*, 115(B00B05).
- Hastie, T., R. Tibshirani, J. Friedman, T. Hastie, J. Friedman, and R. Tibshirani (2009), *The elements of statistical learning*, vol. 2, Springer.
- Heliker, C., and T. N. Mattox (2003), The First Two Decades of the Pu‘u O‘o-Kupaianaha eruption: Chronology and Selected Bibliography, *The Pu‘u O‘o-Kupaianaha eruption of Kilauea Volcano, Hawai‘i, the first twenty years: US Geological Survey Professional Paper*, 1676, 121–136.
- Hellweg, M. (2000), Physical models for the source of Lascar’s harmonic tremor, *Journal of Volcanology and Geothermal Research*, 101(1), 183–198, doi:10.1016/S0377-0273(00)00163-3.
- Hodge, K. F., G. Carazzo, and A. M. Jellinek (2012), Experimental constraints on the deformation and breakup of injected magma, *Earth and Planetary Science Letters*, 325, 52–62, doi:10.1016/j.epsl.2012.01.031.
- Hoover, S., K. Cashman, and M. Manga (2001), The yield strength of subliquidus basalts—experimental results, *Journal of Volcanology and Geothermal Research*, 107(1), 1–18, doi:10.1016/S0377-0273(00)00317-6.
- Hotelling, H. (1933), Analysis of a complex of statistical variables into principal components., *Journal of educational psychology*, 24(6), 417, doi:10.1037/h0071325.

- Hotovec, A., S. Prejean, J. Vidale, and J. Gomberg (2013), Strongly gliding harmonic tremor during the 2009 eruption of Redoubt Volcano, *Journal of Volcanology and Geothermal Research*, 259, 89–99, doi:10.1016/j.jvolgeores.2012.01.001.
- Houghton, B., D. Swanson, J. Rausch, R. Carey, S. Fagents, and T. Orr (2013), Pushing the volcanic explosivity index to its limit and beyond: Constraints from exceptionally weak explosive eruptions at Kīlauea in 2008, *Geology*, 41(6), 627–630.
- Hsieh, W. W. (2009), *Machine Learning Methods in the Environmental Sciences: Neural Networks and Kernels*, Cambridge University Press.
- Hurst, A., and S. Sherburn (1993), Volcanic tremor at Ruapehu: characteristics and implications for the resonant source, *New Zealand journal of geology and geophysics*, 36(4), 475–485.
- Ibs-von Seht, M. (2008), Detection and identification of seismic signals recorded at Krakatau volcano (Indonesia) using artificial neural networks, *Journal of Volcanology and Geothermal Research*, 176(4), 448–456, doi:10.1016/j.jvolgeores.2008.04.015.
- Ichihara, M., J. J. Lyons, and A. Yokoo (2013), Switching from seismic to seismo-acoustic harmonic tremor at a transition of eruptive activity during the shinmoe-dake 2011 eruption, *EARTH PLANETS AND SPACE*, 65(6), 633–643.
- Jaggard, T. (1920), Seismometric investigation of the Hawaiian lava column, *Bulletin of the Seismological Society of America*, 10(4), 155–275.
- Jain, A. K. (2010), Data clustering: 50 years beyond K-means, *Pattern Recognition Letters*, 31(8), 651–666, doi:10.1016/j.patrec.2009.09.011.
- Jaupart, C., and S. Vergnolle (1988), Laboratory models of Hawaiian and Strombolian eruptions, *Nature*, 331, 58–60, doi:10.1038/331058a0.
- Jellinek, A., and D. Bercovici (2011), Seismic tremors and magma wagging during explosive volcanism, *Nature*, 470, 522–525, doi:10.1038/nature09828.
- Jellinek, A. M., R. C. Kerr, and R. W. Griffiths (1999), Mixing and compositional stratification produced by natural convection: 1. Experiments and their application to Earth's core and mantle, *Journal of Geophysical Research*, 104(B4), 7183–7201, doi:10.1029/1998JB900116.
- Johnson, D. J. (1992), Dynamics of magma storage in the summit reservoir of Kilauea volcano, Hawaii, *Journal of Geophysical Research*, 97(B2), 1807–1820, doi:10.1029/91JB02839.
- Johnson, D. J. (1995), Molten core model for Hawaiian rift zones, *Journal of Volcanology and Geothermal Research*, 66(1), 27–35, doi:10.1016/0377-0273(94)00066-P.
- Johnson, J., and J. Lees (2000), Plugs and chugs—seismic and acoustic observations of degassing explosions at Karymsky, Russia and Sangay, Ecuador, *Journal of Volcanology and Geothermal Research*, 101(1-2), 67–82, doi:10.1016/S0377-0273(00)00164-5.

- Johnson, J., J. Lees, and E. Gordeev (1998), Degassing explosions at Karymsky volcano, Kamchatka, *Geophysical Research Letters*, 25(21), 3999–4002, doi:10.1029/1998GL900102.
- Jones, J., R. Carniel, and S. Malone (2012), Decomposition, location, and persistence of seismic signals recovered from continuous tremor at Erta’Ale, Ethiopia, *Journal of Volcanology and Geothermal Research*, 213-214, 116–129, doi:10.1016/j.jvolgeores.2011.07.007.
- Julian, B. (1994), Volcanic tremor: Nonlinear excitation by fluid flow, *Journal of Geophysical Research*, 99(B6), 11,859–11,877, doi:10.1029/93JB03129.
- Julian, B. (2000), Period doubling and other nonlinear phenomena in volcanic earthquakes and tremor, *Journal of Volcanology and Geothermal Research*, 101(1-2), 19–26.
- Kaski, S., J. Kangas, and T. Kohonen (1998), Bibliography of self-organizing map (SOM) papers: 1981–1997, *Neural computing surveys*, 1(3&4), 1–176.
- Ketner, D., and J. Power (2013), Characterization of seismic events during the 2009 eruption of Redoubt Volcano, Alaska, *Journal of Volcanology and Geothermal Research*, 259, 45–62, doi:10.1016/j.jvolgeores.2012.10.007.
- Klose, C. D. (2006), Self-organizing maps for geoscientific data analysis: geological interpretation of multidimensional geophysical data, *Computational Geosciences*, 10(3), 265–277, doi:10.1007/s10596-006-9022-x.
- Köhler, A., M. Ohrnberger, and F. Scherbaum (2009), Unsupervised feature selection and general pattern discovery using Self-Organizing Maps for gaining insights into the nature of seismic wavefields, *Computers & Geosciences*, 35(9), 1757–1767, doi:10.1016/j.cageo.2009.02.004.
- Kohonen, T. (1982), Self-Organized Formation of Topologically Correct Feature Maps, *Biological cybernetics*, 43(1), 59–69, doi:10.1007/BF00337288.
- Kohonen, T. (1990), The Self-Organizing Map, *Proceedings of the IEEE*, 78(9), 1464–1480, doi:10.1109/5.58325.
- Konstantinou, K., and C. Lin (2004), Nonlinear time series analysis of volcanic tremor events recorded at Sangay volcano, Ecuador, *Pure and Applied Geophysics*, 161(1), 145–163, doi:10.1007/s00024-003-2432-y.
- Konstantinou, K., and V. Schlindwein (2002), Nature, wavefield properties and source mechanism of volcanic tremor: a review, *Journal of Volcanology and Geothermal Research*, 119(1-4), 161–187, doi:10.1016/S0377-0273(02)00311-6.
- Konstantinou, K., C. Perwita, S. Maryanto, A. Budianto, M. Hendrasto, et al. (2013), Maximal Lyapunov exponent variations of volcanic tremor recorded during explosive and effusive activity at Mt Semeru volcano, Indonesia, *Nonlinear Processes in Geophysics*, 20(6), 1137–1145, doi:10.5194/npg-20-1137-2013.

- Kovesi, P. (2015), Good Colour Maps: How to Design Them, *arXiv preprint arXiv:1509.03700*.
- Koyanagi, R., B. Chouet, and K. Aki (1987), Origin of volcanic tremor in Hawaii; part I, Data from the Hawaiian Volcano Observatory, in *Volcanism in Hawaii*, vol. 2, edited by R. Decker, T. Wright, and P. Stauffer, pp. 1221 – 1257, US Geological Survey Professional Paper 1350.
- Kumagai, H., M. Nakano, T. Maeda, H. Yepes, P. Palacios, M. Ruiz, S. Arrais, M. Vaca, I. Molina, and T. Yamashima (2010), Broadband seismic monitoring of active volcanoes using deterministic and stochastic approaches, *Journal of Geophysical Research*, 115(B8), B08,303, doi:10.1029/2009JB006889.
- Kuncheva, L. I., and D. P. Vetrov (2006), Evaluation of stability of k-means cluster ensembles with respect to random initialization, *Pattern Analysis and Machine Intelligence, IEEE Transactions on*, 28(11), 1798–1808, doi:10.1109/TPAMI.2006.226.
- Langer, H., and S. Falsaperla (1996), Long-term observation of volcanic tremor on Stromboli volcano (Italy): a synopsis, *pure and applied geophysics*, 147(1), 57–82, doi:10.1007/BF00876436.
- Langer, H., and S. Falsaperla (2003), Seismic monitoring at Stromboli volcano (Italy): a case study for data reduction and parameter extraction, *Journal of volcanology and geothermal research*, 128(1), 233–245, doi:10.1016/S0377-0273(03)00257-9.
- Langer, H., S. Falsaperla, M. Masotti, R. Campanini, S. Spampinato, and A. Messina (2009), Synopsis of supervised and unsupervised pattern classification techniques applied to volcanic tremor data at Mt Etna, Italy, *Geophysical Journal International*, 178(2), 1132–1144, doi:10.1111/j.1365-246X.2009.04179.x.
- Langer, H., S. Falsaperla, A. Messina, S. Spampinato, and B. Behncke (2011), Detecting imminent eruptive activity at Mt Etna, Italy, in 2007-2008 through pattern classification of volcanic tremor data, *Journal of Volcanology and Geothermal Research*, doi:10.1016/j.jvolgeores.2010.11.019.
- Larsen, J., C. Neal, P. Webley, J. Freymueller, M. Haney, S. McNutt, D. Schneider, S. Prejean, J. Schaefer, and R. Wessels (2009), Eruption of alaska volcano breaks historic pattern, *EOS Transactions*, 90, 173–174.
- Larsen, J., C. Neal, J. Schaefer, A. Kaufman, and Z. Lu (2015), The 2008 phreatomagmatic eruption of Okmok Volcano, Aleutian Islands, Alaska: Chronology, deposits, and landform changes, *Tech. rep.*, Alaska Division of Geological & Geophysical Surveys.
- Larsen, J. F., M. G. Śliwiński, C. Nye, C. Cameron, and J. R. Schaefer (2013), The 2008 eruption of okmok volcano, alaska: Petrological and geochemical constraints on the subsurface magma plumbing system, *Journal of Volcanology and Geothermal Research*, 264, 85–106.
- Latter, J. (1981), Volcanic earthquakes, and their relationship to eruptions at Ruapehu and Ngauruhoe volcanoes, *Journal of volcanology and geothermal research*, 9(4), 293–309.

- Lees, J., and M. Ruiz (2008), Non-linear explosion tremor at sangay, volcano, ecuador, *Journal of Volcanology and Geothermal Research*, 176(1), 170–178.
- Lees, J., E. Gordeev, and M. Ripepe (2004), Explosions and periodic tremor at karymsky volcano, kamchatka, russia, *Geophysical Journal International*, 158(3), 1151–1167.
- Leet, R. C. (1988), Saturated and subcooled hydrothermal boiling in groundwater flow channels as a source of harmonic tremor, *Journal of Geophysical Research: Solid Earth*, 93(B5), 4835–4849, doi:10.1029/JB093iB05p04835.
- Leighton, T. (1994), *The acoustic bubble*, Academic press.
- Leonardi, S., S. Gresta, and F. Mulargia (2000), Cross-correlation between volcanic tremor and SO_2 flux data from mount Etna volcano, 1987–1992, *Physics and Chemistry of the Earth, Part A: Solid Earth and Geodesy*, 25(9), 737–740.
- Lesage, P., M. M. Mora, G. E. Alvarado, J. Pacheco, and J.-P. Métaixian (2006), Complex behavior and source model of the tremor at Arenal volcano, Costa Rica, *Journal of Volcanology and Geothermal Research*, 157(1), 49–59, doi:10.1016/j.jvolgeores.2006.03.047.
- Liu, Y., R. H. Weisberg, and C. N. Mooers (2006), Performance evaluation of the self-organizing map for feature extraction, *Journal of Geophysical Research: Oceans (1978–2012)*, 111(C5), doi:10.1029/2005JC003117.
- Lu, Z., and D. Dzurisin (2014), *InSAR imaging of Aleutian volcanoes: monitoring a volcanic arc from space*, Springer Praxis Books - Geophysical Sciences, Springer Science & Business Media.
- Lundgren, P., M. Poland, A. Miklius, T. Orr, S.-H. Yun, E. Fielding, Z. Liu, A. Tanaka, W. Szeliga, S. Hensley, and S. Owen (2013), Evolution of dike opening during the March 2011 Kamoamoia fissure eruption, Kīlauea Volcano, Hawai‘i, *Journal of Geophysical Research*, 118, 897–914, doi:10.1002/jgrb.50108.
- Lyons, J., M. Ichihara, A. Kurokawa, and J. Lees (2013), Switching between seismic and seismo-acoustic harmonic tremor simulated in the laboratory: Insights into the role of open degassing channels and magma viscosity, *Journal of Geophysical Research*, 118, 277–289, doi:10.1002/jgrb.50067.
- Mangan, M., T. Miller, C. Waythomas, F. Trusdell, A. Calvert, and P. Layer (2009), Diverse lavas from closely spaced volcanoes drawing from a common parent: Emmons lake volcanic center, eastern aleutian arc, *Earth and Planetary Science Letters*, 287(3), 363–372.
- Marroquín, I. D., J.-J. Brault, and B. S. Hart (2008), A visual data-mining methodology for seismic facies analysis: Part 1—Testing and comparison with other unsupervised clustering methods, *Geophysics*, 74(1), P1–P11, doi:10.1190/1.3046455.

- Maryanto, S., M. Iguchi, and T. Tameguri (2008), Constraints on the source mechanism of harmonic tremors based on seismological, ground deformation, and visual observations at Sakurajima volcano, Japan, *Journal of Volcanology and Geothermal Research*, 170(3), 198–217, doi:10.1016/j.jvolgeores.2007.10.004.
- Masterlark, T., M. Haney, H. Dickinson, T. Fournier, and C. Searcy (2010), Rheological and structural controls on the deformation of Okmok volcano, Alaska: FEMs, InSAR, and ambient noise tomography, *Journal of Geophysical Research*, 115(B02409), doi:10.1029/2009JB006324.
- Matoza, R., D. Fee, and M. Garcés (2010), Infrasonic tremor wavefield of the Pu‘u ‘Ō‘ō crater complex and lava tube system, Hawaii, in April 2007, *Journal of Geophysical Research*, 115(B12312), doi:10.1029/2009JB007192.
- McGimsey, R., C. Neal, J. Dixon, S. Ushakov, and A. Rybin (2011), Volcanic activity in Alaska, Kamchatka, and the Kurile Islands: summary of events and response of the Alaska Volcano Observatory, *US Geological Survey Scientific Investigations Report*, 5242, 94.
- McGreger, A. D., and J. M. Lees (2004), Vent discrimination at Stromboli volcano, Italy, *Journal of Volcanology and Geothermal Research*, 137(1), 169–185, doi:10.1016/j.jvolgeores.2004.05.007.
- McNamara, D. E., and R. P. Buland (2004), Ambient noise levels in the continental United States, *Bulletin of the seismological society of America*, 94(4), 1517–1527, doi:10.1785/012003001.
- McNutt, S. (1987a), Eruption characteristics and cycles at Pavlof volcano, Alaska, and their relation to regional earthquake activity, *Journal of Volcanology and Geothermal Research*, 31(3-4), 239–267.
- McNutt, S. (1987b), Volcanic tremor at Pavlof Volcano, Alaska, October 1973–April 1986, *Pure and Applied Geophysics*, 125(6), 1051–1077.
- McNutt, S. (1992), Volcanic tremor, *Encyclopedia of Earth System Science*, 4, 417–425.
- McNutt, S. (1994), Volcanic tremor amplitude correlated with eruption explosivity and its potential use in determining ash hazards to aviation, in *Volcanic Ash and Aviation Safety: Proceedings of the First International Symposium on Volcanic Ash and Aviation Safety*, pp. 377–385.
- McNutt, S. (1996), Seismic Monitoring and Eruption Forecasting of Volcanoes: A Review of the State-of-the-Art and Case Histories, in *Monitoring and Mitigation of Volcano Hazards*, edited by R. Scarpa and R. Tilling, pp. 99–146, Springer, New York, doi:10.1007/978-3-642-80087-0_3.
- McNutt, S. (2004), Volcanic tremor and its use in estimating eruption parameters, in *Proceedings of the 2nd International Conference on Volcanic Ash and Aviation Safety*, pp. 49–50, U.S. Dept. of Commerce, NOAA, section 2.
- McNutt, S. (2005), Volcanic Seismology, *Annual Review of Earth and Planetary Sciences*, 33, 461–491, doi:10.1146/annurev.earth.33.092203.122459.

- McNutt, S., and T. Nishimura (2008), Volcanic tremor during eruptions: Temporal characteristics, scaling and constraints on conduit size and processes, *Journal of Volcanology and Geothermal Research*, 178(1), 10–18, doi:10.1016/j.jvolgeores.2008.03.010.
- Messina, A., and H. Langer (2011), Pattern recognition of volcanic tremor data on Mt. Etna (Italy) with KAnalysis—A software program for unsupervised classification, *Computers & Geosciences*, 37(7), 953–961, doi:10.1016/j.cageo.2011.03.015.
- Métaxian, J., P. Lesage, and J. Dorel (1997), Permanent tremor of masaya volcano, nicaragua: Wave field analysis and source location, *Journal of Geophysical Research*, 102(B10), 22,529–22.
- Miller, A., R. Stewart, R. White, R. Lockett, B. Baptie, W. Aspinall, J. Latchman, L. Lynch, and B. Voight (1998), Seismicity associated with dome growth and collapse at the soufriere hills volcano, montserrat, *Geophysical Research Letters*, 25(18), 3401–3404.
- Minakami, T. (1960), Fundamental research for predicting volcanic eruptions (part 1): Earthquakes and crustal deformations originating from volcanic activities, *Bulletin of the Earthquake Research Institute*, 38(4), 497–544.
- Moitra, P., and H. Gonnermann (submitted), *Geochemistry Geophysics Geosystems-G3*.
- Montgomery-Brown, E., D. Sinnett, K. Larson, M. Poland, P. Segall, and A. Miklius (2011), Spatiotemporal evolution of dike opening and décollement slip at Kīlauea Volcano, Hawai‘i, *Journal of Geophysical Research*, 116(B03401), doi:10.1029/2010JB007762.
- Mori, J., H. Patia, C. McKee, I. Itikarai, P. Lowenstein, P. De Saint Ours, and B. Talai (1989), Seismicity associated with eruptive activity at Langila volcano, Papua New Guinea, *Journal of Volcanology and Geothermal Research*, 38(3), 243–255, doi:10.1016/0377-0273(89)90040-1.
- Mullen, K. T. (1985), The contrast sensitivity of human colour vision to red-green and blue-yellow chromatic gratings., *The Journal of Physiology*, 359, 381.
- Muñoz-Salinas, E., V. Manea, D. Palacios, and M. Castillo-Rodriguez (2007), Estimation of lahar flow velocity on Popocatepetl volcano (Mexico), *Geomorphology*, 92(1), 91–99, doi:10.1016/j.geomorph.2007.02.011.
- Murray, T., and E. Endo (1989), A real-time seismic amplitude measurement system (RSAM), *Tech. Rep. 89-684*, U.S. Geological Survey.
- Murtagh, F., and M. Hernández-Pajares (1995), The Kohonen Self-Organizing Map Method: An Assessment, *Journal of Classification*, 12(2), 165–190.
- Nadeau, P., J. Palma, and G. Waite (2011), Linking volcanic tremor, degassing, and eruption dynamics via so2 imaging, *Geophysical Research Letters*, 38(1), L01,304.

- Neuberg, J. (2000), Characteristics and causes of shallow seismicity in andesite volcanoes, *Philosophical Transactions of the Royal Society of London. Series A: Mathematical, Physical and Engineering Sciences*, 358(1770), 1533, doi:10.1098/rsta.2000.0602.
- Neuberg, J., B. Baptie, R. Luckett, and R. Stewart (1998), Results from the broadband seismic network on Montserrat, *Geophysical Research Letters*, 25(19), 3661–3664, doi:10.1029/98GL01441.
- Neuberg, J., R. Luckett, B. Baptie, and K. Olsen (2000), Models of tremor and low-frequency earthquake swarms on Montserrat, *Journal of Volcanology and Geothermal Research*, 101(1-2), 83–104, doi:10.1016/S0377-0273(00)00169-4.
- Newman, S., and J. B. Lowenstern (2002), VolatileCalc: a silicate melt–H₂O – CO₂ solution model written in Visual Basic for excel, *Computers & Geosciences*, 28(5), 597–604, doi:10.1016/S0098-3004(01)00081-4.
- Ogiso, M., and K. Yomogida (2012), Migration of tremor locations before the 2008 eruption of meakandake volcano, hokkaido, japan, *Journal of Volcanology and Geothermal Research*, 217, 8–20.
- Ogiso, M., H. Matsubayashi, and T. Yamamoto (2015), Descent of tremor source locations before the 2014 phreatic eruption of Ontake volcano, Japan, *Earth, Planets and Space*, 67(1), 1–12.
- Oja, M., S. Kaski, and T. Kohonen (2002), Bibliography of self-organizing map (SOM) papers: 1998-2001 addendum, *Neural computing surveys*, 3, 1–156, doi:10.1093/ml/71.2.257.
- Okubo, P. G., H. M. Benz, and B. A. Chouet (1997), Imaging the crustal magma sources beneath Mauna Loa and Kilauea volcanoes, Hawaii, *Geology*, 25(10), 867–870, doi:10.1130/0091-7613.
- Omer, G. C. (1950), Volcanic tremor (part two: The theory of volcanic tremor), *Bulletin of the Seismological Society of America*, 40(3), 175–194.
- Orozco-Alzate, M., C. Acosta-Muñoz, and J. Makario Londono-Bonilla (2012), *The automated identification of volcanic earthquakes: concepts, applications and challenges*, chap. Earthquake Research and Analysis—Seismology, Seismotectonic and Earthquake Geology, ISBN: 978-953-307-991-2, InTech, Croatia.
- Orr, T., M. Patrick, K. Wooten, D. Swanson, T. Elias, A. Sutton, D. Wilson, and M. Poland (2008), Explosions, tephra, and lava: a chronology of the 2008 summit eruption of Kīlauea Volcano, Hawai‘i., *Eos Transactions AGU*, 89(53), fall Meeting Supplement, V11B-2018.
- Orr, T., W. Thelen, M. Patrick, D. Swanson, and D. Wilson (2013), Explosive eruptions triggered by rockfalls at Kīlauea volcano, Hawai‘i, *Geology*, 41(2), 207–210, doi:10.1130/G33564.1.
- Orr, T., M. Poland, M. Patrick, W. Thelen, J. Sutton, T. Elias, C. Thornber, C. Parcheta, and K. Wooten (2015), Kīlauea’s 5–9 March 2011 Kamoamoā fissure eruption and its relation to

- 30+ years of activity from Puu 'Ō'ō, in *Hawaiian Volcanism, from Source to Surface*, vol. 208, edited by R. Carey et al., AGU Monograph.
- Pakhira, M. K., S. Bandyopadhyay, and U. Maulik (2004), Validity index for crisp and fuzzy clusters, *Pattern recognition*, 37(3), 487–501, doi:10.1016/j.patcog.2003.06.005.
- Palma, J. L., E. S. Calder, D. Basualto, S. Blake, and D. A. Rothery (2008), Correlations between so₂ flux, seismicity, and outgassing activity at the open vent of villarrica volcano, chile, *Journal of Geophysical Research: Solid Earth (1978–2012)*, 113(B10).
- Parfitt, E. A., and L. Wilson (1994), The 1983–86 Pu'u 'O'o eruption of Kīlauea Volcano, Hawaii: a study of dike geometry and eruption mechanisms for a long-lived eruption, *Journal of Volcanology and Geothermal Research*, 59(3), 179–205, doi:10.1016/0377-0273(94)90090-6.
- Patanè, D., A. Aiuppa, M. Aloisi, B. Behncke, A. Cannata, M. Coltelli, G. Di Grazia, S. Gambino, S. Gurrieri, M. Mattia, and G. Salerno (2013), Insights into magma and fluid transfer at Mount Etna by a multiparametric approach: A model of the events leading to the 2011 eruptive cycle, *Journal of Geophysical Research Solid Earth*, 118, 3519–3539, doi:10.1002/jgrb.50248.
- Patrick, M., T. Orr, D. Wilson, D. Dow, and R. Freeman (2011a), Cyclic spattering, seismic tremor, and surface fluctuation within a perched lava channel, Kīlauea Volcano, *Bulletin of Volcanology*, 73, 639–653, doi:10.1007/s00445-010-0431-2.
- Patrick, M., D. Wilson, D. Fee, T. Orr, and D. Swanson (2011b), Shallow degassing events as a trigger for very-long-period seismicity at Kīlauea Volcano, Hawai 'i, *Bulletin of Volcanology*, 73, 1179–1186, doi:10.1007/s00445-011-0475-y.
- Poland, M., A. Miklius, T. Orr, J. Sutton, C. Thornber, and C. Wilson (2008), New episodes of volcanism at Kilauea Volcano, Hawaii, *Eos Transactions American Geophysical Union*, 89(5), 37–38, doi:10.1029/2008EO050001.
- Poland, M., A. Sutton, and T. Gerlach (2009), Magma degassing triggered by static decompression at Kīlauea Volcano, Hawai 'i, *Geophysical Research Letters*, 36, L16,306, doi:10.1029/2009GL039214.
- Poland, M., A. Miklius, A. Sutton, and C. Thornber (2012), A mantle-driven surge in magma supply to Kīlauea Volcano during 2003–2007, *Nature Geoscience*, 5(4), 295–300, doi:10.1038/NCEO1426.
- Powell, T., and J. Neuberg (2003), Time dependent features in tremor spectra, *Journal of Volcanology and Geothermal Research*, 128(1-3), 177–185, doi:10.1016/S0377-0273(03)00253-1.
- Power, J., S. Stihler, B. Chouet, M. Haney, and D. Ketner (2013), Seismic observations of Redoubt Volcano, Alaska—1989–2010 and a conceptual model of the Redoubt magmatic system, *Journal of Volcanology and Geothermal Research*, 259, 31–44, doi:10.1016/j.jvolgeores.2012.09.014.

- Radic, V., and G. K. Clarke (2011), Evaluation of IPCC Models' Performance in Simulating Late-Twentieth-Century Climatologies and Weather Patterns over North America, *Journal of Climate*, 24(20), 5257–5274, doi:10.1175/JCLI-D-11-00011.1.
- Reeder, J., and J. Lahr (1987), *Seismological aspects of the 1976 eruptions of Augustine volcano, Alaska*, USGPO.
- Reusch, D. B., R. B. Alley, and B. C. Hewitson (2005), Relative performance of self-organizing maps and principal component analysis in pattern extraction from synthetic climatological data, *Polar Geography*, 29(3), 188–212, doi:10.1080/789610199.
- Richardson, J. P., and G. P. Waite (2013), Waveform inversion of shallow repetitive long period events at Villarrica Volcano, Chile, *Journal of Geophysical Research Solid Earth*, 118, 4922–4936, doi:10.1002/jgrb.50354.
- Ripepe, M., and E. Gordeev (1999), Gas bubble dynamics model for shallow volcanic tremor at Stromboli, *Journal of Geophysical Research*, 104(B5), 10,639–10,654, doi:10.1029/98JB02734.
- Riuscetti, M., R. Schick, and D. Seidl (1977), Spectral parameters of volcanic tremors at Etna, *Journal of Volcanology and Geothermal Research*, 2(3), 289–298.
- Rogowitz, B. E., and L. A. Treinish (1998), Data visualization: the end of the rainbow, *Spectrum, IEEE*, 35(12), 52–59, doi:10.1109/6.736450.
- Ruiz, M., J. Lees, and J. Johnson (2006), Source constraints of tungurahua volcano explosion events, *Bulletin of volcanology*, 68(5), 480–490.
- Rust, A., N. Balmforth, and S. Mandre (2008), The feasibility of generating low-frequency volcano seismicity by flow through a deformable channel, *Geological Society, London, Special Publications*, 307(1), 45–56, doi:10.1144/SP307.4.
- Ryan, M. P., R. Y. Koyanagi, and R. S. Fiske (1981), Modeling the three-dimensional structure of macroscopic magma transport systems: Application to Kilauea Volcano, Hawaii, *Journal of Geophysical Research*, 86(B8), 7111–7129, doi:10.1029/JB086iB08p07111.
- Schaefer, J. (2011), The 2009 eruption of redoubt volcano, alaska, *Report of Investigations*, p. 5.
- Schindwein, V., J. Wassermann, and F. Scherbaum (1995), Spectral analysis of harmonic tremor signals at Mt. Semeru volcano, Indonesia, *Geophysical research letters*, 22(13), 1685–1688.
- Shaw, H., and B. Chouet (1988), Applications of nonlinear dynamics to the history of seismic tremor at Kilauea Volcano, Hawaii, *Tech. Rep. 88-539*, U.S. Geological Survey.
- Shaw, H. R. R. (1969), Rheology of basalt in the melting range, *Journal of Petrology*, 10(3), 510–535, doi:10.1093/petrology/10.3.510.

- Sherburn, S., B. Scott, Y. Nishi, and M. Sugihara (1998), Seismicity at white island volcano, new zealand: a revised classification and inferences about source mechanism, *Journal of volcanology and geothermal research*, 83(3-4), 287–312.
- Sherburn, S., C. Bryan, A. Hurst, J. Latter, and B. Scott (1999), Seismicity of Ruapehu volcano, New Zealand, 1971–1996: a review, *Journal of volcanology and geothermal research*, 88(4), 255–278, doi:10.1016/S0377-0273(99)00014-1.
- Smithsonian Institution (2010), Kilauea, *Bulletin of the Global Volcanism Network*, 35(1).
- Sparks, R., J. Biggs, and J. Neuberg (2012), Monitoring Volcanoes, *Science*, 335, 1310–1311, doi:10.1126/science.1219485.
- Stone, M. (2012), In color perception, size matters, *IEEE Computer Graphics and Applications*, (2), 8–13, doi:10.1109/MCG.2012.37.
- Takeuchi, S. (2015), A melt viscosity scale for preeruptive magmas, *Bulletin of Volcanology*, 77(5), 1–11, doi:10.1007/s00445-015-0929-8.
- Thomas, M., and J. Neuberg (2012), What makes a volcano tick - A first explanation of deep multiple seismic sources in ascending magma, *Geology*, doi:10.1130/G32868.1.
- Thompson, G., S. McNutt, and G. Tytgat (2002), Three distinct regimes of volcanic tremor associated with the eruption of shishaldin volcano, alaska 1999, *Bulletin of Volcanology*, 64(8), 535–547.
- Tibshirani, R., G. Walther, and T. Hastie (2001), Estimating the number of clusters in a data set via the gap statistic, *Journal of the Royal Statistical Society: Series B (Statistical Methodology)*, 63(2), 411–423, doi:10.1111/1467-9868.00293.
- Tilling, R. I., and J. J. Dvorak (1993), Anatomy of a basaltic volcano, *Nature*, 363, 125–133, doi:10.1038/363125a0.
- Toramaru, A. (1989), Vesiculation process and bubble size distributions in ascending magmas with constant velocities, *Journal of Geophysical Research: Solid Earth (1978–2012)*, 94(B12), 17,523–17,542.
- Unglert, K., and A. Jellinek (2015), Volcanic Tremor and Frequency Gliding during Dike Intrusions at Kilauea – A Tale of Three Eruptions, *Journal of Geophysical Research: Solid Earth*, 120(2), 1142–1158, doi:10.1002/2014JB011596.
- Unglert, K., V. Radic, and A. Jellinek (2016), Principal Component Analysis vs. Self-Organizing Maps Combined with Hierarchical Clustering for Pattern Recognition in Volcano Seismic Spectra, *Journal of Volcanology and Geothermal Research*, 320, 58–74, doi:10.1016/j.jvolgeores.2016.04.014.

- Vergnolle, S., and C. Jaupart (1990), Dynamics of degassing at Kilauea volcano, Hawaii, *Journal of Geophysical Research*, 95(B3), 2793–2809, doi:10.1029/JB095iB03p02793.
- Vesanto, J., J. Himberg, E. Alhoniemi, and J. Parhankangas (1999), Self-organizing map in Matlab: the SOM Toolbox, in *Proceedings of the MATLAB DSP Conference*, vol. 99, pp. 16–17.
- Vesanto, J., J. Himberg, E. Alhoniemi, and J. Parhankangas (2000), SOM toolbox for Matlab 5, *Tech. rep.*, SOM Toolbox Team, Helsinki University of Technology Report A57.
- Vila, J., J. Marti, R. Ortiz, A. Garcia, and A. M. Correig (1992), Volcanic tremors at Deception Island (South Shetland Islands, Antarctica), *Journal of volcanology and geothermal research*, 53(1), 89–102.
- Vila, J., R. Macià, D. Kumar, R. Ortiz, H. Moreno, and A. M. Correig (2006), Analysis of the unrest of active volcanoes using variations of the base level noise seismic spectrum, *Journal of volcanology and geothermal research*, 153(1), 11–20, doi:10.1016/j.jvolgeores.2005.10.011.
- Voight, B., R. Hoblitt, A. Clarke, A. Lockhart, A. Miller, L. Lynch, and J. McMahon (1998), Remarkable cyclic ground deformation monitored in real-time on Montserrat, and its use in eruption forecasting, *Geophysical Research Letters*, 25(18), 3405–3408.
- Ward Jr, J. H. (1963), Hierarchical grouping to optimize an objective function, *Journal of the American statistical association*, 58(301), 236–244, doi:10.1080/01621459.1963.10500845.
- Waythomas, C. F., S. G. Prejean, and S. R. McNutt (2008), Alaska’s Pavlof Volcano Ends 11-Year Repose, *Eos, Transactions American Geophysical Union*, 89(23), 209–211, doi:10.1029/2008EO230002.
- Waythomas, C. F., M. M. Haney, D. Fee, D. J. Schneider, and A. Wech (2014), The 2013 eruption of Pavlof Volcano, Alaska: a spatter eruption at an ice-and snow-clad volcano, *Bulletin of Volcanology*, 76(10), 1–12, doi:10.1007/s00445-014-0862-2.
- Wech, A. G., and K. C. Creager (2008), Automated detection and location of Cascadia tremor, *Geophysical Research Letters*, 35(20).
- Werner, C., W. C. Evans, P. J. Kelly, R. McGimsey, M. Pfeffer, M. Doukas, and C. Neal (2012), Deep magmatic degassing versus scrubbing: Elevated CO₂ emissions and C/S in the lead-up to the 2009 eruption of Redoubt Volcano, Alaska, *Geochemistry, Geophysics, Geosystems*, 13(3), doi:10.1029/2011GC003794.
- Wildemuth, C., and M. Williams (1984), Viscosity of suspensions modeled with a shear-dependent maximum packing fraction, *Rheologica acta*, 23(6), 627–635, doi:10.1007/BF01438803.
- Wilson, D., T. Elias, T. Orr, M. Patrick, J. Sutton, and D. Swanson (2008), Small explosion from new vent at Kilauea’s summit, *Eos, Transactions American Geophysical Union*, 89(22), 203, doi:10.1029/2008EO220003.

- Woods, A., and S. Cardoso (1997), Triggering basaltic volcanic eruptions by bubble-melt separation, *Nature*, 385, 518–520, doi:10.1038/385518a0.
- Wu, S., and T. W. Chow (2004), Clustering of the self-organizing map using a clustering validity index based on inter-cluster and intra-cluster density, *Pattern Recognition*, 37(2), 175–188, doi: 10.1016/S0031-3203(03)00237-1.
- Yamamoto, M., H. Kawakatsu, K. Yomogida, and J. Koyama (2002), Long-period (12 sec) volcanic tremor observed at Usu 2000 eruption: Seismological detection of a deep magma plumbing system, *Geophysical research letters*, 29(9), 43–1.

Appendix A

Use of Color Maps and Human Perception

A.1 Challenges with Color Maps

The use of color in figures from geoscience publications has increased significantly with the advent of the digital age (Fig. A.1). In Figure A.1 I choose an arbitrary but systematic sampling system to determine the number of color figures in geoscientific publications and its temporal evolution. I count color figures versus black-and-white figures in the first 5 articles listed online in the Journal of Geophysical Research – Solid Earth, for the April issues of 1981, 1991, 2001, and 2011, and the October issues of 1984, 1994, 2004, and 2014. To avoid bias related to a lack of color figures because of printing costs, only html versions are counted from 2004 onwards, the first year in my sample for which html was available (journals often allow color figures in the online versions of articles at no additional cost). Subfigures are not counted separately, and any supplementary material is ignored. Any figure that has at least one color other than shades between black and white is counted towards color figures. Bias might come from the small sample size and from only considering one journal. Additionally, certain topic areas might be grouped together in the table of contents of an issue, and be more likely to include either mostly color figures, or mostly black-and-white figures on the basis of the respective research field. Yet, these biases are unlikely to remove or reverse the trend of increasing total numbers (left) and percentage (right) of color figures (Fig. A.1).

When multiple datasets or variables are shown in one figure, the use of color allows to effectively add a dimension to our perception. For example, if a set of points are defined by their x - and y -coordinates, and a measurement m is taken at each point, the value of this measurement can either be displayed in a 3D perspective view as a third axis z , or it can be visualized with color in a plane (2D) graph. For higher dimensional datasets, for example, point coordinates x , y , z plus measurement m , the point coordinates alone require a 3D graph, and the color can be used to display the value of m at each point.

In studies of volcanic tremor, one of the most common applications of color maps is to display spectrograms, i.e., the temporal evolution of frequency content of seismic data (e.g., *Benoit and McNutt, 1997; Thompson et al., 2002; Custodio et al., 2003; Lesage et al., 2006; Almendros et al., 2012; Cusano et al., 2015*, and many more). The x - and y -coordinates are time and frequency, respectively, and color is used to visualize spectral power or amplitude at each point in time for each frequency. Unfortunately, the choice of color map has a strong influence on which features of the data are emphasized. Furthermore, many of these colored spectrograms are not accompanied by

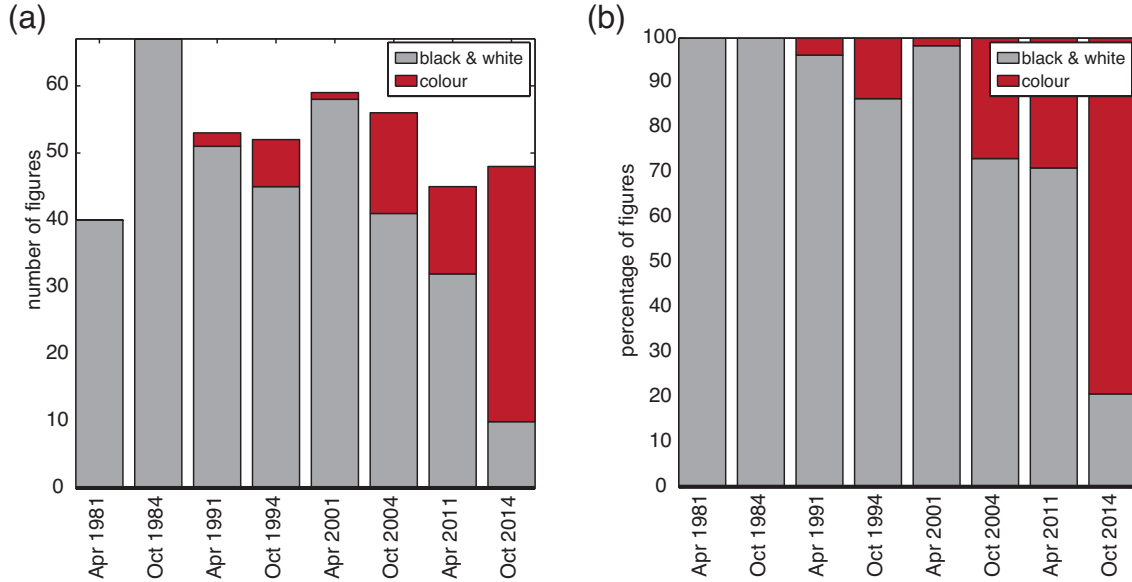


Figure A.1: Color use in geoscience publications, (a) in total numbers and (b) in percent.

a color scale (e.g., Fig.1.2, or *Lesage et al.*, 2006; *Almendros et al.*, 2012) on which the viewer can, for example, quantitatively assess differences in spectral power between different frequencies. The viewer thus has to rely solely on their perception of the colors in the map for interpretation. Most studies with colored spectrograms use a rainbow color map, which, for example, was the default color map in MatLab® before version R2014b, and in many other software packages (*Borland and Taylor*, 2007). It has been shown, that many standard rainbow color maps (including the previously mentioned MatLab® default “jet”) suffer from a number of challenges:

1. Lightness on rainbow color maps generally does not change monotonically. However, at small spatial scales, for example in a figure with many small variations, the human perception is mostly sensitive to lightness as opposed to color (e.g., *Mullen*, 1985; *Stone*, 2012). Rainbow color maps do not work well for visualization of data at small spatial scales.
2. Similarly, rainbow color maps do not follow perceptual ordering like purely luminance based color maps do (*Borland and Taylor*, 2007). Figure A.2 shows a rainbow series of 4 squares derived from 4 evenly spaced samples of the MatLab® color map “jet”. The top row follows the rainbow ordering from blue to red. The second row shows the same colors converted to greyscale. Whereas the blue and red square have the same luminance, the cyan and yellow squares are slightly different from each other. The third row shows a better ordering of the squares in terms of their luminance, and the fourth row shows the equivalent order in color space, which appears counter intuitive based on the wavelength spectrum of the colors.
3. The transition from one hue to the next along a rainbow color map can introduce sharp, artificial contrasts that may be interpreted as strong contrasts in the data (e.g., *Rogowitz and Treinish*, 1998). In addition, some color variations are not easily perceived, and thus apparently cover a larger range of data values compared to others.

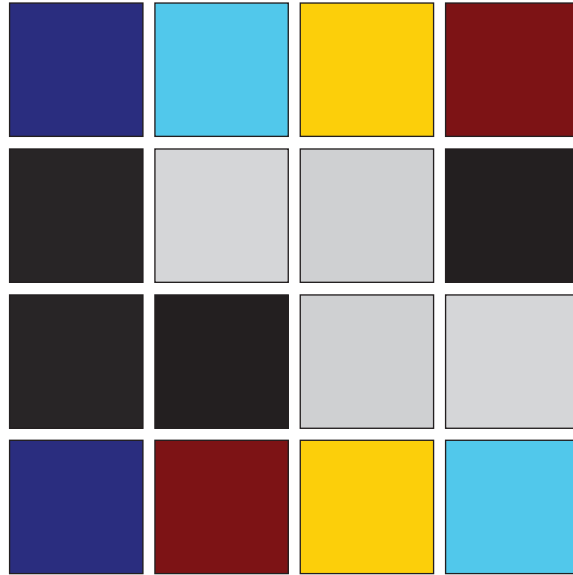


Figure A.2: Ordering issues for rainbow color maps. First row shows ordering of squares based on rainbow color map, second row shows conversion to grey scale. Third row shows reordered squares based on grey scale/luminance, and fourth row translates the new order back to color space. For more discussion see main body of text.

A.2 Some Ideas for Improvement

A.2.1 Using Line Graphs Instead of Images

When color figures were expensive or simply not available in scientific publishing, many authors utilized alternative ways to display the same information. A simple way to convey temporal variation in spectral content of seismic data is to show a series of spectra taken from different time windows (Fig. A.3). When these spectra are plotted at a slight offset from each other, and there are enough spectra over time, this can create the 3D effect shown in Figure A.3(b). An actual 3D graph viewed at an angle could further improve this type of visualization. A disadvantage is that, depending on the level of noise, the scaling, and the number of spectra, visualization of the temporally changing spectral information may be messy and difficult to interpret.

A.2.2 Greyscale Color Maps

An alternative to simple line graphs is to show spectrograms with greyscale color maps. Figure A.4 shows an example for a greyscale spectrogram from *Sherburn et al. (1998)*. Note that no legend or scale bar for the different shades of grey exist, which makes interpretation more subjective. Another example can be seen in Figure 1.2. With greyscale color maps, luminance changes monotonically, and thus no “ordering” issues arise.

However, a challenge persists: The perceived “middle” grey level does not align with the center of the scale for most standard vendor greyscale maps. Bespoke color maps (including greyscale)

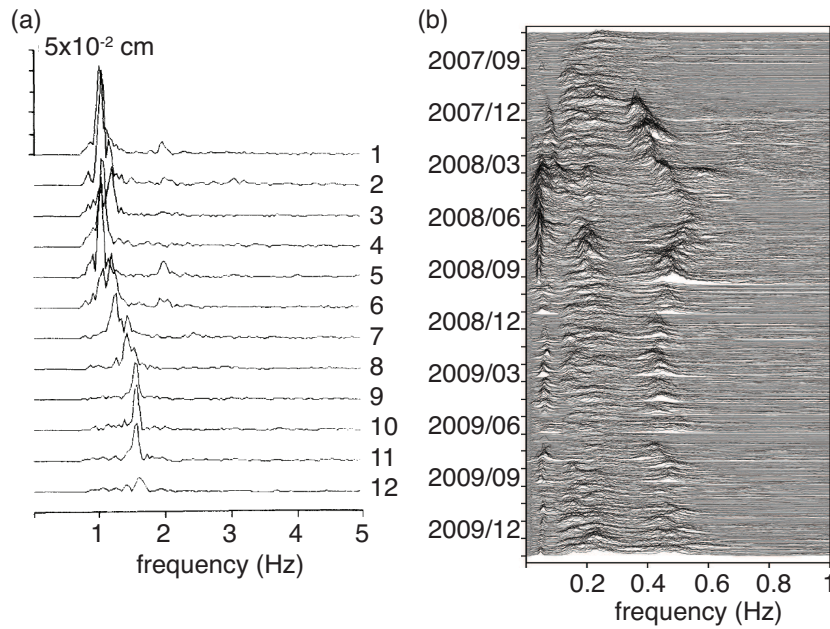


Figure A.3: Line graph spectrograms. (a) Tremor spectrogram over 120 seconds from Langila Volcano, Papua New Guinea, recorded between 1977 and 1986 (*Mori et al.*, 1989). Numbers next to spectra indicate 10 second window number. *Reproduced with permission from Elsevier.* (b) Spectrogram for VLPs from over 2 years at Kīlauea (*Dawson et al.*, 2010). Note the lack of a scale for the spectra. *Reproduced with permission from Wiley.*

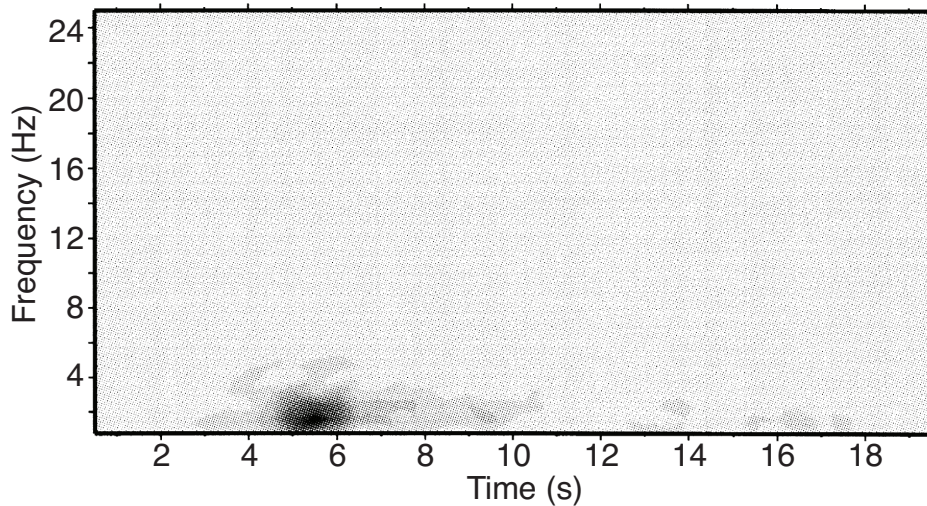


Figure A.4: Greyscale spectrogram from a volcanic earthquake, recorded on White Island, New Zealand, in February 1992 (*Sherburn et al.*, 1998). Greyscale is achieved by displaying different point densities. *Reproduced with permission from Elsevier.*

are thus necessary.

A.2.3 Perceptually Uniform Color Maps

Figure A.5 shows a spectrogram with a variety of features from Kīlauea at station OTL with three different color maps. The top image uses the MATLAB® standard “jet”, which results in an apparent sharp contrast between spectral power values around 10–15 dB (blue to cyan), and then again around 25–30 dB (green to yellow to orange). Whereas the range perceived as mostly uniform blue spans more than 10 dB, the range perceived as cyan only covers up to roughly 5 dB. Furthermore, the lightness gradient between cyan and yellow is very low, which may result in masking of features in the data (Kovesi, 2015). Similar imbalances with the other colors may cause some parts of a given dataset to appear more prominent than others. In order to avoid these issues, Kovesi (2015) designed a series of perceptually uniform color maps, where flat spots as well as sharp artificial contrasts are minimised. For full details of these implementations see Kovesi (2015). Using a better, more perceptually uniform rainbow color map for the spectrogram (Fig. A.5, second spectrogram) shows that the apparent strong change from high to low spectral power and back to high values between Phases I and II is partly an artifact of the color map used in the top spectrogram. Despite this improvement, the second rainbow color map still suffers from a reversal of the lightness gradient from yellow to red (see discussion in Section A.1 and Fig. A.2). A color map based on only one color with a constant lightness gradient can help to alleviate this issue (Fig. A.5, third spectrogram). This approach is equivalent to using a suitable greyscale map.

In summary, all of the approaches mentioned above have their own advantages and disadvantages. There is no unique “best” choice. Instead, the most suitable option depends on the type and distribution of data to be visualized. However, most studies agree that the default rainbow color map, that MATLAB® and other software packages (used to) have built-in, is the least desirable option, and a better choice can almost always be made. At the very least, any data visualization that uses color (including greyscale) should have a legend so that the perceived colors can be referenced against numerical values.

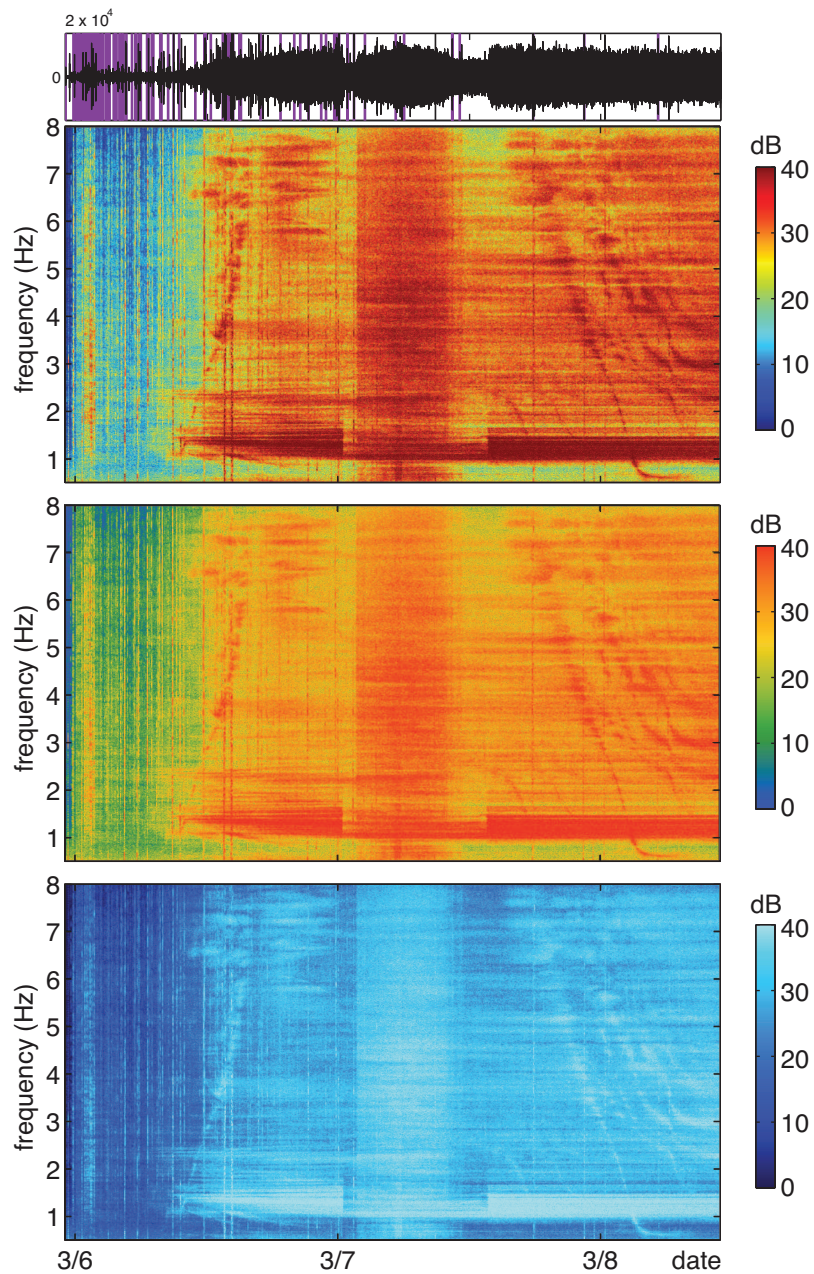


Figure A.5: Spectrogram from Hawai'i at station OTL during intrusion in 2011 with different color maps. For description of the data see Fig. 2.5. Spectrogram panels show (from top to bottom) MATLAB® color map “jet”, a rainbow color map implementation and a linear blue color map implementation by *Kovesi* (2015). The second and third color maps are designed to be more perceptually uniform. Figure modified from Chapter 2, *reproduced with permission from Wiley*.